2D TRANSITION-METAL DICHALCOGENIDE MONOLAYERS AND THEIR JANUS STRUCTURES FOR NEXT-GENERATION ELECTRONICS AND ENERGY CONVERSION: AN *AB-INITIO* STUDY

NITYASAGAR JENA

A thesis submitted for the partial fulfillment of the degree of

Doctor of Philosophy

Institute of Nano Science and Technology Mohali

Phase 10, Sector 64, SAS Nagar, Mohali 160062, Punjab, India.

&

Indian Institute of Science Education and Research Mohali

Knowledge city, Sector 81, SAS Nagar, Manauli PO, Mohali 140306, Punjab, India.

April 2020

Dedicated to the readers…

Declaration

The work presented in this thesis has been carried out by me under the guidance of **Professor Abir De Sarkar** at the Institute of Nano Science and Technology Mohali. This work has not been submitted in part or in full for a degree, a diploma, or a fellowship to any other university or institute. Whenever contributions of others are involved, every effort is made to indicate this clearly, with due acknowledgement of collaborative research and discussions. This thesis is a bonafide record of original work done by me and all sources listed within have been detailed in the bibliography.

Nityasagar Jena

(Candidate)

In my capacity as the supervisor of the candidate's thesis work, I certify that the above statements by the candidate are true to the best of my knowledge.

Professor Dr. Abir De Sarkar

(Thesis Supervisor)

⟨Acknowledgements⟩

My journey towards this Ph.D. degree has procured a significant part of my life, which immensely benefited me as a young researcher in the area of computational material science and significantly contributed in building my overall character as a person of scientific value, an agile thinker, and also in becoming a curious-tolerant mind with noble scientific temper.

First and foremost, I would like to express my utmost gratitude to my Ph.D. supervisor, Prof. Abir De Sarkar (Scientist F & Dean Academics). He who first introduced me to the computational material science. I am immensely thankful to him and much acknowledge all his motivation, encouragement, unconditional support, and enlightening suggestions from the very early days of my joining his esteemed research group at INST-Mohali. It is my great privilege and utter fortune to work under his admirable supervision. To be with him, learning and working are extremely rewarding both in a professorial and personal sense. Prof. De Sarkar has provided me the full privilege to choose my scientific idea and the scientific problems of our mutual interest to embark upon, which is an invaluable treasure for a young researcher like me to work on various aspects of a problem. It was always exciting for me to choose a new frontier of research under his benign supervision. Moreover, his scientific guidance in many of my theoretical projects, as well as joint projects with experimentalists from in and out of INST-Mohali, has hugely benefited me in leveraging my scientific caliber. Many insightful discussions with Prof. De Sarkar and his excellent guidance was an excellent opportunity for me to excel in my scientific and academic pursuit. Moreover, his commendable language skills and effective communication in many instances of our scientific dialogue are of great benefit to be an active science communicator. I am incredibly fortunate to work with such an outstanding individual and feel truly honored to be his 2nd Ph.D. student.

I express my heartfelt thanks and great appreciation to my research group members. I am lucky enough to be with such an exciting research group where constant motivation, the enthusiasm of work, and immediate scientific support was a great benefit to me. I would like to thank Dr. Dimple in particular for his generous support in scientific computing from the day of my joining the group and his profound scholarly background; first-rate computational skill has much supported our mutual research activity in Prof. De Sarkar's group.

I also thank and greatly acknowledge the generous scientific support and mutual understating that I received on our joint collaborative projects with Dr. Kiran Shankar Hazra, Dr. Ramendra Sundar Dey, Dr. S. K. Pal (IISER Mohali), Prof. Goutam De and their research group at INST Mohali.

I greatly acknowledge and thankful to Dr. Seema Gautam, a former national post-doctoral fellow in our research group for her great inspiration, help, and support during her post-doctoral tenure at INST. My research work at INST would not have been possible without the full support of my beloved group members: Ashima Rawat, Manish Kumar Mohanta, Raihan Ahammed, Pradip Nandi, Amal Kishore, and Miss. Fatima from the past few years in being involved with me in many insightful scientific work, discussions, and group meetings. It was a pleasure being involved with them freely in many of the scientific discussions.

I extend my thanks and appreciation to my colleagues and friends: Ruchi, Neha, Renu, Soumen, Anirban, Prabhjot, Kalpesh, Atul, Pulkit, Sandeep, Anup, Ashmeet, and others for being a source of great joy and many of their unmentioned support during my years at INST. I also thank all my teachers who taught me during my course work both at INST and IISER-Mohali.

Finally, I would like to thank the supreme lord, my lovely parents and my large nuclear family back at home for their generous support and blessings, with this, I dedicate this work to the readers of this thesis.

@ Nitya

⟨ABSTRACT⟩

The interplay of charge, spin, and valley pseudospin degrees of freedom (DOF) in a single integrated system is the future prospect of next-generation electronic devices. In this thesis, monolayers (ML) of Group-VIB transition metal dichalcogenides (TMDCs) with generic chemical formula MX_2 (M = Mo, W, etc. and X = S, Se, Te) have been studied as potential candidates for two-dimensional (2D) electronics, spintronics, and valleytronics. Being atomically thin semiconductors, ML-MX_2 is endowed with many fascinating properties, such as intrinsic direct bandgap (E_g ~ 1-2 eV) lying within the visible light region, high room temperature carrier mobility (~ 100-700 $cm^2V^{-1}s^{-1}$) and giant spin-orbit coupling (~148-456 meV) close to the K point where the direct bandgap occurs. Moreover, the lattice inversion symmetry is explicitly broken in the monolayers of MX_2, giving rise to a high degree of piezoelectricity (~ 3-7 pm/V). The exciting valley contrasting Berry curvature at the low energy time-reversal valleys at K and -K points in the Brillouin Zone is an exotic phenomenon, allowing to exploit the spin-valley coupled carriers in these multivalley electronic systems.

More recently, a new class of monolayer MXY, the so-called Janus derivative of MX_2, has drawn a great deal of research attention, where; X ≠ Y. By breaking the out-of-plane chalcogen sublattice symmetry, novel Rashba-type band splitting and large vertical piezoelectricity has been induced in MXY monolayers. Furthermore, the Rashba spin-orbit interaction is highly strain-tunable in MXY on account of the sensitivity of the dipolar contrast between chalcogen sublattices to the application of strain. The valley contrasting phenomena is also found to be strongly modulated via the application of strain, where the effect is found to be greater for tungsten-based systems.

From the family of semiconducting TMDCs, monolayer MoS_2 has drawn a great deal of scientific attention and has been considered to be a perfect semiconducting alternative to semi-metallic graphene. Considering ML-MoS_2 as a candidate system for *ab initio* studies, the potential of this host semiconductor for electronics, spintronics, and valleytronics has been studied under varying in-plane strain. The elastic strength and mechanical stability under various strain modes have been analyzed in detail.

Under the application of uniaxial strain, the conduction band minimum (CBM) of a strained ML-MoS_2 is found to drift nearly 2-times that of the valence band maximum (VBM) about the K-point. The resulting strain induced valley decoherence lifts the valley momentum degeneracy of carriers, thereby affecting the valley contrasting phenomena in a strained MX_2 lattice considerably. The origin of the decoherent valley under applied strain has been ascertained from both geometric and electronic effects, i.e., via alteration in its 2D elasticity and the orbital wave function of low-energy Bloch bands at the respective band-edges.

Raman spectroscopy has proven itself to be a non-invasive tool for atomically-thin monolayers under strain. Using first-principles density functional perturbation theory (DFPT), the behavior of crystal phonons in a strained ML-MoS_2, mainly, the characteristic Raman and IR active vibrations in ML-MoS_2 have been investigated. A large phonon anisotropy and an anomalous

frequency shift in the vibrational modes have been observed under the application of strain. The original two-fold frequency degeneracy in its in-plane E_{2g}^{1} Raman active vibration splits into nondegenerate E_{2g}^{1+} & E_{2g}^{1-} singlet sub-bands under anisotropic lattice deformation. The vibrational anisotropy is found to scale with the strain-induced elastic anisotropy in its planar stiffness tensors, C_{11} and C_{22}, and anisotropic phonon electrostatic coupling in a polar semiconductor like ML-MoS_2. Strong strain-phonon coupling is of crucial importance in accessing the vibrational fingerprints of ML-MoS_2 under the application of various kinds of in-plane strain.

The predictive findings presented in this thesis on Group-VIB transition metal dichalcogenides (TMDCs) with a particular focus on ML-MoS_2 and its strain sensitive properties are of paramount interest in future flexible electronics, where the simultaneous occurrence of various quantum DOF in a single integrated electronic system comprising of MX_2 & MXY monolayer crystals can be gainfully exploited.

----------**********----------

⟨List of Publications⟩

Included as part of this thesis

#1. **Nityasagar Jena**, Dimple, Raihan Ahammed, Ashima Rawat, Manish Kumar Mohanta, and Abir De Sarkar, "*Valley drift and valley current modulation in strained monolayer MoS_2*".

***Phys. Rev. B** 2019, **100,** 165413*

#2. **Nityasagar Jena**, Dimple, Shounak Dhananjay Behere, and Abir De Sarkar, "*Strain-Induced Optimization of Nanoelectromechanical Energy Harvesting and Nanopiezotronic Response in a MoS_2 Monolayer Nanosheet*". ***J. Phys. Chem. C** 2017, **121,** 9181-9190*

#3. **Nityasagar Jena**, Dimple, Raihan Ahammed, Manish Kumar Mohanta, Ashima Rawat, and Abir De Sarkar, "*Anomalous lattice vibration in strained monolayer MoS_2: Breaking the vibrational frequency degeneracy under extreme in-plane strain*". ***[In manuscript]***

#4. **Nityasagar Jena**, and Abir De Sarkar, "*Spin-orbit interaction and valley contrasting phenomena in pure and Janus monolayers of 1H transition-metal dichalcogenides*". ***[In manuscript]***

Not included in the thesis

#5. Dimple, **Nityasagar Jena**, and Abir De Sarkar, "*Compressive strain induced enhancement in thermoelectric-power-factor in monolayer MoS_2 nanosheet*", ***Journal of Physics: Condensed Matter*** *2017,* ***29,*** *225501* ***[Featured in IOP annual highlight]***

#6. Dimple, **Nityasagar Jena**, Ashima Rawat, Raihan Ahammed, Manish Kumar Mohanta, and Abir De Sarkar, "*Emergence of high piezoelectricity along with robust electron mobility in Janus structures in semiconducting Group IVB dichalcogenide monolayers*", ***J. Mater. Chem. A*** *2018,* ***6,*** *24885-24898*

#7. Ashima Rawat, **Nityasagar Jena**, Dimple, and Abir De Sarkar, "*A comprehensive study on carrier mobility and artificial photosynthetic properties in group VI B transition metal dichalcogenide monolayers*", ***J. Mater. Chem. A*** *2018,* ***6,*** *8693– 8704*

#8. Dimple, **Nityasagar Jena**, Ashima Rawat, and Abir De Sarkar, "*Strain and pH facilitated artificial photosynthesis in monolayer MoS_2 nanosheets*", ***J. Mater. Chem. A*** *2017,* ***5,*** *22265-22276*

#9. Manish Kumar Mohanta, Dimple, Ashima Rawat, **Nityasagar Jena**, Raihan Ahammed, and Abir De Sarkar, "*Ultra-low thermal conductivity and super-slow hot-carrier thermalization induced by a huge phononic gap in multifunctional nanoscale boron pnictides*", ***Physica E:*** *Low-dimensional Systems and Nanostructures* 2020, **124**, 114222

#10. Ashima Rawat, Raihan Ahammed, Dimple, **Nityasagar Jena**, Manish Kumar Mohanta, and Abir De Sarkar, "*Solar Energy Harvesting in Type II van der Waals Heterostructures of Semiconducting Group III Monochalcogenide Monolayers*", ***J. Phys. Chem. C*** *2019,* ***123,*** *12666-12675*

#11. Raihan Ahammed, Ashima Rawat, **Nityasagar Jena**, Dimple, Manish Kumar Mohanta, and Abir De Sarkar, "*ZrS_3/MS_2 and ZrS_3/MXY (M=Mo, and W; X, Y=S, Se, and Te) type-II van der Waals hetero-bilayers: Prospective candidates in 2D excitonic solar cells*", ***Applied Surface Science*** *2019,* **499,** 143894

#12. Manish Kumar Mohanta, Ashima Rawat, Dimple, **Nityasagar Jena**, Raihan Ahammed, and Abir De Sarkar, "*Superhigh out-of-plane piezoelectricity, low thermal conductivity and photocatalytic abilities in ultrathin 2D van der Waals heterostructures of Boron Monophosphide and Gallium Nitride*", ***Nanoscale*** 2019, **11**, 21880-21890

#13. Dimple, Manish Kumar Mohanta, Ashima Rawat, **Nityasagar Jena**, Raihan Ahammed, and Abir De Sarkar, "*Ultra-low lattice thermal conductivity and giant phonon–electric field coupling in hafnium dichalcogenide monolayers*", ***J. Phys.: Condens. Matter*** *2020, **32**, 315301*

#14. Manish Kumar Mohanta, Ashima Rawat, **Nityasagar Jena**, Dimple, Raihan Ahammed, and Abir De Sarkar, "*Interfacing Boron Monophosphide with Molybdenum Disulphide for an Ultrahigh Performance in Thermoelectrics, Two-Dimensional Excitonic Solar Cells, and Nanopiezotronics*", ***ACS Appl. Mater. Interfaces*** *2020**, 12,** 3114-3126*

#15. Manish Kumar Mohanta, Ashima Rawat, **Nityasagar Jena**, Raihan Ahammed, and Abir De Sarkar, "*Superhigh flexibility and out-of-plane piezoelectricity together with strong anharmonic phonon scattering induced extremely low lattice thermal conductivity in hexagonal buckled CdX (X= S, Se) monolayers*", ***J. Phys.: Condens. Matter*** *2020**, 32,** 355301*

#16. Ashima Rawat, Manish Kumar Mohanta, **Nityasagar Jena**, Dimple, Raihan Ahammed, and Abir De Sarkar, "*Nanoscale Interfaces of Janus Monolayers of Transition Metal Dichalcogenides for 2D Photovoltaic and Piezoelectric Applications*", ***J. Phys. Chem. C*** 2020, **124**, 19, 10385-10397

In collaboration with experimentalists

#17. Renu Rani, Dimple, **Nityasagar Jena**, Anirban Kundu, Abir De Sarkar, and Kiran Shankar Hazra, "*Controlled formation of nanostructures on MoS_2 layers by focused laser irradiation*", ***Appl. Phys. Lett.*** *2017**, 110,** 083101* **(Featured article in AIP)**

#18. Neha Wadehra, Ruchi Tomar, Soumyadip Halder, Minaxi Sharma, Inderjit Singh, **Nityasagar Jena**, Bhanu Prakash, Abir De Sarkar, Chandan Bera, Ananth Venkatesan, and S. Chakraverty, "*Electronic structure modification of the $KTaO_3$ single-crystal surface by Ar+ bombardment*", ***Phys. Rev. B*** *2017**, 96,** 115423*

#19. Harpreet Singh,Vijay K. Tomer, **Nityasagar Jena**, Indu Bala, Nidhi Sharma, Devadutta Nepak, Abir De Sarkar, Kamalakannan Kailasam, and Santanu Kumar Pal, "*A porous, crystalline truxene-based covalent organic framework and its application in humidity sensing*", ***Journal of Materials Chemistry A*** 2017**, 5,** 21820-21827

#20. Manisha Das, **Nityasagar Jena**, Taniya Purkait, Navpreet Kamboj, Abir De Sarkar, and Ramendra Sundar Dey**,** "*Single-phase Ni_5P_4–copper foam superhydrophilic and aerophobic core–shell nanostructures for efficient hydrogen evolution reaction*", ***J. Mater. Chem. A*** 2019**,** 7**,** 23989-23999 **(Featured as emerging research article)**

#21. Indranee Das, **Nityasagar Jena**, Debtosh Kundu, and Goutam De, "Genesis of Hydration Controlled Boehmite Flexibility toward the Shaping of Unsupported Aluminas", ***[In manuscript]***

#22. Harpreet Singh, Manisha Devi†, **Nityasagar Jena**†, Musthafa Iqbal, Yogendra Nailwal, Abir De sarkar, and Santanu Kumar Pal, "*Proton Triggered Fluorescence Switching in Self-Exfoliated Ionic Covalent Organic Nanosheets for Applications in Selective Detection of Anions*", ***ACS Applied Materials & Interfaces***, 2020,**12,** 13248-13255

† share the co-equal second author

#23. Renu Rani†, **Nityasagar Jena**†, Anirban Kundu, Abir De Sarkar, and Kiran Shankar Hazra, "*Impact of transverse and vertical gate electric field on vibrational and electronic properties of MoS_2*", ***Journal of Applied Physics*** *2020, **127**, 145101*

† share the co-equal first author

In conference proceedings

I. Dimple, **Nityasagar Jena**, Shounak Dhananjay Behere, and Abir De Sarkar, "*The effects of different possible modes of uniaxial strain on the tunability of electronic and band structures in MoS_2 monolayer nanosheet via first-principles density functional theory*", ***Pramana – J. Phys. – Springer 2017, 89: 2, 1-7***

II. **Nityasagar Jena**, Dimple, and Abir De Sarkar, "*First-principles investigation on the lattice thermodynamic properties of strained two-dimensional monolayer MoS_2 nanosheet*", **AIP Conference Proceedings on Advanced Materials**, AIP Conf. Proc. 2005, *090001 (2018)-1-090001*-8; https://doi.org/10.1063/1.5050770, Published by AIP Publishing. *978-0-7354-1721 2/$30.30, 090001-1*.

----------**********----------

⟨Table of Content⟩

----------**********----------

⟨List of Figure⟩

----------**********----------

⟨List of Table⟩

----------**********----------

⟨Abbreviations⟩

TMDCs	Transition-metal dichalcogenides
BEC	Born effective charges
BZ	Brillouin zone
CBM	Conduction band minimum
VBM	Valence band maximum
DFPT	Density functional perturbation theory
DFT	Density functional theory
GGA	Generalized gradient approximation
KS	Kohn-Sham scheme
PBE	Perdew-Burke-Ernzerhof functional
vdWs	van der Waals

⟨Symbols⟩

$\hbar$	Plank constant
Z_{ij}^{*}	Born effective charge tensor
T	Temperature in K
E_c	Cohesive energy per unit cell
W	Work function
m^{*}	Effective mass of electron/hole
σ_{ij}	Elastic stress tensor
ε_{kl}	Elastic strain tensor
C_{ijkl}	Total elastic stiffness tensor
P_i	Polarisation vector
e_{ijk}	Piezoelectric stress coefficient
d_{ijk}	Piezoelectric strain coefficient

"things take time – there are many examples of materials taking more than 20 years to get to market"
Amaia Zurutuza

Chapter 1

In this chapter, we provide a general introduction to the discovery of two-dimensional (2D) material: "graphene" and the emergence of several other 2D materials in the post-graphene-era with particular attention on the emerging properties of transition-metal dichalcogenides (TMDCs) or semiconducting MX_2 monolayers of *Group VIB* elements (where *M* = Mo, W, etc. and *X* = S, Se, Te); and their Janus structures, namely MXY monolayers (where X ≠ Y = S, Se, Te).

INTRODUCTION

1.1 A general introduction to two-dimensional materials

Since prehistoric times, the foundation of our human civilization has great chemistry with its surrounding matter in discovering, understanding, and utilizing various materials to leverage the human potential and ease human life.[1] From the ancient Stone, Bronze and Iron Ages down to the current information age, the search and use of new materials with superior functionalities for sustainable development has always been a significant driver of ambitious technological inventions[2] and future energy systems[3] in the advancement of the human race as a whole.[4]

The better we understand the behavior, composition, and properties of different materials, the more we can push today's technological boundaries for tomorrow's need.[5], [6] The discovery of precious metals, minerals, and polymers in the century past was brought a significant industrial revolution for our immediate ancestors. In this modern information age -with massive digital data & internet of things, the storage and processing capacity for high-speed digital information transfer across the globe at a much faster pace has thrown new material challenges on the current microelectronics that are built upon the decade past silicon technology.[7] To reduce the feature size of processor units in electronic devices with high-end energy-saving performance, the advancement of new nanostructures, multi-functional two-dimensional materials, and hybrid complex structures is of immediate need.[8], [9]

Over the past few decades, the discovery and designing of new materials with sophisticated fabrication techniques have shown tremendous technological potential for future nanoscale electronics and optoelectronics.[9]–[11] Among several other material options, 2D materials are ideal and have a clear advantage to supplement the well-established manufacturing techniques developed for silicon microelectronics in order to fabricate 2D material based

ultrathin, flexible and low power electronic devices.[10], [12]–[14] In recent years, atomically thin 2D materials have shown far greater potential for novel electronics and energy conversion applications.[14]

The research and search of new atomically thin 2D materials with various desired functionalities is currently at its peak[15], and emerging as one of the fastest-growing research areas in contemporary material science that offers rich physics, such as valley Hall effect, spin Hall effect, topological superconductivity, Klein tunneling, circular dichroism, second harmonic effects, and so on[16]–[18] in reduced dimensions that are promising for future multi-functional technological applications.[19], [20]

In a simplified term, "*2D materials*" are referred to as atomically thin crystals consisting of one or a few atomic layers with high aspect (surface-to-volume) ratios that can be potentially isolated and become stable without any surface epitaxial layer. 2D materials offer many exotic properties that are very different and sometimes unique as compared to their host bulk crystals including the ultra-high elastic stiffness (Young's modulus > 1TPa) of graphene,[21] intrinsic direct bandgap (~ 1.8-1.9 eV) in monolayer MoS_2 [22] with high electroluminescence [23] and strong spin-orbit coupling (~ 150-500 meV),[24] and the insulating wide bandgap of (~ 4-6 eV) hexagonal boron nitride.[25], [26] Besides, the pristine surfaces of 2D materials that are free from any surface dangling bonds provide a natural benefit for efficient catalytic activity[27] and greater sensitivity for molecular sensing applications.[28]

The overwhelmingly increasing application potential of 2D materials in recent years has made us believe that the current discoveries and research avenues for 2D materials will continue to evolve in an unprecedented manner with the appearance of many unique properties for future technological challenges for high-speed electronics, optoelectronics and energy applications.[29]

In fact, in the early days of quantum theory (1935), Peierls[30] and Landau[31] theoretically argued the thermodynamical unfavorability of strictly two-dimensional (2D) atomic crystals down to an atomic thickness at any finite temperature. Their empirical deduction pointed out, the fluctuations in the energy of the wave packet can destroy the long-range crystalline order of 2D atomic crystals at any finite temperature, eventually leading to a segregated island of atomic clusters or warping of 2D monolayer sheets into random 3D structures[32]. This pragmatic argument was later supported by Mermin-Wagner[33], [34], and endorsed by the omnibus of experimental observations in due course, ultimately solidifying the hypothesis that atomically thin 2D crystals could not exist at room temperature. Nearly eight-decade this prevalent hypothesis lingered the discovery of 2D materials, until the year 2004 for its disapproval. The groundbreaking discovery of atomically thin films of carbon by *Konstantin Novoselov* and *Andre Geim* in 2004[35] completely mopped this enduring hypothesis by isolating a monolayer sheet of graphite, so-called "graphene." Since then, the thriving properties and divergent application potential of this novel quantum material (graphene) with a magnitude of unique properties demonstrated over the years have revolutionized many areas of science & technology and recognized for the 2010 Nobel Prize in Physics.

The revolutionary discovery of graphene through a simple mechanical exfoliation strategy has spurred tremendous scientific attention in the "*gold rush*" of 2D atomic crystals in their perfectly one-atom-thick flat-land or quasi-2D layered structures of ultrathin monolayers from various van der Waals (vdW) crystals.[12] Extensive studies worldwide in recent years has led to the discovery of many inorganic 2D crystals, including hexagonal-boron-nitride (h-BN), molybdenum disulfide (MoS_2), and phosphorene (a monolayer of black phosphorus) to name a few emerging 2D materials from a large pool of 2D atomic crystals.[12], [36] With the number of currently available 2D materials, it is now possible to cover a wider range of electromagnetic energy starting from near UV (ultraviolet) to the far IR (infrared) spectrum

with the range of electronic character in available materials ranging from semi-metallic graphene, silicene, and germanene[12], [37]–[39] to the semiconducting transition metal dichalcogenides (MoS_2, ReS_2, ZrS_2, $HfSe_2$, TaS_2, $PtSe_2$ and so on),[40], [41] transition metal oxides (VO_2, WO_3, MoO_3),[42] insulating hexagonal boron nitride (h-BN), semiconducting black phosphorus (bandgap ~ 0.3-2 eV),[43], [44] and topological insulators (Bi_2Se_3, Bi_2Te_3, Sb_2Se_3, WTe_2, etc.).[45], [46]

The constellation of 2D materials has been increasing steadily by the utilization of recent data mining approaches and high-throughput quantum simulation methods.[47], [48] The use of intelligent search algorithms and high-performance computing architectures to explore and design new materials with desired properties are evolving in an unprecedented way with the use of computer-aided artificial intelligence (AI) neural network architecture, now, in computational material science.[15], [49], [50]

Using data mining and high-throughput calculations, many new 2D materials have been investigated in recent years, including layered MAX phases,[51] 2D MXenes (Ti_2AlC, Ti_3AlC_2, Ta_4AlC_3 and so on),[9], [52] 2D magnetic structures of metal phosphorous trichalcogenides (MPX_3; M= V, Cr, Mn, Fe, Ni Zn, etc; X = S, Se, Te),[53], [54] complex 2D oxides ($Ba_2Sr_2CaCu_2O_x$)[26], 2D halides (CrI_3)/ carbides (Ti_2C, Zr_2C)/ nitrides (NbN) [55]–[57], and over more than 216 MXY Janus monolayers (MoSSe, WSSe, PtSSe and so on) have been discovered more recently.[58] Moreover, using the same workflow algorithm, many current phases of 2D materials, such as h-BN, TMDCs (MoS_2, WSe_2, etc.) and phosphorene, have been reconfirmed in their most stable structural phases.[59] Besides, several new structural polytypic phases of already existing 2D materials have been discovered through global energy optimization approaches,[15], [59]–[61] such as a new 1T'' phase of MoS_2 with nontrivial band gap ~ 0.42 eV that exhibit quantum spin Hall effect,[62] and stable symmetry reduced charge density wave phase of monolayer 1T-$TiSe_2$.[63]

Many of these 2D crystals have been experimentally synthesized, in recent past, through sophisticated layer isolation techniques from their parent 3D crystals,[60], [63]–[65] including methods, such as surfactant-assisted ultrasonication,[9] synthetic wafer-scale growth via chemical vapor deposition (CVD), liquid-phase exfoliation,[66] ion intercalation, molecular beam epitaxy (MBE), surface segregation[9] and simple micromechanical cleavage technique pioneered by K. Novoselov and A. Geim (2004)[35] for the first isolation of graphene (scotch-tape peeling method). Moreover, the 2D material transfer techniques have been largely improved over the years with efficient sample transfer methods in order to achieve high-quality defect-free monolayer crystals.[9] The weak van der Waals (vdW) interactions that present in families of layered materials, including graphene, h-BN, and MoS_2, make them easy to exfoliate due to weak interlayer binding energy.[67], [68] Moreover, graphite, and bulk crystals of h-BN, and MoS_2 are commonly used as solid or dry-lubricants in friction units owing to their weakly coupled inter-layer structure. Thus, it is easy to exfoliate a single or few-layers of material from their parent bulk crystals for laboratory research to promote the isolation of similar 2D materials for future technological applications.

Furthermore, the method of van-der-Waals epitaxy[68], [69] in the making of multilayer heterostructures[68], [70], [71] and homostructures,[72]–[74] designed by the systematic stacking of atomic crystals in a layer-by-layer sequence with atomic precision to form complex artificial hybrid geometries in a Lego building assembly is appealing to create a plethora of functionalities via the combination of individual unique properties of 2D materials,[75], [76] which also sometimes shows revealing unusual properties, not accessible in individual monolayers. This strategy is fascinating to investigate various novel phenomena in 2D material, such as carrier tunneling and carrier drag in heterostructures, commensurate-incommensurate transitions, excitonic effects, Moiré patterns, and topological currents.[77]–[79]

Taking into account the unprecedented future technological potential of emerging 2D materials, in 2013 the *European Commission* of scientific research has initiated the *Graphene Flagship* project,[80] Europe's highest ever research budget of > 1 billion euros for a span of 10 years [81] that incorporates the scientific work and technological breakthroughs as one of its "Future and Emerging Technology" the vision for Horizon 2020.[82]

In the following section, we provide a pedagogical overview of transition-metal dichalcogenides (TMDCs), widely studied atomic crystals after graphene. The stable crystal geometry and various fundamental properties of TMDCs have been presented in subsequent sections to give an introductory understanding of novel electronic and vibrational properties in TMDCs by taking MoS_2 as an example system.

1.2 Transition metal dichalcogenides: An overview

Layered transition-metal dichalcogenides (TMDCs) are family of van der Waal (vdW) crystals with generic chemical expression MX_2, where M stands for the transition metal atom (M = Mo, W, Zr, Hf, Nb, or Ta, and so on) and X is the chalcogen element (X = S, Se, or Te). In recent years, there has been a resurgence of scientific interest on MX_2 crystals owing to their unique layered structure, anisotropic lattice environment with weakly coupled out-of-plane interactions of individual atomic layers attributed with the excellent electronic, optical, catalytic, and mechanical properties that are remarkably well suited for fundamental scientific studies and high-end technological applications for the achievable future avenues in electronics and optoelectronics.[2], [83] Several recent studies have shown numerous physical properties in monolayer TMDCs that are very different from those of their bulk crystals. Linus Pauling first demonstrated the bulk crystal structure of TMDC (molybdenite) in the year 1923.[84] Over the years, several TMDCs were discovered, and by the end of 1960, about 60 TMDCs were reported with more than 40 layered structures that can be cleaved down to a thickness < 1000 Å.[85] Many of the discovered TMDCs have shown distinctive physical properties

including, direct band-to-band transitions, exciton screening effects, *d*-band formation, charge density waves, and the metal-insulator transitions; also magnetism, superconductivity, and topological properties have been demonstrated.[2], [85]–[87]

In the year 1963, the method of adhesive tapes was first introduced by Robert Frindt in order to isolate and study the physical properties of ultrathin atomic layers of molybdenum disulfides (MoS_2), up to a thickness < 100 Å, via mechanical cleavage technique.[88] In the year 1986, Joensen *et al.* achieved a single-layer MoS_2 via liquid-phase exfoliation method by the intercalation of lithium into MoS_2 suspensions followed by water treatment reactions. Their X-ray diffraction data demonstrated the exfoliated MoS_2 thin layers have one-molecule-thick sheets in the MoS_2 suspension that are randomly stacked over one another.[89] The molybdenum disulfide (MoS_2) is a well-known solid lubricant used in friction units, tribology and also exhibit better catalytic response for the hydrodesulfurization reactions; and serves as an essential precursor for oxide-based fuel cells.[2]

Moreover, followed by the discovery of C_{60} chemistry, the cylindrical nanotubes and inorganic fullerene structures of tungsten disulfide (WS_2) and molybdenum disulfide (MoS_2) were synthesized in large quantities in controlled gas-phase growth conditions in 1992[90] and 1995[91], respectively. The fast pace research in graphene and related 2D materials in 2004 has brought a renewed interest in inorganic layered TMDCs in search of new stable semiconducting materials for photodetection platforms including ultrafast light detection, terahertz frequency generation and integrated optoelectronic systems by solely controlling their dimensionality.[86], [87], [92]

In TMDCs, the individual molecular units of X-M-X are held together by weakly van der Waals (vdW) forces of interactions, whereas, within a given layer, each M-atom is strongly coordinated with six chalcogen atom (X-atom) in a prismatic fashion. The central metal atom

layer (M-atom) in the MX_2 structure is sandwiched between two layers of chalcogen, forming a honeycomb lattice structure similar to graphene. Moreover, TMDCs can exist in various polymorphic structural phases with the difference in their atomic coordination between chalcogen–metal–chalcogen atoms and stacking sequences of individual MX_2 layers within the bulk unit cell or in a multilayer TMDC stacked units. The most common polytypes are trigonal prismatic (2H) phase, the octahedral (1T) phase, the dimerized (1T′) phase, and the orthorhombic ($1T_d$) phase.[93] The chemical composition and crystal symmetry play a crucial role in determining the electronic properties of crystals. Depending on the presence of transition-metal elements of Group-IV, V, VI, VII, IX, or X elements, TMDCs can exhibit in several stable and metastable polymorphic structures with very distinctive electronic properties.[94] For example, the Group VIB transition metals (M= Mo, W) are found to be most stable in their bulk 2H phase by forming trigonal prismatic coordination with surrounding chalcogen (S, Se, Te) elements.[95] In the bulk 2H phase, the Group VIB TMDCs exhibit a semiconducting indirect bandgap in the range of visible light E_g ~ 1-2 eV,[40] where the layers are stacked over one another in an ABA stacking order. On the other hand, the 1T ($P\bar{3}m2$) phase of Group VIB TMDCs is metastable at ambient condition and form octahedral prismatic coordination with chalcogen lattices in a rhombohedral ABC stacking pattern, exhibiting metallic behavior, ideal for electrochemical reactions.[96] In sharp contrast, the 1T phases of Group IVB TMDCs (ZrS_2, HfS_2, $HfSe_2$ and so on) are found to be most stable in their 1T octahedral phase as compared to the most stable 2H trigonal phase of Group VIB TMDCs.[97], [98] In 1T octahedral phase, the Group IVB TMDCs (HfS_2, $HfSe_2$, ZrS_2, and $ZrSe_2$ etc.) exhibit sizable global indirect band gaps in the visible light range E_g ~ 1.07-2.03 eV,[99]–[101] ultrahigh carrier mobility (100-1250 $cm^2V^{-1}s^{-1}$)[99], [102]–[104] at room temperature, much higher than Group VIB semiconducting monolayer TMDCs (MoS_2 ~ 300 $cm^2V^{-1}s^{-1}$),[10], [105] low lattice thermal conductivity of $ZrSe_2$ (k_L= 1.2 $Wm^{-1}K^{-1}$),[106] and *p*-type conductivity in

tunnel field-effect transistors (T-FETs).[107] Free-standing geometry of Group VIB TMDCs are unstable in the 1T phase, undergo lattice reconstruction (*Peierls distortion*) due to on-site electrostatic interactions by forming periodic *zigzag* chains of lattices along one of the crystal axes.[108] The dimerization of 1T octahedral phase due to Peierls distortion reduces the lattice symmetry into lower periodic 1T' ($P2_1/m$) metastable phase[109], [110] or distorted orthorhombic $1T_d$ ($P1m1$) phase that are accompanied by the charge density wave phases.[111] These lower symmetric phases offer rich physics, example includes, the emergence of non-trivial topological bands,[112]–[114] ferroelasticity in 1T'-MX_2 phase,[115] quantum nonlinear Hall effect,[116] non-zero Berry curvature in 1T' phase,[108] metal-insulator transition in 1T'-MoS_2 under the lattice strain,[117] topological superconductivity,[118], [119] and strongly correlated phenomena.[120]

1.2.1 Crystal structure of Group VIB TMDCs

The semiconducting bulk crystals of hexagonal 2H phase (see Figure 1.1) are energetically most stable for group VIB transition metal dichalcogenides that mainly includes widely studied MoS_2, WS_2 crystals and other dichalcogenides of the same group of elements, 2H-MX_2 (where *M* = Cr, Mo, W; and *X* = S, Se, or Te). The honeycomb arrangement of Mo and S atoms in MX_2 is akin to graphene, where the individual monolayers are stacked over one another in an ABA type layer sequence pattern and held together by the weak van der Waal (vdW) forces of interactions in the crystal thickness direction (*c*-axis). The monolayer MoS_2 is prepared by isolating a single layer from the multilayer unit of MX_2 or the bulk samples of 2H-MX_2. A monolayer MoS_2 isolated from the 2H structure is commonly referred to as 1H-MX_2 where the hexagonal symmetry of the lattice structure is retained with space group $P\bar{6}m2$. In 1H-MX_2 structures, the center of inversion is explicitly broken, and the monolayer crystals of Group VIB TMDCs belong to the non-centrosymmetric family of crystals. In a single atomic layer, the individual molecular units of X-M-X are tightly bound together via covalent interactions

with an intercalated M atom layer between hexagonal planes of X atoms in ABA Bernal stacking pattern. The strong covalent interactions in 1H-MX_2 arising from the hybridization of Mo 4*d* and S 3*p* atomic orbitals.

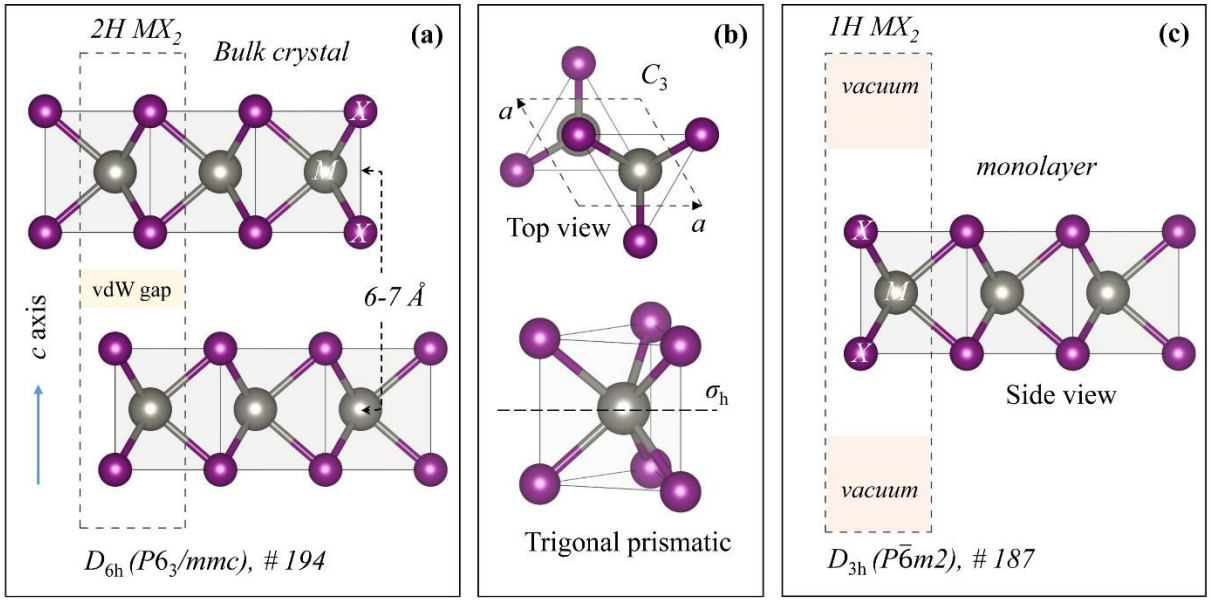

Figure 1.1. Crystal structures of bulk and monolayer MX_2 in semiconducting 2H and 1H phase, respectively. (a) Side view schematic geometry of bulk MX_2 in its 2H polytypic phase (space group $P6_3/mmc$) with two-layer repeating molecular units of MX_2 in a bulk unit cell (dashed line). (b) Top view of 2H-MX_2 in a hexagonal symmetry and trigonal prismatic coordination of chalcogen element (X-atom, in *violet*) around the central transition metal element (M-atom, in *gray*) in sandwich X-M-X structure. (c) A single layer of 2H-MX_2 named as 1H-MX_2 with symmetry reduction and the vacuum spacing around the layer to isolate the structure from surrounding interaction from its periodic replicas.

1.2.2 Electronic structure of TMDCs

The noncovalent interlayer vdW interaction in TMDCs plays a crucial role in determining the electronic properties of MX_2 (e.g., 2H-MoS_2). In Figure 1.2, we have shown the band structure of bulk and monolayer MoS_2. The bulk crystal of MoS_2 exhibits a global indirect energy gap

of about ~ 0.87 eV (experimental gap ~ 1.29 eV) using the DFT+PBE level of theory along its high symmetry line Γ-K [40] [See Figure 1.2 (a)], where the band edge of the valence band top (VBM) is occurring at the Γ point. Whereas, the conduction band edge (CBM) is occurring at the midpoint (Λ) of the line connecting the high-symmetry point Γ with K. When the number of MoS_2 layers reduces to a monolayer limit (only one S-Mo-S unit), a direct fundamental band gap of ~ 1.76 eV (experimental gap ~ 1.8-1.9 eV) emerge at the K point of the Brillouin zone (BZ), as shown in Figure 1.2 (b).[40] The effective masses of electron and hole are different for bulk and monolayer MoS_2 due to the curvature modification at the band edges, where the electron effective mass is smaller as compared to the hole effective mass, this breaks the electron-hole symmetry in MoS_2, as shown in Figure 1.2 (a)-(b). For clarity, we have also shown, in Figure 1.2 (c)-(d), the energy-momentum dispersion for the top of the valence band and bottom of the conduction band in a 2D *k* plane. The energy contour around the Γ point is circular, thus isotropic energy dispersion around the zone center, whereas the same around the K point is triangular and exhibits a 3-fold rotational symmetry in energy contour around the central K point. The occurrence of a global direct bandgap (~ 1.76 eV) at the K point of freestanding monolayer MoS_2 facilitates the vertical optical transition between low energy valleys of electronic band structure with enhancement in luminescence quantum efficiency by a factor > 10^4 with respect to bulk MoS_2 crystals.[121]

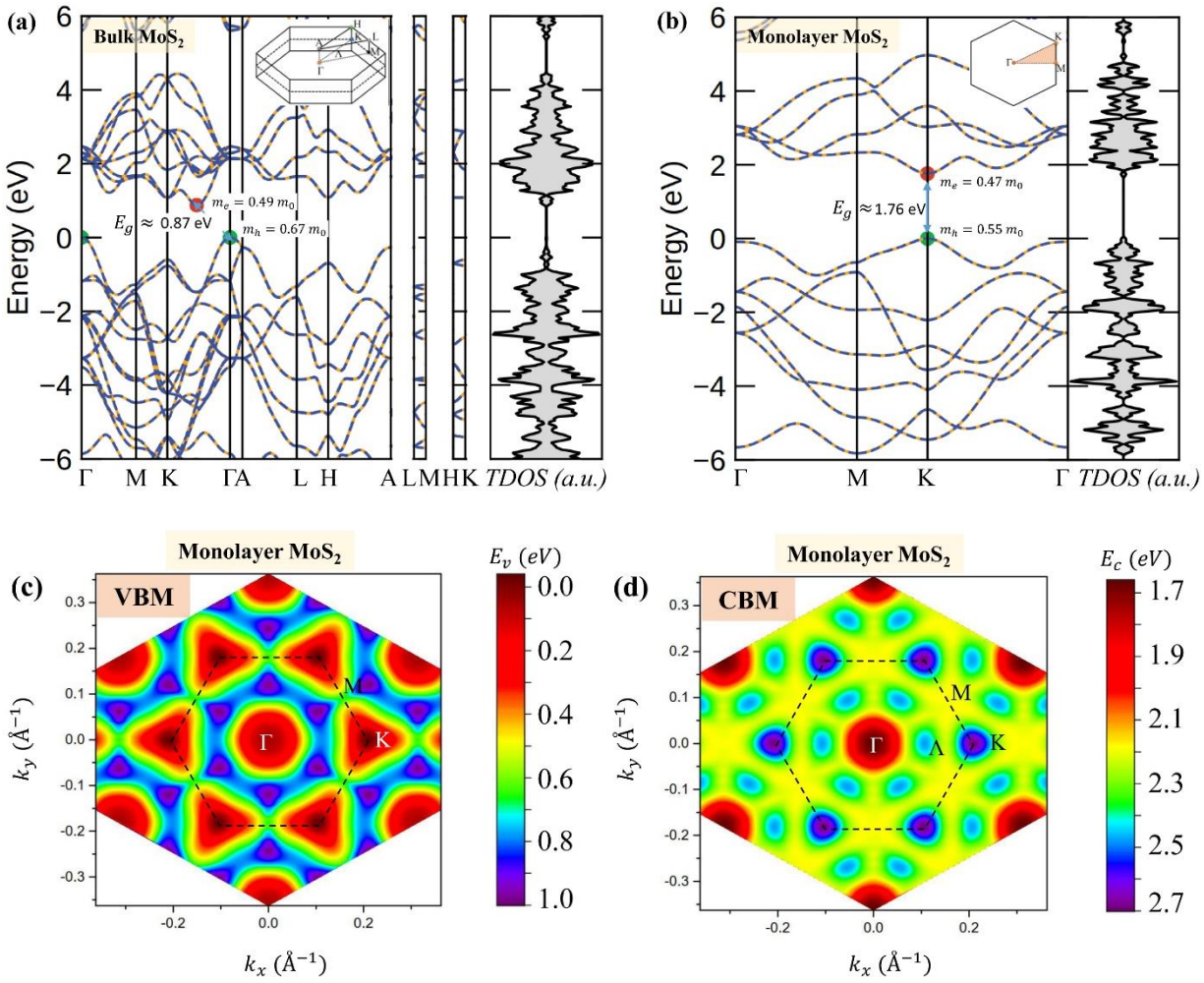

Figure 1.2. Calculated band structure of bulk and monolayer MoS_2 at the DFT-PBE level. (a) Band stru.cture of bulk MoS_2 and total density of states, Figure inset, includes the irreducible Brillouin zone of bulk MoS_2 with high-symmetry points. An indirect bandgap of ~ 0.87 eV occurs along the Γ-K high-symmetry line as indicated by the *arrow* from the top of valence band located at the Γ point (*green* circle) to the lowest energy of conduction band (*red* circle) originates at nearly halfway (Λ) between Γ-K high-symmetry line. (b) Band structure of monolayer MoS_2 (ML-MoS_2) with a direct bandgap ~1.76 eV occurring at the K-point of the Brillouin zone. The electron and hole effective masses are shown at the corresponding band edges in units of the rest mass of the electron (m_0). (c) Energy contour plot of highest of the valence band of monolayer MoS_2, (d) energy contour plot of the lowermost conduction band of monolayer MoS_2 in a 2D *k* plane. The energy of valence and conduction band in the contour

plot referenced with respect to the top of valence band energy and bottom of conduction band energy (or fundamental bandgap).

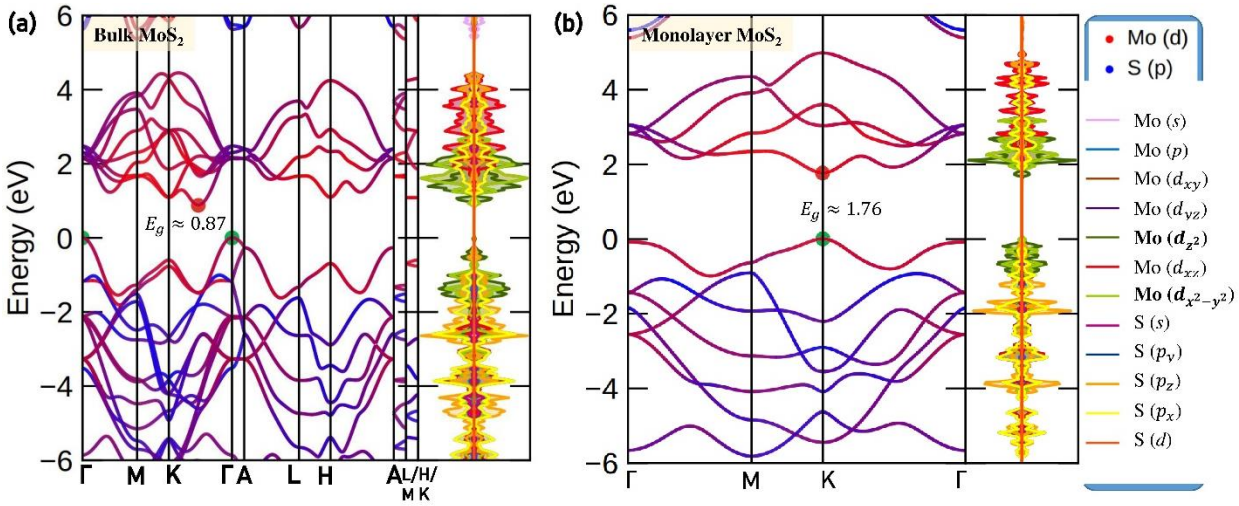

Figure 1.3. Atom and orbital projected band structure of bulk and monolayer MoS_2. The conduction and valence band edges are comprised of Mo-*d* and S-*p* atomic orbital with a majority of orbital contribution arising from the Mo *d* orbitals that are weakly hybridized with the *p* orbitals of S atom. The Bloch bands at the conduction and valence band edges in a monolayer MoS_2 is coupled in nature because of the mixing of Mo-*d* and S-*p* atomic orbitals.

One of the major distinctive features of TMDCs are the conduction and valence band states are composed of Mo (*d*) and S (*p*) atomic orbitals with a majority of the orbital contribution arising from the out-of-plane Mo (d_{z^2}) and in-plane Mo ($d_{x^2-y^2}$) atomic orbitals, as shown in Figure 1.3 of the density of states (DOS) of orbital projections. A small contribution to the band edges also rises from the p_x and p_y orbitals of S atom. The trigonal-prismatic crystal field on free Mo 4*d* orbitals lifts the five-fold degeneracy of atomic orbitals into three major energy groups, that are spread out in energy ranges, giving rise to two doubly degenerate energy levels (i) $4d_{xy}$, $4d_{x2-y2}$ and (ii) $4d_{yz}$, $4d_{zx}$ and one singly degenerate energy level (iii) $4d_{z2}$ [122]. The in-plane $4d_{xy}$, $4d_{x2-y2}$ orbitals, and the out-of-plane $4d_{z2}$ orbitals are symmetric with respect to its horizontal mirror plane (σ_h) passing over the Mo atomic layer.

The out-of-plane mirror symmetry ($z = -z$) in ML-MoS_2 allows hybridization between its 4d_{xy}, 4d_{x2-y2}, and 4d_{z2} orbitals with 3(p_x, p_y), 3(p_z) orbitals of ligand sulfur (S) atoms, which opens up a tunable energy gap in MoS_2.

1.2.3 Spin-orbit coupling in monolayer MoS_2

The absence of lattice inversion symmetry and the presence of frontier Mo 4*d* orbitals lift the spin degeneracy of electronic states near the VBM and CBM band edges due to a strong spin-orbit induced (SOI) spin splitting of bands.[123], [124] Strong spin-orbit coupling (SOC) in monolayer MoS_2 reduces the direct bandgap at *K* point to 1.61 eV (1.76 without SOC), as shown in Figure 1.4. The manifestation of strong SOC in monolayer MoS_2 lifts the Kramer's degeneracy between spin degenerate bands due to missing inversion symmetry, a large energy separation of ~ 149.3 meV in the valence band sector and a small energy separation of ~ 3 meV in the conduction band sector appears with the inclusion of SOC effects into the band structure while keeping the spin-split band edges at the same momentum position (i.e., at *K* point), as shown in Figure 1.4. The same magnitude of spin-splitting with opposite spin polarization also occurs at its opposite momenta, *–K* point in the Brillouin zone, as the *K* and *–K* valleys are time-reversal partners. Strong SOC effects at the low energy valleys of TMDCs provide an ideal playground to investigate the interplay of coupled spin-valley degrees of freedom (DOF) for next-generation integrated spintronic and valleytronic devices which is accompanied by the novel coexistence of spin-momentum locking and coupled spin-valley index of valley carriers in monolayers of MX_2. Strong spin-orbit coupling is desired for spintronic functionalities. For tungsten-based MX_2 monolayers, the spin-orbit splitting energy is substantial ~ 400-500 meV due to different sizes of cation, atomic number, and higher *d* states, making them an ideal candidate for the suppression of spin-valley relaxation in spintronics that prolong the carrier lifetime and suppress electron intrinsic intervalley spin relaxation channels due to D'yakonov–Perel' mechanism.[124], [125] Besides, the optical transitions between the spin split valence

band to the conduction band minimum at the *K* point of monolayer MoS_2 reveals strongly bound *A* and *B* excitons for each spin transition states measured in the photoluminescence spectroscopy with large exciton binding energy ~ 0.5 eV in MX_2 monolayers due to strong Coulomb interaction between carriers.[126], [127]

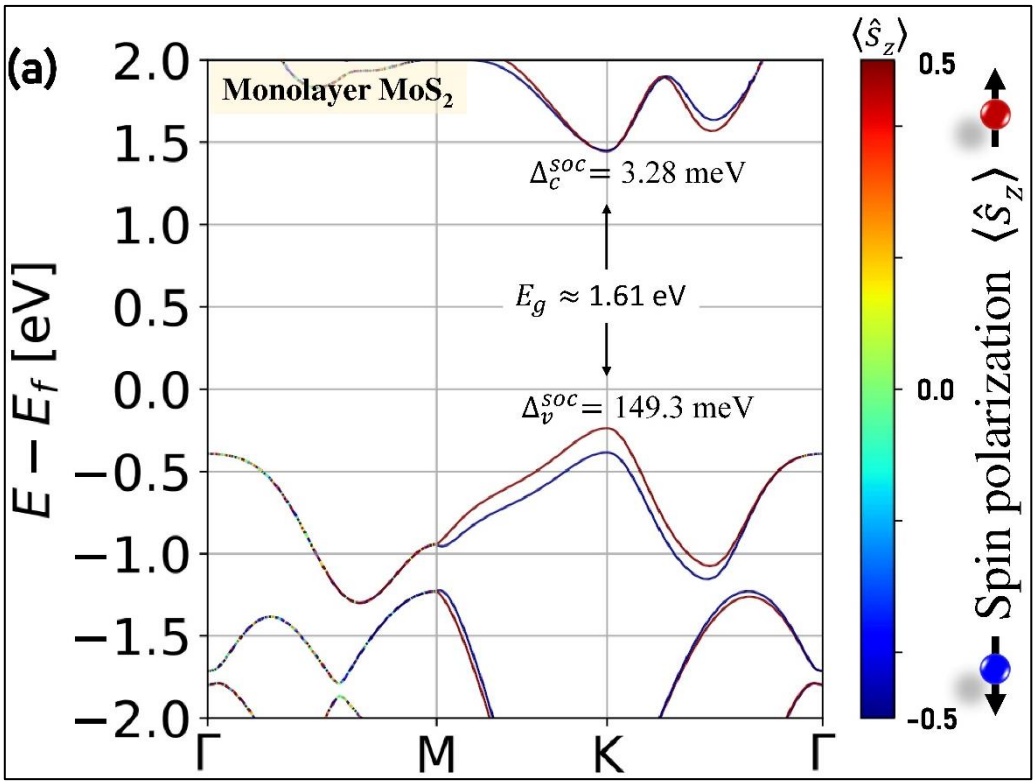

Figure 1.4. Calculated spin-resolved band structure of monolayer MoS_2 with spin-orbit coupling effects. The spin-projection operator, $<S_z>$ (dimensionless spin Pauli matrix), is along the perpendicular direction and normal to the basal plane of ML-MoS_2. The red and blue colors are the indicator of spin-up and spin-down polarization states.

1.2.4 Valley polarization in monolayer TMDCs

Monolayer TMDCs harbor a pair of energy degenerate and symmetry inequivalent time-reversed valleys at the *K* and *K'* points of the Brillouin zone (BZ).[128] The low energy valleys of TMDCs are well-separated in the momentum space, making them ideal for valleytronic devices.[129]–[131] The valley pseudospin refers to the occurrence of multiple

degenerate energy extrema in the low energy electronic spectrum that offers an ideal platform to confine or manipulate the charge carriers in these distinct valleys in order to storage and process discrete digital information bits by systematic controlling the degree of valley polarization of carriers at *K* and *K'* points.[132] Valley polarization in TMDCs can be achieved via optical and electrical means,[130], [133] where the use of polarization selective optical pumping technique via circularly polarized laser radiation have been demonstrated to achieve near 100% valley polarization in monolayer MoS_2.[134]–[136] Theoretically, the valley degrees of freedom in monolayer TMDCs can be manipulated through non-zero Berry curvatures, which acts as an effective magnetic field in the momentum space.[128] The integration of Berry curvature over the entire Brillouin zone gives the transverse Hall conductivity of a material. For a non-zero Berry curvature, either the time-reversal symmetry or the crystal inversion symmetry has to be explicitly broken, while the presence of both the symmetry leads to a vanish of Berry curvature in the entire momentum space (bulk MoS_2). In monolayer crystals of TMDCs, the lattice inversion symmetry is explicitly broken, leading to a non-zero Berry curvature where the time-reversal symmetry is preserved between degenerate valleys located at *K* and *K'* points of BZ. Figure 1.5 (a) shows the Berry curvatures for the valence and conduction bands of monolayer MoS_2. The absence of lattice inversion symmetry and the presence of strong spin-orbit interaction allow the charge carriers in K and -K valley to take opposite Berry curvatures, where the Berry curvature is mainly localized around the *K/K'* valleys and significantly peaked at both the *K* and *K'* points in the BZ with opposite sign, as required by the time-reversal symmetry of the system. Away from *K/K'*, $\Omega(k)$ decays rapidly and eventually vanishes at the Γ point. The charge carriers in *K/K'* valleys are associated with distinct valley index into their real spin moments; hence the inter-valley spin-flip transitions are greatly restricted due to time-reversal symmetry in the system.[137] The valley index is ideal for carrying out various exotic physical phenomena, such as spin Hall and valley Hall

effects, where the valley pseudospin DOF of charge carriers: via optical manipulation can drive counter-propagating valley current when the system is in the presence of an applied external transverse electric field.

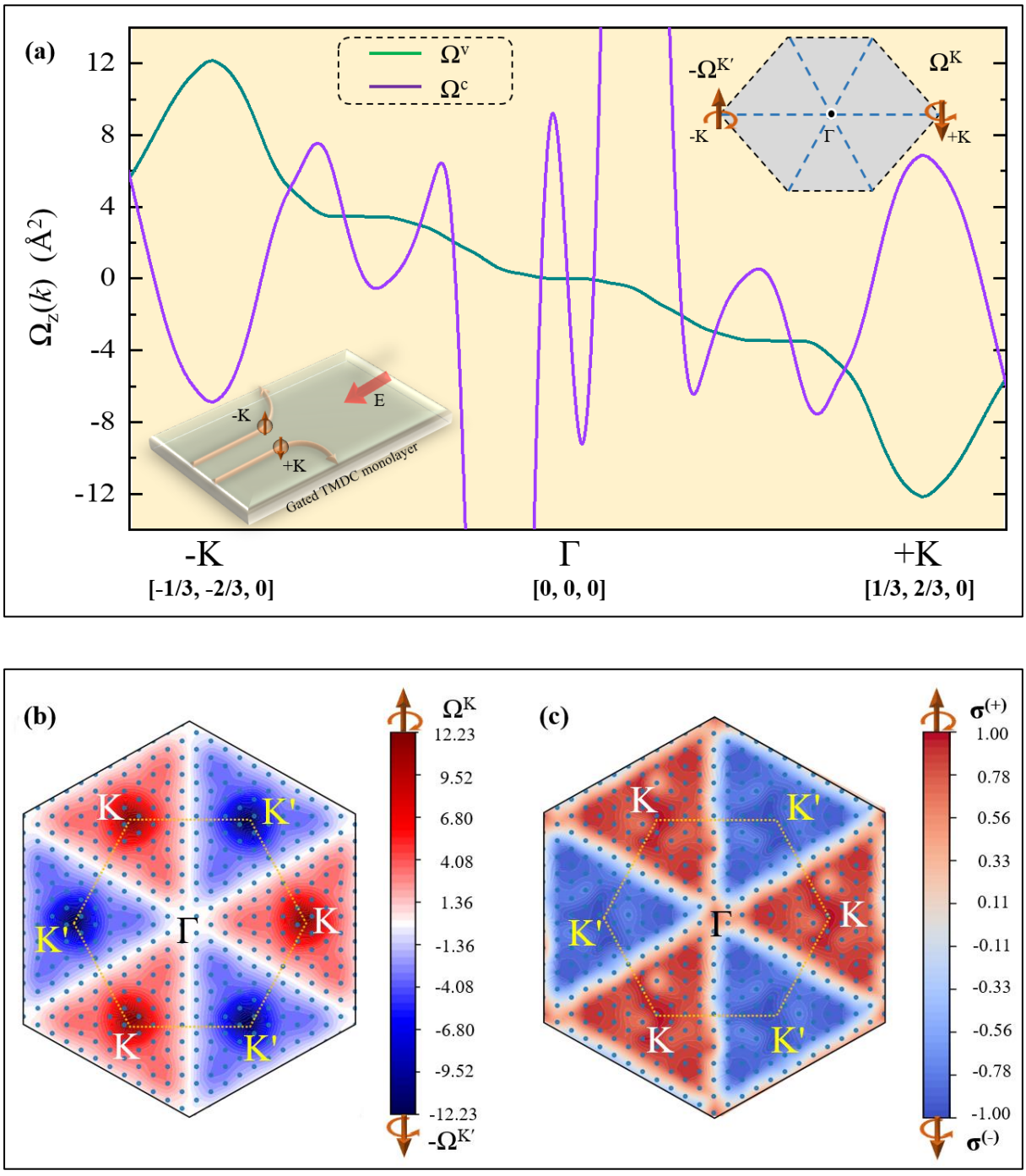

Figure 1.5. (a) The Berry curvature of monolayer MoS_2 for valence and conduction bands. The valence band Berry curvature distribution (Ω^v) is derived for all the occupied states below the

Fermi energy, and the conduction band Berry curvature distribution (Ω^c) is over the two lowermost spin-split conduction bands. (b) Berry curvature distribution for occupied states in a 2D *k*-plane. (c) Polarization resolved circular dichroism for a direct optical transition from the highest of spin-split valence band top at K points to the lowermost spin-split conduction band at the K point. The scale represents the degree of circular polarization.

The local curvature of the electronic wave function corresponding to a given Bloch energy band at a particular momentum position in the band structure is defined as the Berry curvature (BC). This is the geometric property of Bloch electrons in certain solids. The Berry curvature for electronic Bloch states of the n^{th} band is expressed as,

$$\Omega_z^{(n)}(\vec{k}) = i\hat{z}.\left(\nabla_{\vec{k}} u_{\vec{k}}^{(n)^*}\right) \times \left(\nabla_{\vec{k}} u_{\vec{k}}^{(n)}\right) \tag{1.1}$$

$$= -2\left(\frac{\hbar}{e}\right)^2 \sum_{n \neq n'} \frac{Im\langle u_{\vec{k}}^{(n)}|P_x(\vec{k})|u_{\vec{k}}^{(n')}\rangle\langle u_{\vec{k}}^{(n')}|P_y(\vec{k})|u_{\vec{k}}^{(n)}\rangle}{[\epsilon_{\vec{k}}^{(n)} - \epsilon_{\vec{k}}^{(n')}]^2} \tag{1.2}$$

Where $\epsilon_{\vec{k}}^{(n)}$ represents the eigenvalues of the Hamiltonian operator $\widehat{H_{\vec{k}}}$ and $u_{\vec{k}}^{(n)}$ denotes the corresponding eigenfunctions for the n^{th} band at crystal momentum $\vec{k}$. The operator $P_i(\vec{k}) = (e/\hbar)\,\partial\widehat{H_{\vec{k}}}/\partial k_i$ is the current operator.

Moreover, the coexistence of strong SOC and loss of crystal inversion symmetry in monolayer TMDCs uniquely couples the spin and valley DOF of carriers at K and K' points of the BZ. A direct optical transition between spin-split valence and conduction bands at the K point via helicity selective laser excitation can selectively excite the valley carriers from one of the valleys (K/K') due to unique optical selection rules of spin-valley index. The helicity selective optical excitation of carriers from each valley K/K' by the use of circularly polarized radiation of particular handedness (left-handed or right-handed polarization) is a unique phenomenon of circular dichroism (CD). In Figure 1.5 (c), we have shown the CD from the

spin-split valence band at K point to the bottom of the 1st spin-split conduction band at K point in a 2D hexagonal Brillouin zone.

1.2.5 Piezoelectricity in monolayer TMDCs

Certain material shows an innate ability to generate or polarize electric charge within itself under the application of external mechanical load in the form of applied stress or strain.[138], [139] Conversely, one can apply an electric field to deform these materials mechanically. The former is known as a direct piezoelectric effect, while the latter is termed as the inverse piezoelectric effect. The necessary condition for materials to show this effect, is the absence of an inversion center, or, in other words, these materials need to belong to the class of non-centrosymmetric crystals. Piezoelectricity was first studied in bulk quartz crystals in 1880 by *Curie* brothers, *Pierre Curie* and *Jacques Curie*.[140] Since then, the bulk piezoelectricity has been well studied over the years.[141] The well known bulk piezoelectric crystals are AlN,[142] GaN,[143] quartz, zinc oxide (ZnO),[144], and oxide perovskites, such as $BaTiO_3$, and lead zirconate titanate (PZT, $PbZrTiO_3$).[145], [146]

Piezoelectric crystals are ideal for a wide range of applications including low-energy power conversion logic circuits,[147] self-powered devices,[148] mechanical resonators,[149] and high-performance electronics,[150] where the use of smart piezoelectric materials can effectively manage the energy feedback mechanism in micro-electro-mechanical systems (MEMS).[151], [152]

The emergence of a high degree of piezoelectricity at the atomic scale is a relatively new research area for the harvesting/recycling of nanoscale energies.[148], [153], [154] A tiny atomic displacement within the atomically thin 2D crystals can bring colossal changes in the nanoscale piezoelectric and electronic properties.[155] 2D piezoelectricity is very useful for ultrasensitive biological sensors,[156] nanoscale robotics,[157] flexible and wearable self-

powered electronic devices[158] to monitor cellular deformation in various tissues that can immensely benefit the future point of care diagnosis.[139], [159], [160] Many non-piezoelectric crystals, when reduced to their one or few atomic thicknesses, are found to be piezoelectric.[159], [161], [162] In monolayer and an odd number of atomic layers of transition metal dichalcogenides (TMDCs), the inversion symmetry is explicitly broken, and these monolayers belong to the class of non-centrosymmetric crystals. By reducing the number of monolayers in a multilayer MoS_2, Zhu *et al.*[159] has demonstrated a transverse piezoelectric coefficient of ~ 10^{-10} $C.m^{-1}$ (≈ 3 $pm.V^{-1}$) in a single layer MoS_2 free-standing nanosheet.[163] The magnitude of the piezoelectric coefficient increases by decreasing the number of MoS_2 layers, while for even the number of monolayer sheets, the piezoelectricity vanished due to the restoration of the center of inversion.[163]

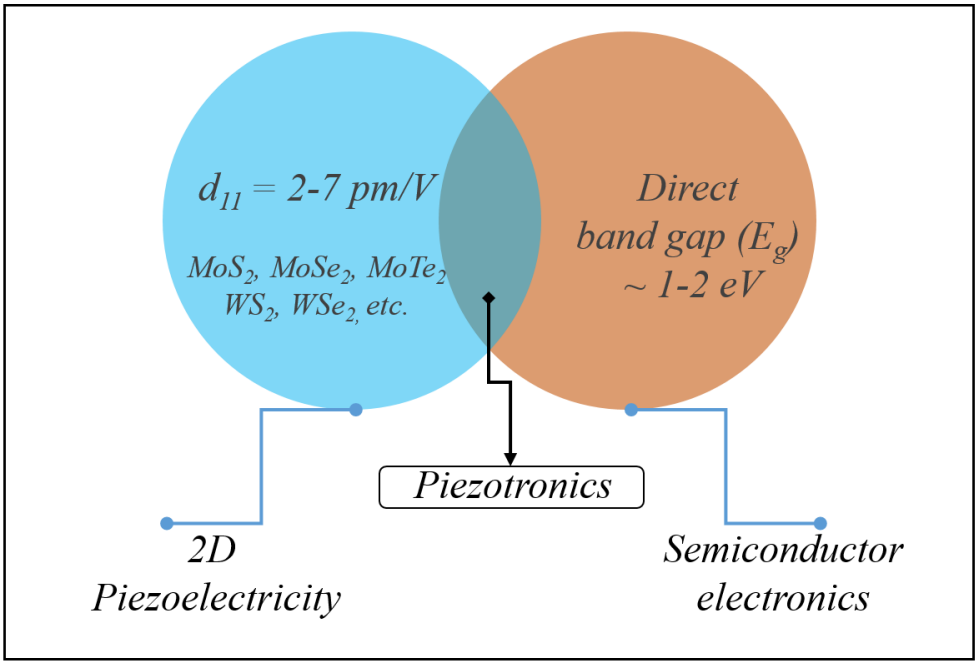

Figure 1.6. Simultaneous coupling of a high degree of piezoelectricity and semiconducting properties in *Group VIB* monolayer TMDCs (MX_2) for adaptive piezotronics.

Moreover, for integrated high performance flexible electronic devices, in monolayers of TMDCs, a simultaneous occurrence of good semiconducting property (direct semiconducting bandgap ~ 1-2 eV, mobility ~ 100-700 $cm^2V^{-1}s^{-1}$),[93], [164], [165] remarkable elasticity (Young's modulus ~ 270±100 GPa),[166] and high in-plane piezoelectricity (3-16 pm/V)[167] can be envisioned for nano-electro-mechanical systems (NEMS).[163], [168], [169] Furthermore, the ultimate crystal thickness, atomic-scale semiconducting properties, superior mechanical strength, thermal-chemical-mechanical stability at ambient condition, and high-quality freestanding surface structures of monolayer TMDCs can be used for biocompatible *piezotronic* energy conversion applications.[93], [139], [155], [169]–[172]

The degree of piezoelectricity in monolayer TMDCs is expressed in terms of piezoelectric stress tensors e_{ij} or piezoelectric strain tensors d_{ij}. In monolayer TMDCs, the hexagonal crystal symmetry D_{3h} reduces the number of tensor coefficients of e_{ij} matrix into a single independent coefficient e_{11}which uniquely determines the piezoelectric strength of the material. The corresponding piezoelectric strain coefficient d_{11} is calculated from e_{11} via in-plane elastic stiffness constants C_{11} and C_{12},

$$d_{11} = \frac{e_{11}}{C_{11}-C_{12}} \tag{1.3}$$

The elastic stiffness constants C_{ij} is evaluated by fitting the second-order polynomial into the changes in the total elastic energy of a strained lattice concerning the in-plane applied strain per unit lattice area along the Basal plane of 2D lattice in a small strain range $-1\% \leq \varepsilon \geq 1\%$ around the equilibrium crystal lattice a_0, where $\varepsilon = \frac{a-a_0}{a_0} \times 100\%$, a is the strained lattice parameter.

The elastic strain energy (E_s) per unit surface area of the 2D lattice plane is defined as,

$$E_s = \frac{1}{2}C_{11}\varepsilon_{xx}^2 + \frac{1}{2}C_{22}\varepsilon_{yy}^2 + \frac{1}{2}C_{11}\varepsilon_{xx}\varepsilon_{yy} + 2C_{66}\varepsilon_{xy}^2 \quad (1.4)$$

Here ε_{xx}, ε_{yy}, and ε_{xy} are planar tensile strain coefficients along *x* and *y* directions of crystal corresponding to lattice vectors *a* and *b* of the unit-cell. The simplest way to introduce strain in monolayer crystals of TMDCs by varying the lattice vectors in the scales of interatomic bond lengths along a given crystal axis, *x*, and *y* directions.

1.2.6 Lattice dynamics in monolayer TMDCs

Lattice dynamics in transition metal dichalcogenides (TMDCs) governs its fundamental physical properties, such as mechanical, thermal, and optical properties of materials are determined by the behavior of crystal phonons.[173], [174] Besides, the electronic transport of charge carriers and optical excitations between low energy valleys is assisted by the interaction of different phonon vibrations.[175], [176] Figure 1.7 (a) shows the phonon dispersion of monolayer MoS_2 along the high-symmetry direction of the Brillouin zone. The absence of imaginary phonon frequency in the entire Brillouin zone is a signature of the dynamical stability of crystal. In experiments, the use of inelastic neutron scattering (INS) technique can determine various phonon branches along different crystal momentum.[177] The phonon dispersion of monolayer MoS_2 shows 3-acoustic and 6-optic branches, where the high energy LA and TA acoustic branch shows linear dispersion close to the zone center (Γ), while the low energy ZA mode display quadratic dependence with crystal moment. The acoustic and optic branches are leveled as per their polarization symmetry of phonon modes near the Brillouin zone center, Γ point. The high energy longitudinal acoustic mode shows maximum phonon group velocity ~ 2.2 km/s. An indirect phononic energy gap ~ 44 cm^{-1} separates the optical modes from the maximum of the acoustic branch at K point. In the phonon density of states (*phDOS*), the acoustic region is dominated by Mo atom, while the lower branches of optical phonon are dominated by S atom, as shown the Figure 1.7 (b).

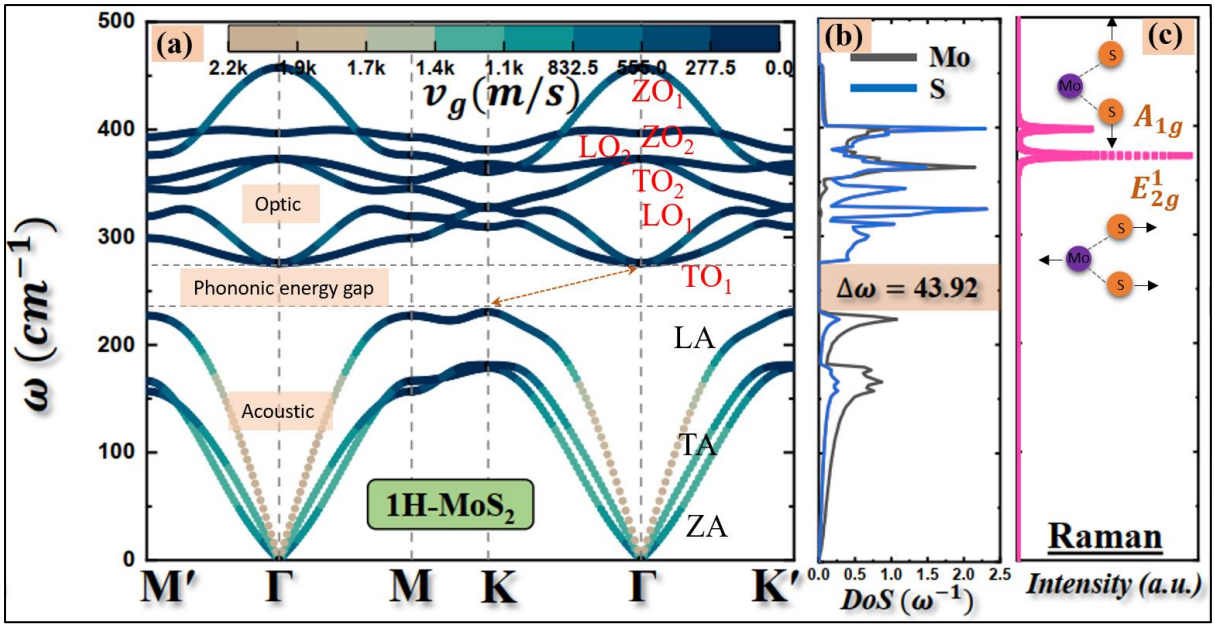

Figure 1.7. Lattice vibration in monolayer MoS_2. (a) Phonon dispersion and phonon group velocity (*inset horizontal color bar*) projected on corresponding phonon branches of acoustic and optic phonons of monolayer MoS_2. (b) Atom projected phonon density of states (*phDOS*) depicting a wide indirect phononic energy gap ~ 43.92 cm^{-1} between acoustic and optical phonon modes. (c) Characteristic Raman active vibrations of monolayer MoS_2.

Raman spectroscopy offers a simple non-destructive versatile technique to characterize structure-property relationships of materials that are directly related to the crystal phonon, including the phonon dispersion and phonon density of states (*phDOS*). In monolayer MoS_2, the characteristic Raman active vibrations are out-of-plane A_{1g}vibration and in-plane E^1_{2g}vibration.[178] Figure 1.7 (c) shows a typical Raman spectrum involving the vibrational modes A_{1g} and E^1_{2g}. These two Raman active modes usually found in experiments to characterize various properties of monolayer TMDCs and widely used to measure, strain in the lattice, the number of layers in TMDCs,[179], [180] electron-hole doping in transport study,[181] and temperature,[182] pressure effects[183] from the behavior of frequency softening/ hardening of A_{1g} and E^1_{2g} vibrations.[178]

1.3 Janus monolayers of transition metal dichalcogenides

The breaking of sublattice crystal symmetry in parent 1H-MX_2 structure of TMDCs can create a completely new structural phase, namely, Janus TMDCs (MXY), where X ≠ Y (X, Y = S, Se, Te). In a well-controlled CVD synthesis process, Lu *et al.* [184] were first able to demonstrate the production of MXY (MoSSe) monolayer Janus structure, where the top S atom layer in pristine MoS_2 monolayer crystal was completely replaced by the Se atoms via sophisticated plasma irradiated atom stripping technique as a synthetic route to achieve perfect X-M-Y atomic structure.[185] The vertical mirror symmetry (D_{3v}) of identical chalcogen atoms of MoS_2 is broken in MoSSe, leading to an out-of-plane polarization or vertical piezoelectricity (d_{33} ~ 0.1-13.5 pm V^{-1}) in mono- to multi-layer stacks of MXY [184], [186]. A non-vanishing built-in perpendicular dipole moment in MXY monolayer/multilayers brings a spontaneous out-of-plane electric field due to a local asymmetric potential perpendicular to it basal plane that can give rise to novel momentum-dependent spin splitting of electronic bands, so-called the Rashba effect at the valence band top at Γ point. These asymmetric MXY structures are ideal to realize the spin-polarized field-effect transistors (spin-FETs) without the use of an external perpendicular electric field and provide a new means to improve catalytic activity in hydrogen evolution reaction (HER) or heterojunction photocatalytic water splitting due to the inherent structural asymmetry of ultrathin Janus XMY.[187], [188]

In *chapter 3*, we have provided the crystal structure and various electronic properties of Janus transition-metal dichalcogenides (J-TMDCs) of *Group VIB* elements.

1.4 Scope of this thesis

The research work presented in this thesis is aimed to explore the electronic, spintronic, and valleytronic functionalities of monolayer transition-metal dichalcogenides (TMDCs) of *Group VIB* elements and their structural Janus derivatives, MXY monolayers. Particular attention has

been given to the monolayer crystal of MoS_2, the pristine and strain responsive properties of this widely explored 2D material has been investigated under various strain geometry. We found the novel pristine properties of monolayer MoS_2 can significantly be manipulated via strain engineering of its crystal lattice. Owing to the high elasticity, monolayer MoS_2 provides ample opportunity to investigate its electronic and lattice properties from a small 0-2% up to an extreme range of 0-10% lattice strain. The strain sensitive investigation of exotic electronic, mechanical, and lattice dynamical properties presented in individual chapters taking monolayer MX_2 and MXY as ideal candidate systems may pave the way to the next-generation 2D flexible electronics and energy conversion applications. A similar investigation for families of other transition metal dichalcogenide groups may be envisioned to explore some novel properties in their pristine and Janus 2D crystals; and their strain responsive fascinating properties.

1.5 Structure of the thesis

The research work presented in this thesis is organized into the following chapters:

Chapter 1 gives an excellent overview of the discovery of two-dimensional (2D) material "graphene" and several other 2D materials that have emerged after graphene. We also have provided a descriptive review and essential properties of transition-metal dichalcogenides by considering MoS_2 as an example system. Specific attention has given to the family of transition metal dichalcogenides of *Group VIB* elements. Towards the end of chapter 1, a brief introduction to the Janus crystal structure of *Group VIB* elements has been provided.

Chapter 2 provides the theoretical background of various computational methods and simulation tools useful in understanding the calculation of results presented in this thesis.

Chapter 3 infers to the *ab initio* study of crystal structure, lattice stability and coupled spin-valley nature of charge carriers in a series of semiconducting monolayers of *Group VIB* transition metal dichalcogenides 1H-MX_2 (where M = Cr, Mo, W, etc.; X = S, Se, or Te) and

their Janus structures 1H-MXY (where X ≠ Y). Here, we have shown the structural stability of Janus monolayers, which we have confirmed from the phonon study and room temperature AIMD simulations. Furthermore, the Janus monolayers of *Group VIB* TMDCs is found to have comparable cohesive energy (~ 2-3 eV/atom) to that of their parent, energetically stable, 1H-MX_2 structure, and this suggests the relative chemical stability of Janus monolayers and their experimental feasibility. In all cases, a semiconducting electronic bandgap (~ 0.25 – 1.7 eV) has been found. The bandgap of M-S-Se and M-Se-Te (where, M = Cr, Mo, W) Janus monolayers are found to be direct at the K-point of the BZ under SOC, whereas in all other cases an indirect bandgap is observed with valence band maximum (VBM) occurring at the Γ–point of the BZ and the conduction band minimum (CBM) situated at the K–point. The variation in the direct and indirect bandgap exhibits a linear dependency as a function of applied mechanical strain within the -3% to +6% of biaxial strain, and the Janus monolayers remain semiconducting within this strain range except for CrSTe strained system that shows a semiconductor-to-metal transition with strain > +3%. The electrostatic potential difference (ΔV) is found to increase with an increase in dipolar contrast between chalcogen lattices, which enhances the SOC splitting energy of spin bands at the K–point of BZ both in the VBM and CBM sectors of the electronic dispersion. The Rashba parameters (E_R & α_R) are found to be highly strain sensitive and significantly get enhanced with lattice compression. The strain sensitive variation in Rashba coefficient α_R is found to exhibit asymmetric behavior about the K'-Γ-K and M'-Γ-M high symmetry line in the 1st BZ. Under compressive biaxial strain the enhancement in α_R along the K'-Γ-K line is nearly 2-orders of magnitude higher than the same along the M'-Γ-M high symmetry line for a given strain value. Furthermore, the strain-tunable alteration in Berry curvature in pristine and Janus monolayer TMDCs can be a potential avenue for the effective controlling of transverse velocities of valley carriers in the future flexible valleytronic device.

Chapter 4 focuses on tailoring of low energy valleys of monolayer (ML) MoS_2 in response to a directional lattice deformation. In this study, we find applied uniaxial strain on ML-MoS_2 nanosheet can drift the low-energy electron/hole valleys far-off *K*/*K*' points in the Brillouin zone (BZ). The magnitude of drift in the low energy spin-split conduction band minimum amounts 2-times than the drift in the valence band maximum with a progressive increase of strain field in an in-plane strain range of 0-10%. As a result of an unequal valley drift at the conduction band edge and valence band edge, the momentum degeneracy of valley carriers at the *K* point gets lost. The underlying valley decoherence of carriers can affect the low-energy valley excitations and valley polarization properties of a stained ML-MoS_2 lattice. We have also demonstrated the effect of a considerable strain on the strength of spin-orbit induced spin splitting of bands at the low energy conduction band and high energy valence band around the *K* point. We find a sizably enhancement (∼7 meV) in the spin-orbit induced spin splitting of bands at the valence band maximum at *K* point that has been tailored simply by the strain-controlled orbital motions of overlapping atomic orbitals. The results and discussion presented in this chapter highlight the importance of strain in tailoring the spintronic and valleytronic potential of ML MoS_2.

Chapter 5 looks at the simultaneous response of high piezoelectricity and novel semiconducting properties of a monolayer MoS_2. Under the application of various in-plane strain mode, we have explored a synergic coupling between semiconducting behavior and a high degree of piezoelectricity for adaptive, flexible nanopiezotronic devices based on a monolayer (ML) MoS_2 sheets. We find the shear strain and uniaxial tensile strain optimally enhances the piezoelectric constants by retaining a semiconducting gap in monolayer (ML) MoS_2. We have further analyzed the elastic limit and critical strain for the mechanical stability of monolayer (ML) MoS_2 nanosheets under various strain geometry. The elastic limit under different strain modes shows well agreement result with recent experiments on ML-MoS_2.

Additionally, charge carrier mobilities have been predicted as a function of uniaxial strain along mutual orthogonal crystal direction of ML-MoS_2 useful for flexible low-power switches and nanoelectromechanical systems.

Chapter 6 investigates the effect of various planar strain modes on the evolution of Raman and IR spectra of a strained monolayer MoS_2 nanosheet. The breaking of two-fold degenerate in-plane atomic vibrations into nondegenerate singlet frequency states has been demonstrated. The broken frequency degeneracy in phonon modes is a signature of lattice anisotropy brought about by an asymmetric strain field that only occurs in the case of uniaxial and shear strain. We have also demonstrated the anisotropy in Young's modulus and Poisson ratio to arise due to asymmetric lattice environment along the mutually orthogonal directions in monolayer MoS_2 when the nanosheet is under an asymmetric strain field.

Chapter 7 concludes this thesis by summarizing the essential outcome of individual studies presented in different chapters. A possible future extension of this research work in a similar work theme for other 2D materials has been suggested with valuable pointers as thoughts on forthcoming research outlook.

----------**********----------

Chapter 2

Theoretical background and Simulation tools

In this chapter, we briefly describe the central theoretical foundations of computational methods that are pivotal to the calculation of results presented in this thesis by the use of different quantum simulation tools. The fundamental aspects of many-body Schrödinger equation, introductory density functional theory (DFT) methods, exchange-correlation functionals, and basis-sets essential to layout various *ab initio* calculations within the DFT have been presented in this chapter. I encourage the readers' to follow-on reference materials provided in each section for a complete description of the theoretical backgrounds of various quantum mechanical methods.

2.1 Elementary quantum chemistry

The surrounding matter in our everyday experience is comprised of a systematic collection of electrons that surrounds a few different kinds of nuclei. Starting from the air molecule, we breathe to the advanced automobile that we drive, all matter in our daily encounter is essentially a soup of many electrons, nuclei, and various interactions among them. In a many-electron quantum system, the fundamental electrostatic interactions between electrons and nuclei are Coulombic in nature and governed by the many-particle Schrödinger equation, and mathematically described as,

$$\hat{H}\Psi_i(\vec{x}_1, \vec{x}_2, \dots\dots, \vec{x}_N, \vec{R}_1, \vec{R}_2, \dots\dots, \vec{R}_M) = \mathrm{E}_i\Psi_i(\vec{x}_1, \vec{x}_2, \dots\dots, \vec{x}_N, \vec{R}_1, \vec{R}_2, \dots\dots, \vec{R}_M) \quad (2.1)$$

Here, $\hat{H}$ is the Hamiltonian operator for an isolated N electron system consisting of M nuclei in the absence of any external perturbations, $\Psi_i(\vec{x}_1, \vec{x}_2, \dots\dots, \vec{x}_N, \vec{R}_1, \vec{R}_2, \dots\dots, \vec{R}_M)$ stands for the wave function of the i^{th} state, and E_i energy eigenvalues of a given quantum state described by Ψ_i.

The Hamiltonian operator describing the total energy of a coupled electron-ion system is defined as

$$\hat{H} = -\frac{1}{2}\sum_{i=1}^{N}\nabla_i^2 - \frac{1}{2}\sum_{A=1}^{M}\frac{1}{M_A}\nabla_A^2 - \sum_{i=1}^{N}\sum_{A=1}^{M}\frac{Z_A}{r_{iA}} + \sum_{i=1}^{N}\sum_{j>i}^{N}\frac{1}{r_{ij}} + \sum_{A=1}^{M}\sum_{B>A}^{M}\frac{Z_A Z_B}{R_{AB}} \quad (2.2)$$

Here, A and B denotations are over the M nuclei present in the system, while i, and j run over the N electrons. The first two terms in the total energy operator are the kinetic energy of N electrons and M nuclei, respectively, where M_A is the mass of the nucleus in units of the electron mass. The remaining three terms in the energy Hamiltonian operator are the attractive electrostatic interaction between the nuclei and the electrons, and repulsive potential due to the electron-electron and nucleus-nucleus interactions, respectively.

Born-Oppenheimer approximation: The wave function $\Psi_i(\vec{x}_1, \vec{x}_2, \dots\dots, \vec{x}_N, \vec{R}_1, \vec{R}_2, \dots\dots, \vec{R}_M)$ of a many-particle quantum system contains essential information and central to describe all the desired physical properties of a given quantum system by various quantum operations. The Schrödinger equation (2.1), can further be simplified by considering the famous clamped-nuclei approximation for nuclear dynamics, comely referred to as *Born-Oppenheimer* approximation. The approximation takes advantage of differences in electron and proton (^{1}H) masses, which for the lightest nuclei (^{1}H), proton mass is 1800 times more than a single electron mass. Thus, the motion of nuclei is much slower as compared to the electron dynamics, and electronic motion happens within a fixed field of nuclear potential; therefore, the clamped-nuclei approximation is, in principle, an excellent approximation to simplify the problem by ceasing the nuclear dynamics. The kinetic energy term for the nuclear motion becomes zero under the *Born-Oppenheimer* approximation, and the rigid potential energy due to nucleus-nucleus repulsion becomes constant. The total energy operator can be rewritten under the *Born-Oppenheimer* approximation as the electronic Hamiltonian

$$\widehat{H}_e = -\frac{1}{2}\sum_{i=1}^{N}\nabla_i^2 - \sum_{i=1}^{N}\sum_{A=1}^{M}\frac{Z_A}{r_{iA}} + \sum_{i=1}^{N}\sum_{j>i}^{N}\frac{1}{r_{ij}} = \hat{T} + \hat{V}_{Ne} + \hat{V}_{ee} \qquad (2.3)$$

Where the first term $\hat{T}$ is the kinetic energy of *N* electrons in the system, the attractive potential acting on electrons due to the nuclei in the second term $\hat{V}_{Ne}$ is the nuclei-electron interaction potential and often termed as the external potential $V_{ext.}$ in density functional theory (DFT), while the last term $\hat{V}_{ee}$ represents the electron-electron interaction potentials. The solution of Schrödinger equation (2.1) for electronic Hamiltonian $\widehat{H}_e$ is the electronic wave function Ψ_e and the corresponding electronic energy eigenvalues E_e. The electronic wave function Ψ_e explicitly dependent on electron coordinates only and the nuclear coordinates enter only parametrically, which do not appear explicitly in Ψ_e. Then the total

energy E_T become the sum of electronic energy E_e part and constant nuclear repulsion term E_n, the electronic Schrödinger equation is expressed as

$$\hat{H}_e \Psi_e = E_e \Psi_e \tag{2.4}$$

and

$$E_T = E_e + E_n; \text{ where } E_n = \sum_{A=1}^{M} \sum_{B>A}^{M} \frac{Z_A Z_B}{R_{AB}} \tag{2.5}$$

The above many-electron Schrödinger equation (2.4) for a given quantum system is essentially a simple story that describes everything about a system. The wave function itself is not an observable quantity in quantum mechanics and commonly interpreted by the probability density, which is the square of the wave function when multiplied with its complex conjugation. To solve the Schrödinger equation (2.4) for an arbitrarily chosen quantum system, first, the Hamilton operator for the target system needs to be set. The electronic Hamiltonian in equation (2.3) infers that the specific part of the total energy operator $\hat{H}$ that is relevant to an actual system depends only on the number of electrons in the system *N* and external potential $V_{ext.}$. The later is completely determined through the position and charge of all nuclei within the system, and the remaining parts of $\hat{H}$, such as kinetic energy or the electron-electron repulsion, are independent of the system under our consideration. Since the eigenfunctions Ψ_i is dependent on corresponding eigenvalues of $\hat{H}$, all properties of the system can be derived once the Ψ_i is fully determined. The operation of appropriate operators on the wave function can extract the desired physical properties of the system if and only if Ψ_i is fully described. However, these simple-sounding steps are hard in practice even for simple atomic and molecular systems due to the absence of adequate technique to solve the many-particle Schrödinger equation precisely by wave function determination method, which is a central quantity in this model.

Nonetheless, over the years this simplified description has traversed a long path in predicting and describing the structure-property relation of various real materials starting from the simple atomic and molecular structures to the solving of complex DNA structures, polymers, proteins, and solid crystals in the conventional electronic wave function minimization strategy to get the ground state wave functions and corresponding low energy states of material using variational methods, and Hartree-Fock approaches. These all-electron wave function minimization schemes are computationally way more expensive for a system containing a large number of electrons to be exactly solvable by the wave function minimization methods and often suffer for its computation volume of the problem.

The present-day computational approach in solving the many-electron Schrödinger equation takes a simple route via density functional theory (DFT) approach, where the consideration of electron density $\rho(\vec{r})$ of materials has simplified the enormity of solving the many-electron wave function Ψ_i for complex materials. In recent years, the use of sophisticated computational methods by clever algorithms has enabled the predictive accuracy of ground-state electronic properties of materials with near exactness.

In the following section, we present the basic foundations of modern-day density functional theory methods for a non-relativistic, interacting Coulomb system based on electron density and approximate functionals.

2.2 Electron density theory

The density functional theory (DFT) or electron density theory reformulates the many-electron Schrödinger equation in terms of electron density $\rho(\vec{r})$ of materials that give a reliable computational measure and efficiency to solve the many-electron quantum system for various complex materials. The electron density or the probability density $\rho(\vec{r})$ of an N electron system

is the central variable in DFT and defined as the integral over the spin coordinates of all N electrons within a volume element of $d^3\vec{r}$.

$$\rho(\vec{r}) = N \int \dots \int |\Psi_i(\vec{x}_1, \vec{x}_2, \dots, \vec{x}_N)|^2 d^3\vec{r} \tag{2.6}$$

The probability density $\rho(\vec{r})$ is a non-negative function of position variables of N electrons which vanishes when $\vec{r} \to \infty$ and integrates to the total number of electrons N present in the system. The electron density $\rho(\vec{r})$ is then used to calculate various material properties that are directly or indirectly related to the ground-state electron density and the corresponding total minimum energy of the system E_0. In principle, $\rho(\vec{r})$ is an observable quantity and can be experimentally measured by X-ray diffractions. The basic foundation of the density-based approach to describe the behavior of electrons in a quantum system was first theoretically demonstrated by Hohenberg and Kohn in their seminal work back in 1964 and Kohn-Sham in 1965, for which Walter Kohn was awarded the Nobel Prize in Chemistry in 1998. Their density-based approaches in solving the electronic structure of materials are still the most successful theoretical approach in density functional theory. However, the initial attempt to this simplified density-based approach to describe the properties of many-body quantum systems in terms of their electron density dates back to 1927 in Thomas-Fermi (TF) model of approximation, where the non-interacting kinetic energy functional of a many-electron system was approximated by the uniform electron gas with electron density $\rho(\vec{r})$.

$$T_{TF}[\rho[\vec{r}]] = \mathrm{A} \int d^3\vec{r}\, \rho^{5/3}(\vec{r}) \tag{2.7}$$

Where $\rho(\vec{r})$ is the electron density of homogeneous non-interacting electron gas, and A is a numerical constant $\frac{3}{10}(3\pi^2)^{2/3}$. The total energy of a system was determined by adding electrostatic energies using the classical expression for the nuclear-nuclear potential and the electron-electron potential.

$$E_{TF}[\rho[\vec{r}]] = A\int d^3r\ \rho^{5/3}[r] - \mathrm{Z}\int \frac{\rho[r]}{r}\ d^3r + \frac{1}{2}\iint \frac{\rho[r]\rho[r']}{|r-r'|} d^3r d^3r' \qquad (2.8)$$

The first term in the above expression is the non-interacting kinetic energy density of a many-electron system, whereas the second term represents the energy of the ion-electron interaction energy or Coulombic term, and the third term is the classical Hartree energy.

The total energy of a many-electron system can be obtained by minimizing non-interacting wave function corresponding to a given electron density in some external potential, as given in equation (2.3), where the total electron number N in the system remains constant.

However, the description for total energy in the original Thomas-Fermi model overestimates the ground-state energy of many quantum systems because of an improper account of exchange-correlation energy, which is completely neglected in the Thomas-Fermi model which is expected to further lower the ground-state energies for interacting particles.

In summary, though the basic structure of a many-electron system based on Thomas-Fermi approximation provides a reasonable approximate result for non-interacting electronic systems with a few numbers of electrons, it fell short of predicting electrons in many real materials. Nonetheless, the use of electron density mapping over the conventional many-electron wave function method, without any additional information as a variable, established by the Thomas-Fermi model can describe divergent properties of materials and eventually gave birth to the foundation of modern density functional theory.

2.2.1 Hohenberg-Kohn theorem

The modern density functional theory methods that we use today was first established in 1964 by Hohenberg and Kohn. Hohenberg–Kohn (HK) stated, ‘the ground state of any interacting many-electron system with a given fixed inter-particle interaction is a unique function of the

electron density $\rho(\vec{r})$'; where the ground-state wave function Ψ_0 can be written as a unique functional of ground-state electron density n_0 as, $\Psi_0 = \Psi[n_0]$.

The equation (2.4) can now be rewritten in terms of the ground-state energy E_0 as a unique functional of ground-state electron density n_0, which enables one to establish a single physical quantity to describe all the properties of an interacting many-particle system.

$$E_0[\Psi[n_0]] = <\Psi[n_0]|\hat{T} + \hat{V}_{Ne} + \hat{V}_{ee}|\Psi[n_0]> \quad (2.9)$$

***First HK theorem*:** In the first Hohenberg-Kohn (HK) theorem, they proved, the ground state electron density n_0 uniquely determines the Hamiltonian operator thereby can determine the number of electrons (*N*) and external potential $V_{ext.}(\vec{r})$ to within a constant that fixes $\hat{H}$ for many-particle interacting ground states.

***Second HK theorem*:** In the second Hohenberg-Kohn theorem, they proposed a universal functional: *Hohenberg-Kohn functional*, $F_{HK}[\tilde{\rho}]$ as a function of certain unknown ground state density $\tilde{\rho}$, where $F_{HK}[\tilde{\rho}] = T[\tilde{\rho}] + V_{ee}$ that exists completely independent of the choice of the system to be solved the many-electron Schrödinger equation (2.4), exactly! However, the explicit form of these functionals is still under mystery. The functional $F_{HK}[\tilde{\rho}]$ delivers the ground state energy of the system independent of the external potential into its lowest energy configuration if and only if the input electron density is close to the actual ground-state density ρ_0 of material. The second Hohenberg-Kohn theorem was the simplified version of the variational principle with a trial density $\tilde{\rho}$.

$$E_o \leq E[\tilde{\rho}] = \hat{T}[\tilde{\rho}] + \hat{V}_{Ne}[\tilde{\rho}] + \hat{V}_{ee}[\tilde{\rho}] \quad (2.10)$$

This trial density $\tilde{\rho}$ in Hohenberg-Kohn theorem satisfies the necessary boundary conditions, $\tilde{\rho}(\vec{\boldsymbol{r}}) \geq 0$, $\int \tilde{\rho}(\vec{\boldsymbol{r}})\, d^3r = N$, and associate the external potential $V_{ext.}$ that give rise an upper bound to the true ground state energy $\boldsymbol{E_o}$ of a quantum system.

In summary, the Hohenberg-Kohn theorems have provided necessary methods to calculate all physical properties of a material as a unique functional of its ground-state density and some external potential $V_{ext.}(\vec{r})$ in terms of a universal trial function $F_{HK}[\tilde{\rho}]$ through the variational procedure that associate to an unknown density $\tilde{\rho}$ to determine the true ground state density of electrons n_0. However, the application of the Hohenberg-Kohn theorem is only limited to the ground state material properties and intricate to generalize the method for the excited state problems due to challenges in Hohenberg-Kohn functional.

2.2.2 Kohn-Sham formalism

The second seminal contribution to the development of modern density functional theory was come by Kohn and Sham in 1965, a year after the Hohenberg-Kohn theorem (1964). Kohn-Sham introduced the concept of a non-interacting reference system built from a set of orbitals in a way such that the kinetic energy part of the universal Hohenberg-Kohn functional $F_{HK}[\tilde{\rho}]$ can be calculated with sufficient accuracy.

The true ground state energy of a system can be obtained as a function of the trial density where the universal functional $F_{HK}[\tilde{\rho}]$ contains the kinetic energy, classical Coulomb potential, and non-classical interactions

$$E_0 = min_{\tilde{\rho}\to N}(F_{HK}[\tilde{\rho}] + \int \tilde{\rho}(\vec{r})\,\hat{V}[\tilde{\rho}]\,d^3r) \tag{2.11}$$

$$F_{HK}[\tilde{\rho}] = \hat{T}[\tilde{\rho}] + \hat{J}[\tilde{\rho}] + \hat{E}[\tilde{\rho}] \tag{2.12}$$

Where $\hat{J}[\tilde{\rho}]$ is the classical part of the energy, $\hat{T}[\tilde{\rho}]$ kinetic energy part and $\hat{E}[\tilde{\rho}]$ self-interaction correction, exchange, and Coulomb correlation.

The exact kinetic energy part which is poorly described in the Thomas-Fermi model as well as in Hohenberg-Kohn theorems for a non-interacting reference system with the same density as the real interacting system is obtained by the energy functional $E[n[r]]$ as a global minimum

to the total energy of the system corresponding to electron density $n[r]$ within a fixed number of electrons *N* by incorporating the exchange-correlation functional parts into the equation (2.9)

$$\frac{\delta}{\delta n(r)}\left[E[n(r)] - \mu \int n(r)dr\right] = 0 \tag{2.13}$$

where μ is a Lagrange multiplier and the corresponding Euler equation:

$$\frac{\delta E[n(r)]}{\delta n(r)} = \mu \tag{2.14}$$

Kohn-Sham (KS) separated the universal Hohenberg-Kohn energy functional $F[n(r)]$ into 3-parts so that the energy functional $E[n(r)]$ become

$$E[n(r)] = T[n(r)] + \frac{1}{2}\iint \frac{n(r)n(r')}{|r-r'|} + E_{XC}[n(r)] + \int n(r)V_{ext}(r)dr \tag{2.15}$$

where $T[n(r)]$ is the kinetic energy part of a non-interacting electron system with electron density $n(r)$.

In terms of effective KS potential, $V_{KS}(r)$, equation (2.13) can be expressed as

$$\frac{\delta T[n(r)]}{\delta n(r)} + V_{KS}(r) = \mu \tag{2.16}$$

where

$$V_{KS}(r) = V_{ext}(r) + \frac{\delta E_H[n(r)]}{\delta n(r)} + \frac{\delta E_{XC}[n(r)]}{\delta n(r)} \tag{2.17}$$

$$= V_{ext}(r) + V_H(r) + V_{XC}(r)$$

and

$$V_H(r) = \int \frac{n(r')}{|r-r'|}dr' \tag{2.18}$$

By using a well defined external potential $V_{KS}(r)$ for a give, non-interacting reference system the Kohn-Sham orbitals of the electronic wave function can uniquely determine the ground state properties that are based on gound state electron density n_0 and minimum total ground state energy E_0 (equation 2.10) by iteratively solving the one-particle Schrödinger equations through effective KS potentials $V_{KS}(r)$,

$$\left(-\frac{1}{2}\nabla^2 + V_{KS}(r)\right)\Psi_i(r) = \varepsilon_i\,\Psi_i(r) \tag{2.19}$$

where $\Psi_i(r)$ is the one-electron wavefunction of a non-interacting reference system that is dependent on the electron density $n(r)$

$$n(r) = \sum_{i=1}^{N} |\Psi_i(r)|^2 \tag{2.20}$$

One should note here if the exact form of $V_{XC}(r)$ and $V_{KS}(r)$ is known to us, by using the Kohn-Sham strategy, one could get the exact ground-state electron density n_0 of a non-interacting real system when the density of reference system approaches to its real value in an effective Kohn-Sham potential.

Strictly speaking, in Kohn-Sham approach the exchange-correlation functional $E_{XC}[n(r)]$ is unknown, and the orbitals have no physical significance, except the highest occupied orbital (negative of exact ionization energy). To describe a real interacting quantum system the description of accurate exchange-correlation functionals $E_{XC}[n(r)]$ is of utmost importance. Two widely studied approximate exchange-correlation functional $E_{XC}[n(r)]$ methods arise after the Kohn-Sham theory in the name of *local density approximation* (LDA) [189] and the *generalized gradient approximations* (GGA). [190]

2.2.3 Exchange-correlation functionals

2.2.3.1 Local Density Approximations

The LDA approximation for approximate exchange-correlation functionals is the general basis of all other density-based approximations. The LDA model is based on uniform electron gas where the motion of the electron is considered under a positive, ionic background charge distribution, with a total neutral charge ensemble of particles. In LDA, the exchange-correlation energy at a point r per particle remain the same in an ideal homogeneous electron gas with electron density $n(r)$. In this approximation the exchange-correlation functional $E_{XC}[n(r)]$ takes the following form

$$E_{XC}^{LDA}[n(r)] = \int n(r)\epsilon_{XC}^{hom}n(r)dr \tag{2.21}$$

$$= \int n(r)[\epsilon_{X}^{hom}(n(r)) + \epsilon_{C}^{hom}(n(r))]dr \tag{2.22}$$

$$= E_{X}^{LDA}[n(r)] + E_{C}^{LDA}[n(r)] \tag{2.23}$$

The exchange-correlation functional $E_{XC}[n(r)]$ in LDA assumption splits into two parts, the exchange part $E_{X}^{LDA}[n(r)]$ and the effective correlation contribution $E_{C}^{LDA}[n(r)]$. The exchange part gives the exchange energy of an electron in a homogeneous electron gas of particular density $n(r)$, and initially deduced by Bloch and Dirac around the late 1920s.

The exchange part $E_{X}^{LDA}[n(r)]$ in the exchange-correlation functional $E_{XC}[n(r)]$ can be derived analytically for a system of uniform electron gas with density $n(r)$:

$$E_{X}^{LDA}[n(r)] = \int n(r)\epsilon_{X}^{hom}n(r)dr \tag{2.24}$$

$$= -\frac{3}{4}\left(\frac{3}{\pi}\right)^{1/3}\int n(r)^{4/3}dr \tag{2.25}$$

where

$$\epsilon_X^{hom} = -\frac{3}{4}\left(\frac{3}{\pi}\right)^{1/3} n(r)^{1/3} \tag{2.26}$$

is the homogeneous electron density for the exchange part in LDA.[191]

No such analytical expression for the correlation part $E_C^{LDA}[n(r)]$ explicitly exist in the LDA approximation for a system of uniform electron gas with density $n(r)$ leading to an overestimation of the correlation energy up to a factor of 2, which is rather smaller for real materials. On the other hand, the accuracy of exchange energy in LDA ~ 10%. The underestimation of exchange energy in LDA formalism and the overestimation of correlation energy error partially cancel one another and gives a moderate accuracy for ionization energies of atoms, dissociation energies of molecules, and cohesive energies ~ 10-20%. However, the bond lengths of molecules and solids are obtained with remarkable accuracy ~ 2% at the LDA level.

The moderate accuracy of *local density approximation (LDA)* is insufficient for most solids for practical applications in material science, it also failed miserably for heavy fermions, and systems that are primarily dominated by the electron-electron interactions.

Most DFT+LDA formalism uses the analytic forms for ϵ_C to fit the accurate quantum simulation results for the correlation energy by considering an intermediate density, that is used to map out the results obtained at the high- and low-density limits. In theory, the *local density approximation* works well for systems with slowly varying electron density and with rapid density variation, the LDA tends to underestimate bond-length by 1-2% [192], vibrational frequencies of molecules within 5-10 % accuracy, overestimate the binding energies by 10-50% [193], [194], and largely underestimate the fundamental transition energy gaps or bandgap of solids by up to ~ 50% [195].

2.2.3.2 Generalized Gradient Approximations

Since the exchange-correlation energy of a homogeneous electron distribution widely differs for a real material with non-local density variations, the first thoughtful step to go beyond the LDA formalism is the use of not only the information about the density $n(r)$ at a particular point r in space, but to supplement this uniform density with gradient correction of the charge density, $\nabla n(r)$ that accounts for the non-homogeneity of the actual electron density. Thus, the exchange-correlation energy in the generalized gradient approximation (GGA) becomes,[196]

$$E_{XC}^{GGA}[n(r), n(r')] = \int f\,[n(r), n(r'), \nabla n(r), \nabla n(r')]dr \qquad (2.27)$$

The GGA is found to work much better than the LDA in predicting material properties to their approximate real value in the Kohn-Sham method. The overcorrection of the local electronic density of uniform electron gas by gradient corrected density was hugely successful useful for semiconducting systems which largely reduce the ground state properties such as lattice constants were smaller by < 0.6% than an experiment, cohesive energy, dielectric function, elastic constants within 3% of its experimental value, and bandgap underestimation problem of LDA within 0.2 eV of its experimental value in GGA.[197], [198]

Over the years many progress has been made in deriving the successful GGA functionals.[199], [200] The most commonly used GGA formalism in DFT is Perdew-Wang (PW91)[201] and Perdew-Burke-Ernzerhof exchange-correlation energy for the GGA's.[200] In most of our DFT calculation results, we have used the Perdew-Burke-Ernzerhof variant of the generalized gradient approximation (GGA), which incorporates some inhomogeneity effects that are well suited for predicting the electronic properties of various semiconducting systems. The combination of GGA and PBE provides better accuracy than normal GGA's, results close to the experimental results for layered materials.[202] However, the prediction of material properties using GGA's still remains to the electronic ground state and fail measurably

in predicting the excited state properties of semiconductors such as optical transition energies, excitation banding energy, accurate band edges of electron-hole and optical absorption in most semiconducting materials. Nonetheless, due to its higher computing efficiency and reasonable accuracy of results, it has remained the primary choice to study various trends in material properties such as the bandgap engineering and lattice dynamics under external perturbation in the form of lattice strain, pressure, and electric field.[203]–[206]

2.2.3.3 Hybrid functionals

In a conventional local density approximation or gradient corrected density functional approximation, we have repeatedly seen that the exchange contribution E_X is usually much larger than the corresponding correlation E_C effects. Even the semilocal correction effects do not reproduce the reasonable bandgap in semiconductors due to self-interaction errors and missing derivative discontinuity in electron density. Hence, a reasonable accuracy of exchange functional is a prerequisite to get meaningful results in DFT. A straightforward way to get the most accurate exchange-correlation energy is the use of exact exchange energy in the Kohn–Sham density functional theory.

In hybrid density functionals, we include certain parts of the exact Hartree-Fock exchange energy to improve the results of our GGA calculations. However, the use of hybrid density functionals is computationally costly for most materials and very much dependent on the size of the system. In 1992, Axel D. Becke *et al.* [207] established a simple but rather powerful strategy to link the Hartree-Fock-based methods with the density functional theory calculation, the so-called "Hartree-Fock-Kohn-Sham" scheme by using an adiabatic connection to the nonlocal exchange potential in which the non-local Fock exchange operator replaces a part of the local exchange energy.[208]

The exchange-correlational energy in hybrid approximation,

$$E_{XC}^{hyb.} = aE_X^{KS} + (1-a)E_{XC}^{GGA} \quad (2.28)$$

where E_X^{KS} is the exchange energy of the exact Kohn-Sham wave function, E_{XC}^{GGA} approximate energy in GGA and a is a fitting parameter which determines the amount of non-local exchange part in the hybrid approximation, typically $a \sim$ ¼ % of Hartree-Fock mixing.

The widely used hybrid functional in DFT is the Heyd–Scuseria–Ernzerhof (HSE) screened Coulomb potential were a part of short and long-range interaction of PBE exchange functional is replaced by the short-range non-local Hartree-Fork exchange interaction. [209], [210]

The use of HSE functionals in DFT significantly improved the lattice parameters, bandgap, and elastic properties for many nonmetallic systems where the errors in the fundamental bandgap of semiconductors get reduce to 50% than the same calculated by using the GGA functionals alone.[211]

In a nutshell, the predictive potential of different functionals through incorporating various exchange-correlation parts to the density functional theory is progressively improving the accuracy of theoretical results close to the experimental values, where the accuracy in the bandgap: LDA < GGA < hybrid functional is scaling with the computing need of the problem. Using HSE functionals, the errors in ionization energy and affinity have reduced to ~ 0.2 eV for many semiconducting materials, including transition metal dichalcogenides.[212]–[215]

2.2.4 Basis sets

Slater-type-orbitals (STO): For the wave function computation of atomic and diatomic systems, the STO seems to be the natural choice for basis functions. They are exponential functions that decay at long range and provide cusp condition in a short-range mimicking the exact eigenfunctions of the hydrogen-like atom. A typical STO is expressed as,

$$\eta^{STO} = Nr^{n-1}\exp\left[-\beta r\right]Y_{lm}(\theta,\varphi) \quad (2.29)$$

Here, η corresponds to the principal quantum number, and the orbital exponent is denoted by β and the spherical harmonics Y_{lm}. Unfortunately, many-center integrals are complicated to compute with an STO basis, and they do not play a significant role in quantum chemistry.

Gaussian-type-orbitals (GTO): The Gaussian basis sets are the usual choice in computational chemistry and molecular physics. GTO is used to describe electron orbitals in a range of atomic and molecular structures and expressed as

$$\eta^{GTO} = N x^l y^m z^n \ \exp[-\alpha r^2] \tag{2.30}$$

N is a normalization factor ensuring $\langle \eta_\mu | \eta_\mu \rangle = 1$, α is the orbital exponent. *L* = *l*+*m*+*n* is used to classify the GTO as s-functions (L = 0), p-functions (L = 1), etc. The GTO requires a large number of basis functions for predicting molecular properties, decay rapidly at a larger r and does not have a cusp condition around the nuclei.

Plane-wave-basis (PWB): For periodic solids, the plane wave basis is most suited to express cell-periodic functions using Fourier analysis. Using Bloch theorem, the eigenfunctions of Kohn-Sham equation with wave vector ***k*** can be expressed as

$$\Psi_k(r) = e^{ik.r} \mathrm{u}_k(r) \tag{2.31}$$

where $\mathrm{u}_k(r)$ is the cell-periodic function that can be expanded in a Fourier series:

$$\mathrm{u}_k(r) = \frac{1}{\sqrt{\Omega}} \sum_G c_k(G)\, e^{iG.r} \tag{2.32}$$

here G reciprocal lattice vector, Ω unit cell volume, $c_k(G)$ expansion coefficient to G, and $e^{iG.r}$ is the exponent to phase. The eigenfunction $\Psi_k(r)$ can be expanded using a plane-wave basis as:

$$\Psi_k(r) = \frac{1}{\sqrt{\Omega}} \sum_G c_k(G)\, e^{i(k+G).r} \tag{2.33}$$

In a crystalline solid, many elements contribute to a band structure, and the free electron model can be used to interpret the orbitals of different elements. Only the valence electrons majorly participate in the orbital interactions, and it is convenient to use the pseudopotential theory to represent the interaction of valence electrons with an effective ionic core. Since the core is frozen, the pseudopotential wavefunctions can be built to match the wavefunctions of valence electrons independent of atomic positions, where the plane wave basis provides a natural periodicity to the electronic wavefunctions, they are orthogonal and complete functions. The number of electrons in a typical solid ~ 10^{28} per mole of atoms, thus, the number of plane wave basis part used in DFT to describe the gound state density is significantly large and depends on the volume of the unit cell and plane-wave cutoff energy. The accuracy of DFT results for a reference material system is improved mainly by using a large energy cutoff to estimate the ground state energies of materials. The plane-wave basis can also be used for non-periodic systems as the basis function treats all regions of space equally; however, there is an added memory get unnecessarily utilized while treating the molecules in a vacuum space.

2.2.5 Density-functional perturbation theory

Many physical properties of a material are dependent on its response to an external perturbation in the form of lattice displacement or an applied external electric field. The lattice dynamics of crystalline solid can determine many such properties including the polarizability, elastic stiffness, phonon vibrational modes, thermal expansion of solids, specific heat, electron-phonon interactions, charge transport mechanism, superconducting properties, phonon dispersion, and thermal properties via *ab initio* density functional perturbation theory (DFPT) calculations. The determination of vibrational properties of materials from its crystal phonon is one of the astonishing success of modern electronic structure theory. The density functional theory (DFT) deals with the electronic part of the system, while the DFPT is a linear response method to deal ionic part of the problem and the interaction among electron-phonon. The linear

response properties in DFPT are calculated from the interatomic force constants for each atomic displacements, where a small perturbation is applied to the equilibrium lattice structure in terms of strain or electric field.[216]

2.2.5.1 Perturbation in Kohn-Sham scheme

The standard perturbation strategies in the form of small strain or electric field perturbations to the lattice displacement enter into the DFT scheme through an effective potential $V_{eff}(r)$ in the Kohn-Sham equation.[217] Moreover, a linear variation in perturbation will remain dependent on the ground state density of electrons. The effective potential under the Kohn-Sham scheme is defined as

$$\delta V_{eff}(r) = \delta V_{ext}(r) + \delta V_{scr}(r) = \delta V_{ext}(r) + \int d^3r' I(r,r')\,\delta n(r') \qquad (2.34)$$

$$I(r,r') \equiv \frac{\delta V_{scr}(r)}{\delta n(r')} = \frac{\delta V_H(r)}{\delta n(r')} + \frac{\delta V_{XC}(r)}{\delta n(r')} \qquad (2.35)$$

The perturbation induces the 1st-order variation in the single-particle wave function and defined as

$$\delta\psi_i(r) = \sum_{j(\neq i)} \frac{< j|\delta V_{eff}|i >}{\epsilon_i - \epsilon_j}\psi_j(r) \qquad (2.36)$$

Using a similar expression for $\psi_i{}^*(r)$ gives

$$\delta n(r) = \sum_{i\neq j} \frac{f_i - f_j}{\epsilon_i - \epsilon_j} < j|\delta V_{eff}|i > \psi_i{}^*(r)\psi_j(r) \qquad (2.37)$$

An iterative solution to the equation (2.19) using (2.36) and (2.37) gives a 1st – order variation in density and corresponding total energy change of the system.

2.2.5.2 Lattice dynamics approach

The lattice dynamics under the Kohn-Sham perturbation scheme is the ionic displacement in solids.[217] Using the Hellmann-Feynman theorem, the potential corresponding to an applied perturbation is expressed in the Talyor expansion:

$$V_\lambda(r) = V_0(r) + \lambda\frac{\partial V}{\partial \lambda} + \lambda^2\frac{\partial^2 V}{\partial \lambda^2} + \cdots \tag{2.38}$$

The corresponding electron density n(r) and wave function ψ(r) under such perturbation

$$n_\lambda(r) = n_0(r) + \lambda\frac{\partial n}{\partial \lambda} + \lambda^2\frac{\partial^2 n}{\partial \lambda^2} + \cdots \tag{2.39}$$

$$\psi_\lambda(r) = \psi_0(r) + \lambda\frac{\partial \psi}{\partial \lambda} + \lambda^2\frac{\partial^2 \psi}{\partial \lambda^2} + \cdots \tag{2.40}$$

The 1st order solution to the equation (2.19) will be the 1st order Schrödinger equation under perturbation terms in equation (2.38)-(2.40) that leads to the Hellman-Feynman theorem to define the expectation value of the derivative of the Hamiltonian operator to get the eigenvalues of the system

$$\frac{\partial E}{\partial \lambda} = < \psi \left| \frac{\partial H}{\partial \lambda} \right| \psi > \tag{2.41}$$

Using Hellman-Feynman theorem and 1st-order perturbation of electron density, the total energy expression of a perturbed system becomes:

$$E = E_0 + \sum_i \lambda_i \int n_0(r)\frac{\partial V(r)}{\partial \lambda} dr + \frac{1}{2}\sum_{i,j}\lambda_i\lambda_j \int \left(\frac{\partial n(r)}{\partial \lambda_i}\frac{\partial V(r)}{\partial \lambda_j} + n_0\frac{\partial^2 V(r)}{\partial \lambda_i \lambda_j}\right) dr \tag{2.42}$$

and Taylor series expansion of total energy

$$E = E_0 + \frac{1}{2}\sum_{L,L'}\sum_{i,j} u_i(R_L)u_j(R_{L'})C_{i,j}(R_L, R_{L'}) \tag{2.43}$$

2nd order term to the force constant becomes

$$C_{i,j}(R_L, R_{L'}) = \int \left(\frac{\partial n(r)}{\partial u_i(R_L)} \frac{\partial V(r)}{\partial u_j(R_{L'})} + n_0 \frac{\partial^2 V(r)}{\partial u_i(R_L)\partial u_j(R_{L'})} \right) dr \tag{2.44}$$

In equation (2.41) a 1st order perturbation to the electron density is required to evaluate the 2nd order force constants. Ref. [217] gives further details on density functional perturbation theory methods to calculate the phonon and related crystal properties of materials.

2.3 Vienna *ab-initio* simulation package

The calculation results presented in this thesis were carried out by the Vienna Ab-initio Simulation Package (VASP). VASP is a sophisticated quantum simulation tool to perform *ab initio* calculations within the density functional theory at zero Kelvin temperature. The interaction between ions and electrons is described by the projector-augmented wave (PAW) pseudopotential methods using a plane-wave basis set to solve the Kohn-Sham equations in DFT with kinetic energy cut off > 500 eV. The all-electron Kohn-Sham wave function is linearly transferred into a pseudo wave function in PAW for computational convenience implemented in VASP. For periodic solids, the use of a plane-wave basis set is advantageous over the other localized orbital basis, and the results produced are well endorsed by the computational material science community. The optimization of electronic wave functions leads to an instantaneous ground-state electron density by using efficient iterative matrix diagonalization schemes (RMM-DISS, and blocked Davidson) that allow a sufficient reduction in the number of plane-waves per atom, typically ~ 100 plane waves per atom in bulk solids. The Hellman-Feynman forces acting on various atomic species and a full stress matrix can be evaluated using VASP, whereas for each self-consistency cycle the minimum energy and

corresponding stress matrix is determined, to minimize the same, with respect to the previous iteration till a reasonable accuracy is achieved in total energy change. The convergence in total energy is controlled by the cut off energy and *k* mesh sampling. The execution time in VASP scales with N^3, where *N* number of valence electrons in the system. VASP is useful for systems containing a number of valence electrons by up to 4000. The code also uses different symmetry reduction schemes for the efficient calculation of bulk properties of materials. Electronic smearing methods such as Fermi, Gaussian, and tetrahedron smearing are used in the integration of band structure energy in the Brillouin zone. The Blöchl's corrections for the semiconductors are used in our calculation to remove the quadratic errors in the linear tetrahedron smearing method that leads to faster convergence of energy. VASP runs well in many computing platforms, both in vector computers and parallel computers, at nearly the same speed.

The Vienna Ab-initio Simulation Package (VASP) consists of 4 input files for the calculation of various material properties: INCAR, POSCAR, POTCAR, and KPOINTS. Besides, an execution script is required to submit the VASP calculation in a high-performance computing platform.

INCAR: The INCAR file contains all the input commands implemented in the VASP code to calculate the desired properties of a material. It usually contains a large number of input parameters and certain default flags that are central to a specific calculation of properties.

KPOINTS: This file contains the wave vector coordinates or reciprocal lattice coordinates in a weighted mesh form (*k*-point grid) for the Brillouin zone integration. The denser is the *k* mesh grid, the higher will be the CPU time and accuracy of results.

POSCAR: The POSCAR file contains the real space lattice information (lattice position and unit-cell vectors) of different elements present within a material.

POTCAR: The POTCAR is the pseudopotential file for individual elements of the system that contains valence and core electronic information.

The job execution script depending on the computing architecture, is used to submit the VASP job to obtain the electronic properties of a given material specified in the POSCAR file. In the initial step, the geometry of a given crystal is optimized to its ground state crystal structure within DFT, and the corresponding optimized lattice coordinates appear in the CONTCAR file. The process is achieved by minimizing the total energy, and the Hellmann-Feynman forces exerting on individual atomic species in the stress matrix printed in the OUTCAR file. All desired properties of a material can be extracted from the WAVECAR and CHGCAR file, the WAVECAR file contains the wave function information of Kohn-Sham equation, and the CHGCAR file contains the ground state change density of a material, respectively.

----------**********----------

Chapter 3

Coupled spin-valley phenomena in monolayers of Group-VIB transition metal dichalcogenides & their Janus derivatives: A strain-dependent study

This chapter is based on the following unpublished work:

Nityasagar Jena, Raihan Ahammed, and Abir De Sarkar*, "*Spin-orbit interaction and valley contrasting phenomena in pure and Janus monolayers of Group-VIB 1H transition-metal dichalcogenides*", ***[In manuscript]***

3.1 INTRODUCTION

Spin-orbit interactions (SOI) in non-magnetic semiconductors with missing inversion symmetry can lift the spin degeneracy of electronic states due to an asymmetry in crystal-field potential [218], [219]. Spintronics, the mechanism to manipulate and control electron spin degrees of freedom (DOF) in information processing, is radically a new frontier in the pursuit of spin-based integrated electronics [220], [221]. Atomically thin monolayers of group-VIB transition-metal dichalcogenides (TMDCs) or commonly referred as 1H-MX_2 (where M = Cr, Mo, W, etc; X = S, Se, or Te) [93], [222], [223] are family of noncentrosymmetric semiconductors with intrinsic direct band gaps E_g ~ 1.1-1.9 eV in the range of visible light [93], [224], [225], good charge carrier mobility ~ 200-700 $cm^2.V^{-1}.s^{-1}$ in field-effect transistors

(FETs) operating at room temperature, and giant spin-splitting energy (~148-456 meV) [86], [123] originating from the domination of frontier *d*-orbitals of transition metal atoms have recently recognized as ideal hosts for next-generation innovative electronics, optoelectronics [226], [227] and spintronics [86], [228]. Besides, the honeycomb lattices of 1H-MX_2 acquire a pair of symmetry inequivalent time-reversed (TR) valleys situated at opposite edges of a 2D hexagonal Brillouin zone (BZ), at the corner K (+K) and K' (-K) points of 1st BZ, respectively. A simultaneous entanglement of charge, spin, and valley pseudospin DOF are perspective phenomena in these monolayers to exploit this distinctive quantum DOF for novel coupled spin-valley physics, including valley-selective circular dichroism (CD) [229], spin-Hall effect (SHE) [86], [230], and valley-Hall effect (VHE) [231], [232]. All these exciting physics is possible in these ultrathin atomic crystals due to the fascinating chiral nature of its valley carriers at K/K' points. The valley contrasting phenomena that drive this interlinked quantum DOF through optical and electrical selectivity are exotic signatures of Berry-phase curvature distribution $\Omega(k)$ of low-energy Bloch bands that are occurring close to the fundamental direct band gap of 1H-MX_2 semiconductors [135], [136], [233]. The orbital and crystal symmetry guided spin-momentum locking, and quantum control of valley pseudospins are compelling events towards the inventive design of integrated excitonic circuits [234], so-called valleytronic devices [16], such as valley filter and valley valves [129].

Additionally, the absence of inversion symmetry in MX_2 monolayers and the same in the odd-numbered layers of it gives rise to sizeable in-plane piezoelectricity (3-7 pm/V). [163] The occurrence of a high degree of piezoelectricity in MX_2 monolayers is a sought-after phenomenon for high-performance piezotronic energy conversion,[22] and piezoelectric actuation, [235], [236] owing to a reversible nanoelectromechanical coupling of electric polarization and external mechanical strain [163], [171]. However, the out-of-plane polarization is restricted ($P_z = 0$) in pristine MX_2 monolayers due to the presence of vertical

mirror symmetry (D_{3v}) of identical chalcogen atoms (X_2) that isotropically sandwitch the central metal atom (M) layer in a X-M-X sequence with a trigonal prismatic coordination geometry of lattices and strong polar covalent bonding of Mo *d* and S *p* atomic orbital overlapping with the basal plane. In recent experiments, this out-of-plane mirror symmetry of chalcogen sublattice is broken by the formation of Janus monolayers, namely MXY structures [184], [185], where X ≠ Y. A well-controlled CVD synthesis process demonstrated by Lu *et al.* [184] have shown it is possible to make thermodynamically stable, perfect MoSSe (E_g ~ 1.68 eV) Janus monolayer structures through a plasma irradiated atom stripping technique as a synthetic route for the production of perfect X-M-Y monolayer structures derivable from their parent MX_2 monolayer crystals. The result of structural inhomogeneity around the central metal atom (M) leads to a spontaneous out-of-plane electric field generated within X-M-Y structures, and this is stemmed from the built-in perpendicular dipole moment of asymmetric sublattice potential over the X and Y atoms [184], [188], [237]. The induced effective vertical electric field couples to the carriers Kramer spin degeneracy through relativistic spin-orbit interactions (SOI) in a broken inversion symmetric system and give rise to the novel momentum-dependent spin splitting of electronic bands, so-called Rashba effect [184], [238], [239] and also brings a large intrinsic vertical piezoelectricity in monolayer/multilayer stacks of Janus MXY systems (d_{33} ~ 0.1-13.5 pm V^{-1}) [184], [186].

Although, the Rashba effect in inversion asymmetric surfaces [240]–[242]; hybrid heterojunctions [221], [228], [243], [244]; and weakly coupled van der Waal (vdW) interfaces [228], [245] resulting from proximity-induced exchange field have long been studied for their spintronic functionalities. The evidence of a large Rashba-type band splitting (Rashba parameter, α_R ~ 2-14 meVÅ) in these new class of ultrathin Janus (MXY) monolayers are quite intriguing to enrich and propel the emerging field of 2D semiconductor-based spintronics, valleytronics and piezotronics[82], [246]. Here, the realization of a long-sought goal of spin-

polarized field-effect transistor (spin-FET) proposed by Datta and Das in their seminal work back in 1990[247] is viable without any requirement of the high magnitude of external electric/magnetic gating [248] or magnetic element doped into the host crystal lattice to induce the Rashba type band splitting.

In this chapter, we theoretically demonstrate a significant intrinsic Rashba effect in *Group VIB* Janus transition metal dichalcogenide monolayers (1H-MXY, M = Cr, Mo, W; X ≠ Y = S, Se, Te) using density functional theory calculations. Here, we attempt to present a comprehensive analysis of electronic structure results for pristine transition metal dichalcogenide monolayers (1H-MX_2) and their Janus monolayer derivatives (1H-MXY) for Group VIB monolayer TMDCs. Further manipulation of the Rashba spin splitting of bands around the Γ point and the Zeeman type spin splitting of bands at the K point in the Brillouin zone (BZ) has been investigated through a uniform strain engineering of Janus monolayer lattices. The extent of orbital overlapping of transition metal d_{z^2} and chalcogen p_z atomic orbitals, together with a changing dipolar contrast due to a lateral Poisson contraction of chalcogen sublattices in response to an applied in-plane biaxial strain, can magnify the intrinsic build in vertical electric field, thereby, offers a broad tunability in Rashba parameters. A colossal change in the Rashba parameter, such as a massive increase in SOC spin splitting energy at K/K' points of low energy valleys of electron and hole states and a strain tunable Berry curvature in 1H-MXY monolayers offers a fertile ground for spintronics and valleytronics in these multi-valley 2D electronic systems.

3.2 COMPUTATIONAL DETAILS

Quantum simulations have been carried out using density functional theory (DFT) based methods implemented within the Vienna *ab-initio* simulation package (VASP *version*: 5.3) [249]–[251]. The generalized gradient approximations (GGA)[190] in its Perdew-Burke-

Ernzerhof (PBE)[252] parametrization has been used for the exchange-correlation functionals. The electron-ion interaction was treated by the projector augmented plane wave (PAW) potentials. An energy cutoff of 600 eV was used to expand the electronic wave functions on a plane wave basis. Conjugate gradient optimization schemes were used for the full relaxation of lattices and interatomic coordinates till the Hellmann–Feynman forces acting on individual atoms reduces to $< 1 \times 10^{-3}$ eV.Å^{-1}. In a self-consistent energy convergence loop, the criterion for total energy convergence between successive cycles was set at 1×10^{-6} eV. For the Brillouin zone integration, a 9 x 9 x 1 Γ-centered mesh was used in the geometry optimization, while a denser mesh of 19 x 19 x 1 was used for the electronic structure calculations with electronic energy smearing of 0.05 eV. The monolayers were isolated by considering a sufficient empty/vacuum spacing > 15 Å on either side of a free-standing slab geometry along the *z*-direction that effectively isolates a monolayer nanosheet in a supercell. The lattice dynamical stability of pure and Janus monolayers was accessed through the calculation of phonon dispersion based on DFPT [217] as implemented in VASP and the Phonopy [253] interface code is used to process the results from the elements of force constant matrix. The Young's modulus and Poisson ratios have been derived from the coefficients of elastic stiffness matrix (C_{ijkl}). The finite difference methods were used to calculate the in-plane relaxed-ion elastic stiffness coefficients, such as C_{11} and C_{12}, including both the electronic and ionic contributions to the total elastic matrix. The piezoelectric constants have been evaluated by using a linear response method within the DFPT as embedded in the VASP code [216]. [216]. Ab initio molecular dynamics (AIMD) simulation approach has been used to access the thermal stability of Janus monolayers using the PBE functionals as implemented in the VASP program. The optimized ground state structures were annealed at room temperature, 300K in NVT ensemble using Nosé–Hoover thermostat for a time duration of 5 *ps* with a step size of 1.0 *fs*.

3.3 RESULTS AND DISCUSSION

3.3.1 Crystal structure and electronic properties

Janus monolayers of transition-metal dichalcogenides (JTMDCs) or chalcogen asymmetric X-M-Y monolayer structures have been prepared from their most stable, parent X-M-X monolayer structures (1H-MX_2), by replacing one of the chalcogen sublattices of MX_2 with a higher chalcogen element, where X ≠ Y (X, Y = S, Se, or Te), as depicted in Figure 3.1 (a)-(b). Analogous to the semiconducting MX_2 monolayers, the atomic layers of Janus MXY exhibit in a hexagonal crystal symmetry with symmetry reduction in the space group from the parent $P\bar{6}m2$ noncentrosymmetric structure to the Janus $P3m1$ symmetry, which is also a noncentrosymmetric space group. The polar Janus monolayers are enforced with the trigonal-prismatic coordination of chalcogen sublattice on either side of the transition metal atom that differs in bond length between M-X and M-Y with an absence of vertical mirror plane as compared to their pristine monolayers. The asymmetry in the chalcogen sublattice in the polar MXY monolayer removes the out-of-plane chalcogen reflection symmetry, thereby, induces a vertical dipole moment and out-of-plane piezoelectricity which found of the order of ~ 0.1-1.0 pm/V in Janus monolayers. Moreover, the in-plane piezoelectricity of pristine and Janus monolayers are of the order of ~ 2-13 pm/V, which is significantly larger as compared to the most common 3D piezoelectric system, such as α-quartz (d_{11} = 2.27 pm/V) and AlN (d_{33} = 5.6 pm/V).

Before going to the results on electronic properties, we first analyze the chemical stability of pristine and Janus monolayers by computationally accessing their relative cohesive energies, which is defined as, $E_{coh} = (nE_M + nE_X + nE_{X/Y} - E_{MX2/MXY})$/N, where E_M, E_X and $E_{X/Y}$ are total energies of transition metal atom and chalcogen atoms within the MX_2 or MXY crystal structure, $E_{MX2/MXY}$ is the total energy of pristine MX_2 or Janus MXY monolayer,

n is the number of atoms of a given atomic species in the corresponding monolayer structure and *N* is the total number of atoms in the unit cell. The cohesive energies of all pristine and Janus monolayers of *Group VIB* TMDCs have been examined and presented in Table 3.1 and Table 3.2, respectively. The calculated cohesive energies of our optimized Janus monolayers are comparable to their stable pristine MX_2 monolayer structures, and the energy trend in cohesive energy decreases with an increase in chalcogenide atomic radius for a given transition metal atom. The relative stability of Janus monolayers infers a robust covalent bonding in the X-M-Y network that is evident from their comparable cohesive energies. The sublattice symmetry breaking of MX_2 monolayers leads to a non-zero out-of-plane polarization in MXY structures that are arising due to the electrostatic potential difference between the top and bottom chalcogen atomic layers of MXY (e.g., WSeTe), as shown in Figure 3.1 (d). The asymmetric chalcogen surfaces of Janus monolayers differ in their work function, and a difference of ~ 0.29 eV originates from the potential difference between the chalcogen atomic layers in a Te-W-Se sandwiched structure, as depicted in Figure 3.1 (d). The potential difference increases with an increase in dipolar contrast between chalcogen lattices, as presented in Table 3.2. However, the same for pristine TMDCs is null due to isotropic chalcogen lattices about the central metal atom layer; thus, a homogenous potential surface on either side of central metal atom in the MX_2 infers isotropy in work function, as tabulated in Table 3.1. Our calculated work function of pristine and Janus monolayers lies in the energy range of 4-6 eV,[254]–[256] which is ideal for many of the commonly used contact electrodes, such as Au (work function W ~ 5.2 eV), and Pd (W ~ 5.12 eV) in the formation of Schottky type metal-semiconductor interface for efficient electron injection to its conduction band.[257] The potential difference caused by the vertical inversion asymmetry of chalcogen sublattices with broken crystal inversion symmetry in MXY can give rise to a giant momentum dependent spin splitting of its Kramer degenerate bands, so-called Rashba-type spin splitting of electronic

bands, as shown in Figure 3.1 (c). Besides, in the formation of Janus monolayers, the intrinsic direct nature of its semiconducting band gap is found to be retained at the K point of the BZ with an enhancement in the Zeeman-type spin splitting of electronic bands occurring around the K and K' valleys in the valence and conduction band sectors of the spin-polarized electronic bandstructure, as shown in Figure 3.1 (c).

Table 3.1 and Table 3.2 summarizes the lattice parameter, cohesive energy, electronic band structure information (e.g., bandgap, SOC splitting energy, and work function), 2D elastic constants (e.g., Young's modulus and Poisson ratio) and piezoelectric coefficients (in-plane d_{11} and out-of-plane d_{31} piezoelectric coefficients) for both pristine and Janus TMDC monolayers. The Young's modulus and Poisson ratio of Janus monolayers are comparable to their parent pristine monolayer TMDCs, where the elastic stiffness of S-Se based Janus system lies within the pristine values of MS_2 and MSe_2 monolayer crystal (where M = Cr, Mo, W). However, Young's modulus values are much smaller as compared to single-layer graphene (Y = 341 N/m) or h-BN (Y = 275.9 N/m).[258]

For pristine monolayer TMDCs (1H-MX_2), the S, Se, and Te based systems are found to exhibit a direct semiconducting bandgap ~ 0.4-1.8 eV at the K point, where the valence band maximum (VBM) and conduction band minimum (CBM) are located at the same K – point in the 1st BZ, whereas, the SOC spin splitting energy at the VBM of K point is found to be of the order of ~ 64-487 meV (Cr-Mo-W) and the SOC energy in CBM at the K point, which is relatively smaller in magnitude is of the order of ~ 2-52 meV. A significant spin splitting of bands close to the fundamental direct band gap of monolayers is desirable for spintronic functionalities where the distinct spin DOF of valley carriers can be exploited in digital information storage and processing.

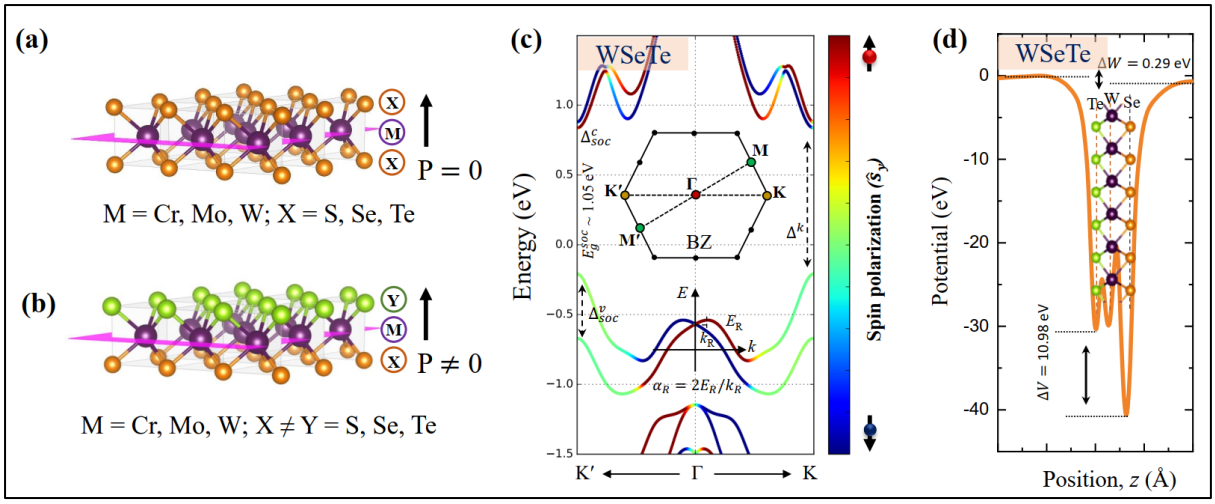

Figure 3.1. (a)-(b) Crystal structure of pristine and Janus monolayer transition-metal dichalcogenides (c) Spin-polarized band structure of Janus WSeTe monolayer with spin projection operator S_y as the spin quantization axis and (d) electrostatic potential of WSeTe monolayer.

Table 3.1. Summary of the lattice parameter (a = b), cohesive energy per atom (E_{coh}) in the unit cell, the work function of pristine monolayer TMDCs, a global energy gap between valence band maximum (VBM) and conduction band minimum (CBM) calculated without and with the exclusion/inclusion of SOC effects into the band structure using the DFT PBE functionals, the valence band spin splitting ($\Delta_{soc}^{v\_K}$) at the K point and the conduction band spin splitting ($\Delta_{soc}^{c\_K}$) at the CBM of K point due to SOC in meV, Young's modulus (Y) and Poisson ratio (ϑ) of monolayer TMDCs, and the in-plane piezoelectric coefficient (d_{11}).

MX_2	a=b (Å)	E_{coh} (eV/atom)	W (eV)	E_g^{PBE} (eV)	$E_g^{PBE+SOC}$ (eV)	$\Delta_{soc}^{v\_K}$ (meV)	$\Delta_{soc}^{c\_K}$ meV	Y ($N.m^{-1}$)	ϑ	d_{11} ($pm.V^{-1}$)
CrS_2	3.04	3.25	5.81	0.93^{K-K}	0.89^{K-K}	68.52	3.54	112.28	0.26	6.22
$CrSe_2$	3.20	2.08	5.26	0.75^{K-K}	0.69^{K-K}	90.34	15	89.94	0.29	8.42
$CrTe_2$	3.47	1.53	4.82	0.53^{K-K}	0.46^{K-K}	106.76	20.18	65.09	0.33	13.65
MoS_2	3.18	3.66	5.88	1.66^{K-K}	1.59^{K-K}	148.05	3.03	137.78	0.24	3.24
$MoSe_2$	3.32	3.13	5.31	1.44^{K-K}	1.33^{K-K}	183.85	20.56	104.37	0.22	4.35
$MoTe_2$	3.55	2.77	4.88	1.08^{K-K}	0.94^{K-K}	214.69	33.48	81.17	0.22	6.81
WS_2	3.18	3.78	5.68	1.81^{K-K}	1.54^{K-K}	431.44	29.38	140.42	0.21	2.19
WSe_2	3.32	3.24	5.12	1.54^{K-K}	1.24^{K-K}	466.97	36.16	116.85	0.18	2.56
WTe_2	3.55	2.86	4.70	1.06^{K-K}	0.73^{K-K}	486.91	51.77	85.95	0.18	4.36

Table 3.2. Summary of the lattice parameter ($a = b$), cohesive energy per atom (E_{coh}) in the unit cell, the potential difference between the chalcogen atomic layers (ΔV_{X-Y}) in MXY structure, a fundamental energy gap between the valence band maximum (VBM) and conduction band minimum (CBM) calculated without and with the exclusion/inclusion of SOC effects into the band structure using the PBE functionals, the valence band spin splitting ($\Delta_{soc}^{v\_K}$) at the K point and the conduction band spin splitting ($\Delta_{soc}^{c\_K}$) at the CBM of K point due to SOC effects in *meV*, Young's modulus (Y) and Poisson ratio (ϑ) of Janus TMDCs, the in-plane piezoelectric coefficient (d_{11}), and the out-of-plane piezoelectric coefficient (d_{31}).

MXY	*a=b (Å)*	E_{coh} *(eV/atom)*	ΔV_{X-Y} (eV)	E_g^{PBE} *(eV)*	E_g^{PBE+SO} *(eV)*	$\Delta_{soc}^{v\_K}$ *(meV)*	$\Delta_{soc}^{c\_K}$ *meV*	Y *(N.m^{-1})*	ϑ	d_{11} *(pm/V)*	d_{31} *(pm/V)*
CrSSe	3.12	3.02	2.61	$0.83^{\Gamma-K}$	0.79^{K-K}	81.52	10.39	98.37	0.26	7.36	0.48
CrSeTe	3.34	1.81	11.99	$0.63^{\Gamma-K}$	0.58^{K-K}	100.13	19.32	76.68	0.31	10.97	0.52
CrSTe	3.27	2.09	10.31	$0.26^{\Gamma-K}$	$0.25^{\Gamma-K}$	94.36	17.81	87.21	0.33	10.04	0.91
MoSSe	3.22	3.32	2.52	1.56^{K-K}	1.47^{K-K}	167.97	13.2	114.37	0.23	4.00	0.20
MoSeTe	3.43	3.08	11.14	1.27^{K-K}	1.15^{K-K}	199.31	29.54	91.16	0.22	5.75	0.20
MoSTe	3.36	3.15	9.38	$1.02^{\Gamma-K}$	$0.99^{\Gamma-K}$	185.08	25.92	101.05	0.22	5.26	0.38
WSSe	3.23	3.52	2.61	1.69^{K-K}	1.41^{K-K}	446.38	29.83	128.01	0.20	2.33	0.14
WSeTe	3.43	3.04	10.98	1.34^{K-K}	1.04^{K-K}	462.39	41.12	101.18	0.17	3.38	0.14
WSTe	3.36	3.28	9.15	$1.22^{\Gamma-K}$	$1.13^{\Gamma-K}$	425.55	29.45	113.15	0.18	3.09	0.27

In monolayer transition metal dichalcogenides (TMDCs), the absence of lattice inversion symmetry and the domination of frontier metal *d* orbitals near the valence and conduction band edges lift the spin degeneracy of electronic states due to a strong spin-orbit induced spin splitting of bands. Figure 3.2 (a)-(b) shows the spin-resolved electronic band structure of pristine MoS_2 and Janus MoSSe monolayers where the spin projection is along the out-of-plane spin quantization axis (S_z).

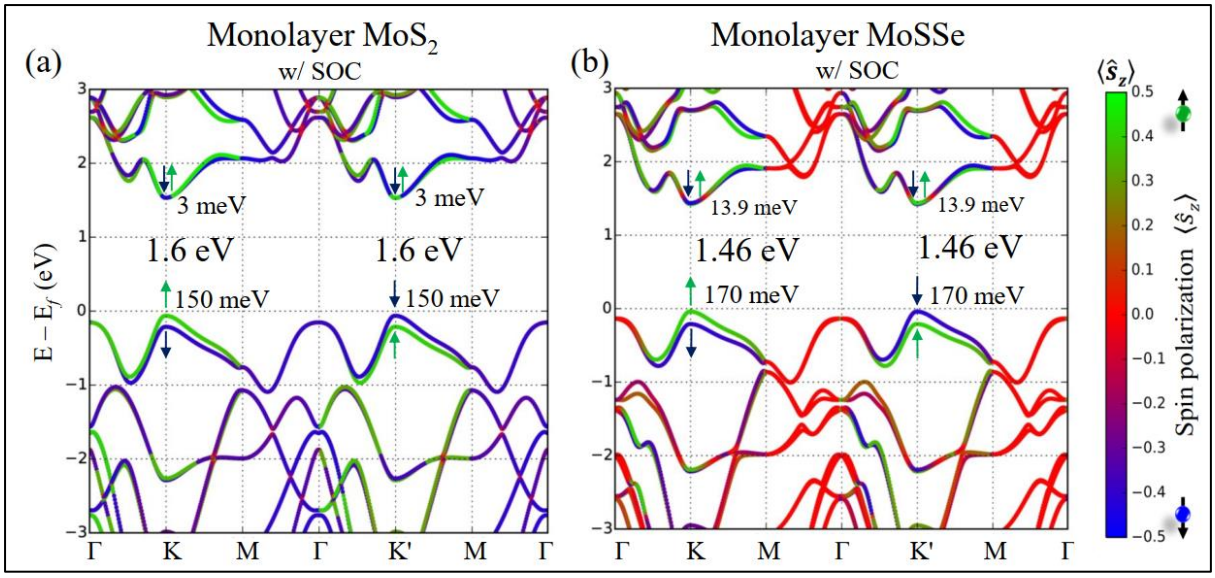

Figure 3.2. (a) Spin-resolved electronic band structure of monolayer MoS_2 and (b) Janus MoSSe monolayer with SOC turned on. The carrier spin projection is along the out-of-plane spin quantization axis, S_z (dimensionless spin Pauli matrix), and perpendicular to the basal plane of the monolayer. The green and blue color is an indicator of spin-up and spin-down polarization state. The spin-orbit induced spin splittings of bands across the valence band sector and the conduction band sector at the K point of Brillouin zone has been presented therein along with the fundamental electronic bandgap of monolayers for a relative comparison of electronic band structure modification.

This out-of-plane spin polarization of carriers in TMDCs is an interplay of planar electronic confinement of *d* electrons' motion and the asymmetry in the crystal potential gradient arising from the broken in-plane inversion symmetric structure of the lattice. The K and K' points in a monolayer TMDC are the time-reversal partner of one another. Hence the electronic states at the K valley remain at least two-fold Kramer degenerate with those of its entangled time-reversed pair at K'. The time-reversal symmetry present in the system requires the spin-split of bands at the opposite momenta, i.e., at K and K' points of the BZ to take the same energy with opposite spin polarization of spin states where the distinct spin-index of

valley carriers are locked to their crystal momentum at the low energy valleys which forms a general basis for their coupled nature of valley carriers that can be exploited in several spin and valley dependent phenomena, such as spin Hall and valley Hall effects. In monolayer MoS_2, the SOC spin splitting energy at the VBM at K point ~ 150 meV, which is significantly higher as compared to the splitting occurring in its conduction band ~ 3 meV at the K point of BZ. Upon the formation of the Janus MoSSe, the SOC spin splitting energy at the K point of BZ increases to 170 meV in the valence band sector and a similar enhancement of 13.9 meV is observed in the conduction band sector of electronic dispersion by keeping a semiconducting direct bandgap at the K point of the BZ. The direct bandgap ~ 1.46 eV and the SOC spin splitting energies of MoSSe monolayer lie in the intermediate range of values than those for the pristine MoS_2 and $MoSe_2$ monolayer, this infers the universality of electronic structure results for Group VIB TMDCs upon the formation of Janus structures that can offer additional functionalities under the out-of-plane chalcogen mirror symmetry breaking, such as Rashba type band splitting around the Γ point due to potential asymmetry in the dissimilar chalcogen lattice (ΔV_{X-Y} = 2.5-12 eV) and large vertical piezoelectricity ~ 0.1-1.0 pm/V potential to the application in spintronics and nanoelectromechanical systems.

3.3.2 Phonon and thermal stability of Janus monolayers

3.3.2.1 Phonon Stability

In order to check the kinetic stability of Janus monolayers, we have calculated the phonon dispersion along the high symmetry lines in the Brillouin zone via density functional perturbation theory methods. Figure 3.3 (a)-(c) shows the phonon dispersion and phonon density of states (*ph*DOS) of Janus CrSSe, MoSSe, and WSSe monolayer, respectively. The absence of any imaginary phonon branch in the 1st Brillouin zone is a signature of the kinetic stability of the Janus structure. The phonon branches for all other cases also exhibit a positive frequency dispersion of acoustic and optical phonon modes, thereby merely confirms the lattice

dynamical stability of MXY monolayers of *Group VIB* TMDCs. The group velocity of different phonon branches has been projected into their corresponding phonon branches, as shown in Figure 3.3 (a)-(c), respectively. The increase in atomic mass of transition metal atoms from Cr, Mo to W decreases the highest of the phonon group velocity of its longitudinal acoustic (LA) phonon branch from 1.9 km/s to 1.6 km/s, as depicted in Figure 3.3 (a)-(c). The acoustic vibrations are found to be dominated by the heavy transition-metal atom and Se atoms, whereas the high-frequency optical modes are predominantly contributed by the lattice vibrations that involve the light S atoms. Moreover, the highest of the optical phonon frequency decreases from Cr to W via Mo, and this is caused by the differences in their interatomic bonding strength and orbital overlap of transition metal *d* and chalcogen *p* orbitals. The observed phononic energy gaps in Janus MXY structures are very different from their parent MX_2 structures. Here, multiple phononic frequency gaps are observed in the optical frequency, whereas in the case of pristine MX_2, a single frequency gap is primarily observed between optical and acoustic phonons. Furthermore, the intermediate optical phonon modes are less dispersive in MXY structures, thereby can effectively reduce the phonon scattering as compared to their parent pristine monolayer TMDCs. The decrease in the highest of acoustic phonon frequency from Cr to W can increase the phonon scattering rates and reduce the thermal conduction of Janus monolayers. The frequency separation between the highest of the acoustic branch and the lowest of the optical branch increases from CrSSe (5.4 cm^{-1}), MoSSe (17.91 cm^{-1}) to WSSe (43.84 cm^{-1}) that can largely facilitate in the reduction of the acoustic and optical phonon interaction, which is higher in case of heavy transition metal atom, e.g., WSSe.

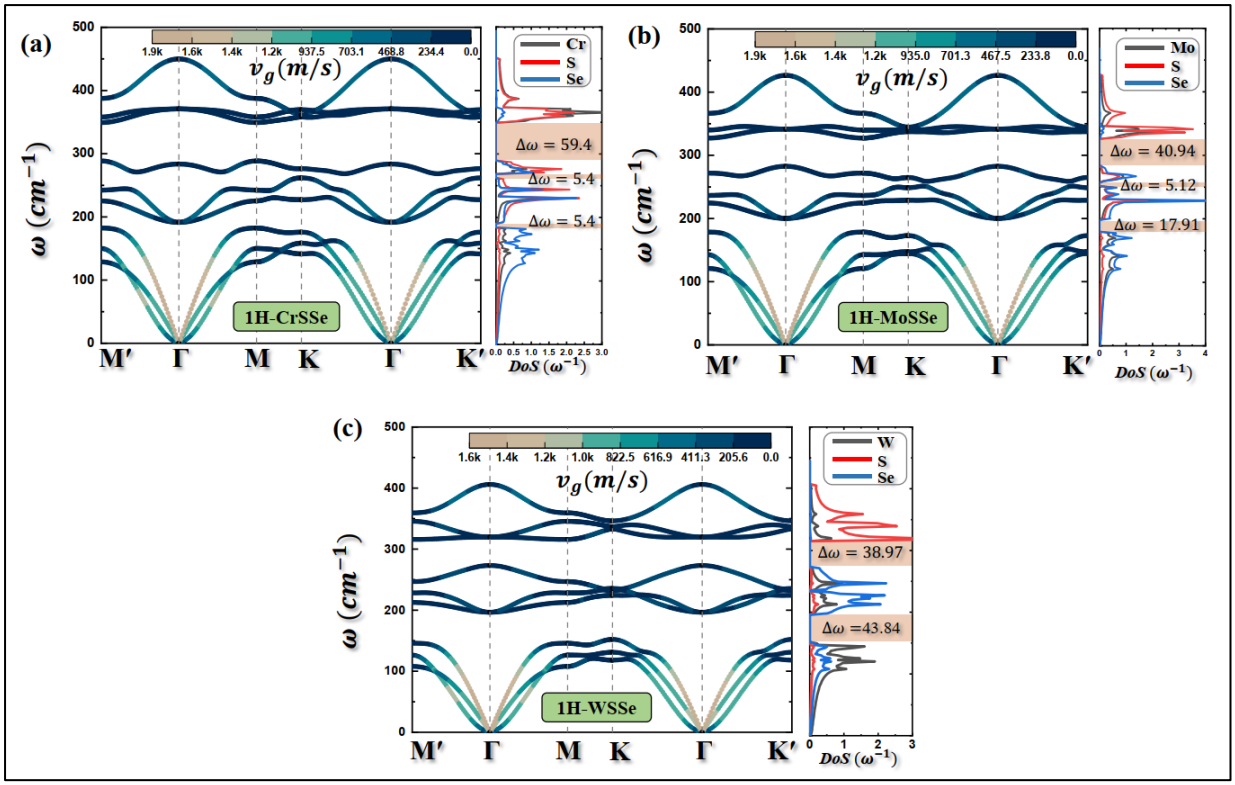

Figure 3.3. (a)-(c) Phonon band structure of Janus CrSSe, MoSSe, and WSSe monolayers of transition metal dichalcogenides in their stable 1H-phase. The atom projected phonon density of states with different phononic energy gap in the phonon spectrum and phonon group velocity of corresponding phonon branches had been included for each case. The absence of any imaginary phonon branch in the phonon dispersion confirms the kinetic stability of Janus monolayers.

3.3.2.2 Thermal Stability

In order to further establish the thermal stability of Janus monolayers, we have performed ab initio molecular dynamics (AIMD) simulations at room temperature, 300 K. We have used a relatively large 3 x 3 supercell to access the free energy change, pressure variation and temperature fluctuation for a duration of 5 *ps* with an interval of 1.0 *fs*. Figure 3.4 (a)-(c) shows the AIMD simulation results for energetically most preferable Janus monolayers, CrSSe, MoSSe, and WSSe, respectively. The average free energy change is found to be the lowest for

WSSe ($\tilde{E}$ = -202.29±0.54 eV) monolayer followed by the MoSSe ($\tilde{E}$ = -186.66±0.46 eV) and CrSSe ($\tilde{E}$ = -169.52±0.34 eV) structures, respectively. The pressure exerted on the Janus monolayers for each interval of AIMD simulation has also been calculated, and the average change in pressure in the unit cell is much smaller, which is of the order of ~ 1 ± 2 kBar. The temperature fluctuation during the AIMD remains around room temperature, 300 K, and the temperature fluctuation lies with the temperature range of ± 60 K, as shown in Figure 3.4 (a)-(c). A snapshot of the corresponding monolayer structure has been presented as the Figure insets at the end of the 5 *ps* of simulation in Figure 3.4 (a)-(c). The structural integrity of the Janus monolayers is found to retain at room temperature AIMD without any disruption in the lattice which can be affirmed from Figure 3.4 (a)-(c), thus, provides the room temperature thermal stability of Janus monolayers and its experimental feasibility via different synthesis routes, such as chemical vapor deposition or molecular beam epitaxy.

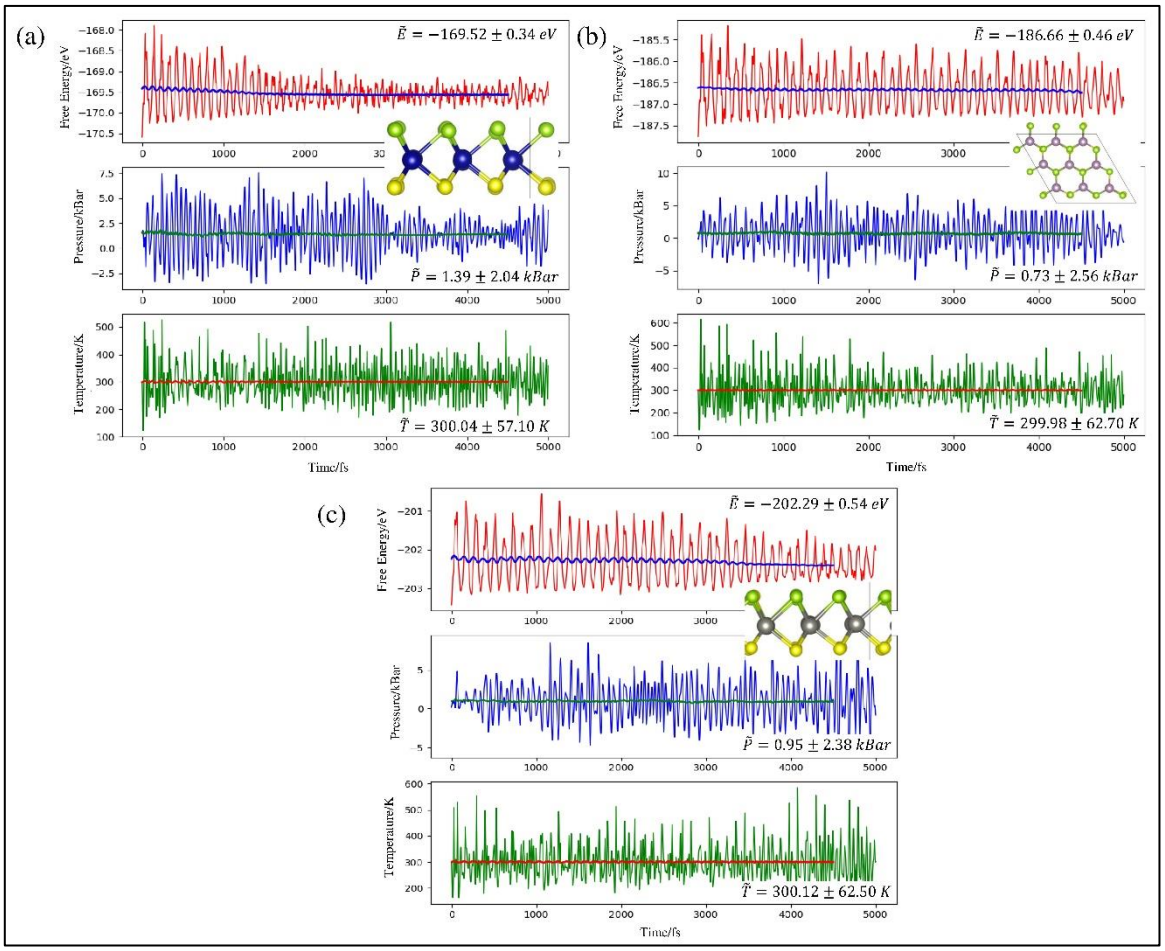

Figure 3.4. (a)-(c) Ab initio molecular dynamics (AIMD) simulations of Janus CrSSe, MoSSe, and WSSe monolayers at room temperature, 300 K. Figure inset shows the snapshots of the equilibrium structure at the end of AIMD simulation, at 5 *ps*. The values over the Figures represent the average value of free energy, pressure, and temperature change for a time interval of 0-5 *ps*. No structural disruption in the lattice structure at room temperature confirms the thermal stability of Janus monolayers.

3.3.3 Strain engineering of Rashba parameters

The out-of-plane mirror symmetry breaking of chalcogen sublattices in the parent MX_2 monolayer can induce an intrinsic build-in electric field perpendicular to the basal plane of Janus MXY owing to a large difference in the electrostatic potential between chalcogen lattices. The mirror symmetry breaking and strong SOC in MXY structures can induce the Rashba-type splitting of electronic bands near the Brillouin zone center, at the Γ point. The momentum dependent spin splitting of energy bands are found to be asymmetric about the K'-Γ-K and M'-Γ-M high symmetry lines in the Brillouin zone (BZ), where the Rashba momentum k_R is found to differ along the K'-Γ-K and M'-Γ-M high symmetry path keeping the Rashba energy E_R same along these high symmetry lines. The Rashba energy E_R is found to be maximum for MoSeTe monolayer, which is followed by WSeTe and CrSeTe Janus monolayers, as shown in Figure 3.5 (a). A biaxial strain is found to further enhance the Rashba energy E_R under the lattice compression that reaches close to 90 meV for MoSeTe monolayer at a biaxial lattice compression of -3%. A similar enhancement in the Rashba parameter α_R has been observed under the biaxial compressive strain where the MoSeTe and WSeTe monolayers show higher variation in α_R as a function of biaxial strain along the K'-Γ-K high symmetry line, as shown in Figure 3.5 (b). Figure 3.5 (d) shows a similar variation in the Rashba parameter α_R along the M'-Γ-M high symmetry path depicting an apparent anisotropy in α_R along the K'-Γ-K and M'-Γ-M high symmetry line. Figure 3.5 (c) and Figure 3.5 (e) further provide clarity on the

anisotropic Rashba effect along the K'-Γ-K and M'-Γ-M high symmetry line, respectively, and the modification in the Rashba bands at ±3% tensile/compressive biaxial strain.

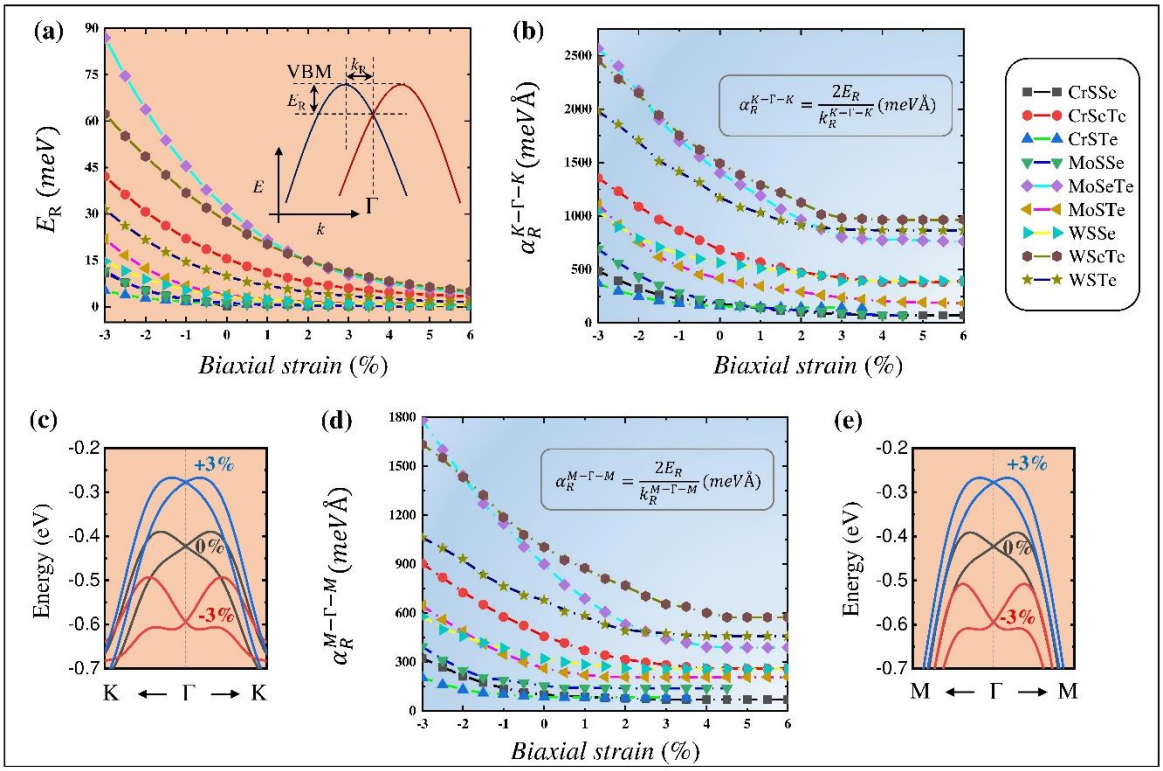

Figure 3.5. (a) Rashba energy E_R of valence band at the Γ-point of BZ as a function of biaxial strain in units of *meV*. (b) and (d) Rashba coefficient α_R along the high symmetry line K'-Γ-K and M'-Γ-M, respectively in units of *meVÅ* depicting a clear anisotropic response in α_R with applied biaxial strain. (c) and (e) Rashba type band splitting along the K'-Γ-K and M'-Γ-M high symmetry line in the 1st BZ under the pristine condition (0% strain) and a biaxial strain of ±3%.

3.3.4 Strain effect on SOC at the K point of VBM and CBM

In Figure 3.6, we have investigated the biaxial strain response on the SOC spin splitting energies of valence and conduction band edges at the K point. Figure 3.6 (a) shows the SOC spin splitting energy at the VBM located at the K point of BZ. Under biaxial tensile strain, we see a maximum increase in SOC energy for WSeTe Janus monolayer, which is followed by WSSe and WSTe Janus monolayers. The Janus monolayers of Mo series and Cr series of

chalcogenides exhibit much smaller variation in the valence band spin splitting energy as compared to the tungsten series of Janus monolayers. A similar enhancement in the conduction band spin splitting energy is observed for WSeTe under the compressive biaxial strain, which is followed by the WSSe and WSTe Janus monolayers, however under the biaxial tensile strain the energy splitting in CBM decrease in all cases. This altered response in SOC spin splitting energy at the VBM and CBM band edges at the K point under the biaxial strain is because of their orbital nature of Bloch bands corresponding to the respective band edges and the rehybridization and redistribution of overlapping atomic orbitals of metal *d* and chalcogen *p* atomic orbitals at these low energy valleys or high energy hills at the K point, as shown in Figure 3.6 (c)-(d).

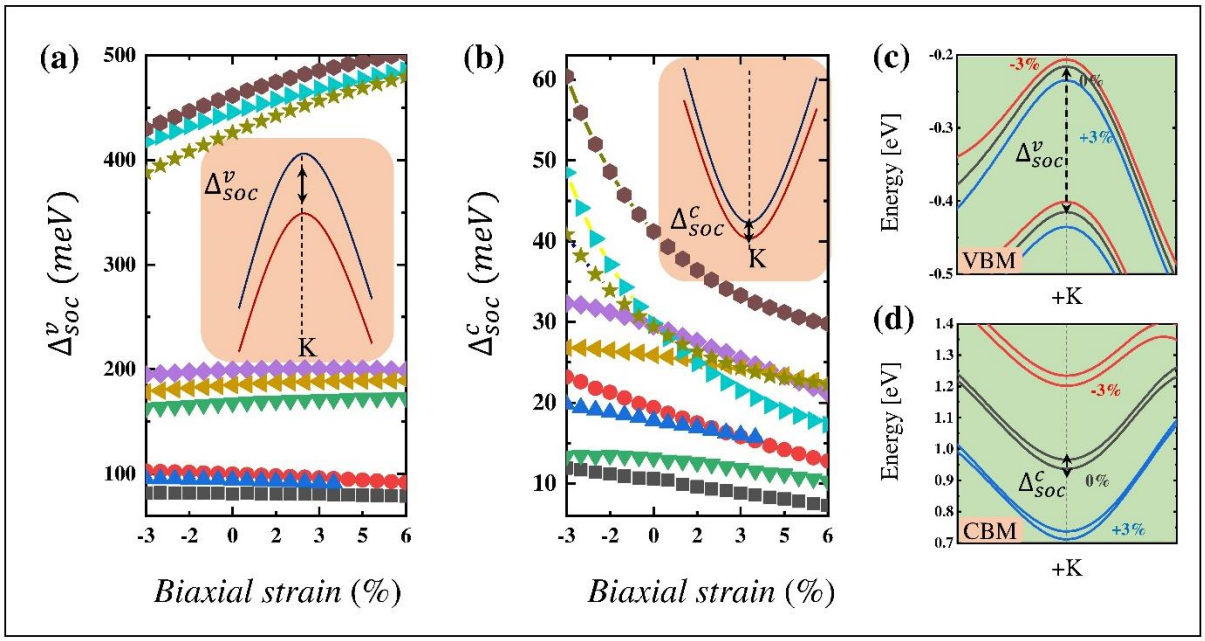

Figure 3.6. (a) Variation in SOC energy at the valence band maximum (VBM) at K-point of BZ as a function of biaxial strain. (b) The SOC energy variation at the conduction band minimum (CBM) at the K-point. (c)-(d) SOC spin-split electronic band at the VBM and CBM at +K point of BZ under pristine condition (0% strain) and ± 3% of biaxial strain. Figure inset in (a) & (d) pictorially depicts the SOC spin band of spin split VBM and CBM at the K point of the 1st BZ.

3.3.5 Variation in direct and indirect bandgap under strain

In Figure 3.7 (a), we have shown a typical spin-polarized electronic band structure of Janus monolayer of *Group VIB* transition metal dichalcogenide (TMDC), e.g., WSeTe monolayer. The fundamental direct bandgap lies at the K points of the Brillouin zone with valence band maximum (VBM) and the conduction band minimum (CBM) occurring at the same K point. The neighboring valence band maximum, which occurs at the Γ point lies at lower energy with respect to the valence band top at the *K* point. Figure 3.7 (b)-(c) shows the variation in the direct (E_g^{K-K}) and indirect ($E_g^{\Gamma-K}$) bandgap energy as a function of biaxial strain. Nearly linear variation in the bandgap is observed for the direct and indirect transition energy as a function of biaxial strain. The compressive strain tends to increase the magnitude of the direct and indirect bandgap in a near-linear progression, while the tensile strain tends to decrease the same in a regressive manner. Except for the CrSTe monolayer, all other monolayer Janus structures exhibit a semiconducting bandgap under the range of applied biaxial strain from -3% to +6%, whereas a semiconductor-to-metal transition is found to occur in CrSTe under biaxial tension exceeding the +3%.

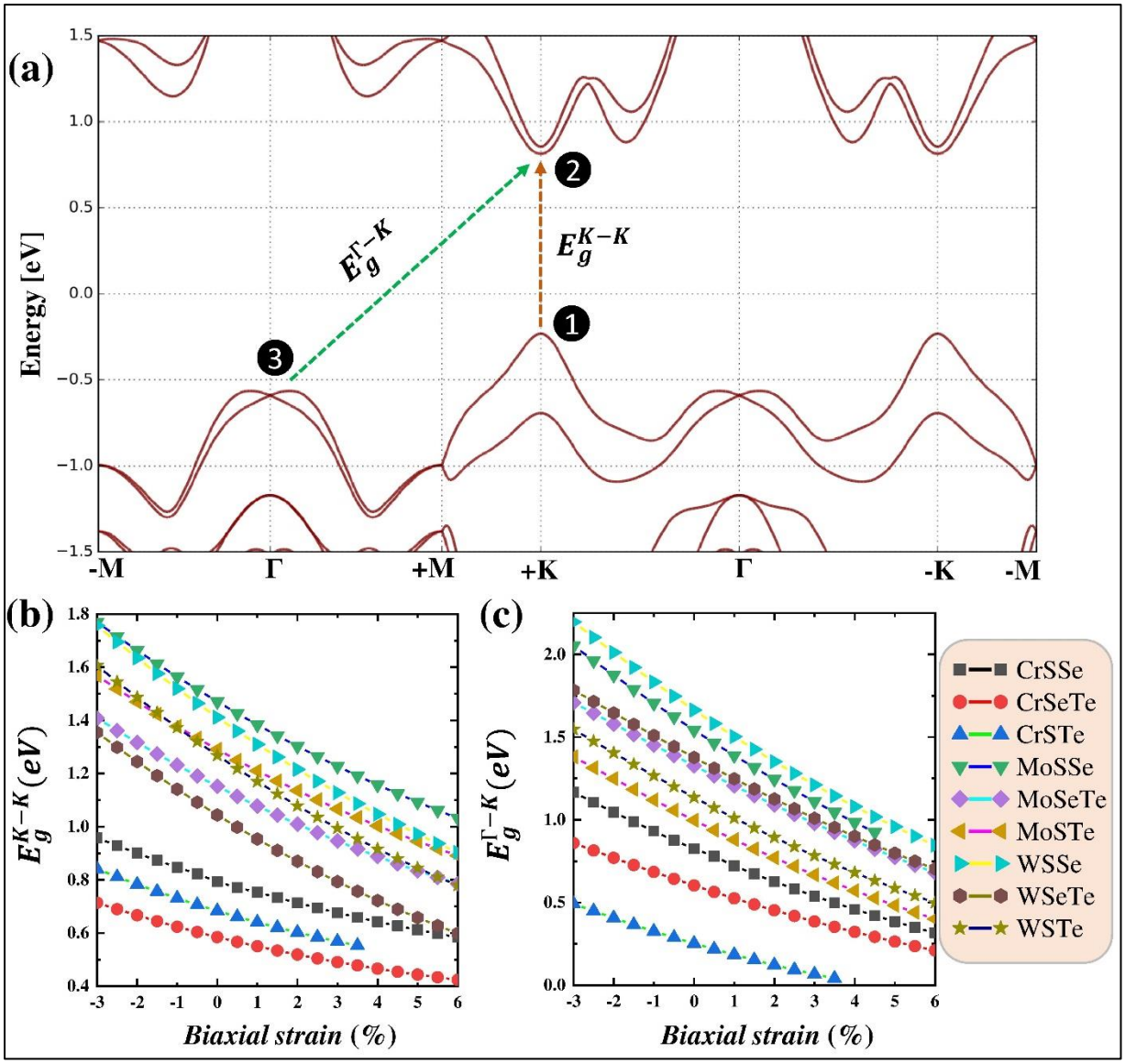

Figure 3.7. (a) Spin-orbit coupled (SOC) electronic band structure of a typical Janus monolayer of *Group VIB* transition metal dichalcogenide (TMDC). (b) The variation in the direct bandgap (E_g^{K-K}) at the K-point of the Brillouin zone (BZ) as a function of applied biaxial strain. (c) Changes in the indirect bandgap ($E_g^{\Gamma-K}$) as a function of biaxial strain in the strain range from -3% to +6%. In all cases, a semiconducting bandgap is observed; however, a semiconductor-to-metal transition has been observed for Janus CrSTe monolayer with tensile biaxial strain > 3%.

3.3.6 Strain tunable Berry curvature

The missing inversion symmetry and strong SOC at the low energy valleys of pristine and Janus monolayers are good candidates for valleytronic applications. The valley pseudospin at the time-reversal invariant (TRI) points, such as +K and –K, can be optically addressable through valley selective optical pumping. Using the helicity of circularly polarized (right or left) laser radiation, one can address the valley carriers at TRI points via optical selection. In theory, the Berry curvature of electronic Bloch bands is central to distinguish the energy degenerate valley states at +K and –K points of the BZ. The broken lattice inversion symmetry and stong SOC creates non-vanishing Berry curvature at +K and -K points of the BZ with opposite polarity as dictated by the time-reversal symmetry of the system. As shown in Figure 3.8 (a), the valence band Berry curvature distribution of Janus WSeTe monolayer is significantly peaked near the TRI points and sharply decays around it that eventually vanishes at any other high symmetry points in the BZ. The applied biaxial strain is found to modulate the curvature distribution around the +K and –K points in the BZ in a similar manner with opposite polarity where the tensile strain is found to increase the Berry curvature at TRI while the compressive strain decreases the same. In Figure 3.8 (b), we have computed the strain-dependent Berry curvature modulation for pristine and Janus monolayers of Group VIB transition metal dichalcogenides (TMDCs). The strain-dependent variation in Berry curvature is found to be maximum for WTe_2 followed by $CrTe_2$ in the case of pristine monolayer TMDCs, whereas for the Janus structures, the WSeTe monolayer shows a linear variation with a maximum positive slope in the biaxial strain range of -2.5% to +2.5%. Both the theoretical and experimental findings have demonstrated the unprecedented mechanical strength and elastic stability of monolayer TMDCs. Hence, the strain-tunable alteration in Berry curvature can be a simple, effective tool in controlling the transverse velocities of charge carriers in a future flexible valleytronic device.

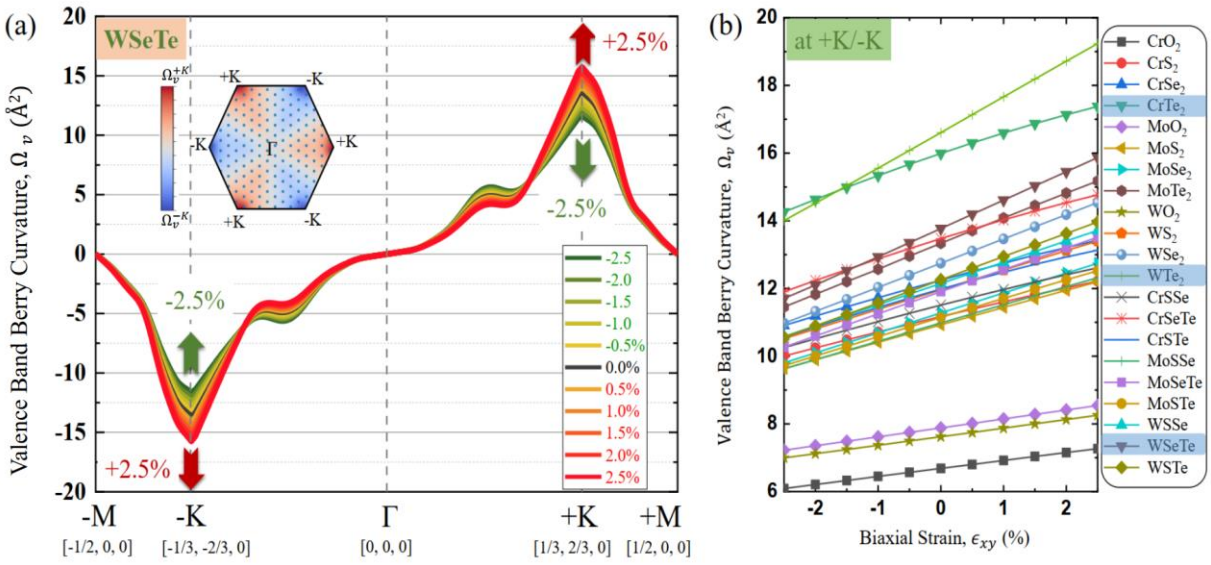

Figure 3.8. (a) Berry curvature distribution $\Omega_v(k)$ of monolayer WSeTe over all the occupied Bloch states in units of Å^2 along the high-symmetry momentum path [–M]-[–K]-[Γ]-[+K]-[+M] in the 1st Brillouin zone (BZ), under varying degrees of biaxial strain field from -2.5% to +2.5%. Figure inset shows the contour map of Berry curvature of occupied bands in a 2D *k* plane. (b) Strain tunable Berry curvature distribution of valence band for pristine and Janus monolayers in a biaxial strain range of -2.5% to +2.5% at +K or –K points in the BZ. The Berry curvature exhibit a linear variation as a function of biaxial strain, where the tensile strain increases the curvature distribution around the K point, and the compressive strain reduces the same. The pristine monolayer WTe_2 shows the maximum variation in Berry curvature, whereas, from the Janus series, the monolayer WSeTe shows the maximum slope with applied strain.

3.4 CONCLUSIONS

In summary, we have theoretically demonstrated the crystal structure, lattice stability and coupled spin-valley nature of the charge carriers in a series of semiconducting monolayers of *Group VIB* transition metal dichalcogenides 1H-MX_2 (where M = Cr, Mo, W, etc.; X = S, Se, or Te) and their Janus structures 1H-MXY (where X ≠ Y). Atomically thin MXY monolayers are found to be structurally stable, which we have confirmed from the phonon study and room temperature AIMD simulations. Furthermore, the Janus monolayers of *Group VIB* TMDCs possess comparable cohesive energy (~ 2-3 eV/atom) to that of their parent, energetically stable, 1H-MX_2 phase, this suggests the relative chemical stability of Janus monolayers. In all cases, a semiconducting electronic bandgap (~ 0.25 – 1.7 eV) has been found in Janus monolayers. The bandgap of M-S-Se and M-Se-Te (where, M = Cr, Mo, W) Janus monolayers are found to be direct at the K-point of the BZ under SOC, whereas in all other cases an indirect bandgap is observed with valence band maximum (VBM) occurring at the Γ–point of the BZ and the conduction band minimum (CBM) situated at the K–point. The variation in the direct and indirect bandgap exhibits a linear dependency as a function of applied mechanical strain within the -3% to +6% of biaxial strain, and the Janus monolayers remain semiconducting within this strain range except for CrSTe strained system that shows a semiconductor-to-metal transition with strain > +3%. The electrostatic potential difference (ΔV) is found to increase with an increase in dipolar contrast between chalcogen lattices, which enhances the SOC splitting energy of spin bands at the K–point of BZ both in the VBM and CBM sectors of the electronic dispersion. The Rashba parameters (E_R & α_R) are found to be highly strain sensitive and significantly get enhanced with lattice compression. The strain sensitive variation in Rashba coefficient α_R is found to exhibit asymmetric behavior about the K'-Γ-K and M'-Γ-M high symmetry line in the 1st BZ. Under compressive biaxial strain the enhancement in α_R along the K'-Γ-K line is nearly 2 orders of magnitude higher than the same

along the M'-Γ-M high symmetry line for a given strain value. Furthermore, the strain-tunable alteration in Berry curvature in pristine and Janus monolayer TMDCs can be a potential avenue for the effective controlling of transverse velocities of valley carriers in a future flexible valleytronic device.

----------**********----------

Chapter 4

Valley-engineering under strain: decoherent valley-drift

This chapter is based on the work published in:

Nityasagar Jena, Dimple, Raihan Ahammed, Ashima Rawat, Manish Kumar Mohanta, and Abir De Sarkar*, "*Valley drift and valley current modulation in strained monolayer MoS_2*", ***Phys. Rev. B** 2019, **100,** 165413*

4.1 INTRODUCTION

Apart from a unit electric charge and discrete spin configurations, electrons in certain crystalline semiconductors acquire another valley pseudospin degrees of freedom for their low-energy valley carriers due to the occurrence of multiple energy extrema in the electronic band spectrum[259]. Monolayer MoS_2 (ML-MoS_2) and other members of *Group VIB* transition-metal dichalcogenides (TMDCs), such as 1H- MX_2 (M = Mo, W and X = S, Se) have been a subject of intense focus in recent times owing to its direct semiconducting band gaps (E_g ~ 1–2 eV) and rich *d*-electron states[260]. While bulk MoS_2 is an indirect-gap semiconductor (E_g ~1.29 eV) [121], [261], a direct semiconductor bandgap (~1.8–1.9 eV) emerges at its two symmetry-inequivalent but energy-degenerate valleys (*K/K'*), when the bulk MoS_2 lattice is scaled down to its ultimate two-dimensional (2D) limit, i.e., single-layer MoS_2 [262]. In ML-MoS_2, the *K* and *K'* valleys are time-reversal partners and form a binary index in the low-energy electronic spectrum for valley-selective carrier excitations under a polarization selective

photoexcitation[135]. The presence of unique high-symmetry valleys (*K/K'*) and strong SOC endows this material with novel coupled spin-valley physics such as spin Hall and valley Hall effects [259]. The chiral nature of exotic valley carriers at *K/K'* points has been demonstrated in recent experiments, which can serve as a building block in future integrated spintronic and valleytronic devices[135], [136]. Additionally, the pristine surfaces of TMDCs devoid of any surface dangling bonds allow a facile integration with various substrates, and charge transport through them remains free from carrier localization or charge traps from surface roughness scattering, thereby leading to a high room temperature mobility ~200 $cm^2.V^{-1}.s^{-1}$ in a top/bottom gated $HfO_2/MoS_2/SiO_2$ dielectric environment, where the current on/off ratios of a single-layer MoS_2 transistor can exceed (1×10^8) [263] [9], which is ideal for next-generation low-power digital electronics.

In recent years, strain engineering of the electronic structure has emerged as an efficient strategy to improve the performance of monolayer devices[264]–[267]. Elastic strain in MoS_2 has proved to reversibly modulate its tunnel resistance[268], charge carrier mobility[269], [270], and optical absorption/emission efficiency to a large extent[205], [265]. The unprecedented elastic tolerance of single- to few-layer-thick suspended MoS_2 nanosheets have been demonstrated in previous experiments, where an elastic deformation under a spherical nanoindenter (atomic force microscopy tip) reveals a surprisingly high average Young's (Y) modulus of 0.33 ± 0.07 TPa[166], [271], which is *1/3* lower than the stiffness of freestanding graphene (1.0 TPa)[21], but higher than a freely suspended reduced graphene oxide (rGO, ~ 0.25 TPa)[272]. A strong in-plane ionic (polar) covalent bonding in ML-MoS_2 [121] emanating from a strong overlap between 4*d* orbitals of molybdenum (Mo) and 3*p* orbitals of sulfur (S)[273] has enabled the sustenance of reversible dilation deformation in the range of strain from 6–11%, and the critical breaking strength can exceed 23 GPa (15 ± 3 $N.m^{-1}$)[166], [274], [275]. Besides, ML-MoS_2 is insensitive to a lateral electric field in terms of its bandgap

modulation[276], [277]. Thus, mechanical strain within the elastic bound is the most effective strategy in altering the bandgap and optoelectronic response of ML-MoS_2. The ease of applying mechanical strain reversibly in low-dimensional structures[278]–[280] and the alteration in optoelectronic properties with strain as a potential device have led to the emergence of straintronics[281]–[283], a new frontier in tailored nanoelectromechanics. It is now well established that the electronic transport and optical excitations in a crystalline semiconductor (e.g., ML-MoS_2) is solely dependent on the characteristics of its electronic band dispersion, *E(k)* and local curvature of bands (low-energy band topology) in the immediate vicinity of the Fermi energy (E_F),[267] thus, the conduction band minima (CBM) correspond to the excited states of electrons, and the valence band maxima (VBM) refer to the excited states of holes. An understanding of energy valley dynamics of low-energy states with respect to a symmetry lowering elastic strain is of prime importance in strain engineering of a multi-valley electronic material such as ML-MoS_2. Moreover, a simultaneous occurrence of strong SOC and broken lattice inversion symmetry in ML-MoS_2 allows valley selective optical excitations between its time-reversed valley pairs (*K/K'*). It can be optically driven through helicity selective circularly polarized laser radiation, which causes excitonic excitations governed by its chiral optical valley selection rules (*k* space valley physics)[135], [136], [259], [284]. A range of exciting possibility opens up to manipulate charge carriers in these time-reversed valley points with contrasting Berry-phase curvatures for *electron/holes* near the *K/K'* valleys (valley-Hall effects)[285]. Furthermore, valley and spin properties in these monolayers are closely related to the crystal symmetry and wave function of atomic orbitals at the energy band extremum[286]. Therefore, an alteration in these properties is expected under a symmetry-lowering uniaxial strain[137], similar to the experimental observation in an AlAs two-dimensional electron system[287].

In this chapter, the effects of in-plane lattice deformation on monolayer MoS_2 have been systematically investigated. The energy valley dynamics of low-energy valleys are found to differ distinctively as a function of a directional strain perturbation; we find the conduction band minimum (CBM) exhibit a pronounced drift of energy band relative to the valence band maximum (VBM). Furthermore, the energy-valley drift response is more massive when the strain direction is along the zigzag (*ZZ*) axis of MoS_2 in comparison to the armchair (*AC*) axis. The underlying asymmetry in the band drift is attributed to two physical effects brought about simultaneously by a symmetry-breaking strain: one is the geometric effect under a direction-dependent strain, which leads to the anisotropy of elastic constants, while the other one is the electronic effect due to a changing orbital manifold, and the overlap of states at the local band edges, i.e., CBM/VBM energy valleys. The asymmetry in valley drift leads to the anomalous valley current in a strained nanosheet of monolayer MoS_2, and the Berry curvature distribution around the *K* point gets considerably modified under a direction-selective strain perturbation. Under extreme strain (~ 10%), we also notice a finite enhancement in the SOC spin split bands across the VBM and CBM around the *K* and *K* points, where a strong coupling between strain and electronic spin degrees of freedom can manipulate the spintronic capability of this material.

4.2 COMPUTATIONAL DETAILS

The density functional theory (DFT) calculations have been performed based on projector augmented wave (PAW) [288], [289] pseudopotentials implemented within the plane-wave Vienna *ab initio* simulation package (VASP, *version*: 5.3) [290]–[292]. Generalized gradient approximations (GGAs) for the exchange-correlation (XC) energy in its Perdew-Burke-Ernzerhof (PBE) [293], [294] parametrization has been used to describe the electronic wave functions in a plane-wave basis set. The electronic and ionic relaxation was based on the conjugate-gradient (CG) algorithm with a kinetic energy cutoff of 520 eV and Γ-centered 16 × 9 × 1 *k*-mesh for the Brillouin- zone (BZ) integration. The valence electronic

configurations for Mo and S atoms are $4p^6 5s^1 4d^5$ and $3s^2 3p^4$, respectively. Energy tolerance for the total energy convergence in a self-consistent iteration was set to 1.0×10^{-8} eV, where the individual atoms are allowed to relax till the Hellmann-Feynman forces acting on each atom reaches less than 1.0×10^{-3} eV/Å. The periodic slabs in the supercell were decoupled by considering a large vacuum spacing > 14 Å (the dimension of the supercell along the *c* axis was > 18 Å). Furthermore, dipole corrections have been incorporated to eliminate the spurious dipolar interactions between the periodic replicas of nanosheets along the direction normal to the surface of ML-MoS_2. Fully relativistic SOC effects were considered for the self-consistent ion relaxation of strained geometries. The Berry curvatures were calculated with SOC effects turned on using the methods discussed in Ref. [295].

4.3 RESULTS AND DISCUSSION

The results and discussion presented in this chapter are divided into following subsections and the essential observations have been concluded at the end of chapter 4.

4.3.1 Strain geometry and Brillouin zone folding

A honeycomb lattice structure of monolayer (ML) MoS_2 was composed of covalently bonded triatomic planes of S-Mo-S atoms with a transition-metal (Mo) layer sandwiched between two staggered hexagonal sublattices of chalcogen (S) in an *ABA* Bernal stack sequence, as schematically represented in Figure 4.1 (a) and 1(b). An orthorhombic supercell was constructed for the purpose of applying strain independently along two of the most relevant crystallographic orientations of MoS_2, namely, the zigzag (*ZZ*) and armchair (*AC*) directions [283]. The inherent hexagonal symmetry of MoS_2 is retained in an orthorhombic supercell upon geometry optimization, where the input experimental bulk lattice constant, a = 3.16 Å ($d_{Mo–Mo}$) for a primitive hexagonal unit cell, converges to a = 3.17 Å ($d_{Mo–Mo}$), b = 5.50 Å for an orthorhombic supercell, shown in Figure 4.1 (a)-(ii). The optimized lattice parameters shown

in Figure 4.1(a) and 4.1(b) are in very close agreement with earlier numerical results using similar exchange-correlation functionals and supercell symmetry[296], [297]. Investigations reported herein are based on an orthorhombic supercell.

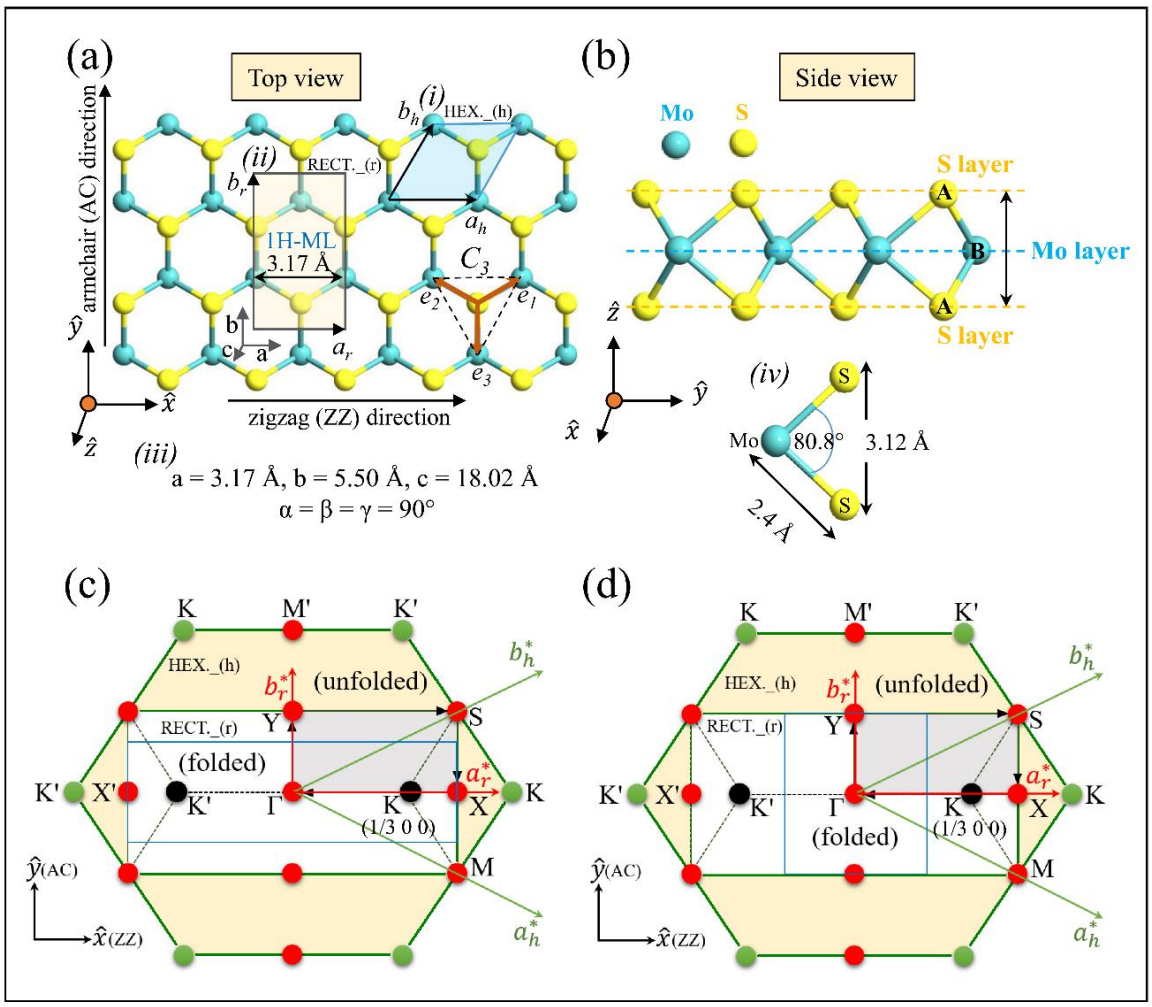

Figure 4.1. (a) Schematic of monolayer (ML) MoS_2: (i) optimized geometry in a primitive hexagonal unit cell, and (ii) rectangular supercell with lattice parameters presented in panels (iii) and (iv), respectively. The lattice vectors for hexagonal and rectangular cells are $\mathbf{a}_h$, $\mathbf{b}_h$ and $\mathbf{a}_r$, $\mathbf{b}_r$, respectively, whereas, $\mathbf{e}_1$, $\mathbf{e}_2$, $\mathbf{e}_3$ are the nearest neighbor vectors about a C_3-rotation axis centered over the S atom in a Mo-S trigonal-prismatic coordination. (b) A side view schematic of ML-MoS_2 with an A-B-A type trilayer S-Mo-S atomic packing. The dashed blue line in (b) over the central Mo layer is an indicator of the plane of mirror symmetry (σ_h) in broken

inversion symmetric ML-MoS_2. (c)–(d) A schematic representation of the 2D unfolded hexagonal Brillouin zone (BZ) (yellow filled region) and folded rectangular BZ (white filled region) for a primitive hexagonal and orthorhombic supercell superimposed with relevant high-symmetry k points.

The BZs of the unstrained system is constructed by a proper folding of its hexagonal Brillouin zone (yellow filled region) into a rectangular zone (white filled region), as shown in Figure 4.1(c) and 4.1(d), where the high-symmetry *K* point of a hexagonal BZ is folded into the midpoint of the line connecting *K* and (in the hexagonal BZ), i.e., the symmetry point *K* (*1/3 0 0*) (black dot), located at a *2/3* length of the *Γ-X* high-symmetry line in a rectangular BZ[298], [299]. The blue rectangular line inside of folded rectangular BZ in Figure 4.1(c) and 4.1(d) shows the first BZ of strained MoS_2 when strain is along its ZZ/AC direction in an orthorhombic supercell.

4.3.2 Impact of strain on low-energy valleys

Figure 4.2(a) shows the energy-momentum dispersion, E(*k*) of strain-free monolayer MoS_2 in an orthorhombic supercell. Without explicit inclusion of the SOC effect, a direct semiconducting bandgap, E_g(K-K) ~ 1.69 eV, occurs along the *X*- high symmetry line, where the band extrema of electron/hole states lie over a single folded *K* point (*1/3 0 0*), positioned at *2/3* of the length of the *Γ-X* line. The highest occupied states (VBM) occurring at E_K and that lying at a slightly lower energy (~20 meV offset) E_Γ show excellent agreement with previous theoretical results using a similar level of DFT methodology[300][301]. Next, uniaxial tensile strain in a dilation deformation range of 0–10% was applied along both the *ZZ* as well as *AC* directions of ML-MoS_2. The evolution in the band dispersion and curvature of bands around the Fermi energy (E_F) within an energy range of *E(k)* ± 2 eV is shown in Figure 4.2(b). We find a robust strain-valley coupling between low-energy Bloch bands and mechanical strain

near the CBM/VBM band edges, where an applied uniaxial deformation significantly drifts around the CBM valleys and VBM hills far away from *K/K'* points in the momentum space, as shown in Figure 4.2(b).

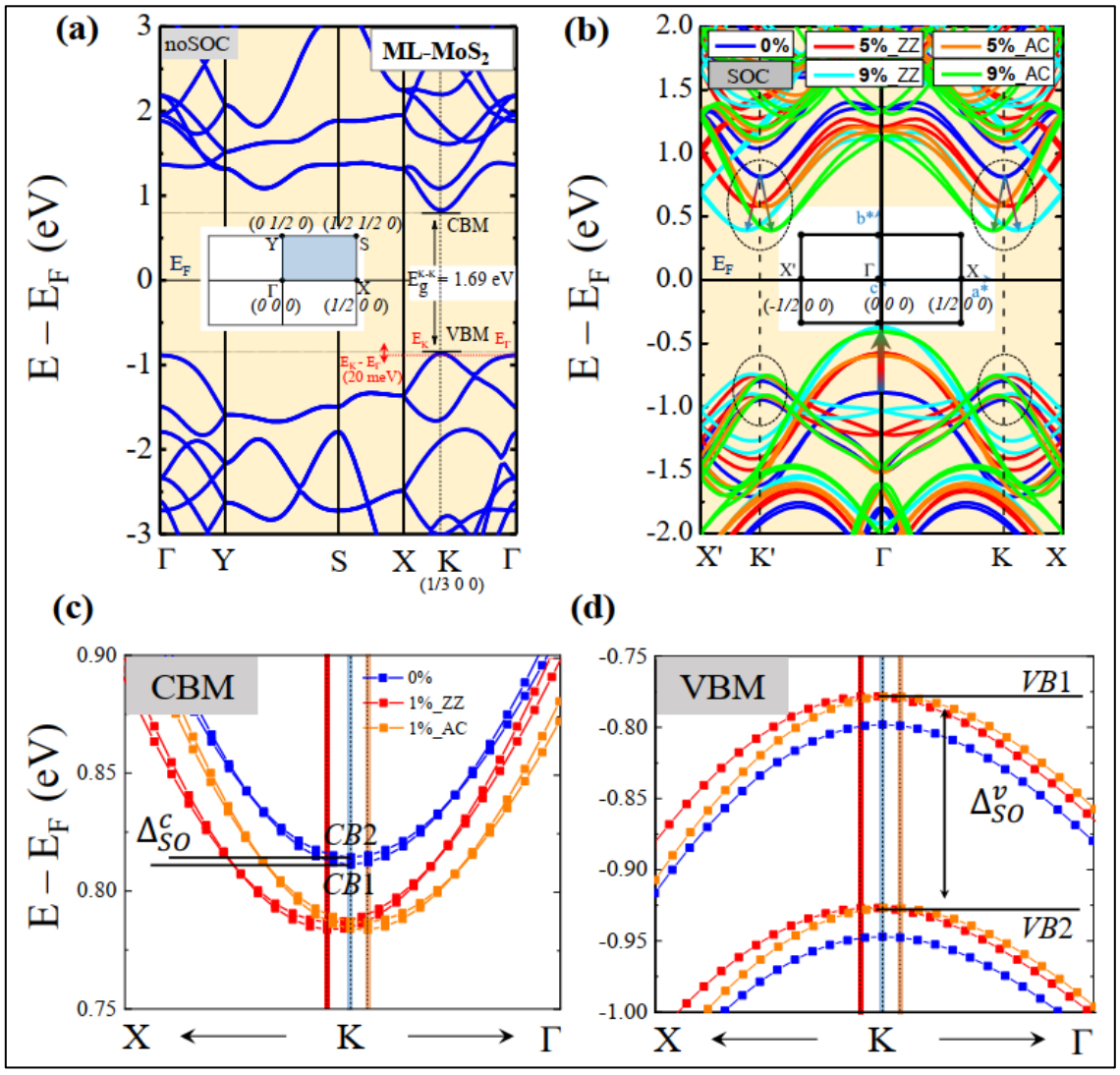

Figure 4.2. (a) The band structure of strain-free ML-MoS_2 in an orthorhombic supercell shows a direct semiconducting bandgap, E_g = 1.69 eV (without SOC), along the X- high symmetry line. (b) Evolution in the band structure of unstrained (0%) and uniaxially strained (5%, 9%) ML-MoS_2 along the ZZ/AC direction. The CBM valleys near K/K′ show a strong strain-dependent momentum drift over the valence band hills. The band structure shown in (b) includes the effect of SOC. (c)–(d) Low-energy spin-split conduction band minima (CB1, CB2)

and valence band maxima (VB1, VB2) around the K point, when ML-MoS_2 is strained by 1%. The CBM/VBM valleys drift along the opposite direction in response to lattice strain along the ZZ/AC direction. The vertical color bars represent the position of energy band top or bottom.

This arc-shaped drift response is found to be stronger in the electron sector of band dispersion than the hole sector, with several band extrema crossing around *K* and *K'* point for different values of uniaxial strain. In the limit of a small strain of 1%, in Figure 4.2(c) and 4.2(d), we have shown the energy valley drift in the lowermost spin split conduction band (*CB1*, *CB2*) and the uppermost valence band (*VB1, VB2*). The parabolicity of electron subbands gets more heavily deformed than the hole bands with energy vertices crossing around the *K* point, when strained along the *ZZ/AC* axis [see Figure 4.2(c) and 4.2(d)]. The curvature distortion can introduce particle-hole asymmetry due to a nonidentical band dispersion around the *K* point [267], [302]. Microscopically, the origin of this strong strain-valley coupling is due to a changing geometric effect that reduces the symmetry of the underlying lattice and a changing orbital hybridization effect (wave-function overlap effect) for relevant local Bloch states at the CBM/VBM band edges. A strain-induced modification in the band-edge orbital wave functions generates a scalar potential of varying strength for corresponding Bloch bands that are described by the low-energy electron and hole valleys of a monolayer MoS_2.

4.3.3 Isoenergy contours of low-energy valleys

To make this energy valley drift response more evident, in Figure 4.3 we present the constant energy contours of highest occupied (VBM) and lowest unoccupied (CBM) bands near the *K* point. Unlike graphene, the VBM/CBM isoenergy contours of monolayer MoS_2 are not isotropic in close proximity of the *K* point, and a trigonal warping (TW) effect of energy bands can be seen in the equienergy lines around the *K* point (this feature is also true for energy vertices around the *K'* point, as a consequence of time-reversal symmetry in the system) [24],

[303]. When uniaxially stained (5%), an increase in the warping effect distorts the isoenergetic lines around the energy valleys due to a continuous reduction in threefold planar rotational symmetry (C_{3v}) and translational symmetry along its mutually perpendicular lattice directions. The TW effect is more pronounced at a larger *k*, and increases with an increasing strain field with an antisymmetric warping strength, when strain is along the *ZZ/AC* direction. In the immediate proximity of *K*, the *hole* surface is more strongly warped than the *electron*, where the low-energy contours of a strained system (along the *ZZ* direction) show an elliptic warping of band topology extending to a much higher energy with flattening of convexity revolution around the *K* point along the direction of applied strain, while it is closer to a triangular shape along the *AC* direction.

The uniaxial strain-induced anisotropy in electronic band dispersion (trigonal warping effect) Coulomb drags the charge carriers anisotropically due to a strong interparticle-particle correlation that lead to an anisotropy in carrier mass/carrier mobilities and optical anisotropy in absorption coefficient as seen in our previous strain-engineering studies [304], [305]. The CBM drift is larger than the VBM hills, with energy valleys drifting along opposite directions when strained along the *ZZ/AC* direction. This observation is in line with the result of our band structure calculation presented in Figure 4.2(b).

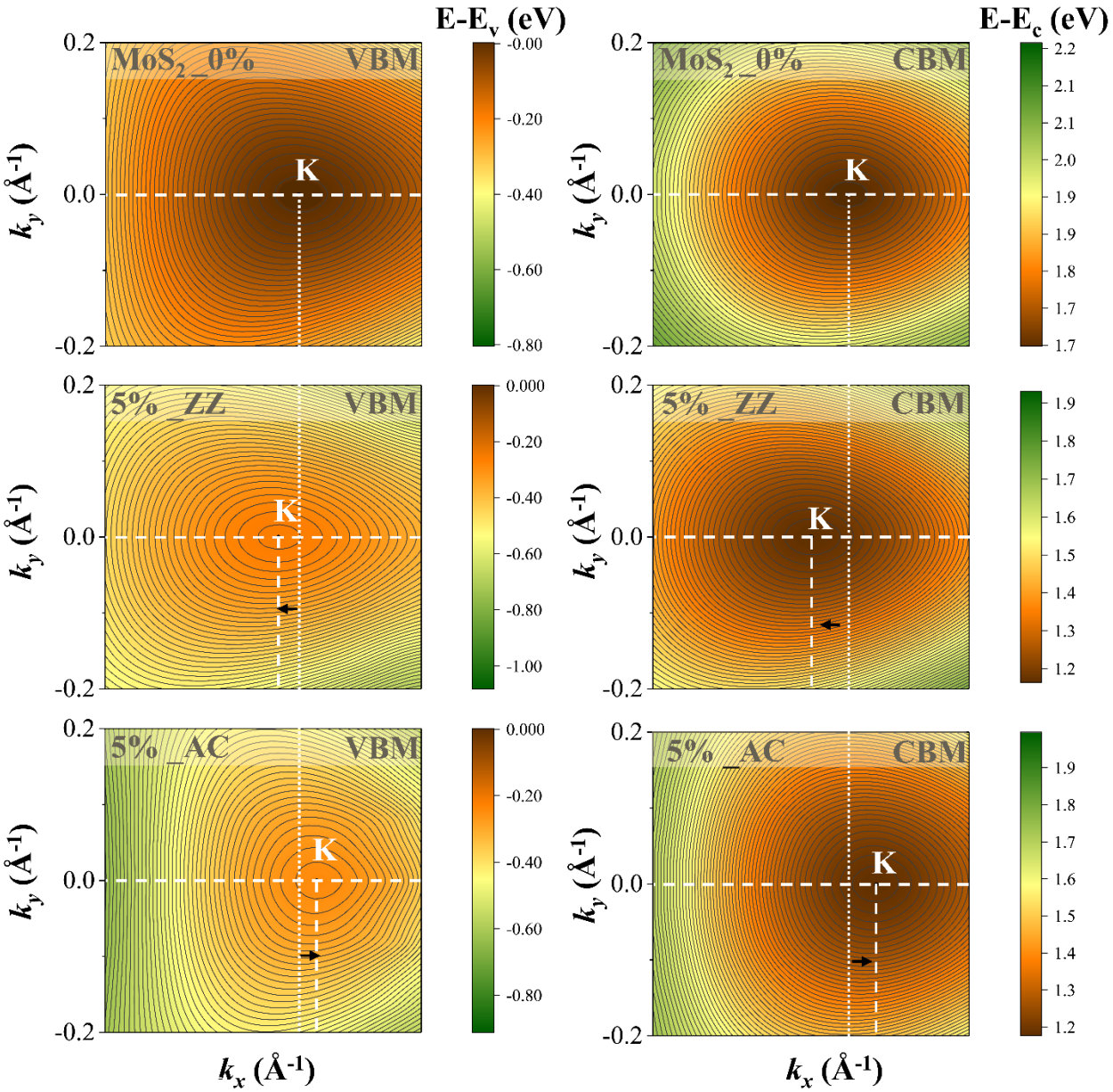

Figure 4.3. Isoenergy contours of low-energy valence and conduction bands in a 2D k plane for unstrained (0%) and 5% strained ML-MoS_2 along the ZZ/AC direction. The dashed line and arrows illustrate the energy valley drift near the K point. This energy contour feature is also true for its symmetry inequivalent K point due to time-reversal symmetry. The VBM/CBM constant energy contours have been scaled with respect to the energy of the valence band top and conduction band bottom at the K point. Under strain, we see a strong effect of trigonal warping (TW) of energy bands near the K point, where the energy valleys drift along opposite directions under the ZZ/AC strain.

4.3.4 Measure of valley drift, 2D elasticity, and bandgap under strain

In the following, we quantify the energy valley drift in the lowermost spin-split conduction band (*CB1*) and the uppermost valence band (*VB1*). We further study the band-edge deformation energies of spin-split CBM (*CB1*, *CB2*) and VBM (*VB1*, *VB2*) and, concurrently, the changes in elastic constants such as Young's modulus, the Poisson ratio, and band-gap variations with strain, as the SOC is turned *off* or *on*. The changes in the above-mentioned quantities have been analyzed in a strain range of 0–10% along the *ZZ* as well as *AC* direction. Uniaxial strain, which gets applied asymmetrically along a given crystal axis (*ZZ/AC* direction), reduces the original hexagonal symmetry in ML-MoS_2 about a C_3 rotation axis. As a result, both the translational symmetry and rotational symmetry are broken due to asymmetric Mo-S bond stretching[137].

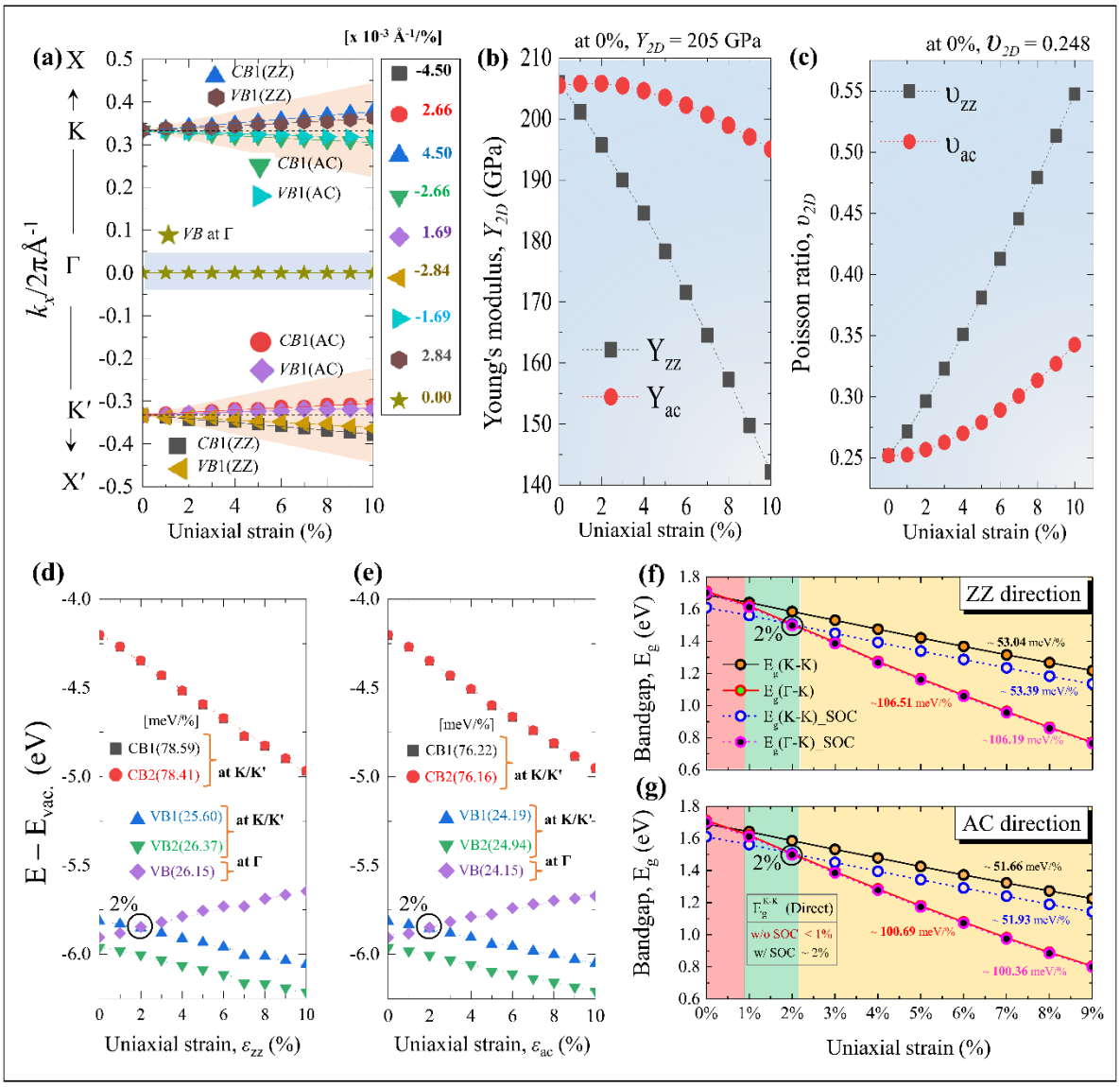

Figure 4.4. (a) Momentum drift in the lowermost spin-split conduction band (CB1) and uppermost valence band (VB1) at K/K' points as a function of uniaxial strain along the ZZ/AC direction in a strain range of 0–10%. Variation in Young's modulus (b) and Poisson's ratio (c) with strain. A strong strain-dependent anisotropy in elastic parameters can be seen in (b) and (c) when strain is along its ZZ/AC direction. (d)–(e) Functional relationship of band-edge deformation energy with uniaxial strain applied along the ZZ/AC direction. CB1, CB2 is the spin-split conduction band minima (CBM) and VB1, VB2 is the spin-split valence band maxima (VBM) near the K/K' point, while VB is the spin-degenerate valence band top at the Γ point. The bracketed numbers are their variation rates in units of meV/strain%, with energy-

referenced to the absolute vacuum energy ($E_{vac.}$). (f)–(g) Variation in the direct, E_g(K-K) and indirect, E_g(Γ-K) band gaps with the uniaxial tensile strain (0–10%) along the ZZ/AC direction, with (w/) and without (w/o) explicit inclusion of SOC effects into the band structure calculation. The red and green shading in (f) and (g) is the strain range for direct-to-indirect band-gap crossover w/o, and w/ SOC effects turned on.

As shown in Figure 4.4(a), the lowermost spin-split CBM (*CB1*) drifts off the *K/K'* point at a rate (*CB1/ZZ*) ~ 4.50×10^{-3} $Å^{-1}$ /1% when strain is along the *ZZ* direction, while it drifts towards the zone-center (*Γ*) at a rate (*CB1/AC*) ~ 2.66×10^{-3} $Å^{-1}$ /1% when strain is along the *AC* direction. We find the energy valley drifts in spin-split *CB1* is higher (>1.5 times) along the *ZZ* direction than the corresponding drift along its *AC* direction. The momentum drift rates are found to be equal in magnitude at *K* and *K'* but of opposite nature in their slopes. A similar drift response is found for the valence band hills, where the uppermost spin-split valence band top (*VB1*) drifts away from *K/K'* at a rate (*VB1/ZZ*) ~ 2.84×10^{-3} $Å^{-1}$ /strain % when strain is along the *ZZ* direction, while it drifts towards the zone center (*Γ* point) at a rate (*VB1/AC*) ~ 1.69×10^{-3} $Å^{-1}$ /strain % when strained along the AC direction.

A higher drift in momentum-space for both *CB1* and *VB1*, when applied strain is along the *ZZ* direction, is attributed to a drastic change in elastic constants, such as Young's modulus (*Y*) and Poisson ratio (*υ*), as shown in Figure 4.4(b) and 4.4(c). A significant drop in the Poisson ratio along its *ZZ* lattice direction has a profound effect on the Brillouin zone deformation, which scales linearly with strain applied along the *ZZ* direction. Valley drift shows a large strain dependency. The CBM valley drift is nearly two times the drift in its VBM hill. Consequent to the application of uniaxial strain, the electron/hole valleys at *K* or *K'* points no longer coincide. As a result, the valley symmetry between excitons (valley coherence) gets destroyed due to a strong strain-induced electron-hole valley asymmetry near the *K* point.

Since the valley degrees of freedom emerge from the local band extrema, the drift could soften the valley-selective optical selection rules due to changes in the optical matrix elements and excitonic wave functions, which in turn can have profound effects on intervalley optical excitations and electron dynamics due to radiative dephasing of carriers in a strained ML-MoS_2 lattice. This uniaxial strain-induced valley asymmetry in the vicinity of transition point (*K/K'*) could be the reason for a drastic reduction in the degree of circular polarization (*K*-valley polarization) in uniaxially strained ML-MoS_2 in the experimental observation led by Zhu *et al.* [137] in polar photoluminescence (PL) emission measurement, where the degree of valley polarization gets reduced with increase in strain magnitude.

It is worth noting here that, although the low-energy valleys of strained ML-MoS_2 show a strong momentum-dependent valley drift around *K/K'* points, no energy difference between *K* and *K'* is observed, i.e., the energy degeneracy in the symmetry inequivalent valleys of strained ML-MoS_2 is retained even up to a large uniaxial strain of 10%. This shows that the uniaxial elastic deformation alone (without a real external magnetic field) is not sufficient to lift the valley energy degeneracy between *K* and *K'* by a strain-induced fictitious gauge-field vector potential (which generates a uniform pseudo magnetic field) due to its time-reversal-invariant (TRI) nature. However, a pure shear strain that induces a spatially varying strain field can lift the valley degeneracy in transition-metal dichalcogenide monolayers, including ML-MoS_2 [232], similar to the observed phenomenon in a nonuniformly shear strained monolayer graphene [306]. Figures 4.4(d) and 4.4(e) track the subband energy evolution (band-edge deformation potentials) of spin-split conduction band minima (*CB1*, *CB2*) and valence band maximum (*VB1*, *VB2*) as a function of uniaxial strain. *VB* lies at the edge of the spin-degenerate valence band at the *Γ* point. ML-MoS_2 shows a direct gap with *CB1* and *VB1* coinciding at the *K* point. When influenced by a uniaxial deformation, the spin split CBM (*CB1*, *CB2*) at the *K/K*' point show a stiff energy variation at a rate 76–78 meV/% due to a strong out-of-plane

character of Mo $4d_{z2}$ orbital states, when strain is along the *ZZ/AC* direction, while the spin-degenerate VBM (*VB*) at Γ point varies at a rate (24–26 meV/%) with a valence band crossover occurring at 2% strain. On the other hand, the spin-split *VB1, VB2* exhibit a smaller energy shift at a rate of 24–26 meV/strain % due to the pure in-plane nature of Mo $4d_{xy}$ + $4d_{x2-y2}$ orbitals which gets weakly influenced by an in-plane strain. Figures 4.4(d) and 4.4(e) shows the band-edge deformation potential to be highly strain tunable for low energy Bloch bands having out-of-plane orbital character (i.e., CBM at *K*). Figures 4.4(f) and 4.4(g) show the energy evolution in the direct (*K*-*K*) and indirect (Γ-*K*) band-gap energies (E_g), with (w/) and without (w/o) explicit inclusion of SOC effects. Inclusion of SOC effects leads to a giant spin splitting at VBM (*VB1, VB2*) that reduces the direct bandgap in ML-MoS_2 by 80 meV (w/o SOC, $E_g \sim 1.69$ eV; w/ SOC, $E_g \sim 1.61$ eV)[126] while keeping the band edges at the *K* point, where the spin-split valence band top *VB1* shifts up in energy by an amount 57.2 meV and *VB2* shifts down by 92 meV with respect to the spin-degenerate valence band (w/o SOC) at the *K* point. An energy separation of 149.3 meV between spin-split *VB1* and *VB2* in our calculation shows very close agreement with experimentally measured values for strain-free monolayer MoS_2 (146 meV)[279] and a numerical calculation reporting a value of 148 meV [123]. The valence band energy offset between E_K and E_Γ increases by a factor of 4 under SOC (~ 92.58 meV) with respect to the energy offset w/o SOC (~ 20 meV), which is much higher than the room temperature thermal energy (~ 26 meV). This important feature in the band structure of ML-MoS_2 has not received much attention, but it moves the critical strain limit to ~ 2% for a direct-to-indirect band-gap crossover. Our theoretical calculation shows excellent quantitative agreement with several experimental observations where the direct-to-indirect band-gap transition in ML-MoS_2 occurs at a critical strain strength of ~ 2% [266], [307], [308], whereas without SOC this crossover in bandgap occurs at < 1% of lattice strain due to a relatively small energy offset (~ 20 meV) between occupied bands. This also agrees with the numerical results,

where the SOC effects have not been explicitly included in the band structure calculation [300], [301]. The VBM energy at the *Γ* point is found to be lower by 14 meV under SOC than that of w/o SOC. In Figure 4.4(f) and 4.4(g), for all cases, the bandgap decreases monotonically with increasing strength of the uniaxial strain, maintaining a nearly linear redshift in energy gaps. The redshift rate in the direct bandgap is E_g(*K*-*K*) ~ 53 meV/(% of strain) along the *ZZ* direction and E_g (*K*-*K*) ~ 51 meV/(% of strain) along the *AC* direction. The redshift rates with and without inclusion of SOC effect show excellent quantitative agreement with experimentally observed redshift rates in the direct-gap optical transition energies: ~ 35 meV/% strain[309], ~ 45 ± 7 meV/% strain [307], and ~ 48 meV/% strain [137] measured in several optical absorption and photoluminescence (PL) measurements. Moreover, the redshift in their indirect band gap, E_g(Γ-K) ~ 100 meV/%, is in good accord with its theoretical value of 94.6 ± 2.2 meV/%[308]. The energy band-gap redshift rate is slightly higher along the *ZZ* direction as compared to the *AC* direction, attributed to a faster decline in elastic constants along the *ZZ* direction, which seems to be the elastically soft direction in ML-MoS_2 with respect to its relatively stiff *AC* direction [see Figure 4.4(b) and 4.4(c)].

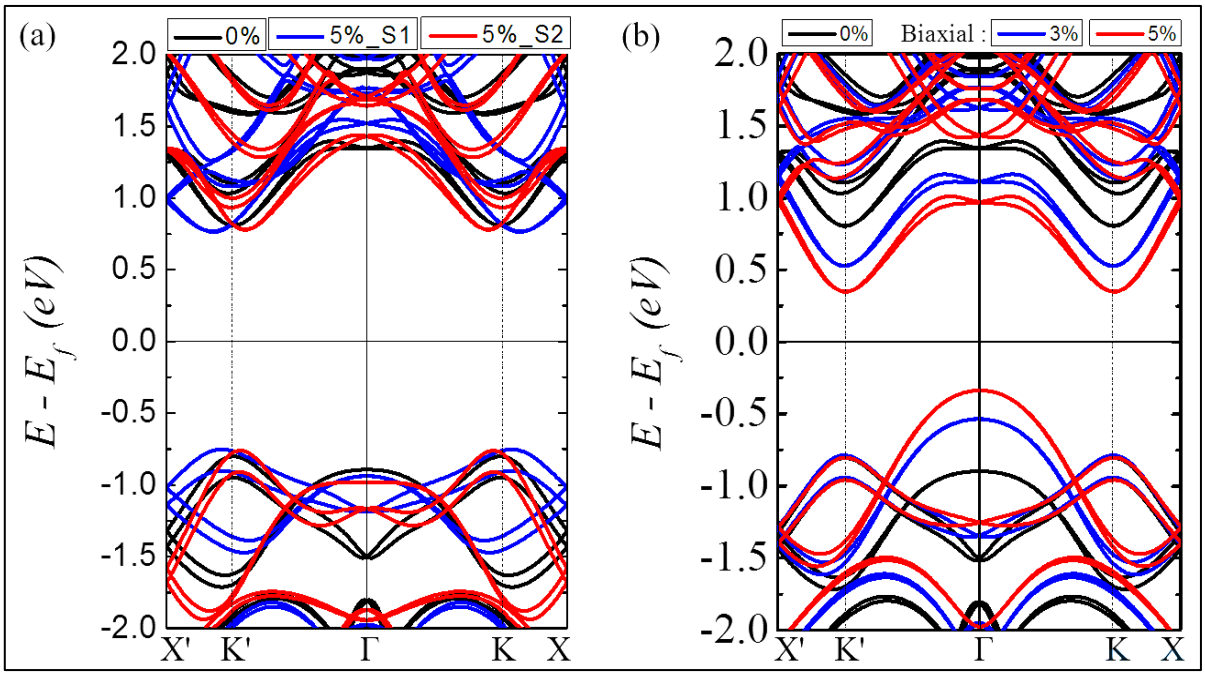

Figure 4.5. (a) Band-edge valley drift at 5% shear (S_1 and S_2) mode of strain. S_1 (where the tensile and compressive strain of 5% magnitude has been simultaneously applied along zigzag and armchair directions) and S_2 (where the tensile and compressive strain of 5% magnitude has been simultaneously applied along armchair and zigzag direction, respectively). Band gap remains direct up to 5% of shear (S_1 and S_2) strain. (b) Band structure evolution with the biaxial tensile strain of 3%, 5% relative to pristine unstrained ML-MoS_2. In all cases, the band structure includes the effect of SOC.

We have also explored shear and biaxial strain modes. Due to a relatively low elastic-bound of shear strain ~ 5–6%, we have not considered this as our main discussion[274]. However, interestingly, even at high value of shear strain ~ 5%, the bandgap remains direct at *K/K'* [see Figure 4.5 (a)]. Priya Johari *et al.*[310] attribute this to the inability of shear strain to delocalize the electronic charge density isosurfaces of MoS_2. In contrast, the biaxial strain mode does not affect the valley degeneracy lifting due to the isotropic nature of the strain field that preserves the symmetry of underlying crystal [see Figure 4.5 (b)].

4.3.5 Strain effect on Bloch orbitals at band edges

Apart from a strain-induced geometric effect that reduces the symmetry of a hexagonal lattice, another microscopic physical effect underlying energy valley drift is the asymmetry in the orbital overlap of electronic states under a symmetry breaking lattice displacement. In Figure 4.6(a)–4.6(c), we have carefully mapped the orbital wavefunctions of relevant band edge states that describe the low-energy electron and hole dispersion of a pure and strained ML-MoS_2 lattice. The orbital wave functions at the band edges are primarily composed of 4*d* orbitals of Mo and 3*p* orbitals of S with a dominance of *d* character in electronic states. In ML-MoS*2*, the trigonal-prismatic crystal field on Mo 4*d* orbitals lifts the fivefold degeneracy of free Mo *d* orbitals into three energy groups, which spread out in energies, giving rise to two

doubly degenerate energy levels (i) $4d_{xy}$, $4d_{x2-y2}$ and (ii) $4d_{yz}$, $4d_{zx}$ and one singly degenerate energy level (iii) $4d_{z2}$ [122]. The in-plane $4d_{xy}$, $4d_{x2-y2}$ orbitals, and the out-of-plane $4d_{z2}$ orbitals are symmetric with respect to its horizontal mirror plane (σ_h) lying over the Mo atomic layer. The out-of-plane mirror symmetry ($z = -z$) in ML-MoS_2 allows hybridization between its $4d_{xy}$, $4d_{x2-y2}$, and $4d_{z2}$ orbitals with $3(p_x, p_y)$, $3(p_z)$ orbitals of ligand sulfur (S) atoms, which opens up a tunable energy gap at its two symmetry inequivalent K/K' valleys. The CBM of a strain-free ML-MoS_2 mainly originates from the mixing of $4d_{z2}$ orbitals of Mo with $3(p_y + p_x)$ orbitals of sulfur (S). A small contribution also arises from Mo 5*s* orbitals. The bandwidth analysis of each contributing orbital to the relevant band-edge states is summarized in a table in Figure 4.6, which shows that each Mo atom contributes a total of 92% spectral weight to its CBM antibonding state, while each S atom puts in 4%. The VBM states at the *K* point are constructed by a linear combination of doubly degenerate $4(d_{xy} + d_{x2-y2})$ bonding orbitals of Mo, with an orbital weight of 42%, contributed in equal proportion hybridized with sulfur $3p_y$ and $3p_x$ orbitals each contributing 3.8% of the spectral weight. A vanishing contribution to VBM (at *K*) also arises from Mo $4p_y$ and $4p_x$ orbitals, each having 0.2% spectral weight. The nearby valence band tops at the point (VBM_*Γ*), resulting from the hybridization of Mo ($4d_{z2}$) orbitals with antibonding $3p_z$ orbitals of S, each contribute 79% and 9.3%, respectively, with weakly contributing 5*s* and 3*s* orbitals of Mo and S atoms. Under the application of uniaxial strain, the bandwidths of the contributing orbitals show a pronounced change that arises due to a change in the crystal field splitting between metal and ligand (Mo-S) in the trigonal prismatic coordination geometry. It strongly affects the low-energy band topology of a strained ML-MoS_2 lattice.

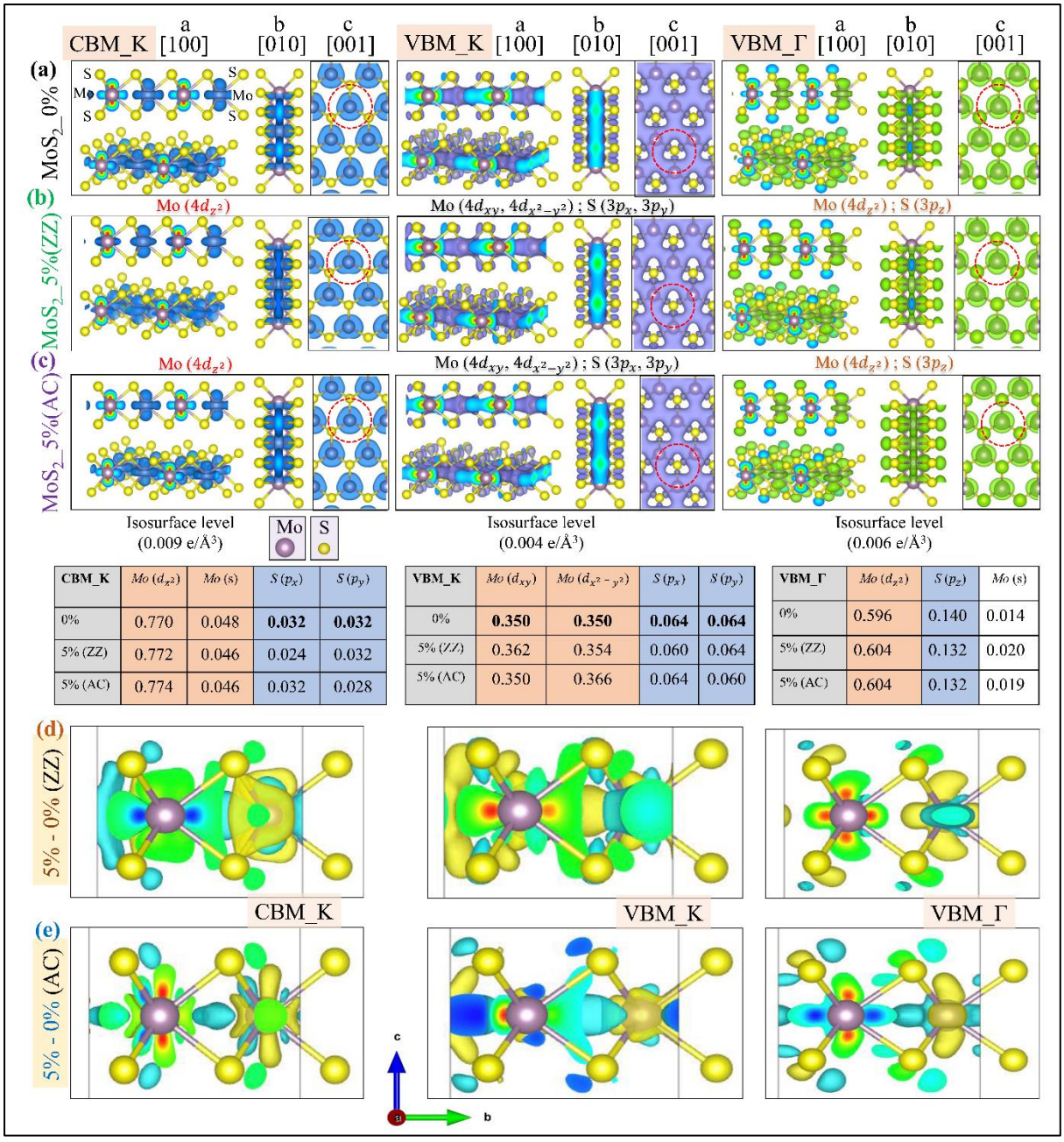

CBM_K	Mo (d_{z^2})	Mo (s)	S (p_x)	S (p_y)
0%	0.770	0.048	**0.032**	**0.032**
5% (ZZ)	0.772	0.046	0.024	0.032
5% (AC)	0.774	0.046	0.032	0.028

VBM_K	Mo (d_{xy})	Mo ($d_{x^2-y^2}$)	S (p_x)	S (p_y)
0%	**0.350**	**0.350**	**0.064**	**0.064**
5% (ZZ)	0.362	0.354	0.060	0.064
5% (AC)	0.350	0.366	0.064	0.060

VBM_Γ	Mo (d_{z^2})	S (p_z)	Mo (s)
0%	0.596	0.140	0.014
5% (ZZ)	0.604	0.132	0.020
5% (AC)	0.604	0.132	0.019

Figure 4.6. Bloch states at various k points, orbital wavefunction of electronic states at the vertices of the conduction band valley (CBM_K), and valence band hills (VBM) located at K and Γ points for strain-free (a), and 5% strained ML MoS_2 along the zigzag (b) and armchair (c) directions. The orbital structure of Bloch states is projected from different crystallographic viewpoints with their orbital character labeled therein. The charge density isosurfaces have the same isolevel along a particular column in (a)–(c) in units of e/Å^3. The table summarizes the orbital composition of Bloch states at the band edges of CBM/VBM. (d)–(e) Difference in

Bloch wavefunction along the ZZ/AC direction for relevant edges at an isosurface level of 0.6 × 10-3 e/Å^3. A strong delocalization effect can be seen when strain is along the ZZ direction.

In Figure 4.6(d) and 4.6(e), a higher deformation in the orbital charge density distribution is noticed when strain is along the *ZZ* direction as compared to the *AC* direction. The charge density redistribution leads to non-negligible changes in the orbital occupancy that lifts the orbital degeneracy of Bloch states that were initially degenerate for a given electron/hole band at CBM/VBM. The *d* and *p* orbitals that are along the strain axis get higher in energy, and the orbital wave functions become more stretched along the direction of applied strain. Uniaxial strain-induced orbital motion reduces the orbital overlap between ions, and, in turn, the covalency gets partially reduced with progressive domination of ionicity in the metal-chalcogen bond. As a result, the *d* bandwidth resulting from the orbital overlap or covalency in the bonds can show a considerable change in the orbital projected density of states [see Figure 4.7].

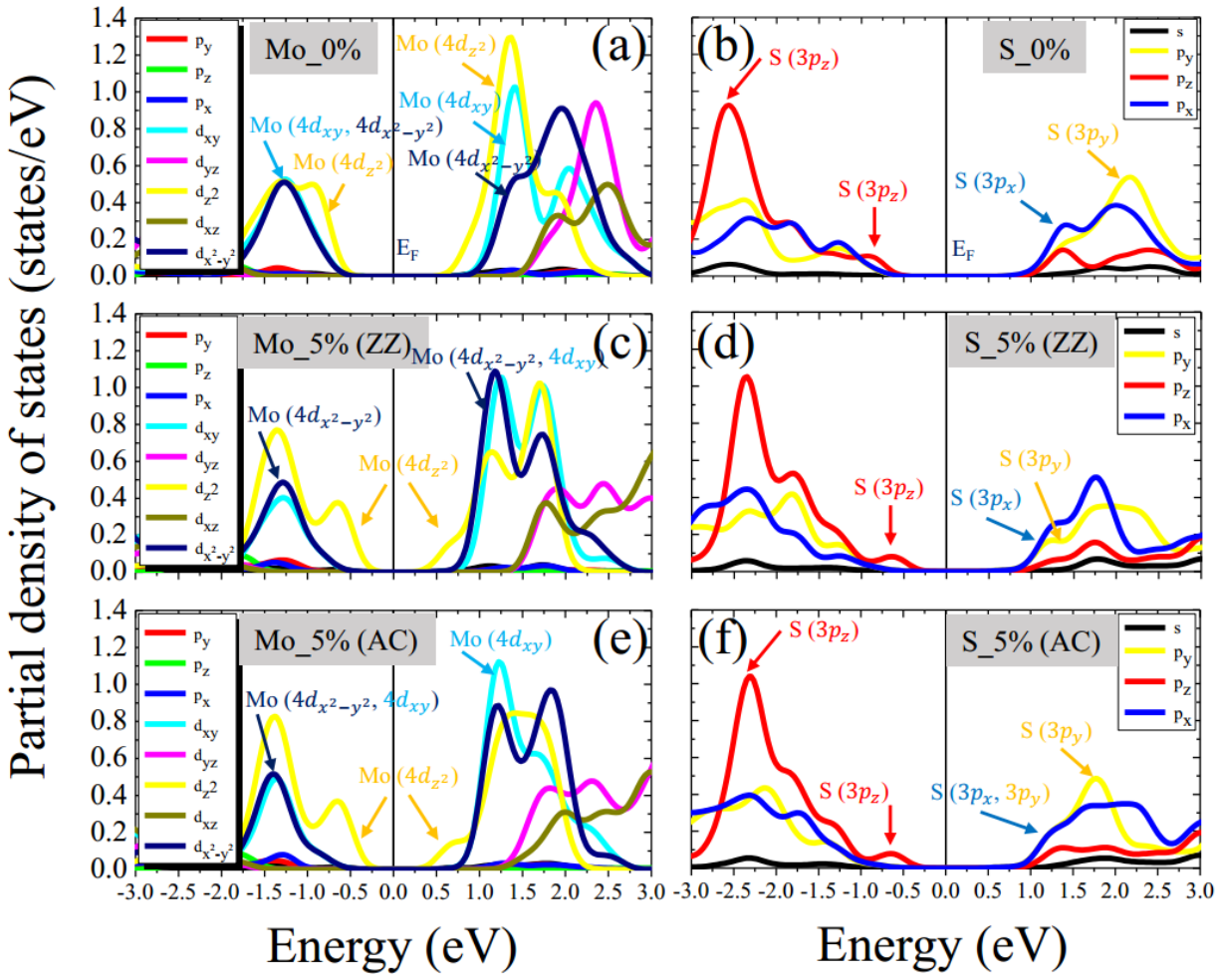

Figure 4.7. Orbital projected partial density of states of a strain-free and strained monolayer MoS_2. The orbital projection has been made on Mo and S orbitals, separately, and the orbital states across the band-edges have been marked therein. The Fermi level is set to zero energy as a standard reference.

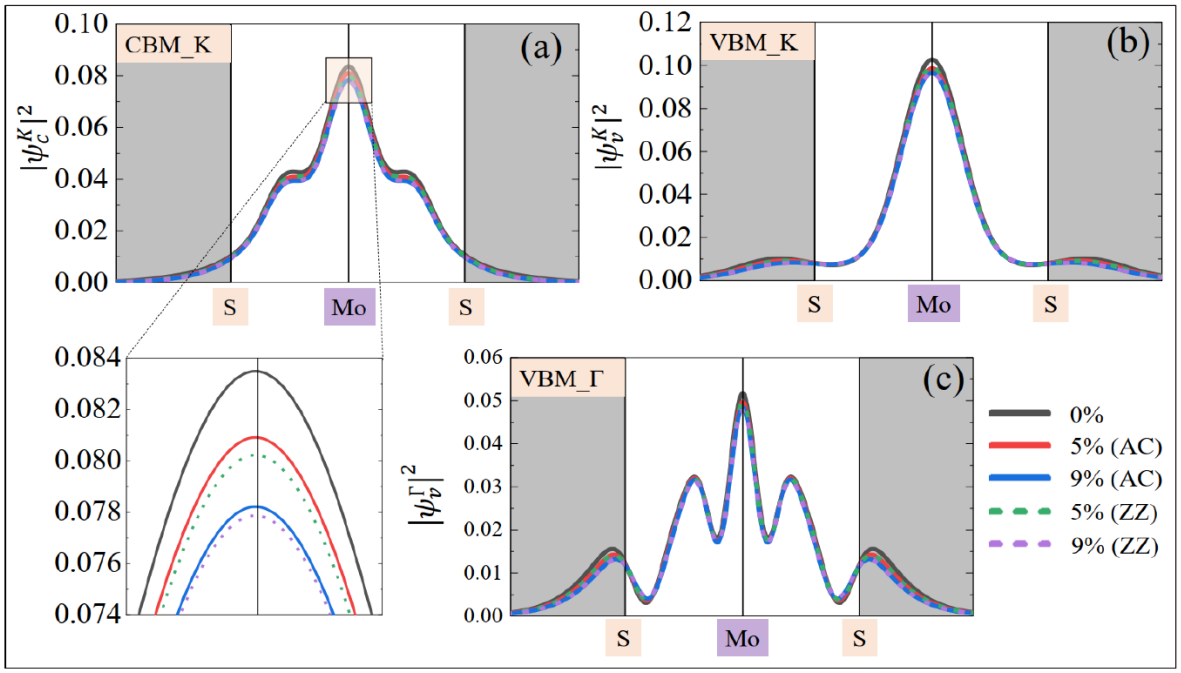

Figure 4.8. (a) Spatial distribution of Bloch wave functions at the band edges, CBM (at K), and (b)–(c) VBM at K and Γ, respectively, when strained along the ZZ/AC direction. The planar-average squared wave functions ($|\psi|^2$) have been projected along the direction perpendicular to the basal surface of ML-MoS_2 (width direction). The atomic positions have been marked therein with solid vertical lines on S-Mo-S.

In Figure 4.8, we have shown the spatial profile of Bloch wave functions for relevant band-edge states projected along the direction perpendicular to the MoS_2 surface. Under strain, the stretching of the Mo-S bond reduces the probability density of the wave functions, which shows a higher drop when strain is along the *ZZ* direction.

4.3.6 Impact of strain on Berry curvatures

In direct intervalley optical excitations via a circularly polarized light, the optical field only couples to the orbital part of the Bloch wave functions, near the *K/K'* valleys, while the spin component of carriers remains unaffected during this process. The modification in the onsite electronic energy and orbital occupation factor of a given Bloch state can significantly

alter the strength of the Berry curvature distribution of valley carriers that associate valley Hall and spin Hall effects in ML-MoS_2, due to an asymmetric momentum drift in its low-energy Bloch bands[137]. In ML-MoS_2, the degenerate electron/hole bands are energetically indistinguishable around *K/K'*. Nevertheless, the valley carriers can be identified by their opposite nature of Berry curvature distributions, $\Omega(k)$. In this section, we have studied the effect of a uniaxial tensile deformation on the $\Omega(k)$ of electron/hole bands, near *K/K'*–points.

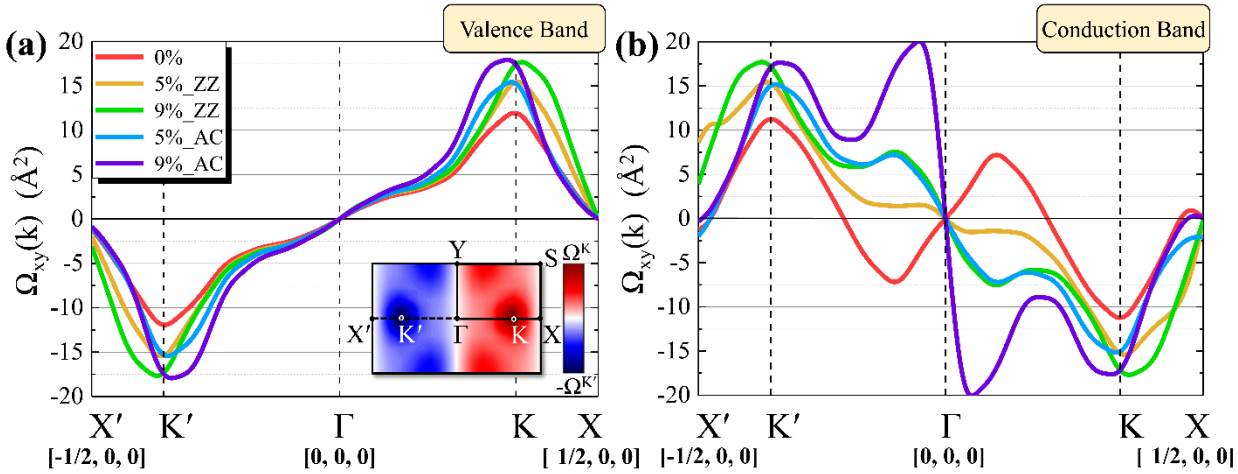

Figure 4.9. (a) Berry curvature distribution Ω(k) over all the occupied Bloch bands in units of Å^2 along the high-symmetry *k*-line X'-K'-Γ-K-X, under varying degrees of strain (5%, 9%) along the ZZ/AC direction. (b) Berry curvature distribution of two lowermost unoccupied bands under strain. Inset in (a): contour map of Berry curvature distribution in a 2D k plane for occupied bands.

Figure 4.9(a) shows the Berry curvatures of all the occupied bands below the Fermi energy for strain-free and strained ML-MoS_2, and Figure 4.9(b) represents $\Omega(k)$ for two lowest unoccupied bands along the high-symmetry line *X'-K'-Γ-K-X*. The lattice inversion symmetry breaking and strong spin-orbit interaction allows charge carriers in these valleys to take opposite spin polarization and Berry curvatures, where the Berry curvature is mainly localized around the *K/K'* valleys and significantly peaked at both the *K* and *K'* points in the BZ with

opposite sign, as required by the time-reversal symmetry of the system. Away from *K/K'*, Ω(*k*) decays rapidly and eventually vanishes at the *Γ* point. When uniaxially strained along the *ZZ/AC* direction, the intensity profile of Ω(*k*) shows a strong drift around *K/K'*, similar to the energy valley drift response in the low energy Bloch bands. The drift is opposite around *K/K'*, with Ω(*k*) crossing *K/K'* when tensile strain is along the *ZZ/AC* direction. Importantly, the Ω(*k*) distribution is symmetric [Ω (−*k*) = Ω −(*k*)] about the point along the *Γ*-*X* and *Γ*-*X'* high-symmetry lines for both unstrained and strained systems. So, the total valley Chern number (C_q) will be null as the valleys at *K/K'* follow $C_K = -C_K$, which is expected from a system that respects time-reversal symmetry under strain. However, an increase in Ω(*k*) flux intensity together with a drift would affect the dynamics of valley carriers due to a strong coupling between external strain and carriers' valley pseudospin at the band edges that could conveniently alter the valley current (valley Hall conductivity) in uniaxially strained ML-MoS_2, when the system is under an applied transverse electric field. The anomalous transverse velocity gained by the dissociated valley carriers (two different longitudinal charge current polarization for each valley index) could be addressed in a controlled valley-dependent transport experiment where the associated charge carriers are expected to be deflected under an asymmetric strain perturbation[259], [311].

4.3.7 Strain effect on SOC energy splitting

Since a large strain-field can substantially alter the electronic states around *K/K'* points, it is worthwhile to address the effect of a uniaxial strain-field in an extensive strain range of 0–9% on the changes in spin-split valence band maxima (*VB1, VB2*) and conduction band minima (*CB1, CB2*) at *K/K'* points. In ML-MoS_2, the *K/K'* valleys are associated with strong SOC. The absence of lattice inversion symmetry and the presence of frontier Mo 4*d* orbitals lift the spin degeneracy of electronic states near VBM/CBM due to a strong spin-orbit induced spin splitting of bands[123], [124]. Figures 4.10 (a–c) show the spin-resolved electronic structure

of strain-free (0%) and strained (9%) ML-MoS_2 along the *ZZ/AC* direction, where the spin projection of carriers is along the out-of-plane spin quantization axis (S_z). Under SOC, electronic states at each valley (*K*) remain at least twofold Kramer degenerate with those of its entangled time-reversed pair (*K'*). The spin-split bands at *K/K'* valleys remain degenerate in electronic energy with opposite spin polarization and crystal momenta in the Brillouin zone, as required by the time-reversal symmetry in the system, with the spin index of carriers locked to their valley index, which forms a general basis for coupled spin-valley physics in ML-MoS_2. Pure out-of-plane spin polarization is the result of an interplay of planar electronic confinement of *d* electrons' motion and the asymmetry in the crystal potential gradient arising from the broken in-plane inversion symmetry[123], [312]. A giant spin splitting observed at the VBM, ~ 149.3 meV, and a relatively small splitting at the CBM, ~ 3.28 meV, in our DFT calculations shows great agreement result with earlier numerical findings reported using both the analytical $\boldsymbol{k} \cdot \boldsymbol{p}$ Hamiltonian model and *ab initio* calculations[24], [124]. In ML-MoS_2, the SOC effects primarily arise from the inner orbitals of Mo atoms, and the modification in the geometry of the *d* orbital wave functions of Bloch electron/holes at the band edges has a sizable effect on the spin-split energies of CBM/VBM under a symmetry-breaking strain, as shown in Figure 4.9.

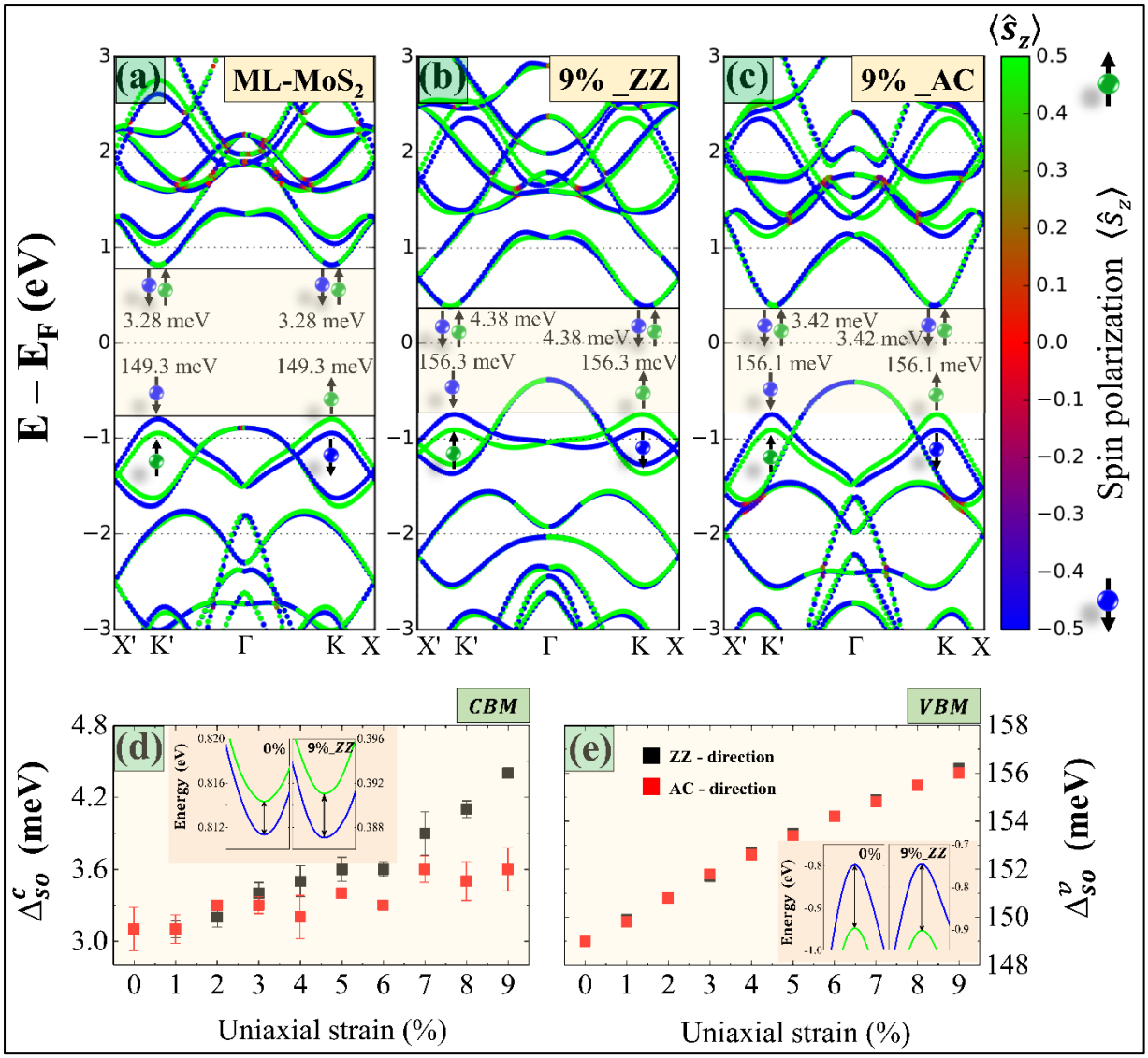

Figure 4.10. (a)–(c) Spin-resolved band structure of strain-free (0%) and uniaxially strained (9%) ML-MoS_2 along the ZZ/AC direction. The spin projection is along the out-of-plane spin-projection operator, Sz (dimensionless spin Pauli matrix), and perpendicular to the basal plane of ML-MoS_2. The green and blue colors indicate spin-up and spin-down polarization states. (d) Spin-orbit induced spin splittings of the conduction band (CB1, CB2) and (e) valence band (VB1, VB2) under varying degrees of uniaxial strain along the ZZ/AC direction. Insets in (d) and (e) show the CBM and VBM band dispersions for strain-free (0%) and 9% strained cases along the ZZ direction.

A giant spin splitting in the VBM mainly arises from the hybridization between degenerate Mo $4d_{xy}$ and $4d_{x2-y2}$ orbitals, where the spatial redistribution of the valley carriers lifts the orbital degeneracy of relevant states under a uniaxial strain by altering their orbital occupancies. This induces a strain-controlled visible splitting in VBM which increases linearly with strain, and reaches ~ 7 meV at 9% of strain, as indicated in Figure 4.10(e), while the CBM of ML-MoS_2 is a result of weak mixing between in-plane S $3p_y + 3p_x$ and out-of-plane Mo $4d_{z2}$ orbitals. Therefore, the CBM shows a small spin splitting ~ 1 meV under the application of strain. However, fluctuation in spin splitting at some intermediate strain values is observed in Figure 4.10(d). This fluctuation in the spin-split conduction band edge (CBM) could be due to an asymmetric hybridization (i.e., a random spatial overlap) between out-of-plane (Mo $4d_{z2}$) and in-plane (S $3py + 3px$) Bloch states on sublattices, which in turn leads to a potential asymmetry around Mo atoms accompanied by the elongation in Mo-S bond.

In contrast, the VBM at the point plays no role in spin splitting due to its pure out-of-plane orbitals, S $3pz$ and Mo $4dz2$, arising from the crystal symmetry of ML-MoS_2. The occurrence of inversion symmetry along the *z*-direction causes no spin splitting at the Γ point. Since the robustness of valley and spin indexes of valley carriers is closely associated with the carriers' relaxation time, an increase in the SOC energy difference in hole bands (~ 7 meV) can hold the spin orientations of carriers for a longer time, and the hole relaxation is expected to be slower due to the suppression of Dyakonov-Perel spin relaxation[313]. In ML-MoS_2, the direct interband optical transitions from a spin-split valence band (*VB1*, *VB2*) to the conduction band (*CB1*, *CB2*), at the *K* point, give rise to strongly bound A and B excitons, with optical selection rules maintaining spin conservation of valley carriers [124][314][279]. Strong spin-strain coupling in a strained ML-MoS_2 is expected to widen the energy separation between A and B excitons leading to a strain tunable exciton splitting under a large strain field (0–9%). Experiments on ML-MoS_2 shows the ability of ML-MoS_2 to withstand a sufficiently large

elastic strain field as high as 6% to 11% without undergoing any mechanical failure[166]. Therefore, SOC spin splitting at the VBM/CBM can be considered carefully in studies pertaining to a large strain engineering in MoS_2 monolayers, where the spin degrees of freedom of valley carriers can be manipulated simply by controlling the spatial distribution of their Bloch orbitals.

4.4 CONCLUSIONS

In conclusion, using first-principle calculations, we have shown the impact of a symmetry reducing mechanical deformation on the low-energy carrier dynamics in strained ML-MoS_2, around *K/K'* points. We find a robust strain-valley coupling for low-energy valley carriers, where the energy extrema of electron/hole bands drift away from *K/K'* points in response to a symmetry lowering uniaxial strain. A significant valley asymmetry between electron and hole states (i.e., the CBM valley drift is nearly 2-times that of the VBM hills) can conveniently lift the valley symmetry (valley momentum degeneracy at *K/K'*) of *electrons/holes*. The resulting effect considerably influences the valley selective optical excitations and valley polarization properties in a multi-valley electronic system like ML-MoS_2. A drastic drop in the degree of circular polarization (*K* valley polarization) can be optically addressed by a polar PL emission measurement[137]. Besides, the *K*-valley coherence effect can manipulate the valley-contrasting Berry curvature distributions around *K/K'*, where the rise in flux profile together with a drift can lead to anomalous valley current in strained ML-MoS_2 [259]. The strain-induced modification in Bloch states can substantially alter the strength of valley-contrasting phenomena in a strained ML-MoS_2 leading to an anomalous valley current for different Kramer channels that can mechanically be controlled by a strong strain-valley coupling near K and K' points. This strong valley asymmetry between valley carriers under a directional lattice strain is the interplay of geometric and orbital overlap effects

that breaks the lattice symmetry and symmetry between orbital wave functions at the relevant band-edge points.

Moreover, the spatial redistribution and rehybridization of states near the band edges can potentially pave the way to controlling the spin degrees of freedom in a uniaxially strained ML-MoS_2, where the SOC induced spin-splitting energy at the VBM can be sizably enlarged by an amount of ~ 7 meV at a strain of 9%. This could potentially alter the spintronic capability of this material and allow manipulating the spin degrees of freedom in a strained MoS_2 lattice. The spin relaxation times of carriers are expected to be prolonged by the suppression of Dyakonov-Perel spin relaxation due a strain-induced increase in the spin-splitting energy. The theoretical findings in this report may drive further experimental investigations of ML-MoS_2 under the application of in-plane lattice strain to realize its future technological applications.

----------**********----------

Chapter 5

Strain-induced optimization of nanopiezotronic response in monolayer MoS_2

This chapter is based on the work published in:

Nityasagar Jena, Dimple, Shounak Dhananjay Behere, and Abir De Sarkar*, "*Strain-Induced Optimization of Nanoelectromechanical Energy Harvesting and Nanopiezotronic Response in a MoS_2 Monolayer Nanosheet*", ***J. Phys. Chem. C** 2017, **121,** 9181-9190*

5.1 INTRODUCTION

In comparison to one-dimensional materials (1D), two-dimensional (2D) nanostructures have drawn a surge of research interest for their potential applications as a channel material in next-generation nano transistors, owing to the relative ease in fabricating complex structures from them. Graphene is certainly the most studied 2D nanomaterial. However, the absence of a finite semiconductor bandgap in pristine graphene precludes its applications in nanoelectronics, where a semiconducting bandgap of material is of utmost desire. The engineering of bandgap in graphene elevates the fabrication complexity and either reduces carrier mobility to the level of strained silicon[315]–[321] or requires high voltage[322], [323]. Lately, semiconducting transition-metal dichalcogenide monolayers (mTMDCs, with general chemical formula MX_2, where M = Mo, W, etc. and X = S, Se, or Te)

have been emerging as promising alternatives to graphene, owing to their intrinsic semiconducting band gap in the range (1-2eV)[266], [324]–[326], commendable performance (high on/off ratios) in transistors, inherent flexibility, transparency, and atomically layered planar structures arranged in a hexagonal honeycomb lattice.[165], [327] Besides, their pristine interfaces devoid of out-of-plane dangling bonds facilitate their facile integration with various substrates. Moreover, mTMDCs show strong piezoelectricity owing to the absence of inversion symmetry, unlike their bulk counterparts, which are centrosymmetric.[163][328][329]

Recently, piezoelectric properties have been experimentally investigated in free-standing monolayer MoS_2 (ML-MoS_2) and nanosheets containing an odd number of MoS_2 layers.[163], [330] Furthermore, Rezk *et al.* have also investigated intrinsic piezoelectricity in ML-MoS_2 via acoustically driven trion and exciton modulation.[331] The world's thinnest nanoscale energy-generator happens to be ML-MoS_2 nanosheet.[163], [330], [332] Broken inversion symmetry together with strong spin-orbit coupling in monolayer TMDCs such as ML-MoS_2 leads to the emergence of robust spin and valley related properties, such as valley-selective circular dichroism, valley-contrasting spin splitting, and valley and spin Hall effects.[136], [259], [333], [334] These are of enormous scientific interest in the potential application of these materials in valleytronics- and spintronics-based devices.

Nanopiezotronics[330], [335], which couples piezoelectricity to semiconducting electronics at the nanoscale, is a vibrant domain of research that can potentially have a wide range of applications in nanoscale energy conversion for self-powered nanosystems, harvesting/recycling energy from the environment, low-power switches in digital electronics, and electromechanically coupled sensors and actuators. However, this relatively new research area is in its infancy for 2D piezoelectricity. A microscopically clear understanding of the mechanism underlying piezoelectricity in atomically thin nanomaterials and its synergic coupling to the semiconducting properties is indispensable for its gainful exploitation in vivid

applications such as strain-gated piezoelectric field-effect transistors (PE-FET), piezoelectric diodes, strain sensors, and futuristic self-powered two-dimensional semiconducting nanodevices for nanoelectromechanical energy harvesting (i.e., conversion of mechanical energy into electrical energy). Moreover, the utility of such systems can be integrated into some futuristic devices, such as self-powered artificial retina, cardiac activity monitoring devices (e.g., self-powered pacemakers), contact lenses, and artificial skin sensors, which can monitor several bodily activities and can be potentially beneficial in future point-of-care diagnosis.

Although a plethora of first-principles studies on strain-induced bandgap engineering in semiconducting nanostructures,[336]–[339] investigations on piezoelectric properties are relatively sparse.[340]–[342] Apart from the semiconducting band gap in ML-MoS_2, piezoelectricity occurs due to the broken inversion symmetry. This underlines the need to reveal the simultaneous response of the semiconducting (SC) and the piezoelectric (PE) properties to the application of mechanical strain for its worthwhile utilization in nanopiezotronic devices. To the best of our knowledge, a concerted interplay of the SC and PE properties in semiconducting nanosheets, which is of utmost importance from both scientific and technological perspectives, has not been addressed so far. The piezoelectric response of the ML-MoS_2 sheet has been experimentally studied in terms of its current-voltage characteristics upon the application of mechanical strain and the asymmetric tuning of the Schottky barrier at the metal-semiconductor contacts.[330] Nevertheless, no effort has been made to benchmark the conversion of mechanical-to-electrical energy with the strain of different modes and magnitude. Furthermore, the underlying linear response properties in ML-MoS_2, such as changes in effective dynamical charges along different lattice directions, have not yet been correlated with its piezoelectric strength for an in-depth atomistic insight of the phenomena.

This chapter unravels the atomistic origin of PE properties in ML-MoS_2 through their direct correlation with the changes in intrinsic polarization in ML-MoS_2. The simultaneous response of the piezoelectric (PE) and semiconducting (SC) properties in ML-MoS_2 to the application of different modes of strain has been presented in this chapter to realize a seamless merger between these two intrinsic properties in nanopiezotronic applications. The uniqueness of this finding lies in the first-time calibration of piezoelectric properties in ML-MoS_2 with the strain of various modes, within the bounds, where ML-MoS_2 remains elastic and semiconducting, thereby enabling one to ascertain the optimal piezoelectric strength and the maximal nanoelectromechanical energy harvestable in nanopiezotronic applications. Through this systematic approach, the multifunctionality of a particular nanomaterial can be fully explored for its fruitful integration into futuristic two-dimensional (2D) semiconducting self-powered nanoscale devices.

5.2 COMPUTATIONAL DETAILS

Ab initio calculations were performed within the density functional theory (DFT)[189], [343], as implemented in the plane wave Vienna *ab-initio* simulation package (VASP, *version*: 5.3).[292], [344] Projector-augmented wave (PAW)[289] pseudopotentials and the exchange-correlation (XC) functional at the level of the Perdew-Burke-Ernzerhof (PBE) variant of the generalized gradient approximation (GGA)[293], [345] have been employed in all calculation results presented in this chapter. The lattice geometry of ML-MoS_2 nanosheet has been optimized in a supercell with rectangular symmetry, as shown in Figure 5.1. Upon geometry optimization, the lattice constants reach to 3.17 (a) × 5.50 (b) × 18.02 (c) Å. This has been used for subsequent calculations on strained geometries. In a supercell approach, a vacuum thickness larger than 14 Å has been introduced along the direction perpendicular to the MoS_2 nanosheet in order to decouple the periodic images. The Brillouin zone has been sampled through a Γ-centered 16 × 9 × 1 k-mesh with an energy cutoff of 520 eV. Ionic relaxation has been

performed based on the conjugate-gradient (CG) optimization algorithm until the Hellmann-Feynman forces on individual atoms reach less than 0.1 meV/Å. The piezoelectric tensor coefficients have been computed using DFPT, which efficiently calculates the linear response properties of materials, such as piezoelectric stress tensors (e_{ij}) and Born effective charges ($Z^*_{[B]}$). The tensor components reported in this study correspond to the relaxed ion geometry, which is relevant to the experimental situation, where ionic relaxation has been performed on strained lattices to compute polarization-dependent parameters. The elastic stiffness coefficients have been computed using the finite differences approach as implemented in VASP.[216] Furthermore, the elastic limit for various strain modes has been studied.

5.3 RESULTS AND DISCUSSION

The results and discussion presented in this chapter are divided into the following subsections, and essential observations have been concluded at the end of chapter 5.

In order to probe the piezoelectric response of ML-MoS_2 with strain, the optimized nanosheet of ML-MoS_2 has been subjected to different modes and magnitudes of strain. The response in the piezoelectric property to an applied mechanical strain has been quantified by piezoelectric tensor coefficients, such as piezoelectric stress (e_{11}) or piezoelectric strain (d_{11}) tensor coefficients. An enhancement in piezoelectric coefficients at certain levels and modes of strain with respect to pristine, unstrained ML-MoS_2 has been noticed. This enhancement in the magnitude of coefficients is the signature of the increasing piezoelectric strength of ML-MoS_2 nanosheet upon straining. However, at certain specific levels and modes of strain, within the elastic limits, the system has been found to show the maximum piezoelectric response. The underlying mechanism of this enhancement lies in the changes in intrinsic electric polarization of the material upon applying strain, which has been elucidated by computing a polarization-dependent linear response parameter, such as Born-effective charge tensors $Z^*_{[B]}$ on ionic

species (Mo/S) along different in-plane lattice directions (zz/ac). Furthermore, elastic stiffness coefficients (C_{ij}), Young's modulus (Y), and Poisson's ratio (ϑ) have been studied to ascertain the elastic limits of ML-MoS_2 under different strain modes. Experimentally, ML-MoS_2 is found to withstand a mechanical strain higher than 11%.[166] The elastic limits of the sheet lie in the 6−11% range contingent upon different modes of strain applied to it. Therefore, a 10% strain is the maximum strain magnitude that has been considered in all the cases.

5.3.1 Strain geometry

MoS_2 belongs to the family of layered transition-metal dichalcogenides (TMDCs), where the stacked layers are held together by the weak van der Waals forces of attraction. Depending on the stacking pattern, MoS_2 can exhibit in different polytypic structural phases, such as 1*T*, 2*H*, and 3*R*, with *AA*, *AB*, and *ABC* stacking sequences. 1*T* metallic phase and 3*R* semiconducting phase are metastable[346] at the ambient environment and transform to the stable 2*H* semiconducting phase in response to external stimuli, such as thermal treatment, mechanical or electrical perturbations.[347]–[349] The 2*H* phase is the most stable bulk phase of MoS_2 having D_{6h} point group symmetry of hexagonal lattice structure. For the present study, the stable 2*H* phase of ML-MoS_2 having trigonal prismatic coordination belonging to the 1*H* phase has been considered. A monolayer of 2*H*-phase is referred to as the 1*H* phase belongs to D_{3h} point group symmetry.

The monolayer of MoS_2 has a hexagonal honeycomb lattice structure like graphene, but unlike graphene, ML-MoS_2 is a covalently bonded S−Mo−S trilayer, as shown in Figure 5.1 (b), where the hexagonal Mo-layer is sandwiched between two hexagonal S-layers in an *ABA* stacking sequence.

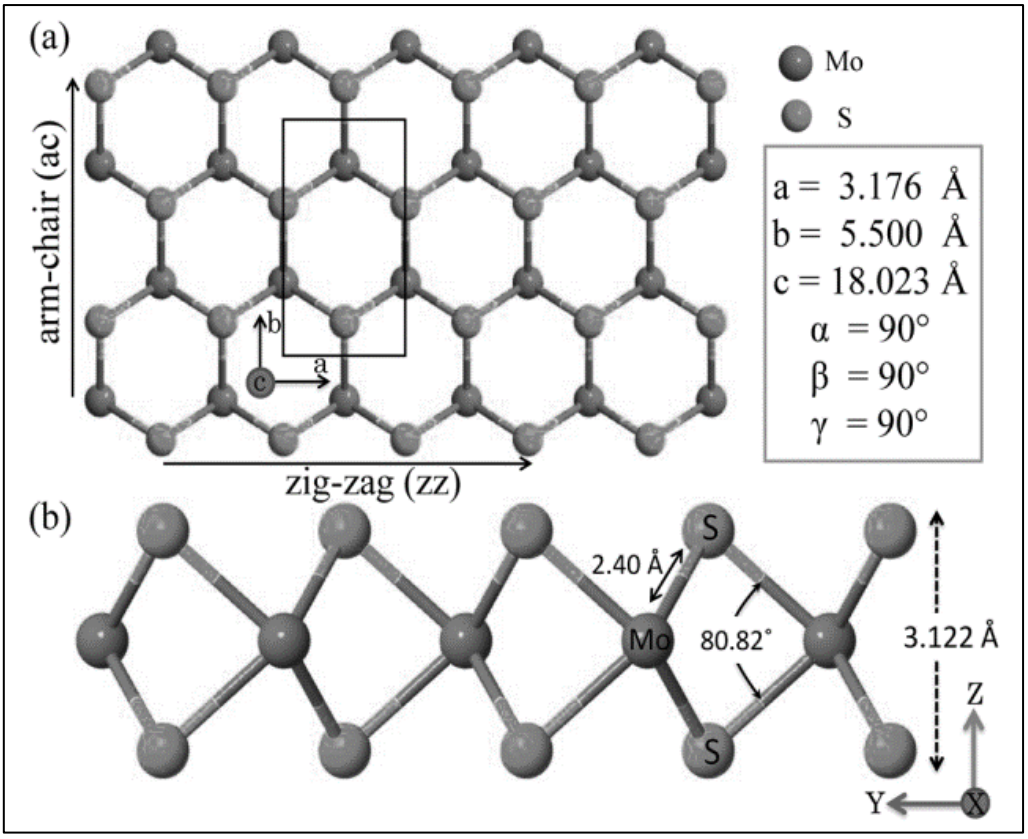

Figure 5.1. (a) Top view of a monolayer MoS_2 (ML-MoS_2) nanosheet. The rectangular box bounds the optimized supercell of strain-free, pristine ML-MoS_2. The optimized cell parameters are listed in the right panel. (b) Lateral view of ML-MoS_2 nanosheet. The strong covalent bonding between Mo (blue sphere) and S (yellow sphere) atoms, bond length, bond angle, and thickness of a pristine, strain-free ML-MoS_2 nanosheet is depicted therein.

The inherent hexagonal symmetry of ML-MoS_2 has been purposefully converted into a rectangular orthorhombic supercell, to enable the application of mechanical strain along two of its nonequivalent lattice directions, namely, the zigzag (*zz*) and the armchair (*ac*) direction, respectively. The optimized geometry and lattice parameters listed in the right panel of Figure 5.1 (a), and also in Table 5.1 are in good accord with the previously reported optimized geometries adopted for this system.[350] The strain has been applied by scaling the lattice constants while relaxing the ionic positions in a supercell with strained lattices, as routinely followed in earlier theoretical reports.[310], [351]–[353]

Table 5.1. Optimized Lattice Parameters (a_{Mo-Mo}), Bond Lengths (d_{Mo-Mo}, d_{S-S}, d_{Mo-S}), Bond Angles [Θ(S-Mo-S)], Piezoelectric Coefficients [stress (e_{11}) and strain (d_{11}) coefficients], and Born Effective Charges ($Z^*_{[B]}$) on Mo and S Ions in Pristine, Monolayer 1H-MoS_2 Calculated in This Study and Benchmarked with Reported Experimental and Theoretical Findings To Ascertain the Reliability of Applied Methods.

	d_{Mo-Mo}, a (Å)	d_{S-S} (Å)	d_{Mo-S} (Å)	Θ (deg)	$e_{11}\times10^{-10}$ (C.m^{-1})	d_{11} (pm/V)	$Z^*_{[Mo]}$(e)	$Z^*_{[S]}$(e)
1H-MoS_2[350]	*3.22*	*3.15*	*2.43*	*80.6*	--	--	*+1.21*	*-0.57*
					2.9[163][b]	--		
					3.62[154]	*3.65*[154]		
1H-MoS_2[354]	*3.19*	*3.14*	--	--	*3.64*	*3.73*		
1H-MoS_2[a]	*3.17*	*3.12*	*2.40*	*80.8*	*3.07*	*2.99*	*+1.06*	*-0.55*

[a] *Present work.* [b] *Experimentally measured value.*

5.3.2 Piezoelectric coefficients

Certain materials show an innate ability to generate or polarize an electric charge within itself under the application of an external mechanical load in the form of stress or strain. Conversely, one can apply an electric field to mechanically deform these materials. The former is known as the direct piezoelectric effect, while the latter is termed as the inverse piezoelectric effect. The necessary condition for materials to show this effect in the absence of an inversion center, or in other words, these materials need to belong to the class of noncentrosymmetric crystals. Both direct and converse piezoelectric effect are related to the intrinsic polarization vector via the Maxwell relation;

$$e_{ijk} = (\partial P_i / \partial \varepsilon_{jk})_{E,T} \quad \text{(for the direct piezoelectric effect),}$$

$$\text{and, } e_{ijk} = -(\partial \sigma_{jk} / \partial E_i)_{\varepsilon,T} \text{ (for the converse piezoelectric effect),}$$

where e_{ijk} is a third-rank piezoelectric stress tensor, P_i is the electric polarization vector, ε_{jk} is the strain tensor, σ_{jk} is the stress tensor, E_i is the macroscopic electric field, and T is the temperature; $i, j, k \in \{1, 2, 3\}$, and 1, 2, and 3 correspond to *x*-, *y*-, and *z*-directions, respectively.

Piezoelectric properties of a material are generally expressed by the piezoelectric strain tensor (d_{ijk}), which is related to the piezoelectric stress tensor (e_{ijk}) via the elastic stiffness tensors (C_{ijkl}). The Maxwell relation for piezoelectric strain tensor coefficients is $d_{ijk} = (\partial P_i / \partial \sigma_{jk})_{E,T} = (\partial \varepsilon_{jk} / \partial E_i)_{\sigma,T}$.

MoS_2 belongs to the class of centrosymmetric crystals in its bulk form; however, when thinned down to a monolayer or an odd number of a few layers, inversion symmetry is broken, and hence, the piezoelectric effect is induced in ML-MoS_2, which has been theoretically mapped and experimentally verified by Zhu *et al.*[163]

As reported by Duerloo *et al.*,[354], the presence of the D_{3h} point group in ML-MoS_2 reduces the number of nonvanishing piezoelectric tensor coefficients (e_{ijk} *or* d_{ijk}) to only one independent coefficient, which thereby uniquely quantifies the piezoelectric property of this system of materials. Under this symmetry, the nonvanishing piezoelectric stress tensor components in Voigt notation are related as follows:

$$e_{111} = e_{11}$$

$$e_{122} = e_{12} = -e_{11}$$

$$e_{212} = e_{221} = e_{26} = -e_{11}$$

In our study, the piezoelectric stress tensor component e_{21} (where $e_{21} = -e_{11}$) has been considered to calculate the piezoelectric property. The in-plane piezoelectric properties of this system have been quantified by the piezoelectric strain tensor coefficient d_{11}, which is related to e_{11} via in-plane elastic stiffness coefficients (C_{11} and C_{12}) as $d_{11} = e_{11} / (C_{11} - C_{12})$. The

piezoelectric response has been calculated on tracking the changes in d_{11} coefficients under various strain modes. The piezoelectric coefficients for a pristine and a strained ML-MoS_2 sheet have been analyzed using DFPT, which efficiently calculates linear response properties of materials, like piezoelectric stress coefficient (e_{ij}) and Born-effective charge tensor components ($Z^*_{[ij]}$), which arise due to small perturbations applied to the system in the form of electric field or strain.

In order to check the reliability of the applied method, we have first computed piezoelectric stress coefficients e_{11} for a pristine ML-MoS_2 nanosheet. e_{11} = 0.49 C/m^2 obtained in our calculations is found to be in excellent agreement with the experimental value of $e_{11} = 2.9 \times 10^{-10}$ C/m (or e_{11} = 0.5 C/m^2, when normalized by the thickness of the ML-MoS_2 sheet)[163], and close to the numbers reported in various theoretical studies, $e_{11} = (2.9 \pm 0.5) \times 10^{-10}$ C/m.[154], [354] The values are tabulated in Table 5.1 for a direct comparison with other reported works on pristine ML-MoS_2. Upon yard sticking e_{11} and d_{11} for the unstrained sheet, different possible strain modes have been realized on the ML-MoS_2 nanosheet, and the resultant changes in the piezoelectric strain coefficient d_{11} as a function of different strain modes are shown in Figure 5.2 (a). An optimal enhancement in d_{11} is noticed for certain strain modes. At low magnitudes of applied strain (piezoelectric strain coefficient d_{11} and electronic band gap E_g with strain has been drawn, in Figure 5.2 (c-d). Shear (S_1) mode of strain and uniaxial strain along the zigzag (*zz*) direction have been chosen for their abilities to induce a greater enhancement in d_{11}. The encircled regions represent a favorable zone in nanopiezotronics where piezoelectricity synergistically meets semiconducting nanoelectronics for its fruitful integration into nanopiezotronic devices.

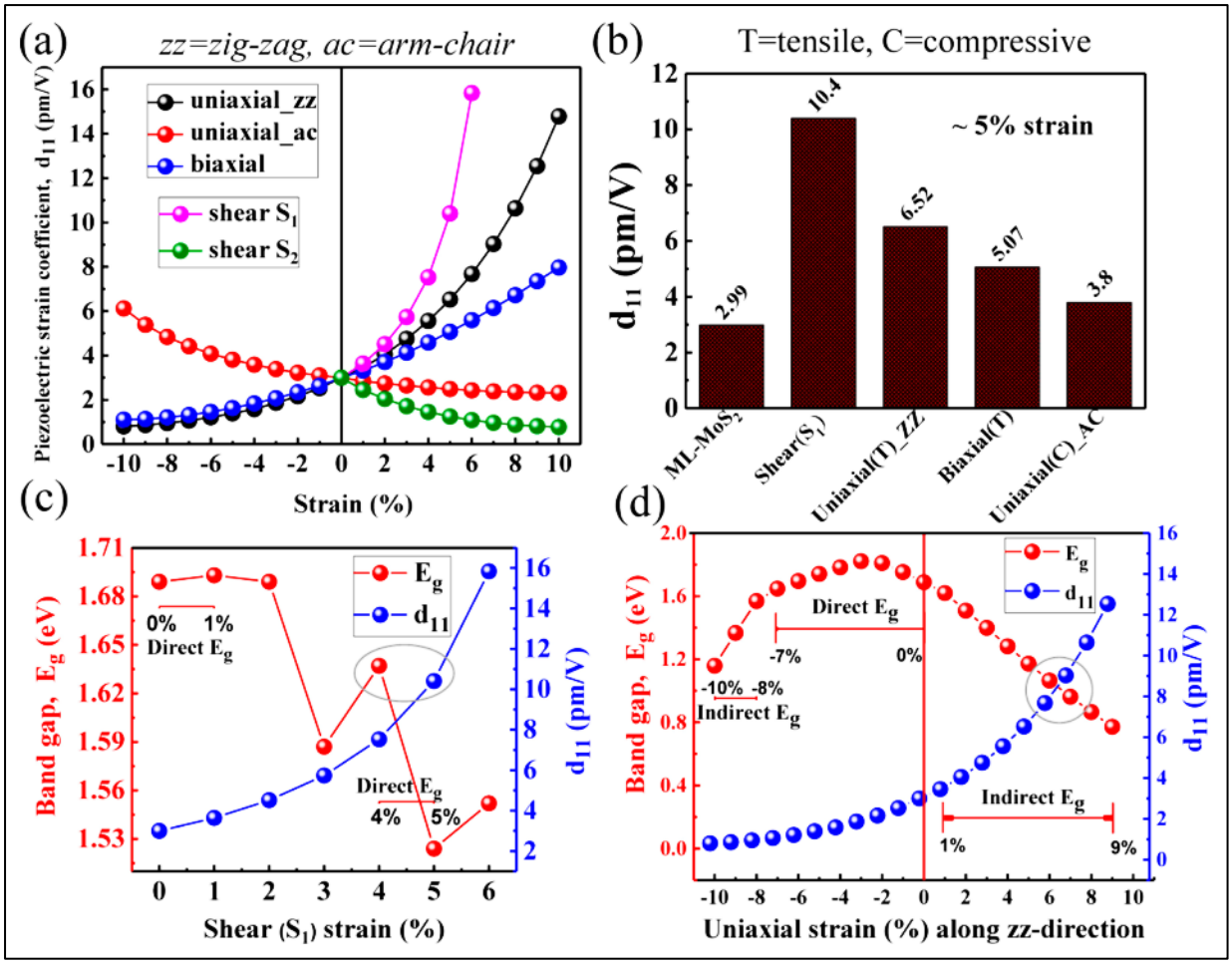

Figure 5.2. Assessment of piezoelectric and semiconducting properties and their synergic coupling in adaptive nanopiezotronics. (a) Variation in piezoelectric strain coefficient d_{11} with the strain of different modes applied to ML-MoS_2; negative values imply compressive strain, while positive ones signify tensile strain. (b) Bar diagram comparing the piezoelectric response to different strain modes at the lower elastic limit for all strain types studied: d_{11} at 5% strain. (c, d) Simultaneous variation in d_{11} and semiconducting electronic bandgap (E_g) with shear (S_1) mode of strain and uniaxial strain applied along the zigzag (zz) direction. The directness in bandgap in a specific range of strain has been indicated in the panels. [Shear strain S_1 indicates the simultaneous application of tensile strain along the zigzag (zz) direction and compressive strain of the same magnitude along the armchair (ac) direction.] The enclosed regions represent the favorable zone for nanopiezotronic applications, where d_{11} is maximized. At the same time,

the semiconducting bandgap of the system is retained.

Figure 5.2 (c-d) shows that nanopiezotronic properties are maximally utilizable around 4−5% of the shear (S_1) mode of strain, and 6−7% uniaxial tensile strain along the zigzag direction. More importantly, the directness of the bandgap has been observed around 4−5% of the shear (S_1) mode of strain corresponding to a high value of d_{11}, whereas in the case of uniaxial tensile strain applied along the zigzag direction, the bandgap turns indirect under tensile strain with respect to the direct bandgap in pristine ML-MoS_2. However, the bandgap, which remains semiconducting at 6−7% uniaxial tensile strain, shows a smooth decrement with further application of strain until it reaches the elastic limit of 9%.

5.3.3 Born-effective charges

The dynamical or Born-effective charge ($Z^*_{[B]}$), provides microscopic details of the polarization change on ionic species along different lattice directions under strain. The macroscopic current and spontaneous polarization change arising due to the displacement of ions is quantifiable through $Z^*_{[B]}$.[355] Born-effective charge tensors also provide microscopic insight into the enhancement in piezoelectric coefficients via changes in intrinsic polarization in the system and is related to the electric polarization vector as $Z^*_{[ij]} = \Omega/e(\partial P_i/\partial u_j) = 1/e(\partial F_i/\partial E_j)$, where $i, j = x, y, z$, and Ω is the unit cell volume, u is the strain, E is the electric field, and F is the Hellmann−Feynman forces acting on ionic species. Ataca *et al.* have reported the Born effective charges for pristine 1*H*-MoS_2 to be of $Z^*_{[B]}$ [Mo] = +1.21 electronic charge on each Mo atom and $Z^*_{[B]}$ [S] = −0.57 electronic charge on each S atom, respectively.[350] These numbers for the pristine 1*H*-ML-MoS_2 are close to the ones found in our study and have been tabulated in Table 5.1 for a direct comparison with reported work. Due to the inherent symmetry of the structure of ML-MoS_2, the positive and negative charge centers in the supercell coincide, and as a result, unstrained, pristine ML-MoS_2 shows no intrinsic

polarization. However, ionic displacements brought about by the application of strain cause charge centers to shift away from each other along the armchair direction. This results in the occurrence of an intrinsic polarization vector along the armchair direction, the magnitude of which varies with the type and magnitude of strain. The variation in in-plane effective dynamical charges, $Z^*_{[zz]}$ and $Z^*_{[ac]}$, with different modes of strain, are shown in Figure 5.3. For a pristine ML-MoS_2 sheet, the in-plane effective dynamical charges on Mo and S ions are found to be of the same magnitude. In all strain modes studied, changes in the Born-effective charges on ionic species have been observed.

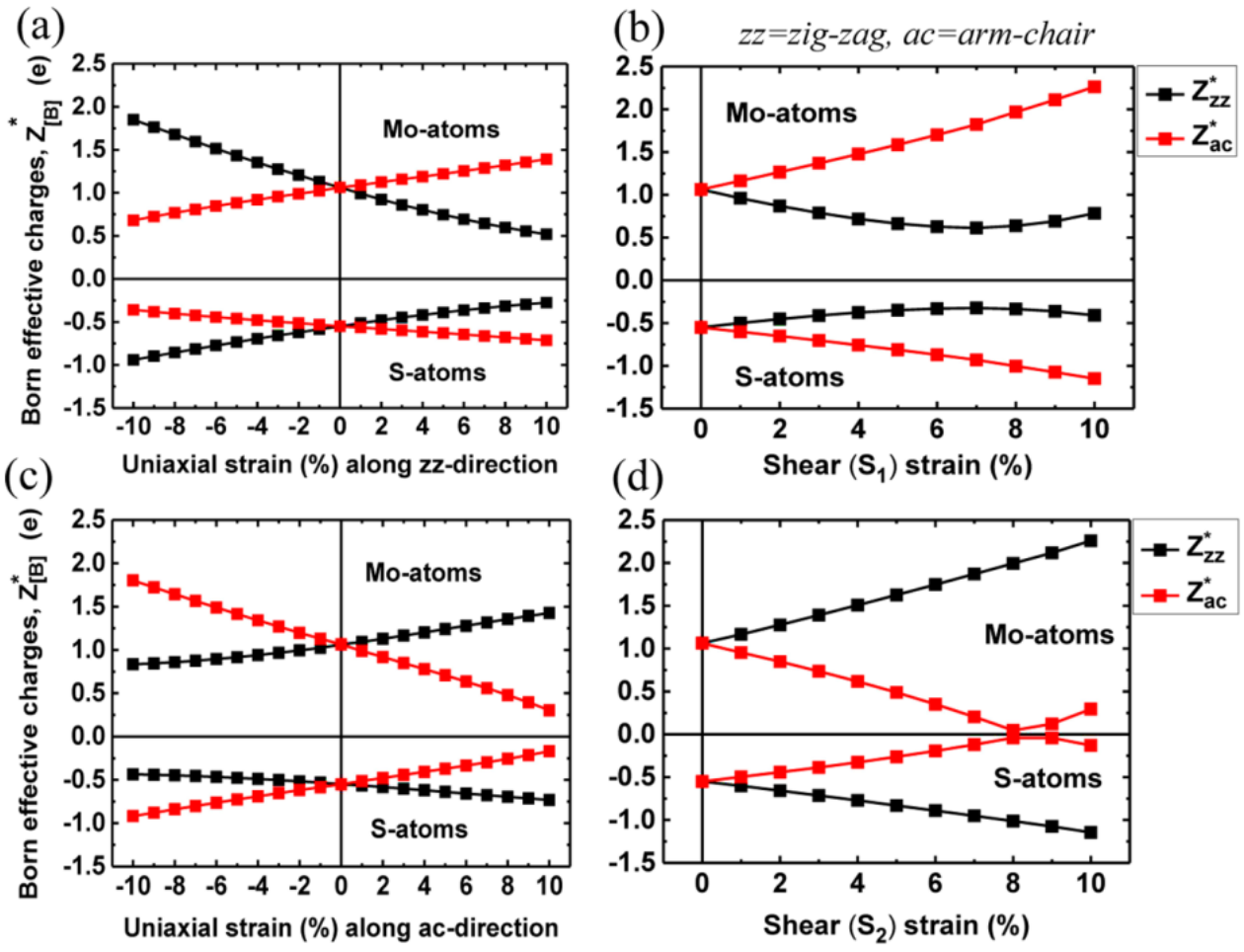

Figure 5.3. Born effective charges on each Mo and S ion. (a-d) Variation in the effective dynamic charges $Z^*_{[B]}$ on the ionic species with the strain (Born effective charge, $Z^*_{[B]}$; in-plane

tensor components along zigzag and armchair lattice directions, $Z^{*}_{[zz]}$ and $Z^{*}_{[ac]}$, respectively.

Considerable enhancement in piezoelectric coefficients has been noticed when the effective dynamical charges on Mo and S ions increase in numerical value along the *y*- or the armchair direction and decrease along the *x*- or the zigzag direction in response to the applied strain. This occurs in uniaxial strain applied along the zigzag direction and compressive strain applied along the armchair direction. These two effects add up in the case of shear (S_1) mode of strain and thereby maximizes the piezoelectric coefficient under the shear (S_1) mode of strain. The increment in the Born-effective charges on the ions enhances the intrinsic polarization vector along the armchair direction. The aforementioned 3-strain types enhance the intrinsic polarization vector along the armchair direction, which scales with the strain magnitude. So, the mechanism underlying the enhancement in the piezoelectricity in ML-MoS_2 is revealed through the increase in the Born-effective charges on the ions and, in turn, the increase in the intrinsic polarization vector along the armchair direction. Therefore, the alteration in piezoelectric response is found to be intimately correlated with the Born-effective charges via the changes in electric polarization.

Furthermore, the strain-induced enhancement in intrinsic polarization along the *y*- or the armchair direction builds up a potential, known as the piezo potential, along the *y*-direction. The magnitude of this piezo potential is proportional to the magnitude of the applied strain. For current flow along the *x*-direction (i.e., zigzag), the piezo potential along the *y*- (i.e., armchair) or transverse direction may serve as the gate voltage, which is tunable by the degree of applied strain. Conversely, for current to flow along the armchair direction, the strain-induced piezo potential along the longitudinal direction will facilitate the transport of charge carriers. The shear (S_2) mode of strain (where S_2 denotes lattice compression along the zigzag direction and dilation by the same magnitude along the armchair direction) causes a large decrement in

effective dynamical charges on both the ions along the armchair direction and a significant increase in the same along the zigzag direction. This results in a significant reduction in the intrinsic polarization vector along the armchair direction, which can be utilized for piezoresistive purposes.

5.3.4 Elastic coefficients

In order to calibrate the elastic strength of ML-MoS_2 nanosheet and to ascertain the elastic limits for different types of strain considered, elastic stiffness tensors (C_{ij}) have been investigated under different modes and magnitude of strain. Moreover, the piezoelectric strain tensor coefficient (d_{11}) is related to the stress coefficient (e_{11}) via the elastic stiffness of the material as $d_{11} = e_{11}/(C_{11} - C_{12})$. Young's modulus (Y) and Poisson's ratio (ϑ) are important elastic parameters to calibrate the mechanical strength and stability of a system under the application of external load. These elastic parameters can be derived from the elastic stiffness tensor coefficients (C_{ij}) from the relation as follows:

$$Y = \left(\frac{C_{11}^2 - C_{12}^2}{C_{11}}\right) \quad \text{and,} \quad \vartheta = \frac{C_{12}}{C_{11}}$$

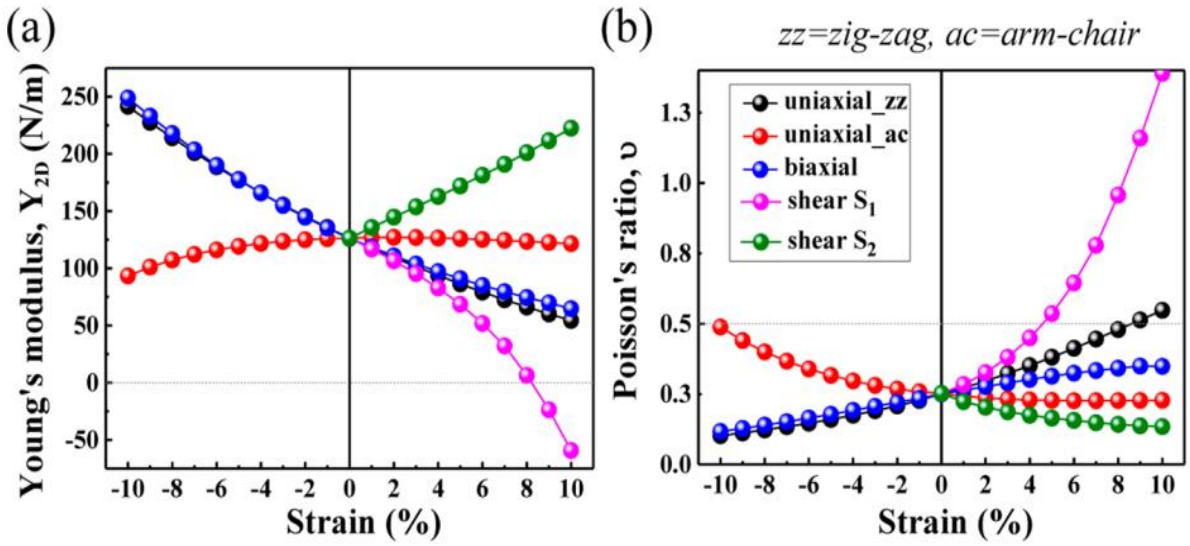

Figure 5.4. Elastic constants for the assessment of mechanical stability or elastic limits in ML-MoS_2. (a) Changes in Young's modulus (Y) and (b) Poisson's ratio (ϑ) with strain.

The variation in Young's modulus (Y) and Poisson ratio (ϑ) with strain has been shown in Figure 5. 4 (a-b). A significant decrease in Y has been observed for the shear mode of strain S_1 followed by the uniaxial tensile strain along the *zz*-direction, biaxial tensile strain, and uniaxial compressive strain along the *ac*-direction. The variation in Y with strain in all these cases has been found to scale inversely with the piezoelectric response. Y is found to reach close to zero for shear strain S_1 exceeding 7%, signifying the instability of ML-MoS_2 for shear strain $S_1 > 7\%$. However, the stability/elastic limit under shear strain S_1 is found to be 5% from the analysis of Poisson's ratio (ϑ). In the case of shear strain S_1, the gradual occurrence of the negative value of Y indicates the onset of mechanical instability above 6% strain. Poisson's ratio (ϑ) for most of the materials lies between −1 and 0.5. In contrast, a negative Poisson's ratio (ϑ) corresponds to the materials belonging to the auxetic family of material classes, which is mechanically a sporadic phenomenon and of great scientific interest. A value of ϑ exceeding 0.5 is generally a sign of a mechanically anisotropic response arising in the system. However, in our studies, $\vartheta > 0.5$ noticed for ~ 5% shear strain and ~ 9% uniaxial tensile strain, as evident from Figure 5.4 (b), is a clear sign of mechanical instability. A compressive strain of up to 3% has been demonstrated to be experimentally feasible and realizable in monolayer lattice structures.[169], [355]–[357] Large compressive strain beyond Euler's critical load may cause buckling or ripple in the sheet. The buckling or rippling in the lattice inducible at large compressive strain would be manageable to some extent under experimental conditions through the usage of an underlying flexible substrate, like PDMS, confined within vertical support or by using a channel material of short length. It will inhibit rippling or buckling in the sheet in the direction perpendicular to the sheet. With the progressive advancement in the experimental tools and techniques, the application of higher magnitudes of compressive strain is foreseeable in the near future. In theoretical studies, the compressive strain has been routinely varied over a wide range to understand or predict the trend.[269], [357], [358] Therefore, results for small

to large values of compressive strain have been included in the current work for completeness. In the present study, the structure is found to remain mechanically stable under the compressive strain of up to 10%, as evident from Figure 5.4.

5.3.5 Carrier mobility

From the perspective of nanoelectronics, the mobility of electron (*e*) and hole (*h*) in ML-MoS_2 nanosheet and its variation with uniaxial strain applied along two lattice directions have been studied. Out of all strain modes studied, the uniaxial strain has been deliberately chosen for the sake of simplicity and also for the following reasons. Uniaxial tensile strain along the zigzag direction is found to be most effective in nanopiezotronic applications owing to the smooth tunability in bandgap and an optimal enhancement in piezoelectric property with the application of this strain. Moreover, the zigzag direction also turns out to be mechanically softest to the application of uniaxial strain, as it is able to sustain its elasticity up to 9% strain. The acoustic phonon limited carrier mobility has been calculated, which is based on the effective mass and the deformation-potential approximation proposed by Bardeen and Shockley.[359] In inorganic semiconductors at room temperature, the coherent wavelength of thermally agitated carriers (*electrons* & *holes*) is much larger than their lattice constants. It is close to acoustic phonon modes at the zone center of the Brillouin zone, where coupling between electron and acoustic phonons dominates over carrier scattering in the low-energy regime. Therefore, in this limit, carrier mobility can be effectively derived from the effective mass and the deformation potential approximation. Moreover, this approach has been extensively used[296], [360]–[362] to study charge carrier mobility in 2D materials using the relation: $\mu(mobility) = 2e\hbar^3 C_{2D}/3k_BT|m^*|^2E_{2D}^2$, where the in-plane elastic stiffness constant is designated as C_{2D}, effective mass as m^* in units of the rest mass of an electron (m_o), acoustic phonon limited deformation potential as E_{2D}, and relaxation time as $\tau = m^*\mu/e$.

Table 5.2. Charge Carrier Mobility (μ) at T = 300 K for Electrons (μ_e) and Holes (μ_h) along zz and ac Lattice Directions, Elastic Stiffness Constant (C_{2D}), Carrier Effective Mass (m*, in units of rest mass of an electron, m_o), Acoustic Phonon Limited Deformation Potential (E_{2D}), and Relaxation Time (τ) for a Pristine Monolayer MoS_2 Nanosheet.

carrier type	C_{2D} (N/m)	m^* (m_o)	E_{2D} (eV)	μ ($cm^2.V^{-1}.s^{-1}$)	τ (fs)
e(zz)	134.9	0.468	-10.94	73.08	19.42
h(zz)	134.9	0.57	-5.84	172.88	55.97
e(ac)	134.9	0.468	-11.84	62.39	16.58
h(ac)	134.9	0.57	-5.58	189.37	61.31

The mobility of electron (μ_e) and hole (μ_h) calculated at 300 K is found to be highly anisotropic under uniaxial strain applied along zigzag and armchair directions, respectively. The strain-free, pristine ML-MoS_2 nanosheet shows higher electron mobility (73.08 $cm^2.V^{-1}.s^{-1}$) along the *zz* direction as compared to the *ac* direction (62.39 $cm^2.V^{-1}.s^{-1}$) as shown in Table 5.2. Under uniaxial tensile strain, μ_e decreases along the *zz*-direction, whereas μ_e increases along the *ac*-direction up to 3% of strain and then drops smoothly. However, the extent of decrement is not considerable under the tensile strain along the *ac*-direction as compared to the *zz*-direction, as shown in Figure 5.5 (a).

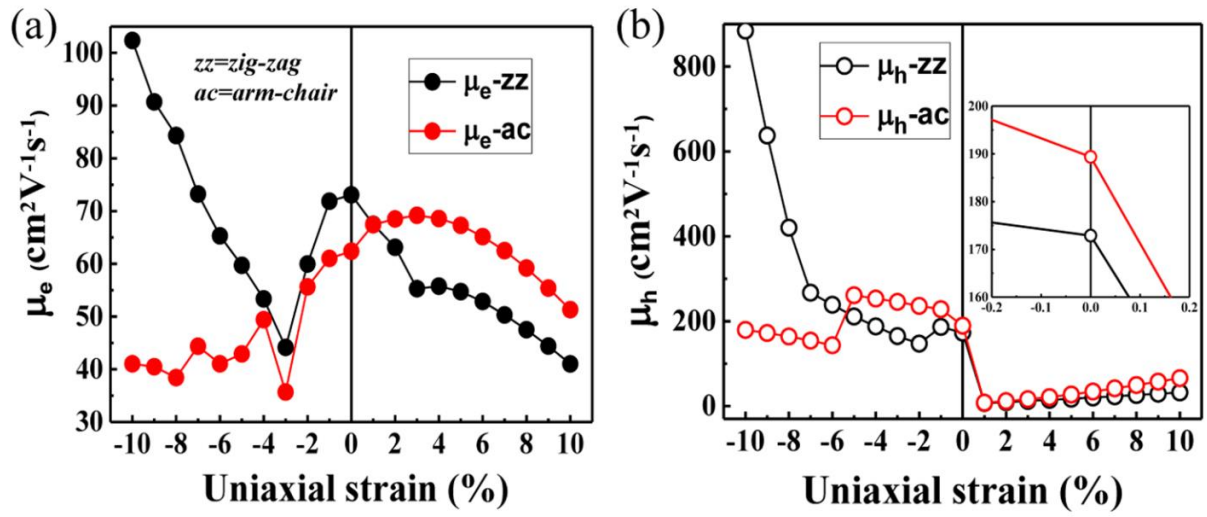

Figure 5.5. Charge carrier mobilities under lattice deformation. (a, b) Mobility of electrons (μ_e)

and holes (μ_h) along the zigzag (zz) and armchair (ac) lattice directions, respectively. (*Inset*: a closeup to show higher hole mobility along the ac direction as compared to the zz direction).

While under the compressive strain along the *zz*-direction, a significant rise in μ_e has been observed after a sharp drop at 3% compressive strain. This is attributable to the lowering of the bandgap for compressive strain greater than 3%, while the bandgap remains direct up to 7%. However, along the *ac*-direction, the same drastic drop occurs again at 3% strain. After that, a damped oscillatory behavior has been observed for compressive strain greater than 3%. The abrupt drop in μ_e at 3% compressive strain along both the directions may be potentially utilized in designing switches where the unstrained and pristine ML-MoS_2 nanosheet will serve as the on-state, while the same under 3% compressive uniaxial strain will function as the off-state of the device. Hole mobility (μ_h) turns out to be higher along the *ac* direction than along the *zz*-direction, as shown in the inset of Figure 5.5 (b) and in Table 5.2 for a pristine sheet. Under a uniaxial tensile strain of 1%, μ_h falls sharply from its unstrained, pristine value along both the directions, as shown in Figure 5.5 (b). This occurs due to the fact that under ≥ 1% uniaxial tensile strain, the top of the valence band switches from *K* point to *Γ* point in the Brillouin zone, whereas the bottom of the conduction band remains around the *K* point, thereby making the system an indirect bandgap semiconductor. The drastic drop in hole mobility (μ_h) at 1% tensile strain can be exploited in developing switches. For tensile strain exceeding 1%, μ_h increases along both the *zz*- and *ac*-direction with respect to μ_h at 1% tensile strain; however, the rate of increase is higher along the *ac* direction. Upon compression, μ_h rises along the *zz*-direction, while it declines along the *ac* direction. Compressive strain along the *zz*-direction is effectual in enhancing the mobility of both of the carriers. As the hole mobility is much higher than the electron mobility, a metal with a high work function may be used as contacts/leads to lower the Schottky barrier and, in turn, the contact resistance. As carrier mobility is found to increase under the uniaxial compressive strain along the zigzag direction, ML-MoS_2 serving as

the channel material needs to interface the electrodes on either side along its zigzag directions. The zigzag direction along the channel length would be favorable for the conduction of both types of carriers.

5.4 CONCLUSIONS

A systematic investigation of the nanopiezotronic response of ML-MoS_2 nanosheet to different modes of applied strain has been performed. Our study shows that shear strain S_1 and uniaxial tensile strain applied along the zigzag direction are most effective in reinforcing the nanopiezoelectric response in ML-MoS_2, which is followed by biaxial tensile strain and uniaxial compressive strain applied along the armchair direction. Polarization-dependent linear response properties, such as Born effective charges ($Z^*_{[B]}$), have been investigated to attribute the change in piezoelectric response to the alteration in the intrinsic polarization vector. The simultaneous variation in piezoelectric and electronic bandgap with the shear strain (S_1) and uniaxial tensile strain along the zigzag direction has been studied to ascertain the optimal strain values where piezoelectricity couples synergistically to the semiconducting properties for the maximal utility of ML-MoS_2 in nanopiezotronic devices. It is found to occur around 4−5% shear strain and about 6−7% uniaxial tensile strain. Furthermore, the variation in carrier mobilities with strain has been addressed. Under the application of uniaxial compressive strain along both the zigzag and the armchair directions, electron mobility drops drastically at 3% strain. Likewise, hole mobility falls abruptly at 1% uniaxial tensile strain along both the zigzag and armchair directions. These behaviors in charge carrier mobility may find useful applications in designing low-power switches. Under uniaxial compressive strain, the charge carrier mobility is found to increase along the zigzag direction. Therefore, the channel material needs to interface the electrodes along the zigzag direction for higher carrier injection. Moreover, ML-MoS_2 has been fortuitously found to be softest (or least stiff) along the zigzag direction, which shows higher strain sustainability and greater elastic limit. Our predictive

findings can facilitate in realizing energy-efficient nanopiezotronic devices by controlling the conversion of mechanical to electrical energy in 2D nanomaterials such as ML-MoS_2.

----------**********----------

Chapter 6

Anomalous lattice vibration in monolayer MoS_2: Breaking the vibrational degeneracy under extreme strain

This chapter is based on the following unpublished work:

Nityasagar Jena, Dimple, Raihan Ahammed, Manish Kumar Mohanta, Ashima Rawat, and Abir De Sarkar*, "*Anomalous lattice vibration in strained monolayer MoS_2: Breaking the vibrational frequency degeneracy under extreme in-plane strain*", ***[In manuscript]***

6.1 INTRODUCTION

In recent years, monolayers of molybdenum disulfide (ML-MoS_2), a well-known member from the Group of semiconducting transition-metal dichalcogenides (MX_2; M = Mo, W, etc.; X = S, Se, or Te) has emerged as one of the perfect semiconductive counterparts to the semi-metallic graphene.[121], [363], [364] Unlike graphene, which is a perfect one-atom-thick honeycomb lattice of carbon atoms. The monolayer crystals of MoS_2 are quasi-2D structures with a covalently bonded lateral sandwich of S-Mo-S atomic layers arranged in a trigonal prismatic molecular geometry.[222], [365] Subject to significant dimensional confinement, a spectrum of novel physical properties arises in ML-MoS_2 that has brought this 2D material into prominence.[366]–[368] Some remarkable attribute of this atomically flat semiconductor is *1)* emergence of an intrinsic direct bandgap (1.8-1.9 eV)[40], [278] at the *K* point of Brillouin

zone (BZ), when scaling down from its host bulk crystal (which is an indirect-gap semiconductor, E_g ~ 1.29 eV)[94], [121]; *2)* a dramatic increase in photoluminescence (> 10^4 -fold) than that of bulk MoS_2[121]; *3)* endurance to a large elastic mechanical deformation (> 6-11%) without structurally falling apart[166], and last but not least *4)* novel coupled spin-valley physics, such as Spin-Hall & Valley-Hall effects with the explicit breaking of crystal inversion symmetry in their monolayer lattices.[259], [368], [369] Besides, due to an excellent pliancy of its metal-chalcogen (Mo-S) covalent bonding, the semiconducting gap of ML-MoS_2 is highly strain sensitive, and capable of being modulated further via external perturbations, such as external mechanical strain (0-10%).[205], [280], [310], [370] The elastic strength and mechanical failure of free-hanging ML-MoS_2 membrane have recently experimented under a scanning probe (AFM nanoindentation set-up), where highly crystalline sheets of MoS_2 suspended over the substrate pre-patterned shallow depressions.[371], [372] The experiment demonstrates a high effective in-plane stiffness of 180±60 $N.m^{-1}$, while the breaking (or elastic failure) occurs close to 11% of lattice deformation for pure and defect-free samples.[166] This ultrahigh mechanical strength in ML-MoS_2 provides an unprecedented opportunity to modify its electronic and optical properties for strain mediated flexible electronics.[205] On the other hand, elastic lattice deformations in ML-MoS_2 are known to drive a direct-to-indirect bandgap transition because of a very low electronic energy offset (~ 20-90 meV) between its indirect and direct transition energies, which occur at a small strain limit of 1-2%.[205], [266], [300], [310] Under extreme strain > 10-11%, a semiconductor-to-metal transition has also been reported in highly strained ML-MoS_2 nanosheets.[283]

Apart from strain-induced tailoring of its semiconducting bandgap and transport characteristics[305], [310], elastic mechanical deformations in ML-MoS_2 has profound effects on its phonon dispersion and vibrational modes.[308], [373] A theoretical investigation of its crystal phonon analysis in response to lattice strain of several types under varying strain scale

(0, ±10%), within the elastic limit bound, can provide microscopic details of its vibrational characteristic for an efficient electronic and thermal management. Recent theoretical and experimental studies have predicted the capability of an anisotropic uniaxial tensile strain towards the breaking of twofold frequency degenerate E_{2g}^{1} vibration of a ML-MoS_2 into E_{2g}^{1+} & E_{2g}^{1-} singly nondegenerate sub-band frequency components with polarization of splitted eigenvectors (E_{2g}^{1+} & E_{2g}^{1-}) orthogonal to one aonther.[205], [369] In an isotropic hexagonal lattice (e.g., ML-MoS_2), this twofold frequency degenerate E_{2g}^{1} vibration can only be lifted under an asymmetric strain-field (i.e., under uniaxial/shear strain), that breaks the underlying hexagonal symmetry and 3-fold triangular symmetry (C_{3v}) of sub-lattices (Mo/S) around a C_3 rotation axis.[205], [278] Using micro-Raman spectroscopy, Conley *et al*.[205] have experimentally demonstrated the influence of a symmetry-breaking uniaxial tensile strain in a single-layer MoS_2. The phonon softening and breaking-off its twofold frequency degenerate, E_{2g}^{1} mode into distinct frequencies (E_{2g}^{1+} & E_{2g}^{1-}) were analyzed in a strain range of 0-2.2%. The study finds, the splitting occurs at 0.8% uniaxial tensile strain with a redshift in both E_{2g}^{1+} and E_{2g}^{1-} nondegenerate phonon modes. This uniaxial tensile strain-induced frequency split-off response was also observed by Wang *et al*.[369] in their experimental study in a uniaxial tensile strain limit of 0-0.71%. However, the direction of applied tension is arbitrarily chosen in these studies.

In a similar study, using polarization-dependent Raman set-up, Wang *et al*.[278] has reported a red-shift (phonon softening) in E_{2g}^{1} mode and polarization response of E_{2g}^{1+} and E_{2g}^{1-} mode in response to an increasing uniaxial tensile strain that could serve as a potential indicator of its crystallographic orientation. Biaxial tensile strain in a strain range of 0-2.5% were analyzed by Lloyd *et al*.[370] in suspended monolayer nanosheets of MoS_2. They found no splitting in the in-plane E_{2g}^{1} mode within the studied range of strain.

Besides, in all these studies, the strain is only limited to the tensile elastic deformation, the effects of compressive strain, and tensile strain of higher magnitude (within its experimental failure limit < 11%[374]) along the mutual orthogonal crystallographic axis, namely; the zigzag (ZZ) and armchair (AC) direction of ML-MoS_2 together with the response of shear strain on its vibrational fingerprints of Raman and IR-active modes have severely been limited in experimental and theoretical phonon studies. Nonetheless, strain in 2D crystals is intrinsic in the process of sample preparation and underlying substrate effects due to incommensurate lattice interactions.[375] In some cases, we also apply stain intentionally to boost the charge carrier mobilities of semiconductors[376], likewise in case of strained silicon technology for microelectronics. Even though the electronic structure modification in ML-MoS_2 from small (< 2%)[205], [308] to an extensive strain limit (> 10%) has been substantiated in scientific literature,[265], [308], [310] yet comprehensive knowledge of various in-plane strain effect on its phonon modes has not been well established.

Therefore, in this work, we set out to perform a full comprehensive *ab initio* study of various in-plane strain effects on lattice dynamics and frequency shift of distinct phonon modes that correspond to the signature Raman and IR – active vibrations of a freestanding ML-MoS_2. Uniaxial (tensile/compressive) strain along ZZ as well as AC lattice direction, together with biaxial (tensile/compressive) strain, in a wide strain range from -10% to +10% have been investigated systematically in this chapter. We also study the response of shear mode of strain, which we have modeled in two distinct ways, the shear strain of type - S_1 & S_2. In S_1 type: simultaneous tensile and compressive strain has been applied along its mutual orthogonal direction, and for S_2 type in an opposite manner. An in-plane symmetry preserving isotropic biaxial strain and symmetry breaking anisotropic uniaxial/shear strain that displaces the sub-lattice positions within the basal plane of a hexagonal lattice symmetrically/asymmetrically along its ZZ or AC crystallographic axis is found to show anomalous frequency variation in

the Raman/IR-active modes. The twofold frequency degenerate in-plane E_{2g}^{1} optical mode splits into E_{2g}^{1+} and E_{2g}^{1-} singly nondegenerate phonon modes, under the application of uniaxial and shear strain, with eigenvectors parallel and perpendicular to the principal strain axis. The splitting occurs due to an increasing lattice anisotropy and consequent anisotropy in the electronic charge density distributions along the applied strain axis and the direction perpendicular to it. Depending on strain type, the anisotropy in electron-phonon interaction with strain-induced electrostatic field shifts the sub-band E_{2g}^{1+} and E_{2g}^{1-} phonon frequencies several tens of cm^{-1} and the separation between them scale with the magnitude of applied strain. The critical strain range to observe such frequency splitting varies between 1-3%, depending on the nature and direction of applied strain. On the other hand, the isotropic planar elasticity of strain-free ML-MoS_2 become anisotropic under the application of uniaxial and shear strain, eventually leading to a strain-dependent anisotropy in Young's modulus (Y) and Poisson's ratio (ϑ) along the mutual orthogonal crystallographic axis, which we have carefully addressed in this work upon considering the lateral Poisson contraction of strained lattices in response to a transverse strain. The uniaxial and shear strain-induced frequency split-off response in the IR-spectra is found to be more sensitive than the Raman-spectra at a lower critical strain range of ~ 1-2%. We believe, together with Raman spectra, IR spectral response of a strained ML-MoS_2 can provide a rapid characterization technique to measure the amount of lattice anisotropy in an isotropic hexagonal honeycomb lattice (e.g., ML-MoS_2). To our best interest, new Raman (E_{2g}') and IR-active (A_{1g}') vibrations start to appear in the frequency spectrum under extreme values of lattice deformations (8-10%). The appearance of new phonon modes in the frequency spectrum is due to a substantial modification in the crystal symmetry and orbital overlap effects due to a colossal change in charge density and electrostatic potential asymmetry over the vibrating ions (Mo/S). The Grüneisen parameter (γ_m) and shear deformation potentials (β_m) of corresponding Raman and IR-active vibrations have also been derived for all strain types. Our

systematic, comprehensive *ab initio* study is of fundamental scientific interest to characterize ML-MoS_2 under extreme strain (0 ~10 %), for monitoring its several crystal phonon responses with a future aspiration to a flexible ML-MoS_2 based adaptable phononic and nanoelectromechanical system.

To the best of our known knowledge, a systematic Raman and IR-spectral monitoring of distinct phonon modes of ML-MoS_2, and the frequency splitting of its twofold degenerate E_{2g}^1 mode into E_{2g}^{1+} & E_{2g}^{1-} nondegenerate singlets, under various in-plane strain geometry, in a broad strain range of -10% to +10% do not exist in the present scientific literature. Thus, our study provides a first-time comprehensive description in this respect.

6.2 COMPUTATIONAL DETAILS

Plane-wave pseudopotential methods have been used to carry out the computation of equilibrium and strain structures of ML-MoS_2 based on spin-polarized density functional theory (DFT) within the framework of projector augmented-wave (PAW)[252], [377] for electron-ion interaction as implemented in the Vienna *ab initio* Simulation Package (VASP; *version* 5.4.4).[250], [291], [292], [378], [379] The generalized gradient approximation (GGA) for the exchange-correlation functionals in its Perdew-Burke-Ernzerhof (PBE)[293] parametrization were employed for the expansion of Kohn-Sham wavefunctions in a plane-wave basis. The electronic and ionic energy cutoff was set at 500 eV in the optimization steps. An orthorhombic supercell was constructed from the equilibrium primitive hexagonal lattice of ML-MoS_2, as shown in Figure 6.1(a), for a systematic strain-engineering of monolayer lattice. A sufficient empty space, at least > 18 Å, was introduced along the lateral direction (i.e., along its *c* axis) to avoid any unwanted interaction with its periodic replicas in a periodic boundary condition (PBC), thereby, effectively isolating a freestanding ML-MoS_2 structure. In an orthorhombic cell, the zigzag (ZZ) and armchair (AC) axis are independent. Thus, a pure

uniaxial strain can be applied along one of the lattice directions (i.e., ZZ/AC) without affecting the other lattice direction. We have applied uniaxial tensile and compressive strain along ZZ as well as AC direction in a strain range of 0 to ±10% (+ tensile, and - compressive). A symmetry-preserving biaxial tensile/compressive strain (hydrostatic) has been realized by symmetrically stretching/compressing the lattice vectors isotopically in the same strain scale. Whereas the shear strain, which preserves the area of the unit cell was modeled in two distinct ways, the S_1-type: where tensile strain is along the ZZ axis, and the compressive strain was along the AC axis, S_2-type: tensile strain along the AC axis and compressive strain along the ZZ axis. The strain is applied by scaling the lattice vectors along *a* and *b* axis, while under strain, the atomic coordinates of strained lattices were fully relaxed to minimize the total energy and inter-atomic forces on strained supercells in a manner similar to the other theoretical studies.[283], [296] An energy convergence tolerance of 1 x 10^{-6} eV with a Γ – centered 16 x 9 x 1 *k* mesh was considered for the electronic energy minimization using the conjugate gradient technique until the forces on individual atoms reach to a value < 1 x 10^{-3} eV/Å. Phonon dispersion and phonon eigenvectors of vibrational modes of equilibrium and strained lattices were evaluated from the interatomic force constants (IFC) using a linear response theory: DFPT methods implemented within the VASP[380], and the same is interfaced with PHONOPY[381] for the post-processing of results from the elements of second-order harmonic force constant matrix. In all cases, the Raman and IR-spectra are fitted with a Lorentzian with a frequency smearing of 1.2 cm^{-1}.

6.3 RESULTS AND DISCUSSION

We organize the result and discussion section of this chapter into the following subsections. In Sec. 6.3.1; phonon dispersion, phonon density of states (phDOS), Raman, and IR-spectra of a strain-free equilibrium ML-MoS_2 lattice have been presented. In Sec. 6.3.2, the spectral evolution of Raman modes for different strain geometries have been provided. In Sec.

6.3.3, we provide the spectral evolution in the IR modes and the corresponding frequency variation as a function of lattice strain. Sec. 6.3.4, describes the anisotropy in 2D elastic properties by the application of a symmetric (biaxial)/asymmetric (uniaxial & shear) lattice deformation. Essential observations have been concluded at the end of this chapter.

6.3.1 Phonon dispersion and vibrational modes of pristine ML-MoS_2

As a starting point, we first investigate the phonon dispersion and phonon density of states (*ph*DOS) of a strain-free ML-MoS_2 and identify the symmetry of different phonon modes at the Brillouin zone (BZ) center (i.e., Γ-point). Figure 6.1(a)-6.1(b) shows the top and side view representation of a freestanding ML-MoS_2. The 6-atom or 2-molecular units of MoS_2 within a rectangular supercell is constructed from its 3-atom equilibrium primitive hexagonal lattice, as shown in Figure 6.1(a).[382] The optimized lattice parameters and inter-atomic bond distances are in excellent quantitative agreement with earlier DFT studies using a similar level of computational setting.[283], [382]

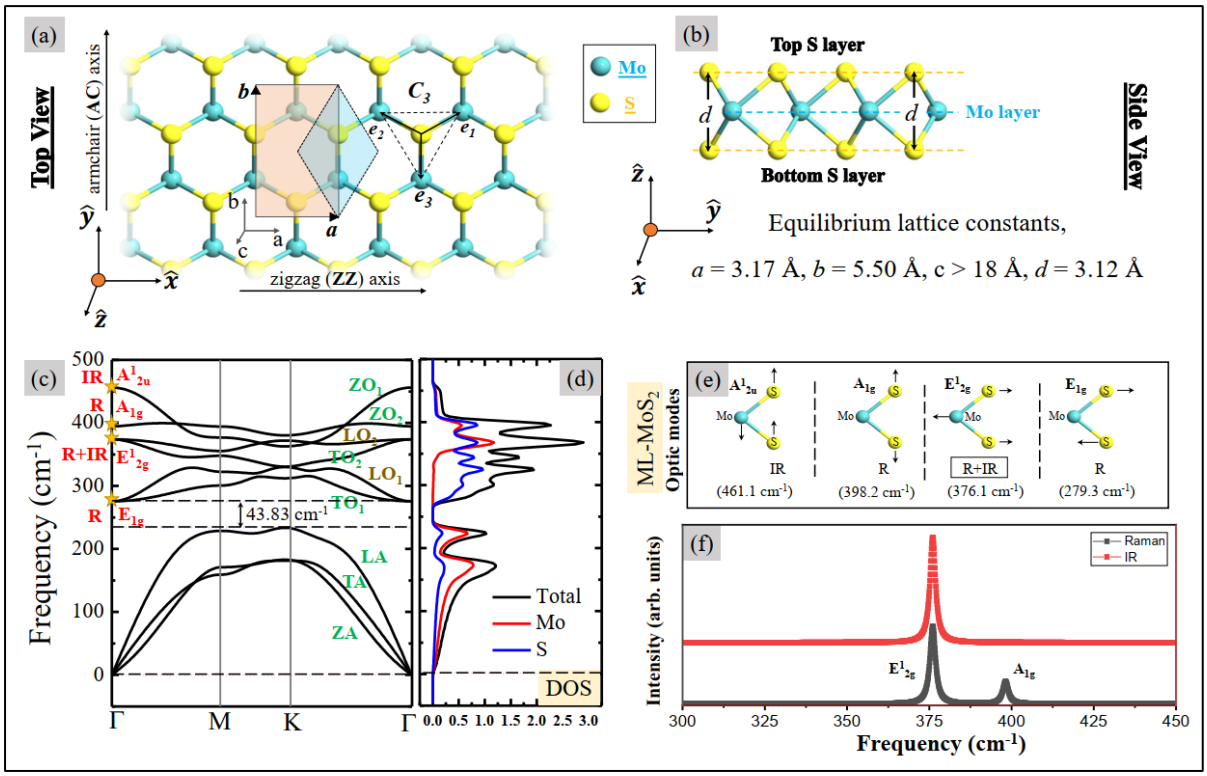

Figure 6.1. (a)-(b) Top and side view schematic of monolayer MoS_2 (ML-MoS_2) in a primitive hexagonal unit cell (green shade) and rectangular supercell (yellow shade) with equilibrium lattice parameters. (c) Phonon dispersion, (d) phonon density of states (phDOS) with symmetry assignment of different phonon eigenvectors at the Brillouin zone center (Γ-point) determined via DFPT. The acoustic and optic phonon branches are labeled as per their standard symmetry representations. (e) Atomic displacements of Raman and IR-active modes of pristine ML-MoS_2, and (f) shows the representative Raman and IR-spectra of a freestanding ML-MoS_2 in a Lorentzian fit with a peak smearing of 1.2 cm^{-1}.

Figure 6.1 (c-d) shows the representative phonon dispersion and phDOS of a strain-free ML-MoS_2 in a primitive hexagonal lattice. We find a total of nine phonon branch within the first-BZ that comprise of 3 acoustic and 6 optic phonons. The phonon branches are labeled as per their polarization symmetry assignment of vibrational eigenvectors in Figure 6.1(c). The high-energy LA/TA mode exhibit a linear dependency with wavevector q close to the BZ center (Γ point); whereas, the low-energy ZA mode shows a quadratic dependency (q^2 relation), and is a signature of D_{3h}^1 point group symmetry of the 2D hexagonal lattice, such as graphene, silicene.[383] The lower branch of optic phonon at Γ is well separated from the highest of its acoustic phonon at K point by an indirect phononic energy gap of ~ 43.83 cm^{-1} ($\Delta\omega$). A large frequency gap ($\Delta\omega$) within the phonon spectrum is due to a higher crystal symmetry and large atomic mass difference between the cation (Mo) & anion (S). This apparently protects the vibrations of acoustic phonons from being scattered by its optical phonons, thereby, effectively reduces the number of phonon scattering events in pristine ML-MoS_2. The phonon dispersion and phDOS, as shown in Figure 6.1(c-d) are in good agreement with earlier *ab initio* studies on ML-MoS_2.[373], [384] Figure 6.1(e) shows the atomic displacements of phonon eigenvectors of various optical modes near the Γ point that corresponds to the characteristic Raman and IR-active vibrations of a strain-free ML-MoS_2. The factor group analysis of a non-

centrosymmetric D_{3h}^{1} crystal lattice recognizes 3 Raman-active and 2 IR-active vibrations within the phonon dispersion. A detail discussion related to the polarization symmetry assignment of different phonon branches and their corresponding vibrational eigenvectors is well established in the previous scientific literature.[373], [383] The high-frequency A_{2u}^{1} mode is purely IR-active vibration with Mo and S atoms vibrating along the lateral direction in anti-phase to one another, whereas, the twofold degenerate E_{2g}^{1} mode (polar TO_2 - LO_2 phonon mode) is both Raman and IR-active, and attribute to a broken lattice inversion crsyal such as ML-MoS_2. This anti-parallel atomic displacement of Mo and S atoms in E_{2g}^{1} mode induces planar dipole moment within the basal plane, thus, lead to an anomalous phonon electric field coupling in strained lattices of polar semiconductors (e.g. ML-MoS_2). Whereas, the out-of-plane A_{1g} vibration and the low-energy E_{1g} optic mode are purely Raman-active vibrations with atomic motions involving only the displacements of S atoms along the out-of-plane direction (for the former) and within the basal plane (for the latter) in counter-phase with respect to the top/bottom S-layers, as pictorially depicted in Figure 6.1(e).

In pristine ML-MoS_2, the twofold degenerate E_{2g}^{1}-mode (in-plane vibration) and the nondegenerate A_{1g}-mode (out-of-plane vibration) are two most prominent signature Raman-active vibrations that are mainly observed in a typical backscattering micro-Raman spectroscopy.[205], [278] In our DFPT study, the first-order nonresonant Raman-active A_{1g}-vibration and the doubly degenerate E_{2g}^{1}-vibration of a freestanding ML-MoS_2 were observed at 398.2 cm^{-1} & 376.1 cm^{-1}, respectively. Our calculation Raman frequencies are very close agreement with that of experimental observations ~ 403±2 cm^{-1} (A_{1g}) and 384±2 cm^{-1} (E_{2g}^{1}), respectively.[22], [205], [385], [386] The deviation of < 1% in the peak frequency position between theory and experiment could possibly due to the different laser wavelength used for the sample excitations in various micro-Raman measurement set-ups[205], [387] or the

inhomogeneity of monolayer membranes on different sample-substrate interfaces via the Van der Waals forces of interactions.[22], [94], [375] Besides, pH conditions during the growth process are found to alter the Raman frequency positions of both the vibrational modes of ML-MoS_2 to an extent ~ 3 cm^{-1}.[388] The A_{2u}^1 IR-mode (461.1 cm^{-1}) and E_{1g} Raman-active vibration (279.3 cm^{-1}) have been excluded from the frequency spectrum in this study, due to their undetectably weak intensity and corresponding phDOS.

6.3.2 Evolution in Raman-spectra under various strain geometry

In a strain-free equilibrium ML-MoS_2 lattice, the in-plane Raman-active E_{2g}^1-mode remains twofold energy degenerate at the Brillouin zone center (at Γ point). The E_{2g}^1 mode associated with two distinct eigenvectors E_{2g}^{1+} & E_{2g}^{1-}, that are mutual orthogonal vibrations in a hexagonal lattice, and remain overlapped in the vicinity of Γ point for a strain-free, equilibrium ML-MoS_2 lattice, or under a symmetry preserving isotropic biaxial strain. When the honeycomb lattice of ML-MoS_2 is subject to an asymmetric lattice displacement, which only occurs in case of a pure uniaxial or shear strain, the hexagonal symmetry of its honeycomb structure gets broken. Thus, the lattice environment becomes anisotropic along the mutual orthogonal crystallographic axis, *i.e.*, along zigzag (ZZ) and armchair (AC) direction of ML-MoS_2. Moreover, the anisotropy scales with the magnitude of applied uniaxial/shear strain due to a gradual reduction in 3-fold sub-lattice rotational symmetry (C_{3v}), and translational symmetry around a given basis. In a honeycomb lattice, like ML-MoS_2, this leads to an anisotropic charge density and potential distribution along its mutual orthogonal crystallographic directions.[283]

Besides, the spatial extent of overlapping orbitals between Mo *d* and S *p* orbitals become different along the strain axis than the direction perpendicular to it, where the wave function of overlapping orbitals (Mo: *d*, S: *p*) become more spread-out along the principal strain

axis.[310], [389] This simultaneous coupling between strain and crystal symmetry has a fascinating consequence for a honeycomb lattice system like ML-MoS_2, where an anisotropic lattice deformation (i.e., uniaxial and shear strain) can lift the vibrational energy degeneracy of its doubly degenerate in-plane E_{2g}^{1} vibration into singly nondegenerate E_{2g}^{1+} & E_{2g}^{1-} sub-bands. The split sub-bands can exhibit anomalous frequency variation, depending on the nature and magnitude of applied strain. This apparent anomalous frequency variation of Raman-active modes can be a valid indicator of the amount and the type of strain present in the lattice when ML-MoS_2 is subject to various strain geometries. For all asymmetric strain cases (i.e., uniaxial and shear strain), the frequency separation between E_{2g}^{1+} & E_{2g}^{1-} mode scales with the magnitude of applied strain-strength with the polarity of eigen vectors E_{2g}^{1+} & E_{2g}^{1-} orthogonal to each other.

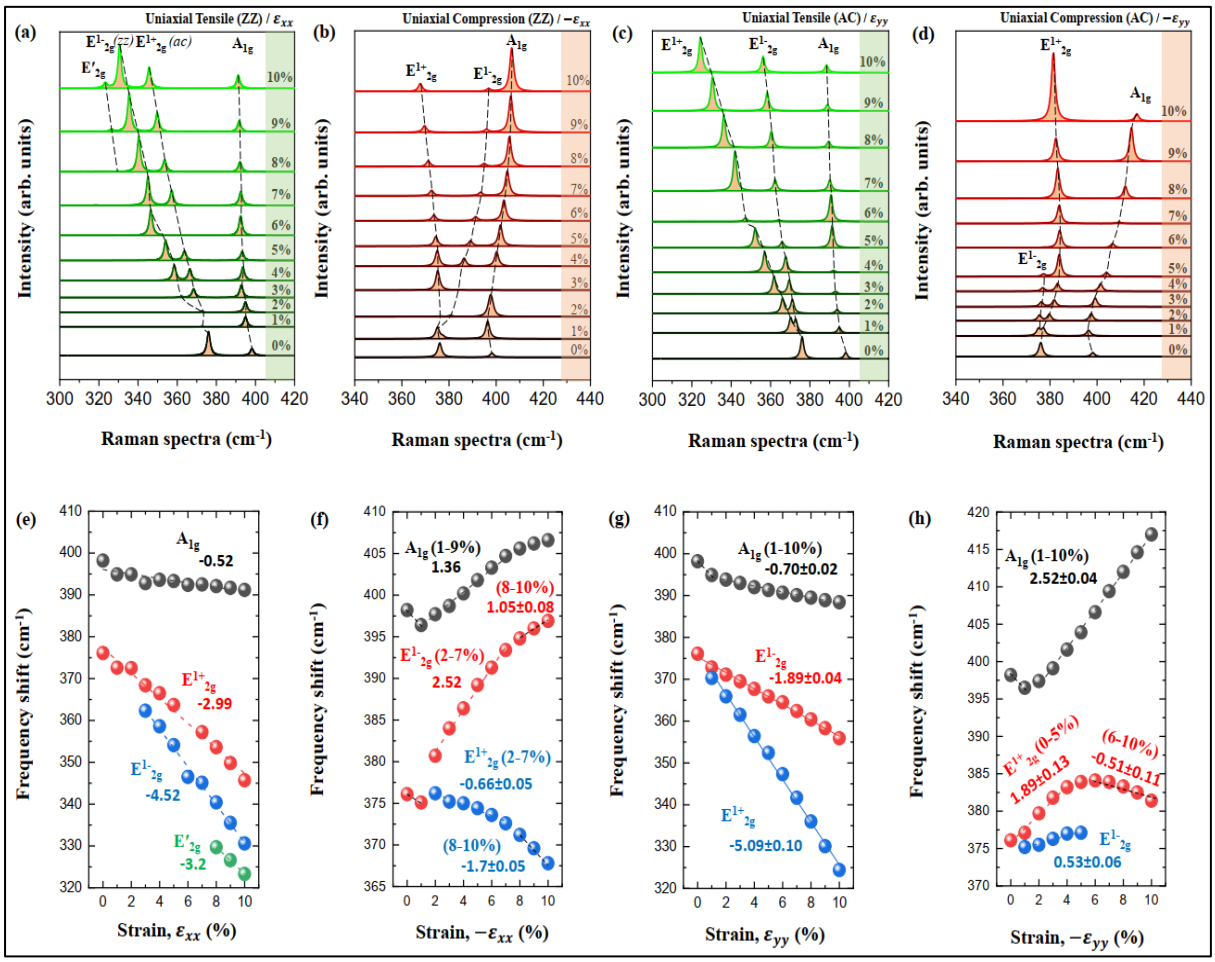

Figure 6.2. (a)-(b) Evolution of Raman spectra as a function of uniaxial tensile (ϵ_{xx}), and compressive ($-\epsilon_{xx}$) strain, when the applied strain is purely only along the ZZ direction of ML-MoS_2, (c)-(d) the same strain along the AC direction. (e)-(h) Functional dependency of Raman peak frequency position under various uniaxial strain condition. The dotted lines are linear fits to the selected portion of the data in order to extract the rates of their frequency variation with applied strain.

Figure 6.2 (a)-(b) shows the evolution of Raman-spectra under uniaxial tensile/ compressive strain, when the applied strain is purely only along its ZZ direction (ϵ_{xx}), and Figure 6.2 (c)-(d) along its AC direction. Under an increasing uniaxial tensile strain (ϵ_{xx} = 0-10%), a clear red-shift (phonon softening of vibrational modes) in both A_{1g} and E_{2g}^{1}-mode has been observed. The overlapped frequency between its twofold degenerate E_{2g}^{1} mode splits into E_{2g}^{1+} and E_{2g}^{1-} singlet sub-bands, at strain higher than 2%, and remain degenerate for smaller strain up to 1-2%. The E_{2g}^{1-} mode red-shifts in a linear regression (-4.52 cm^{-1}/%). The E_{2g}^{1-} mode involves in-plane atomic vibrations along the strain axis (i.e., ZZ direction), thus, experiencing a higher phonon softening than that of E_{2g}^{1+} mode (-2.99 cm^{-1}/%), which vibrates orthogonal to it (along AC direction). The frequency separation between E_{2g}^{1+} and E_{2g}^{1-} modes are found to scale with the applied strain strength, as shown in Figure 2(e), for $\epsilon_{xx} > 2\%$. To our best interest, a new Raman-active mode pop-up in the Raman spectrum under uniaxial tensile strain (ϵ_{xx}) higher than 7%. This additional peak (E'_{2g}) in the Raman spectrum within the same frequency scale is resulting from the atomic oscillations involving the vibration of neighboring chains of S-atoms along the AC direction in counter-phase to one another. At higher strain (8-10%), this new E'_{2g} Raman-active vibration redshifts at a rate of -3.2 cm^{-1}/%. On the other hand, the out-of-plane transverse Raman-active vibration, A_{1g}-mode, does not seems to express a considerable frequency shift (-0.52cm^{-1}/%) even under a considerable uniaxial tensile strain,

ϵ_{xx} = 0-10%. This subtle frequency reduction of A_{1g}-mode is close consistent with the experimental measurements led by Rice *et al*.[390], Wang *et al*.[278] and Conley *et al*[205], thus illustrating the result of our theoretical calculations, are well suited to make a further computational prediction of physical parameters with reasonably well agreement results with that of experimental findings. Besides, under uniaxial lattice compression ($-\epsilon_{xx}$), a significant blue-shift at a rate of 1.36 cm^{-1}/% is observed in the A_{1g} mode. This is due to a large Coulomb screening attended with substantial modification in charge density distribution and the electrostatic potentials over the out-of-plane vibrating S atoms.[283] However, there is no evidence of any frequency splitting in the A_{1g} mode even under a very large uniaxial strain of ±10%. On the other hand, under the uniaxial compressive strain ($-\epsilon_{xx}$), we find a very altered frequency shift in the E_{2g}^{1+} and E_{2g}^{1-} modes with polarity opposite to that of uniaxial tensile strain (ϵ_{xx}), where the E_{2g}^{1+} mode red-shifts at a rate of -0.66 cm^{-1}/% and E_{2g}^{1-} mode blue-shifts at a rate of 2.52 cm^{-1}/% in a compressive strain range of 2-7%. The frequency separation between the E_{2g}^{1+} and E_{2g}^{1-} modes become much wider ~ 30 cm^{-1} when strain ($-\epsilon_{xx}$) reaches a value of 10%. The frequency shift in E_{2g}^{1+} and E_{2g}^{1-} Raman-active mode is very unique to $-\epsilon_{xx}$ strain, therefore, can be persuaded to calibrate ($-\epsilon_{xx}$) strain along its ZZ lattice orientation.

We find a similar frequency splitting in the E_{2g}^{1} mode, when uniaxial tensile strain (ϵ_{yy}) is along the AC lattice orientation [See Figure 6.2 (c)]. But in this case, the splitting is found to occur at a much smaller strain scale of ~ 0-1%, with the polarization of E_{2g}^{1+} & E_{2g}^{1-} mode opposite to that of uniaxial tensile strain (ϵ_{xx}). The A_{1g} mode red-shifts at a rate -0.70±0.02 cm^{-1}/%, which is a bit higher over the same shift along the ZZ direction. While the E_{2g}^{1+} mode redshifts at a much higher proportion at a rate -5.09 cm^{-1}/%, and E_{2g}^{1-} mode at a moderate rate of -1.89 cm^{-1}/%, respectively. The frequency separation between E_{2g}^{1+} and E_{2g}^{1-} mode become significantly wider for ϵ_{yy} strain with several orders of magnitude higher for more significant

strains (> 5%) [See Figure 6.2 (g)], as compared to the same along its ZZ direction (ϵ_{xx}) within the same strain limit. We attribute this wide frequency separation between E_{2g}^{1+} and E_{2g}^{1-} mode with the uniaxial strain-induced electrostatic field in polar semiconductors like ML-MoS_2, where strain along its AC direction induces a crystal dipole moment (polarization, *P*) parallel to the AC axis. The electronic contribution to the dielectric susceptibility becomes higher in the presence of an electrostatic-field that enhances the TO_2 phonon interaction with a static electric field, as compared to its LO_2 phonon that lies along the strain axis. Hence, the coupling of orthogonal E_{2g}^{1+} & E_{2g}^{1-} vibrations with electrostatic-field via phonon electric-field coupling can produce a wider frequency separation between E_{2g}^{1+} & E_{2g}^{1-} -mode in a noncentrosymmetric ML-MoS_2 crystal.

Under uniaxial lattice compression ($-\epsilon_{yy}$) along AC direction, the A_{1g} mode blue-shifts at a significantly higher rate of 2.52±0.04 cm^{-1}/% [See Figure 6.2 (d)]. This is highest for A_{1g} mode under all uniaxial strain types, whereas, the in-plane E_{2g}^{1+} & E_{2g}^{1-} mode distinctly differ in the frequency with opposite polarization to that of tensile strain (ϵ_{yy}) along the AC direction. Furthermore, in sharp contrast to the case of uniaxial compressive strain along ZZ direction ($-\epsilon_{xx}$), here, both E_{2g}^{1+} & E_{2g}^{1-} mode blue shifts under the compressive strain ($-\epsilon_{yy}$) along AC direction. The blue-shift in E_{2g}^{1+} mode (1.89±0.13 cm^{-1}/%) saturates at 5% of lattice compression and then starts to red-shift upon further increase of strain, as seen in Figure 6.2 (h). While the blue-shifts in E_{2g}^{1-} mode occurs at a much lower rate of 0.53 ± 0.06 cm^{-1}/%, and the activity of this mode nearly vanishes beyond 5% strain. This peculiar behavior of E_{2g}^{1+} & E_{2g}^{1-} mode under uniaxial lattice compression along the AC lattice direction has yet to be understood. However, intuitively this is due to the unusual changes in the inter-atomic force constants attended due to a strong Coulomb repulsion between vibrating ions under enormous compressive strain that reinforce the effective harmonic force constants towards the quasi-

harmonic or anharmonic limit. Such anharmonic effects on phonon modes, including the anharmonicity in force constants and anharmonic contribution to the derivative of electric susceptibility in the first-order Raman process, fall outside the scope of our present discussion. Besides, it is noteworthy to mention, in an isolated monolayer crystal, a very high value of lattice compression is impracticable. The nuclear or ion-core effects will start to dominate with neighboring atoms approaching a very close distance under extreme lattice compression. Furthermore, the basal-plane of freestanding monolayers would instead bend/ripple along the *c* axis (along the direction normal to the basal plane) before attaining such high lattice compressions. However, for the sake of completeness, here, we have provided both the tensile/compressive strain in a range from -10% to +10%.

Theoretically, the effect of an arbitrary in-plane strain (ϵ_{ij}) and the corresponding strain effects on the Raman and IR spectra, such as frequency split of degenerate E_{2g}^1 phonon mode and frequency shift ($\Delta\omega/\epsilon$) correlation as a function of applied strain are expressed as follows.

In a two-dimensional crystal, the generic form of strain tensor takes the following form

$$\epsilon_{ij} = \begin{pmatrix} \epsilon_{xx} & \epsilon_{xy} \\ \epsilon_{yx} & \epsilon_{yy} \end{pmatrix} \tag{6.1}$$

In the presence of strain, the secular phonon equation[391], [392] of phonon mode *m* describe the frequency shift rate as,

$$\Delta\omega_m^{\pm}/\epsilon = -\omega_m^0\gamma_m\epsilon_h \pm (\omega_m^0\beta_m\sqrt{\epsilon_s{}^2 + 4\epsilon_{xy}^2})/2 \tag{6.2}$$

Any arbitrary in-plane strain perturbation to a hexagonal lattice is decomposed into a hydrostatic $\epsilon_h = (\epsilon_{xx} + \epsilon_{yy})$, and shear $\epsilon_s = \sqrt{(\epsilon_{xx} - \epsilon_{yy})^2 + 4\epsilon_{xy}^2}$ component, by assuming its planar strain components remain unaffected $\epsilon_{xy} = \epsilon_{yx}$ (verified in elastic stiffness tensor, $C_{12} = C_{21}$), where ϵ_{xx} is the longitudinal strain component parallel to the strain axis and ϵ_{yy}

relative transverse strain resulting from transverse lattice shrinkage or Poisson contraction along the direction perpendicular to the applied strain. ω_m^0 and ω_m are frequency of *m* phonon in the absence and presence of an external strain. Grüneisen parameter (γ_m) and shear deformation potential (β_m) of mode *m*.

For a pure uniaxial strain along the ZZ direction, $\epsilon_{xx} = \epsilon$ (principal strain axis), the resulting transverse strain become $\epsilon_{yy} = -\vartheta\epsilon$. The strain components get reversed for strain applied along the AC direction. ϑ is the Poisson's ratio of a free-standing ML-MoS_2. The frequency shift in the non-degenerate E_{2g}^{1+} and E_{2g}^{1-} modes are expressed by reducing the general phonon secular eqn. (6.2) into the following form:

$$\Delta\omega_{E_{2g}^{1\pm}}/\epsilon = -\omega_{E_{2g}^1}^0 \gamma_{E_{2g}^1}(1-\vartheta) \pm \omega_{E_{2g}^1}^0 \beta_{E_{2g}^1}(1+\vartheta)/2 \tag{6.3}$$

Here, $\omega_{E_{2g}^1}^0$ and $\Delta\omega_{E_{2g}^{1\pm}}$ are the mode shift in twofold degenerate E_{2g}^1 mode in the absence and presence of uniaxial strain (ϵ). From eqn. (3), the Grüneisen parameter ($\gamma_{E_{2g}^1}$), and shear deformation potential ($\beta_{E_{2g}^1}$) under the uniaxial strain along ZZ direction is expressed as

$$\gamma_{E_{2g}^1}(uniax./ZZ) = -(\Delta\omega_{E_{2g}^1}^+/\epsilon + \Delta\omega_{E_{2g}^1}^-/\epsilon)/\,[2\omega_{E_{2g}^1}^0\,(1-\vartheta)] \tag{6.4}$$

$$\beta_{E_{2g}^1}(uniax./ZZ) = (\Delta\omega_{E_{2g}^1}^+/\epsilon - \Delta\omega_{E_{2g}^1}^-/\epsilon)/\,[\omega_{E_{2g}^1}^0\,(1+\vartheta)] \tag{6.5}$$

Considering the Poisson's ratio of free-standing ML-MoS_2 to be 0.248 (from our DFT calculation), and the frequency of E_{2g}^1 mode at equilibrium lattice ($\omega_{E_{2g}^1}^0$ = 376.1 cm^{-1}). The Grüneisen parameter ($\gamma_{E_{2g}^1}$) and shear deformation potential ($\beta_{E_{2g}^1}$) of E_{2g}^1 mode results in 1.3 ($\gamma_{E_{2g}^1}$) and 0.3 ($\beta_{E_{2g}^1}$), respectively, under uniaxial tensile strain (ϵ_{xx}) along ZZ direction, and the same under uniaxial compressive strain ($-\epsilon_{xx}$) become -0.32 ($\gamma_{E_{2g}^1}$) and -0.67 ($\beta_{E_{2g}^1}$),

respectively, by considering the slope of $\Delta\omega/\epsilon$ correlation in a uniaxial compressive strain ($-\epsilon_{xx}$) range of 2-7%.

The Grüneisen parameter ($\gamma_{A_{1g}}$) of singly nondegenerate A_{1g}-mode is defined as

$$\gamma_{A_{1g}}(uniax./ZZ) = -(\Delta\omega_{A_{1g}}/\epsilon\,)/[\omega^0_{A_{1g}}(1-\vartheta)] \tag{6.6}$$

Since only the hydrostatic component of stress is present, the A_{1g} Raman-active vibration does not split, and the shear deformation potential cannot be evaluated for the A_{1g} mode. Using the equilibrium phonon frequency of A_{1g} mode 398.2 cm^{-1}, the Grüneisen parameter ($\gamma_{A_{1g}}$) become 0.17 for uniaxial tensile strain (ϵ_{xx}) along the ZZ direction and -0.46 for uniaxial compressive strain ($-\epsilon_{xx}$).

Since the Grüneisen parameter ($\gamma_{E^1_{2g}}$) and shear deformation potential ($\beta_{E^1_{2g}}$) is a measure of lattice anharmonicity of interatomic potentials, the corresponding values along the AC direction would be a comparable measure. The same relation, as in eqn. (6.4)-(6.5) remain valid for uniaxial strain along its AC direction with a sign change in $\gamma_{E^1_{2g}}$ and $\beta_{E^1_{2g}}$, as the strain components get reverse for uniaxial strain along the AC direction, where $\epsilon_{yy} = \epsilon$ and $\epsilon_{xx} = -\vartheta\epsilon$. The Grüneisen parameter ($\gamma_{E^1_{2g}}$) and shear deformation potential ($\beta_{E^1_{2g}}$) for uniaxial tensile strain (ϵ_{yy}) along AC direction become -1.23 ($\gamma_{E^1_{2g}}$) and 0.68 ($\beta_{E^1_{2g}}$), respectively, where the $\gamma_{E^1_{2g}}$ along AC direction is comparable to that of uniaxial tensile strain (ϵ_{xx}) along ZZ direction, but the shear deformation potential is got almost doubled. Thus, a large shear deformation occurs when tensile strain is along the AC direction; the same is confirmed in our elasticity study in a subsequent section. The Grüneisen parameter ($\gamma_{A_{1g}}$) for A_{1g}-mode also changes sign for strain along AC direction, and become -0.23 for uniaxial tensile strain (ϵ_{yy}) along AC direction. Under compressive strain ($-\epsilon_{yy}$) along AC direction, the Grüneisen

parameter ($\gamma_{E^1_{2g}}$) and shear deformation potential ($\beta_{E^1_{2g}}$) of E^1_{2g} vibrational mode becomes 0.42 ($\gamma_{E^1_{2g}}$) and -0.28 ($\beta_{E^1_{2g}}$), respectively, that is much lower in values as compared to the (ϵ_{yy}) strain case, as both E^{1+}_{2g} and E^{1-}_{2g} mode blue-shifts under uniaxial lattice compression. While the Grüneisen parameter ($\gamma_{A_{1g}}$) for A_{1g} mode under compressive strain ($-\epsilon_{yy}$) become 0.84, that is much higher over the corresponding tensile strain (ϵ_{yy}) along the AC direction.

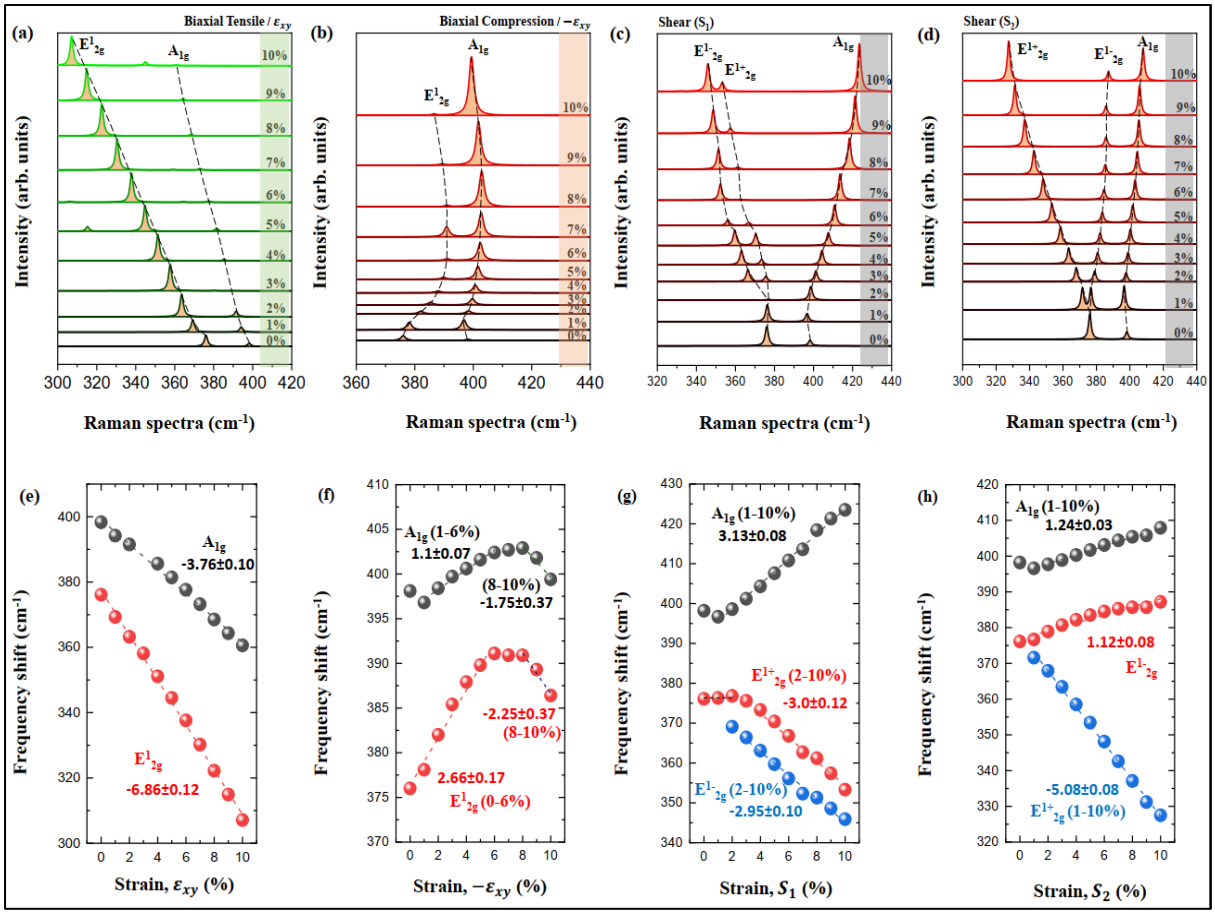

Figure 6.3. (a)-(b) Evolution of Raman-spectra under biaxial tensile (ϵ_{xy}) and compressive ($-\epsilon_{xy}$) strain. (c) Raman spectrum under the shear strain of type, S_1, and (d) for type, S_2. (e-h) The corresponding Raman peak frequency variation for different biaxial/shear strain geometries. The biaxial strain does not break the frequency degeneracy of E^1_{2g} mode, due to its isotropic nature of the strain-field.

We now turn our discussion towards the effect of biaxial and shear mode of strain over the frequencies of Raman-active vibrations. Figure 6.3 (a)-(b) shows the evolution of Raman spectra under biaxial tensile/compressive strain. Under an isotropic biaxial strain field, the twofold energy degenerate E^1_{2g}-mode does not split into individual components and remains degenerate even up to a sizeable biaxial strain of 0 to ±10%, at the zone-center (Γ point). The isotropic biaxial strain-field that preserve the underlying hexagonal symmetry of ML-MoS_2 holds the two-fold degenerate E^1_{2g} mode at a single phonon frequency. Thus, the frequency of two-fold degenerate E^1_{2g} vibration remain protected (overlapped) under the isotropic biaxial strain. However, the Raman characteristic of the mode E^1_{2g} & A_{1g} show a collective phonon softening (or hardening) upon the increase (or decrease) of biaxial strain % [See Figure 6.3 (a)-(b)]. The frequency shift response under biaxial strain is similar to the experimental observation led by Lloyd *et. al.*[370] for suspended nanosheets of ML-MoS_2.

Under biaxial tensile strain (ϵ_{xy}), the out-of-plane A_{1g} and the in-plane degenerate E^1_{2g} mode significantly downshift in frequency in a perfect linear regression at a rate of -3.76 ± 0.10 cm^{-1}/% and -6.86 ± 0.12 cm^{-1}/%, respectively. The frequency shift in both A_{1g} and E^1_{2g} mode are found to be the highest under biaxial tensile strain (ϵ_{xy}) among all strain types studied in this work. This is because of a rapid changing geometry (Mo-S bond length and S-Mo-S angle) under biaxial strain mode [283], [308] that implies; biaxial tension has a combined effect of individual uniaxial strains along its respective orthogonal crystallographic axis (i.e., ZZ/AC). While under biaxial compressive strain (-ϵ_{xy}), both A_{1g} and E^1_{2g} mode blue-shifts upto 6% of strain at rates, A_{1g} (1.1 ± 0.07 cm^{-1}/%) and E^1_{2g} (2.66 ± 0.17 cm^{-1}/%), respectively, which then starts to red-shift upon further increase of strain (> 6%).

In the case of isotropic biaxial strain, the transverse and longitudinal strain components are the same $\epsilon_{xx} = \epsilon_{yy} = \epsilon$, hence, no shear deformation potential and no frequency splitting

in degenerate E_{2g}^1-mode is noticed, the Grüneisen parameter under biaxial strain is expressed as

$$\gamma_{E_{2g}^1}(biax.) = -\frac{1}{2\epsilon}\frac{\Delta\omega_{E_{2g}^1}}{\omega_{E_{2g}^1}^0} \tag{6.7}$$

And for A_{1g} mode,

$$\gamma_{A_{1g}}(biax.) = -\frac{1}{2\epsilon}\frac{\Delta\omega_{A_{1g}}}{\omega_{A_{1g}}^0} \tag{6.8}$$

The absence of shear deformation potential under the isotropic biaxial strain leaves the Grüneisen parameter-free from any Poisson term in it. Using the eqn. (6.7)-(6.8), the Grüneisen parameter ($\gamma_{E_{2g}^1}$) of E_{2g}^1 mode becomes 0.91 and for A_{1g} mode 0.47, respectively. And the same for biaxial compressive strain ($-\epsilon_{xy}$) within the linear blue shift region up to 7% strain becomes -0.35 ($\gamma_{E_{2g}^1}$) and -0.13 ($\gamma_{A_{1g}}$), respectively.

Due to a reduction in underlying hexagonal symmetry and anisotropy in strain-field, shear strains (S_1 & S_2) are found to have similar effects on the frequency of E_{2g}^1 mode similar to that of uniaxial strain. However, the phonon modes shift in a different proportion under the shear strain of type- S_1 and S_2. Under the shear strain of S_1-type, the A_{1g} mode blue-shifts at a much higher rate of 3.13 ± 0.08 cm^{-1}/% than the shear strain of S_2-type (1.24 ± 0.03 cm^{-1}/%). The in-plane doubly degenerate E_{2g}^1 mode splits into E_{2g}^{1+} and E_{2g}^{1-} components under the shear strain of both S_1 and S_2 type. For S_1 strain, the E_{2g}^{1+} mode red-shifts at a rate -3.0 ± 0.12 cm^{-1}/%, and the atomic displacement of this vibration (E_{2g}^{1+}) is along the AC direction of ML-MoS_2 and the E_{2g}^{1-}-mode that also red-shifts in a nearly similar rate of -2.95 ± 0.10 cm^{-1}/%, due to a simultaneous presence of tensile/compressive deformation within the lattice. Under the shear S_2 strain, the E_{2g}^{1+} mode red-shifts at a much higher rate of -5.08 ± 0.08 cm^{-1}/% as compared to

S_1 strain, while the E_{2g}^{1-} mode blue-shifts at rate 1.12 ± 0.08 cm^{-1}/% under the shear S_2 strain. The frequency separation between E_{2g}^{1+} mode & E_{2g}^{1-} mode almost get doubled under shear S_2 strain to that of uniaxial strain ($-\epsilon_{xx}$). This anomalous behavior is attributed to the anharmonic contributions to the interatomic potentials under the application of shear strain.

6.3.3 Evolution in IR-spectra under various strain

Experimental studies on IR spectra are relatively sparse than that of Raman spectra on ML-MoS_2. This is partly due to its limited spatial resolution and low cross-section. However, the IR-active modes in ML-MoS_2 are critical in interpreting the structural information from its phonon signatures similar to that of Raman active vibrations under strain. The twofold degenerate E_{2g}^{1} Raman-active mode of a pristine strain-free ML-MoS_2 is also IR-active, due to the missing lattice inversion symmetry in its monolayer structure. For simplicity, we assign E_{2g}^{1} Raman-active denotation for IR-active mode as E_{2u}^{1}.

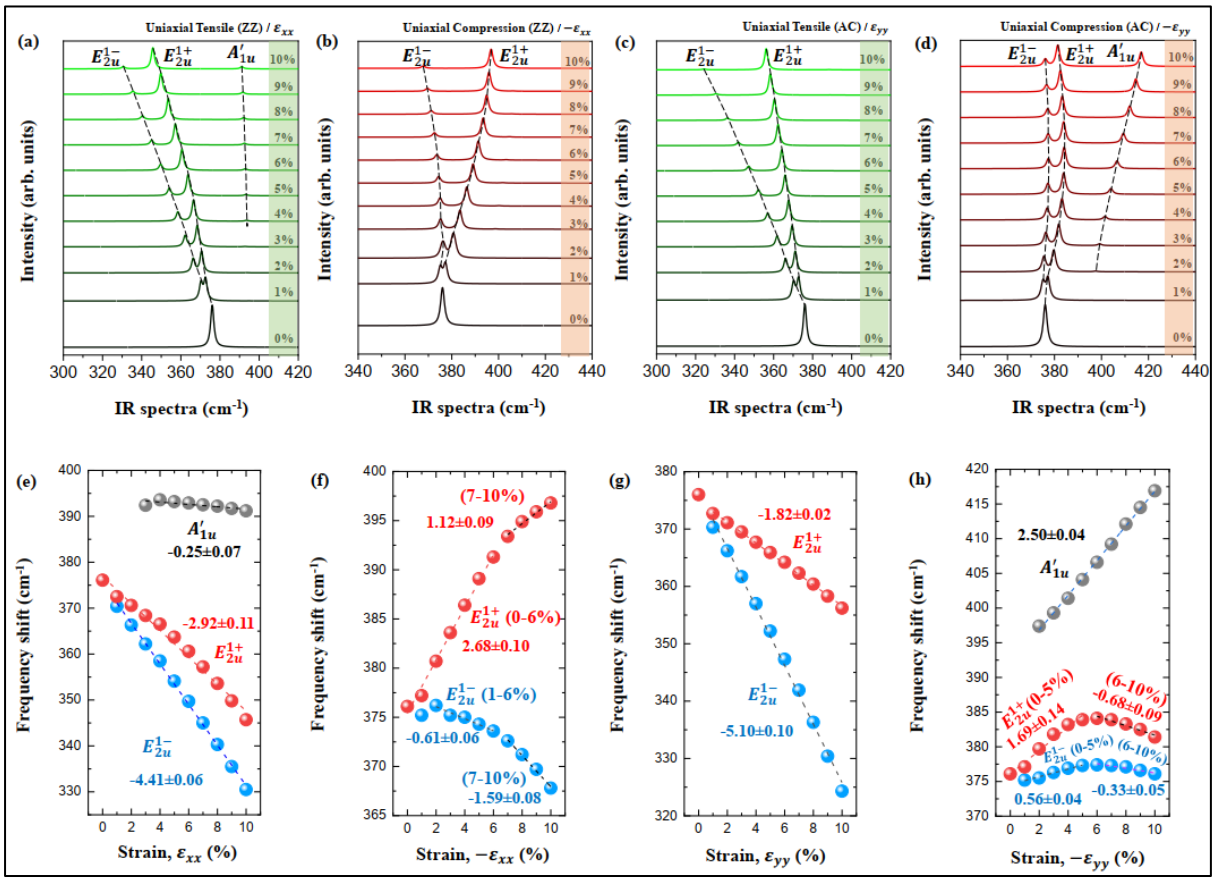

Figure 6.4. (a)-(b) Evolution in IR spectra under uniaxial tensile (ϵ_{xx}) and compressive ($-\epsilon_{xx}$) strain when the applied strain is only along the ZZ axis of ML-MoS_2, (c)-(d) IR spectra when the same strain is along the AC direction (ϵ_{yy} and $-\epsilon_{yy}$). (e)-(h) Frequency shift in the corresponding IR active modes as a function dependent on uniaxial lattice strain.

Figure 6.4 (a)-(b) shows the spectral evolution of its IR –active vibration under uniaxial tensile strain (ϵ_{xx}), when strain is purely only along the ZZ direction. We see a similar frequency splitting in the E_{2u}^{1} IR-active mode that splits into the E_{2u}^{1+} and E_{2u}^{1-} sub-band frequencies even at a very small uniaxial strain of 0-1%, while the same splitting in Raman spectra were observed at a uniaxial tensile strain range of 2-3%. Both E_{2u}^{1+} and E_{2u}^{1-} modes are found to red-shift at a rate -2.92 ± 0.11 cm^{-1}/% (E_{2u}^{1+}), and -4.41 ± 0.06 cm^{-1}/% (E_{2u}^{1-}) with an increase of strain (ϵ_{xx}) from 0-10% [See Figure 6.4 (e)]. Remarkably, new IR-active vibrations (A_{1u}') start to appear at 4-10% of tensile (ϵ_{xx}) strain with a smaller red-shift -0.25 ± 0.07 cm^{-1}/% in A_{1u}' vibration. Under the compressive uniaxial strain ($-\epsilon_{xx}$), the E_{2u}^{1+} mode blue-shifts at a rate of 2.68 ± 0.10 cm^{-1}/% in a strain range of 0-6% and at a rate of 1.12 ± 0.09 cm^{-1}/% in the strain range 7-10%, whereas the E_{2u}^{1-} mode red-shifts at a lower rate of -0.61 ± 0.06 cm^{-1}/% in the range 1-6% and at a rate -1.59 ± 0.08 cm^{-1}/% in the strain range of 7-10%. We do not find any new IR-active vibrations under $-\epsilon_{xx}$ strain. A similar red-shift of E_{2u}^{1+} and E_{2u}^{1-} vibrations have also been observed for uniaxial tensile strain along the AC direction (ϵ_{yy}) with a steep variation in the frequency of E_{2u}^{1-} mode, at a rate of -5.10 ± 0.10 cm^{-1}/%, and E_{2u}^{1+} mode at a lower rate of -1.82 ± 0.02 cm^{-1}/% with the appearance of no new IR-active modes on the same frequency scale. However, under $-\epsilon_{yy}$ strain, a new IR-active mode (A_{1u}') starts to appear in the IR-spectra with a raise in peak intensity that blue-shift at a rate of 2.50 ± 0.04 cm^{-1}/% with the increase in strain from 2-10%. Whereas, the E_{2u}^{1+} and E_{2u}^{1-} modes also found to show a blue-shift in frequency at a rate of 1.69 ± 0.14 cm^{-1}/% (for E_{2u}^{1+}) and 0.56 ± 0.04 (for E_{2u}^{1-})

cm^{-1}/%, respectively, up to a strain range of 0-5%. Upon further increase of $-\epsilon_{yy}$ strain > 5%, the E_{2u}^{1+} and E_{2u}^{1-} mode starts to red-shift at a rate -0.68 ± 0.09 cm^{-1}/% and -0.33 ± 0.05 cm^{-1}/%, respectively. The IR-active modes of ML-MoS_2 are found to be more responsive at a lower critical strain than the Raman modes towards the lattice anisotropy by the breaking of its frequency degeneracy of modes and the emergence of new Raman/IR-active vibrations. Therefore, the strain-dependent spectral response of IR-active modes could be an effective indicator for strain monitoring in a monolayer MoS_2 crystal.

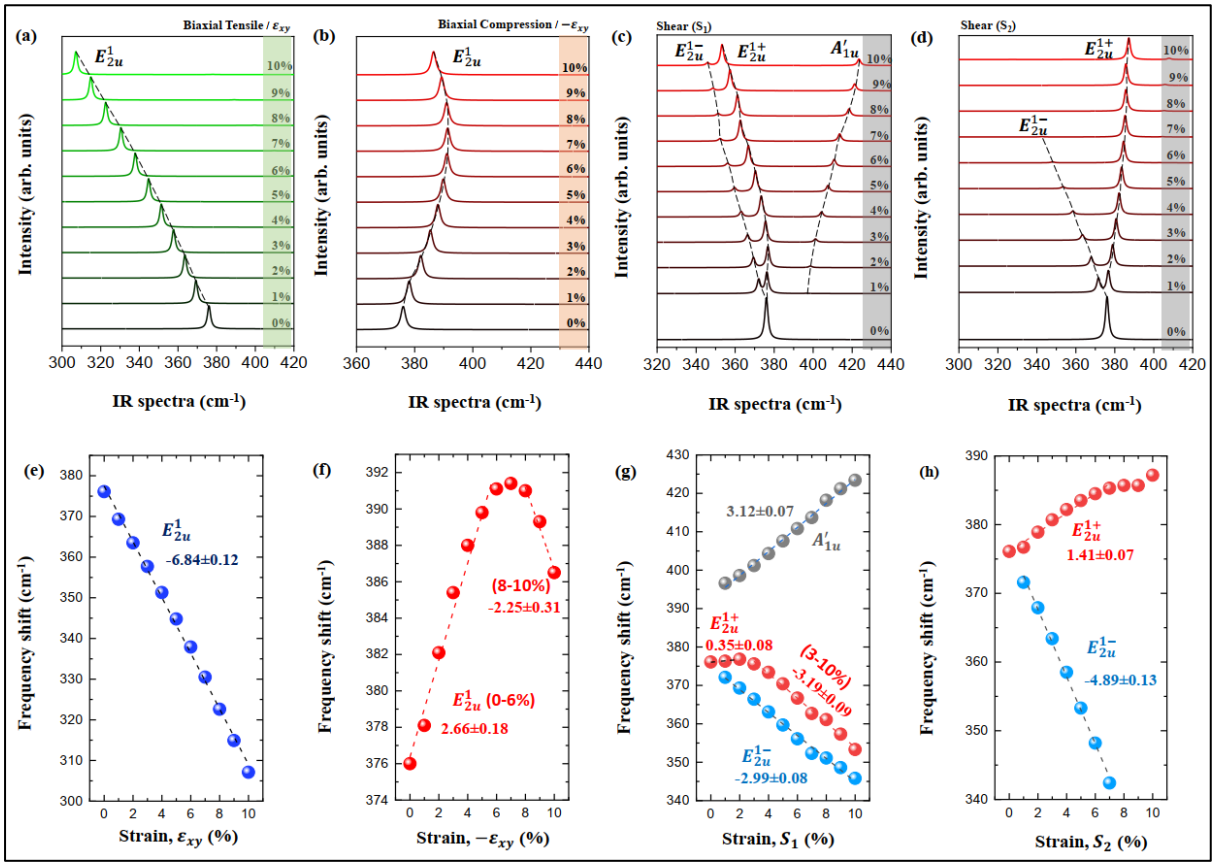

Figure 6.5. (a)-(b) Evolution in IR spectra under biaxial tensile (ϵ_{xy}) and compressive ($-\epsilon_{xy}$) strain, (c) IR spectra under the shear strain of type, S_1. (d) IR spectra under the shear strain of type, S_2. (e-h) Frequency shift in the corresponding IR-active modes under different strain configurations.

Figure 6.5(a)-(b) shows the evolution in IR spectra under biaxial tensile (ϵ_{xy}) and compressive ($-\epsilon_{xy}$) strain. The biaxial strain does not show any frequency split in its E_{2u}^1 mode (namely, the same denotation E_{2g}^1 Raman mode), due to its isotropic strain distribution in a hexagonal honeycomb lattice. Under biaxial tensile strain (ϵ_{xy}), the E_{2u}^1-mode shows a monotonous frequency regression at a much higher rate of -6.84 ± 0.12 cm^{-1}/%, whereas under biaxial compression ($-\epsilon_{xy}$) the E_{2u}^1 mode blue-shifts at a rate 2.66 ± 0.18 cm^{-1}/% up to 7% lattice compression, which then starts to red-shift at a rate -2.25 ± 0.31 cm^{-1}/% for $-\epsilon_{xy}$ strain beyond 7% lattice compression. Both shear *S1* and *S2* strain is found to split the degenerate frequency into E_{2u}^{1+} and E_{2u}^{1-} vibrations with new IR-active mode (A_{1u}') emerging in case of shear *S1* strain, which starts to appear at a minimal value ~ 1% of *S1* and pass on till 10% strain.

6.3.4 Elastic anisotropy under strain

In this section, we briefly study the elastic isotropy (or anisotropy) in ML-MoS_2 under different in-plane strain geometry and ascertain the mechanical strength and stability of a strained ML-MoS_2.

The elastic strength and mechanical stability of a crystalline solid is expressed in terms of its elastic stiffness coefficients (or elastic matrix) C_{ij}. In tensor notation, the C_{ij} is connected with the coefficients of strain tensor (ϵ_j) and the corresponding stress matrix (σ_i) via the generalized Hooke's law,

$$\sigma_i = \sum_{j=1,6} C_{ij}\epsilon_j \tag{6.9}$$

Where an infinitesimal stress component σ_i $(i = 1,6)$ is generated by the application of a small strain component ϵ_i $(i = 1,6)$ applied to the equilibrium crystal structure. The stiffness matrix is 6 × 6 symmetric and comprises of 21 independent stiffness components.[393] The Laue groups of various crystal class and additional symmetry constraints of lattices reduces the

number of independent stiffness coefficients in C_{ij}. The 3D elastic matrix of a hexagonal lattice can reduce to its 2D form in a contracted Voigt notation as:

$$C_{ij} = \begin{pmatrix} C_{11} & C_{12} & . \\ C_{21} & C_{22} & . \\ . & . & C_{66} \end{pmatrix} \tag{6.10}$$

In our study, the atomic positions of strained lattices are allowed to be fully relaxed. Thus, the relaxed-ion stiffness tensors are calculated as the sum of ionic (C_{ij}^{ion}) and electronic (C_{ij}^{ele}) components. The relaxed-ion components are the experimentally observable quantity over the fixed-ion (clamped-ion) components[354].

$$C_{ij} = C_{ij}^{ion} + C_{ij}^{ele} \tag{6.11}$$

Using the finite differences method proposed by Page and Saxe,[394] in a symmetry-general least-squares scheme, we calculate the elastic constants from our *ab initio* results. As shown in Figure 6.6, all eigenvalues of C_{ij}'s are positive, that is the first sign of mechanical stability. But, the elastic stiffness tensors (C_{ij}) has to satisfy the necessary and sufficient stability criterion for a hexagonal lattice to declare the mechanical stability. Recently, the mechanical stability conditions for various crystal classes has been revised by Mouhat and Coudert[393]. This is a recent improvement in the understating of the mechanical stability of non-cubic systems, and provides a generic condition of elastic stability of materials over the well-known "Born-Huang elastic stability criteria." The presence of D_{3h} ($\bar{6}m2$) point group symmetry of ML-MoS_2 lattice yields only 2-independent stiffness tensors (C_{11} and C_{12}) in the elastic matrix and the mechanical stability criterion for such case reads as[393]

$$C_{11}C_{22} - C_{12}^2 > 0, C_{66} > 0, \tag{6.12}$$

Where, $C_{66} = (C_{11} - C_{12})/2$, 2D shear modulus ($G^{2D}$)

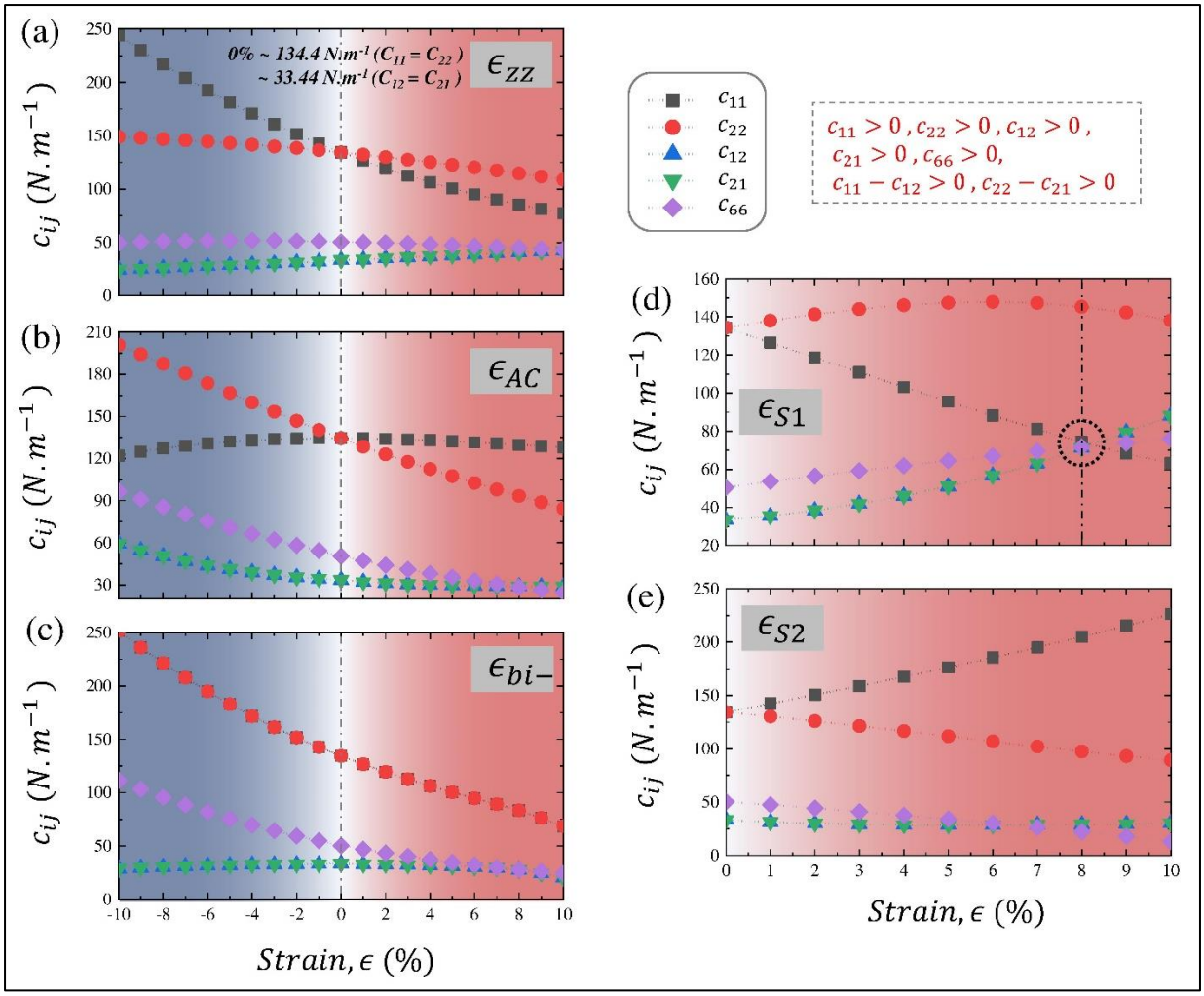

Figure 6.6. Variation in planar elastic stiffness tensors ($C'_{ij}s = C_{11}, C_{22}, C_{12}, C_{21}, C_{66}$) under different in-plane strain geometry. All strain cases within the studied strain range satisfy the mechanical stability criteria for a hexagonal lattice except for shear strain S_1 > 8%, where elastic instability occurs due to a ductile failure as $C_{11} - C_{12} > 0$ condition fails to satisfy.

For a strain-free ML-MoS_2 at equilibrium, the axial (C_{11}=C_{22}= 134.4 N.m^{-1}) and planar component (C_{12}=C_{21}=33.4 N.m^{-1}) of stiffness coefficients (C_{ij}) remains the same [See Figure 6.6 at 0%], thus implies, 2D isotropic elasticity in pristine ML-MoS_2 nanosheet is due to its isotropic crystal structure.[283] Our calculated elastic constants (C_{11}, C_{12}) are found to be in excellent quantitative agreement with other numerical data present in literature.[354], [395], [396] Besides, under a symmetry breaking uniaxial/shear deformation, this isotropy in planar

stiffness tensors goes-off (i.e., $C_{11} \neq C_{22}$), where C_{11} and C_{22} follow different trends in responses to an increasing uniaxial/ shear strain, as shown in Figure 6.6. Under uniaxial strain along the ZZ direction, the C_{11} stiffness component shows a rapid variation with the applied strain-strength over its C_{22} component, and their variation gets reversed when strain is along the AC direction, as shown in Figure 6.6 (a)-(b), respectively. On the other hand, under a symmetry preserving isotropic biaxial strain, the axial ($C_{11}=C_{22}$) and the planar ($C_{12}=C_{21}$) component of C_{ij}'s remains sathe me, this is well expected from an isotropic hexagonal lattice under a biaxial deformation. But, the variation in stiffness tensors ($C_{11}=C_{22}$) become much higher due to a rapid changing geometry for biaxial strain case over the uniaxial deformation.[283], [397] Whereas, under the shear strain of type *S1* and *S2*, the variation in C_{11} and C_{22} is similar to that of uniaxial strain. However, at higher values of shear strain (> 8%) of *S1* type, the elastic instability starts to appear due to a ductile failure, and the system undergoes a nonelastic regime. Notice that the calculated elastic stiffness tensors are all positive, and satisfying mechanical stability condition $C_{11}C_{22} - C_{12}^2 > 0$, $C_{66} > 0$ for all strain cases, except for shear strain S_1 > 8%. Here, we also note, the elastic instability or mechanical failure is not the only criteria to assess the mechanical instability due to a brittle/ductile failure. The phonon instability or the appearance of soft-phonon modes (i.e. imaginary frequency) in the phonon spectrum is also a well-known method to comment on the structural instability under external strain. In Figure 6.7, we have shown the phonon dispersion and atom projected phonon density of states (phDOS) under shear (S_1) strain at a maximum strain value of 10%. The absence of any soft phonon mode around the Brillouin zone center confirm the kinetic stability of strained structures, and the ductile failure at shear S_1 > 8% could possibly due to the generation of reformed bonds due to a simultaneous elongation or shrinkage of bond length and bond angles.

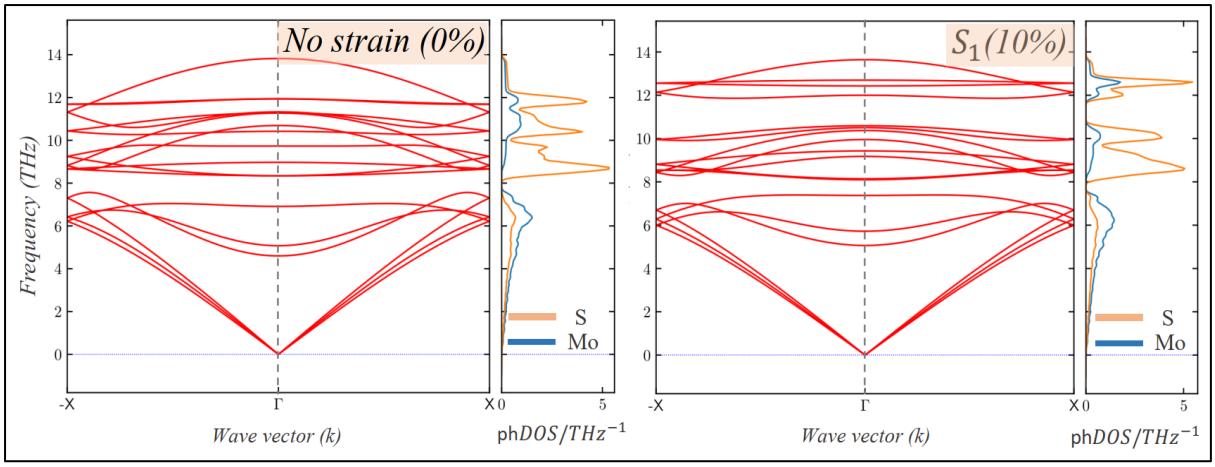

Figure 6.7. Phonon dispersion for strain-free (0%) and shear (S_1) strained ML-MoS_2 nanosheet at 10% indicate no sign of soft phonon mode around the Brillouin zone center, thereby, confirms the kinetic stability of strained structures.

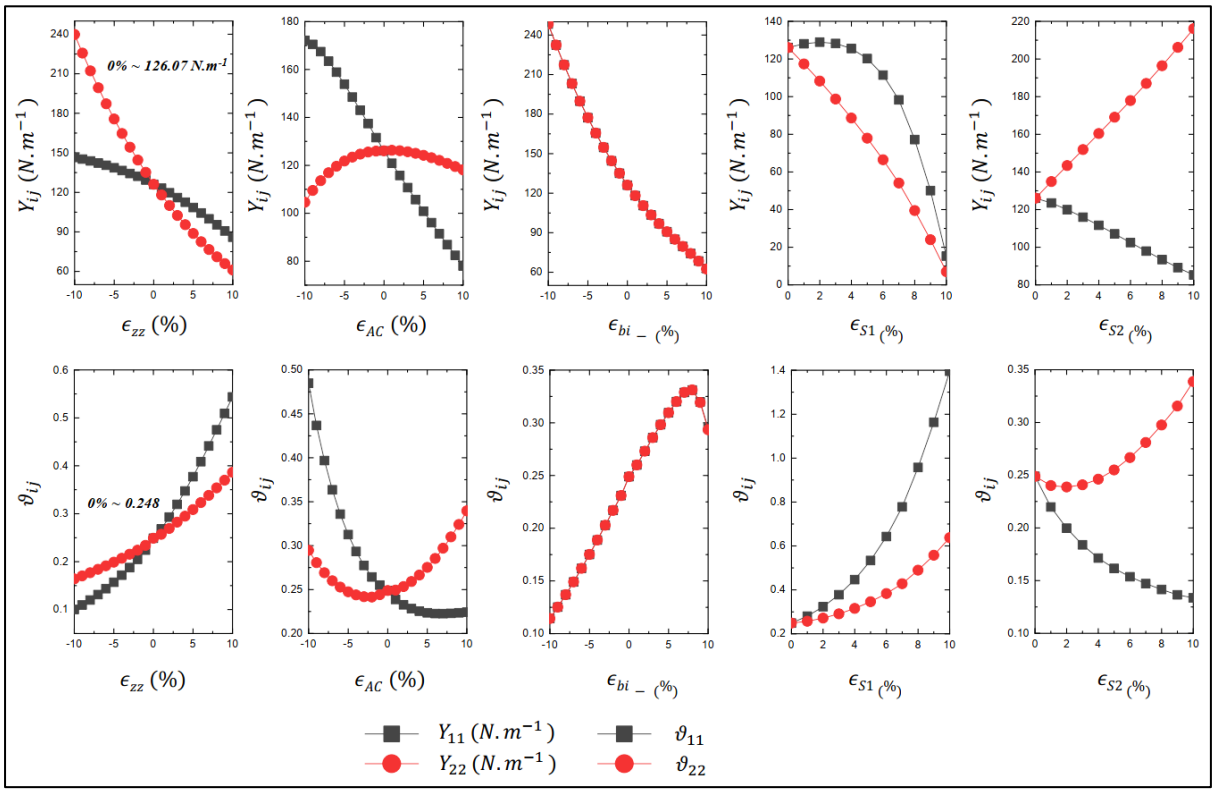

Figure 6.8. 2D Young's modulus (Y_{ij}) in units of N.m^{-1} and Poisson's ratio (ϑ_{ij}) of a monolayer MoS_2 under various strain geometry calculated from the elastic stiffness tensors along mutual orthogonal crystal axis (11 = xx = zigzag, 22 = yy = armchair). 2D Young's modulus ($Y^{2D}_{x/y}$),

and Poisson's ratio ($\vartheta_{x/y}^{2D}$) can be determined by the following relationships from the coefficients of elastic stiffness matrix,

$$Y_x^{2D} = (C_{11}C_{22} - C_{12}C_{21})/C_{22}, \quad Y_y^{2D} = (C_{11}C_{22} - C_{12}C_{21})/C_{11}$$

$$\vartheta_x^{2D} = C_{21}/C_{22}, \; \vartheta_y^{2D} = C_{12}/C_{11}$$

Due to strain-induced lattice anisotropy, the isotopic elasticity in ML-MoS_2 becomes anisotropic due to a transverse shrinkage effect along the mutual orthogonal axis in response to the applied strain axis. Thus, we carefully evaluate anisotropy in Young's modulus and Poisson's ratio for all strain cases in a rectangular unit cell by carefully considering the component of elastic stiffness tensors along the transverse axis of strain. Poisson's ratio that characterizes the material response to a uniaxial load and is defined as the ratio of transverse to an axial component of stiffness tensor. Our calculated value for Young's modulus ($Y_x = Y_y = 126.07\ N.m^{-1}$) and Poisson's ratio ($\vartheta_x = \vartheta_y = 0.24$) for pristine ML-$MoS_2$ lattice, at equilibrium, shows very close agreement result with other *ab initio* studies[283], [398], [399] and remain within the experimental prediction limit of 180 ± 60 $N.m^{-1}$. As shown in Figure 6.8, both the Young's modulus and Poisson's ratio induces a strong in-plane anisotropy along ZZ and AC lattice direction of ML-MoS_2 under different strain geometry. In particular, the anisotropy is more substantial for both modes of shear strain (S_1 & S_2). On the other hand, the elastic constants remain isotropic under the biaxial tensile (or compressive) deformation with a gradual decrease (or increase) in Young's modulus (Y) and Poisson's ratio (ϑ). The result of this elastic anisotropy under uniaxial and shear strain keeps the lattice environment different along the mutual orthogonal direction of ML-MoS_2, in return, enforces unique functionalities to the system in terms of strong electron-lattice coupling and anisotropy in electromechanical properties.

6.4 CONCLUSIONS

A full comprehensive *ab initio* study has been conducted to demonstrate the effects of various in-plane strain on phonon modes and elastic anisotropy in a monolayer MoS_2 nanosheet. The phonon dispersion and vibrational modes that correspond to the characteristic Raman and IR-active vibrations of ML-MoS_2 have been analyzed under various in-plane strain geometry. The response to uniaxial and shear strain in terms of the breaking of vibrational frequency degeneracy of its doubly degenerate E_{2g}^1 mode into two orthogonal non-degenerate singlet sub-bands E_{2g}^{1+} & E_{2g}^{1-} has been demonstrated up to a considerable strain of 10%. The strain-induced lattice anisotropy is the source of this broken frequency degeneracy of modes. The mechanical and kinetic stability of strained lattices has been confirmed within the studied range of strain. The vibrational modes red-shift (blue-shift) in different proportions depending on the magnitude and nature of the applied strain, which has been systematically quantified for all strain cases. The degeneracy of E_{2g}^1-mode is found to be lifted only when the underlying crystal symmetry is broken (i.e., under uniaxial/shear strain), while a biaxial strain is found to preserve the degeneracy due to its isotropic nature of strain field (C_3-symmetry is retained). In certain cases, we found the appearance of new Raman (E_{2g}') and IR (A_{1u}') active vibrations in the frequency spectrum. This is due to colossal modifications in the crystal symmetry and change density isosurface of vibrating ions. The frequency split-off response in the doubly degenerate E_{2u}^1 (IR) mode is found to be more sensitive to the lattice anisotropy, enabling to detect the anisotropy in honeycomb lattices at a shallow magnitude of lattice displacement. We believe, together with Raman spectra, the spectral response of IR modes could be a useful indicator for effective monitoring of lattice strain in a monolayer MoS_2 lattice. The overall results indicate stain-induced phonon engineering by the changes in Raman and IR-active vibrations, and spectral evolution of modes are powerful avenues in interpreting the structural

and vibrational information of ML-MoS_2 nanosheet for its application in phononics, thermoelectrics, and nanoelectromechanical systems.

----------**********----------

Chapter 7

Summary & Outlook

The essential findings of this Ph.D. research work that has been presented in the form of different chapters in this thesis have been summarized in this final Chapter.

In *Chapter 1*, I have provided a pedagogical introduction to the two-dimensional materials with particular attention on *Group VIB* transition-metal dichalcogenide (TMDC) monolayers MX_2 (where M = Mo, W, etc. and X = S, Se, Te). A broad overview of different electronic properties and a brief introduction to the recently discovered Janus transition-metal dichalcogenides (JTMDCs), namely MXY monolayers (where X ≠ Y = S, Se, Te) have been presented in this chapter.

In *Chapter 2*, theoretical methods and computational tools that are pivotal to carry out the calculation of electronic structure results presented in this Ph.D. thesis have been included. Besides, in the subsequent chapters, a computational details section has been devoted to producing the results presented in the chapter using the essential computational settings of VASP calculation. A general input and output file structure of VASP calculation has been provided to obtain some primary electronic structure results and the minimum energy configuration of a given system towards the end of chapter 2.

In Chapter 3, we have theoretically demonstrated the crystal structure, lattice stability and coupled spin-valley nature of the charge carriers in a series of semiconducting monolayers

of *Group VIB* transition metal dichalcogenides 1H-MX_2 (where M = Cr, Mo, W, etc.; X = S, Se, or Te) and their Janus structures 1H-MXY (where X ≠ Y). Atomically thin MXY monolayers are found to be structurally stable, which we have confirmed from the phonon study and room temperature AIMD simulations. Furthermore, the Janus monolayers of *Group VIB* TMDCs possess comparable cohesive energy (~ 2-3 eV/atom) to that of their parent, energetically stable, 1H-MX_2 phase, this suggests the relative chemical stability of Janus monolayers. In all cases, a semiconducting electronic bandgap (~ 0.25 – 1.7 eV) has been found in Janus monolayers. The bandgap of M-S-Se and M-Se-Te (where, M = Cr, Mo, W) Janus monolayers are found to be direct at the K-point of the BZ under SOC, whereas in all other cases an indirect bandgap is observed with valence band maximum (VBM) occurring at the Γ–point of the BZ and the conduction band minimum (CBM) situated at the K–point. The variation in the direct and indirect bandgap exhibits a linear dependency as a function of applied mechanical strain within the -3% to +6% of biaxial strain. The Janus monolayers remain semiconducting within this strain range except for CrSTe strained system that shows a semiconductor-to-metal transition with strain > +3%. The electrostatic potential difference (ΔV) is found to increase with an increase in dipolar contrast between chalcogen lattices, which enhances the SOC splitting energy of spin bands at the K–point of BZ both in the VBM and CBM sectors of the electronic dispersion. The Rashba parameters (E_R & α_R) are found to be highly strain sensitive and significantly get enhanced with lattice compression. The strain sensitive variation in Rashba coefficient α_R is found to exhibit asymmetric behavior about the K'-Γ-K and M'-Γ-M high symmetry line in the 1st BZ. Under compressive biaxial strain the enhancement in α_R along the K'-Γ-K line is nearly 2 orders of magnitude higher than the same along the M'-Γ-M high symmetry line for a given strain value. Furthermore, the strain-tunable alteration in Berry curvature in pristine and Janus monolayer TMDCs can be a potential avenue

for the effective controlling of transverse velocities of valley carriers in the future flexible valleytronic device.

In *Chapter 4*, using first-principle calculations, we have shown the impact of a symmetry reducing mechanical deformation on the low-energy carrier dynamics in a strained ML-MoS_2, around *K/K'* points of the Brillouin zone. We have shown a robust strain-valley coupling for low-energy valley carriers, where the energy extrema of electron/hole bands drift away from *K/K'* points in response to a symmetry lowering uniaxial strain. A significant valley asymmetry between electron and hole states (i.e., the CBM valley drift is nearly 2-times that of the VBM hills) is preferable in conveniently lifting the valley symmetry (valley momentum degeneracy at *K/K'*) of *electrons/holes*. The resulting effect can considerably influence the valley selective optical excitations and valley polarization properties of a multi-valley electronic system like ML-MoS_2. A drastic drop in the degree of circular polarization (*K* valley polarization) is optically addressable by a polar PL emission measurement. Besides, the *K*-valley coherence effect can manipulate the valley-contrasting Berry curvature distributions around *K/K'*, where the rise in flux profile together with a drift can lead to anomalous valley current in a strained ML-MoS_2 lattice system. The strain-induced modification in Bloch states is substantial in order to alter the strength of valley-contrasting phenomena that can lead to an anomalous valley current for different Kramer channels, which are mechanically controllable by a strong strain-valley coupling near K and K' points. This strong valley asymmetry between valley carriers under a directional lattice strain is the interplay of geometric and orbital overlap effects that breaks the lattice symmetry and symmetry between orbital wave functions at the relevant band-edge points.

Moreover, the spatial redistribution and rehybridization of states near the band edges can potentially pave the way in controlling the spin DOF in a uniaxially strained ML-MoS_2, where the SOC induced spin-splitting energy at the VBM can be sizably enlarged by an amount

of ~ 7 meV at a strain of 9%. This could potentially alter the spintronic capability of this material and allow manipulating the spin degrees of freedom in a strained MoS_2 lattice. The spin relaxation times of carriers are expected to be prolonged by the suppression of Dyakonov-Perel spin relaxation due to a strain-induced increase in the spin-splitting energy. The predictive findings presented in this chapter are useful for further experimental investigations on ML-MoS_2 under the application of in-plane lattice strain to realize its strain functional future technological potential for flexible electronic, spintronic, and valleytronic devices.

In *Chapter 5*, a systematic investigation of the nanopiezotronic response of ML-MoS_2 nanosheet to different modes of applied strain was performed. Our study shows that shear strain S_1 and uniaxial tensile strain applied along the zigzag direction are most effective in reinforcing the nanopiezoelectric response in ML-MoS_2, which is followed by biaxial tensile strain and uniaxial compressive strain applied along the armchair direction. Polarization-dependent linear response properties, such as Born effective charges ($Z^*_{[B]}$) have been investigated to attribute the atomistic origin and changes in the large piezoelectric response to the alteration in the intrinsic polarization vector in ML-MoS_2. The simultaneous variation in piezoelectric and electronic bandgap with the shear strain (S_1) and uniaxial tensile strain along the zigzag direction was studied to ascertain the optimal strain values where piezoelectricity couples synergistically to the semiconducting properties for the maximal utility of ML-MoS_2 in nanopiezotronic devices. The synergy is found to occur around 4−5% of shear strain and about 6−7% of uniaxial tensile strain. Furthermore, the variation in carrier mobilities with strain has been addressed along the mutual orthogonal crystal direction of ML-MoS_2. Under the application of uniaxial compressive strain along both the zigzag and the armchair directions, electron mobility drops drastically at a strain of 3%. Likewise, hole mobility falls abruptly at 1% uniaxial tensile strain along both the zigzag and armchair directions. These behaviors in charge carrier mobility may find useful applications in designing low-power switches. Under

uniaxial compressive strain, the charge carrier mobility is found to increase along the zigzag direction. Therefore, the channel material needs to interface the electrodes along the zigzag direction for higher carrier injection. Moreover, ML-MoS_2 has been fortuitously found to be softest (or least stiff) along the zigzag direction, which shows higher strain sustainability and greater elastic limit. The predictive findings presented in this chapter can facilitate in realizing energy-efficient nanopiezotronic devices by controlling the conversion of mechanical to electrical energy in 2D nanomaterial systems such as ML-MoS_2.

Chapter 6 provides a comprehensive *ab initio* study that has been conducted to demonstrate the effects of various in-plane strain on phonon modes and elastic anisotropy in a monolayer MoS_2 nanosheet. The phonon dispersion and vibrational modes that correspond to the characteristic Raman and IR-active vibrations of ML-MoS_2 were analyzed under various in-plane strain geometry. The response to uniaxial and shear strain in terms of the breaking of vibrational frequency degeneracy of its doubly degenerate E_{2g}^1 mode into two orthogonal non-degenerate singlet sub-bands E_{2g}^{1+} & E_{2g}^{1-} has been demonstrated up to a considerable strain of 10%. The strain-induced lattice anisotropy is found to be the source of this broken frequency degeneracy of vibrational modes. The mechanical and kinetic stability of strained lattices has been confirmed within the studied range of strain. The vibrational modes red-shift (blue-shift) in different proportions depending on the magnitude and nature of the applied strain, which has been systematically quantified for all strain cases. The degeneracy of E_{2g}^1-mode is found to be lifted only when the underlying crystal symmetry is broken (i.e., under uniaxial/shear strain), while a biaxial strain is found to preserve the degeneracy due to its isotropic nature of strain field (C_3-symmetry is retained). In some instances, we found the appearance of new Raman (E'_{2g}) and IR (A'_{1u}) active vibrations in the frequency spectrum. This is due to colossal modifications in the crystal symmetry and change density isosurface of vibrating ions. The frequency split-off response in the doubly degenerate E_{2u}^1 (IR) mode is found to be more

sensitive to the lattice anisotropy, enabling to detect the anisotropy in honeycomb lattices at a very low magnitude of lattice displacement. We believe, together with Raman spectra, the spectral response of IR modes could be an effective indicator for effective monitoring of lattice strain in a monolayer MoS_2 lattice. The overall results presented in this chapter indicate that the stain-induced phonon engineering by the changes in Raman and IR-active vibrations and spectral evolution of modes are powerful avenues in interpreting the structural and vibrational information of ML-MoS_2 nanosheet for its application in phononics, straintronics, thermoelectrics, and nanoelectromechanical systems.

----------**********----------

Bibliography

[1] C. S. Smith, “Materials and the Development of Civilization and Science,” *Science (80-.).*, vol. 148, no. 3672, pp. 908–917, 1965.

[2] Q. H. Wang, K. Kalantar-Zadeh, A. Kis, J. N. Coleman, and M. S. Strano, “Electronics and optoelectronics of two-dimensional transition metal dichalcogenides,” *Nat. Nanotechnol.*, vol. 7, no. 11, pp. 699–712, 2012.

[3] P. Preuster, A. Alekseev, and P. Wasserscheid, “Hydrogen storage technologies for future energy systems,” *Annu. Rev. Chem. Biomol. Eng.*, vol. 8, pp. 445–471, 2017.

[4] Jariwala, D., Sangwan, V.K., Lauhon, L.J., Marks, T.J. and Hersam, M.C., 2014. Emerging device applications for semiconducting two-dimensional transition metal dichalcogenides. *ACS nano*, *8*(2), pp.1102-1120.

[5] V. Etacheri, R. Marom, R. Elazari, G. Salitra, and D. Aurbach, “Challenges in the development of advanced Li-ion batteries: a review,” *Energy Environ. Sci.*, vol. 4, no. 9, pp. 3243–3262, 2011.

[6] N. A. Peppas and R. Langer, “New challenges in biomaterials,” *Science (80-.).*, vol. 263, no. 5154, pp. 1715–1720, 1994.

[7] R. W. Keyes, “Fundamental limits of silicon technology,” *Proc. IEEE*, vol. 89, no. 3, pp. 227–239, 2001.

[8] J. N. Tiwari, R. N. Tiwari, and K. S. Kim, “Zero-dimensional, one-dimensional, two-dimensional and three-dimensional nanostructured materials for advanced electrochemical energy devices,” *Prog. Mater. Sci.*, vol. 57, no. 4, pp. 724–803, 2012.

[9] M. Naguib, V. N. Mochalin, M. W. Barsoum, and Y. Gogotsi, “25th anniversary article: MXenes: a new family of two-dimensional materials,” *Adv. Mater.*, vol. 26, no. 7, pp. 992–1005, 2014.

[10] G. Fiori *et al.*, “Electronics based on two-dimensional materials,” *Nat. Nanotechnol.*, vol. 9, no. 10, p. 768, 2014.

[11] X. Huang, C. Tan, Z. Yin, and H. Zhang, “25th anniversary article: Hybrid nanostructures based on two-dimensional nanomaterials,” *Adv. Mater.*, vol. 26, no. 14, pp. 2185–2204, 2014.

[12] M. Xu, T. Liang, M. Shi, and H. Chen, “Graphene-like two-dimensional materials,” *Chem. Rev.*, vol. 113, no. 5, pp. 3766–3798, 2013.

[13] P. Miró, M. Audiffred, and T. Heine, “An atlas of two-dimensional materials,” *Chem. Soc. Rev.*, vol. 43, no. 18, pp. 6537–6554, 2014.

[14] G. R. Bhimanapati *et al.*, “Recent Advances in Two-Dimensional Materials beyond Graphene,” no. 12, pp. 11509–11539, 2015.

[15] J. Zhou *et al.*, “2DMatPedia, an open computational database of two-dimensional materials from top-down and bottom-up approaches,” *Sci. Data*, vol. 6, p. 86, 2019.

[16] Schaibley, J.R., Yu, H., Clark, G., Rivera, P., Ross, J.S., Seyler, K.L., Yao, W. and Xu, X., 2016. Valleytronics in 2D materials. *Nature Reviews Materials*, *1*(11), pp.1-15.

[17] M. I. Katsnelson, K. S. Novoselov, and A. K. Geim, “Chiral tunnelling and the Klein paradox in graphene,” *Nat. Phys.*, vol. 2, no. 9, pp. 620–625, 2006.

[18] J. Wang, Y. Xu, and S.-C. Zhang, “Two-dimensional time-reversal-invariant topological superconductivity in a doped quantum spin-Hall insulator,” *Phys. Rev. B*, vol. 90, no. 5, p. 54503, 2014.

[19] X. Song, J. Hu, and H. Zeng, “Two-dimensional semiconductors: recent progress and future perspectives,” *J. Mater. Chem. C*, vol. 1, no. 17, pp. 2952–2969, 2013.

[20] D. Deng, K. S. Novoselov, Q. Fu, N. Zheng, Z. Tian, and X. Bao, “Catalysis with two-dimensional materials and their heterostructures,” *Nat. Nanotechnol.*, vol. 11, no. 3, p. 218, 2016.

[21] C. Lee, X. Wei, J. W. Kysar, and J. Hone, “Measurement of the elastic properties and intrinsic strength of monolayer graphene,” *Science (80-.).*, vol. 321, no. 5887, pp. 385–388, 2008.

[22] C. Lee, H. Yan, L. Brus, T. Heinz, J. Hone, and S. Ryu, “Anomalous lattice vibrations of single-and few-layer MoS2,” *ACS Nano*, vol. 4, no. 5, pp. 2695–700, 2010.

[23] R. S. Sundaram *et al.*, “Electroluminescence in Single Layer MoS_2,” *Nano Lett.*, vol. 13, no. 4, pp. 1416–1421, 2013.

[24] A. Kormányos, V. Zólyomi, N. D. Drummond, P. Rakyta, G. Burkard, and V. I. Fal’ko, “Monolayer MoS 2: trigonal warping, the Γ valley, and spin-orbit coupling effects,” *Phys. Rev. b*, vol. 88, no. 4, p. 45416, 2013.

[25] K. S. Novoselov *et al.*, “Electric field effect in atomically thin carbon films,” *Science (80-.).*, vol. 306, no. 5696, pp. 666–669, 2004.

[26] Novoselov, K.S., Jiang, D., Schedin, F., Booth, T.J., Khotkevich, V.V., Morozov, S.V. and Geim, A.K., 2005. Two-dimensional atomic crystals. *Proceedings of the National Academy of Sciences*, *102*(30), pp.10451-10453.

[27] B. Luo, G. Liu, and L. Wang, “Recent advances in 2D materials for photocatalysis,” *Nanoscale*, vol. 8, no. 13, pp. 6904–6920, 2016.

[28] F. Schedin *et al.*, “Detection of individual gas molecules adsorbed on graphene,” *Nat. Mater.*, vol. 6, no. 9, pp. 652–655, 2007.

[29] H. Fang, S. Chuang, T. C. Chang, K. Takei, T. Takahashi, and A. Javey, “High-performance single layered WSe 2 p-FETs with chemically doped contacts,” *Nano Lett.*, vol. 12, no. 7, pp. 3788–3792, 2012.

[30] R. Peierls, “Quelques propriétés typiques des corps solides,” in *Annales de l’institut Henri Poincaré*, 1935, vol. 5, no. 3, pp. 177–222.

[31] L. D. Landau, “Zur Theorie der phasenumwandlungen II,” *Phys. Z. Sowjetunion*, vol. 11, no. 545, pp. 26–35, 1937.

[32] L. D. Landau and E. M. Lifshitz, “Statistical Physics. Part I. Pergamon Press, Oxford 1980.”

[33] N. D. Mermin and H. Wagner, “Absence of ferromagnetism or antiferromagnetism in one-or two-dimensional isotropic Heisenberg models,” *Phys. Rev. Lett.*, vol. 17, no. 22, p. 1133, 1966.

[34] N. D. Mermin, “Crystalline order in two dimensions,” *Phys. Rev.*, vol. 176, no. 1, p. 250, 1968.

[35] A. A. Novoselov, K.S., Geim, A.K., Morozov, S.V., Jiang, D.A., Zhang, Y., Dubonos, S.V., Grigorieva, I.V. and Firsov, “Electric field effect in atomically thin carbon films,” *Science (80-.).*, vol. 306, no. 5696, pp. 666–669, 2004.

[36] G. Gao, G. Ding, J. Li, K. Yao, M. Wu, and M. Qian, “Monolayer MXenes: promising half-metals and spin gapless semiconductors,” *Nanoscale*, vol. 8, no. 16, pp. 8986–8994, 2016.

[37] S. Balendhran, S. Walia, H. Nili, S. Sriram, and M. Bhaskaran, “Elemental analogues of graphene: Silicene, germanene, stanene, and phosphorene,” *Small*, vol. 11, no. 6, pp. 640–652, 2015.

[38] Y. Cai, C.-P. Chuu, C. M. Wei, and M. Y. Chou, “Stability and electronic properties of two-dimensional silicene and germanene on graphene,” *Phys. Rev. B*, vol. 88, no. 24, p. 245408, 2013.

[39] M. E. Dávila, L. Xian, S. Cahangirov, A. Rubio, and G. Le Lay, “Germanene: a novel two-dimensional germanium allotrope akin to graphene and silicene,” *New J. Phys.*, vol. 16, no. 9, p. 95002, 2014.

[40] K. Mak, C. Lee, J. Hone, J. Shan, and T. Heinz, “Atomically Thin MoS_{2}: A New Direct-Gap Semiconductor,” *Phys. Rev. Lett.*, vol. 105, no. 13, p. 136805, 2010.

[41] J.-J. Kim, C. Park, W. Yamaguchi, O. Shiino, K. Kitazawa, and T. Hasegawa, “Observation of a phase transition from the T phase to the H phase induced by a STM tip in 1 T− TaS 2,” *Phys. Rev. B*, vol. 56, no. 24, p. R15573, 1997.

[42] N. B. Aetukuri *et al.*, “Control of the metal–insulator transition in vanadium dioxide by modifying orbital occupancy,” *Nat. Phys.*, vol. 9, no. 10, pp. 661–666, 2013.

[43] H. Liu, A. T. Neal, Z. Zhu, D. Tomanek, and P. D. Ye, “Phosphorene: A New 2D Material with High Carrier Mobility,” *ACS Nano*, vol. 4133, pp. 4033–4041, 2014.

[44] L. Li *et al.*, “Black phosphorus field-effect transistors,” *Nat. Nanotechnol.*, vol. 9, no. 5, pp. 372–377, 2014.

[45] C. K. Chiu, J. C. Y. Teo, A. P. Schnyder, and S. Ryu, “Classification of topological quantum matter with symmetries,” *Rev. Mod. Phys.*, vol. 88, no. 3, pp. 1–63, 2016.

[46] G. Q. Huang and Z. W. Xing, “Band-gap tunability and dynamical instability in strained monolayer and bilayer phosphorenes.,” *J. Phys. Condens. Matter*, vol. 27, no. 17, p. 175006, 2015.

[47] J. B. Varley, A. Miglio, V.-A. Ha, M. J. van Setten, G.-M. Rignanese, and G. Hautier, “High-throughput design of non-oxide p-type transparent conducting materials: Data mining, search strategy, and identification of boron phosphide,” *Chem. Mater.*, vol. 29, no. 6, pp. 2568–2573, 2017.

[48] S. Curtarolo, G. L. W. Hart, M. B. Nardelli, N. Mingo, S. Sanvito, and O. Levy, “The high-throughput highway to computational materials design,” *Nat. Mater.*, vol. 12, no. 3, pp. 191–201, 2013.

[49] W. Sitek, J. Trzaska, and L. A. Dobrzański, “An artificial intelligence approach in designing new materials,” *J. Achiev. Mater. Manuf. Eng.*, vol. 17, no. 1–2, 2006.

[50] S. Curtarolo *et al.*, “AFLOW: An automatic framework for high-throughput materials discovery,” *Comput. Mater. Sci.*, vol. 58, pp. 218–226, 2012.

[51] J.-C. Lei, X. Zhang, and Z. Zhou, “Recent advances in MXene: Preparation, properties, and applications,” *Front. Phys.*, vol. 10, no. 3, pp. 276–286, 2015.

[52] X. Zhang, Z. Zhang, and Z. Zhou, “MXene-based materials for electrochemical energy storage,” *J. energy Chem.*, vol. 27, no. 1, pp. 73–85, 2018.

[53] B. L. Chittari *et al.*, “Electronic and magnetic properties of single-layer M P X 3 metal phosphorous trichalcogenides,” *Phys. Rev. B*, vol. 94, no. 18, p. 184428, 2016.

[54] F. Wang *et al.*, “New frontiers on van der Waals layered metal phosphorous trichalcogenides,” *Adv. Funct. Mater.*, vol. 28, no. 37, p. 1802151, 2018.

[55] S. Chen and G. Shi, “Two-Dimensional Materials for Halide Perovskite-Based Optoelectronic Devices,” pp. 1–31, 2017.

[56] M. Naguib *et al.*, “Two-dimensional transition metal carbides,” *ACS Nano*, vol. 6, no. 2, pp. 1322–1331, 2012.

[57] J. Zhang, Y. Chen, and X. Wang, “Two-dimensional covalent carbon nitride nanosheets: synthesis, functionalization, and applications,” *Energy Environ. Sci.*, vol. 8, no. 11, pp. 3092–3108, 2015.

[58] A. C. Riis-Jensen, T. Deilmann, T. Olsen, and K. S. Thygesen, “Classifying the Electronic and Optical Properties of Janus Monolayers,” *ACS Nano*, vol. 13, no. 11, pp. 13354–13364, 2019.

[59] X. Zhang, A. Chen, and Z. Zhou, “High-throughput computational screening of layered and two-dimensional materials,” *Wiley Interdiscip. Rev. Comput. Mol. Sci.*, vol. 9, no. 1, p. e1385, 2019.

[60] N. Mounet *et al.*, “Two-dimensional materials from high-throughput computational exfoliation of experimentally known compounds,” *Nat. Nanotechnol.*, vol. 13, no. 3, pp. 246–252, 2018.

[61] F. Chen *et al.*, “A new phase of monolayer group-V binary compounds with direct bandgap and giant piezoelectric properties,” *J. Appl. Phys.*, vol. 125, no. 21, p. 214303, 2019.

[62] F. X. Ma *et al.*, “Predicting a new phase (T ’ ’) of two-dimensional transition metal di-chalcogenides and strain-controlled topological phase transition,” *Nanoscale*, vol. 8, no. 9, pp. 4969–4975, 2016.

[63] B. Singh, C.-H. Hsu, W.-F. Tsai, V. M. Pereira, and H. Lin, “Stable charge density wave phase in a 1 T–TiSe 2 monolayer,” *Phys. Rev. B*, vol. 95, no. 24, p. 245136, 2017.

[64] F. A. Rasmussen and K. S. Thygesen, “Computational 2D Materials Database: Electronic Structure of Transition-Metal Dichalcogenides and Oxides,” *J. Phys. Chem. C*, vol. 119, no. 23, pp. 13169–13183, 2015.

[65] S. Beniwal *et al.*, “Graphene-like boron–carbon–nitrogen monolayers,” *ACS Nano*, vol. 11, no. 3, pp. 2486–2493, 2017.

[66] J. N. Coleman *et al.*, “Two-dimensional nanosheets produced by liquid exfoliation of layered materials,” *Science (80-.).*, vol. 331, no. 6017, pp. 568–571, 2011.

[67] X. Li and H. Zhu, “Two-dimensional MoS2: Properties, preparation, and applications,” *J. Mater.*, vol. 1, no. 1, pp. 33–44, 2015.

[68] K. S. Novoselov, A. Mishchenko, A. Carvalho, A. H. C. Neto, and O. Road, “2D materials and van der Waals heterostructures,” *Science (80-.).*, vol. 353, no. 6298, p. aac9439, 2016.

[69] Liu, Y., Weiss, N.O., Duan, X., Cheng, H.C., Huang, Y. and Duan, X., 2016. Van der Waals heterostructures and devices. *Nature Reviews Materials*, *1*(9), pp.1-17.

[70] A. Koma, “Van der Waals epitaxy for highly lattice-mismatched systems,” *J. Cryst. Growth*, vol. 201, pp. 236–241, 1999.

[71] L. A. Ponomarenko *et al.*, “Tunable metal–insulator transition in double-layer graphene heterostructures,” *Nat. Phys.*, vol. 7, no. 12, pp. 958–961, 2011.

[72] S. A. Svatek *et al.*, “Gate tunable photovoltaic effect in MoS2vertical p-n homostructures,” *J. Mater. Chem. C*, vol. 5, no. 4, pp. 854–861, 2017.

[73] L. Britnell *et al.*, “Field-effect tunneling transistor based on vertical graphene

heterostructures," *Science (80-.).*, vol. 335, no. 6071, pp. 947–950, 2012.

[74] N. Ding *et al.*, "Controllable Carrier Type in Boron Phosphide Nanowires Toward Homostructural Optoelectronic Devices," *ACS Appl. Mater. Interfaces*, vol. 10, no. 12, pp. 10296–10303, 2018.

[75] Jariwala, D., Davoyan, A.R., Wong, J. and Atwater, H.A., 2017. Van der Waals materials for atomically-thin photovoltaics: Promise and outlook. *Acs Photonics*, *4*(12), pp.2962-2970.

[76] S. J. Haigh *et al.*, "Cross-sectional imaging of individual layers and buried interfaces of graphene-based heterostructures and superlattices," *Nat. Mater.*, vol. 11, no. 9, pp. 764–767, 2012.

[77] C. Dean *et al.*, "Graphene based heterostructures," *Solid State Commun.*, vol. 152, no. 15, pp. 1275–1282, 2012.

[78] R. V Gorbachev *et al.*, "Strong Coulomb drag and broken symmetry in double-layer graphene," *Nat. Phys.*, vol. 8, no. 12, pp. 896–901, 2012.

[79] T. Georgiou *et al.*, "Vertical field-effect transistor based on graphene–WS 2 heterostructures for flexible and transparent electronics," *Nat. Nanotechnol.*, vol. 8, no. 2, pp. 100–103, 2013.

[80] Saini, A., 2014. EU Graphene Flagship project aims for technological breakthroughs: graphene-flagship. eu. *Mrs Bulletin*, *39*(5), pp.393-394.

[81] A. Hirsch, "The Graphene Flagship—A Giant European Research Project," *Angew. Chemie Int. Ed.*, vol. 54, no. 32, pp. 9132–9133, 2015.

[82] S. Roche *et al.*, "Graphene spintronics: the European Flagship perspective," *2D Mater.*, vol. 2, no. 3, p. 30202, 2015.

[83] H. Zeng and X. Cui, "An optical spectroscopic study on two-dimensional group-VI transition metal dichalcogenides," *Chem. Soc. Rev.*, vol. 44, no. 9, pp. 2629–2642, 2015.

[84] R. G. Dickinson and L. Pauling, "The crystal structure of molybdenite," *J. Am. Chem. Soc.*, vol. 45, no. 6, pp. 1466–1471, 1923.

[85] J. A. Wilson and A. D. Yoffe, "The transition metal dichalcogenides discussion and interpretation of the observed optical, electrical and structural properties," *Adv. Phys.*, vol. 18, no. 73, pp. 193–335, 1969.

[86] X. Xu, W. Yao, D. Xiao, and T. F. Heinz, "Spin and pseudospins in layered transition metal dichalcogenides," *Nat. Phys.*, vol. 10, no. 5, p. 343, 2014.

[87] Li, H., Wu, X., Liu, H., Zheng, B., Zhang, Q., Zhu, X., Wei, Z., Zhuang, X., Zhou, H., Tang, W. and Duan, X., 2017. Composition-modulated two-dimensional semiconductor lateral heterostructures via layer-selected atomic substitution. *ACS nano*, *11*(1), pp.961-967.

[88] R. F. Frindt and A. D. Yoffe, "Physical properties of layer structures: optical properties and photoconductivity of thin crystals of molybdenum disulphide," *Proc. R. Soc. London. Ser. A. Math. Phys. Sci.*, vol. 273, no. 1352, pp. 69–83, 1963.

[89] P. Joensen, R. F. Frindt, and S. R. Morrison, "Single-layer mos2," *Mater. Res. Bull.*, vol. 21, no. 4, pp. 457–461, 1986.

[90] R. Tenne, L. Margulis, M. ea Genut, and G. Hodes, "Polyhedral and cylindrical structures of tungsten disulphide," *Nature*, vol. 360, no. 6403, pp. 444–446, 1992.

[91] Y. Feldman, E. Wasserman, D. J. Srolovitz, and R. Tenne, "High-rate, gas-phase growth of MoS2 nested inorganic fullerenes and nanotubes," *Science (80-.).*, vol. 267, no. 5195, pp. 222–225, 1995.

[92] F. H. L. Koppens, T. Mueller, P. Avouris, A. C. Ferrari, M. S. Vitiello, and M. Polini, "Photodetectors based on graphene, other two-dimensional materials and hybrid systems," *Nat. Nanotechnol.*, vol. 9, no. 10, pp. 780–793, 2014.

[93] Manzeli, S., Ovchinnikov, D., Pasquier, D., Yazyev, O.V. and Kis, A., 2017. 2D transition metal dichalcogenides. *Nature Reviews Materials*, *2*(8), p.17033.

[94] A. Splendiani *et al.*, "Emerging photoluminescence in monolayer MoS2," *Nano Lett.*, vol. 10, no. 4, pp. 1271–1275, 2010.

[95] K. F. Mak, C. Lee, J. Hone, J. Shan, and T. F. Heinz, "Atomically thin MoS2: A new direct-gap semiconductor," *Phys. Rev. Lett.*, vol. 105, no. 13, pp. 2–5, 2010.

[96] S. Shi, Z. Sun, and Y. H. Hu, "Synthesis, stabilization and applications of 2-dimensional 1T metallic MoS 2," *J. Mater. Chem. A*, vol. 6, no. 47, pp. 23932–23977, 2018.

[97] S. C. Bayliss and W. Y. Liang, "Symmetry dependence of optical transitions in group 4B transition metal dichalcogenides," *J. Phys. C Solid State Phys.*, vol. 15, no. 6, p. 1283, 1982.

[98] H. Jiang, "Structural and electronic properties of ZrX2 and HfX2 (X= S and Se) from first principles calculations," *J. Chem. Phys.*, vol. 134, no. 20, p. 204705, 2011.

[99] Dimple, N. Jena, A. Rawat, R. Ahammed, M. K. Mohanta, and A. De Sarkar, "Emergence of high piezoelectricity along with robust electron mobility in Janus structures in semiconducting Group IVB dichalcogenide monolayers," *J. Mater. Chem. A*, vol. 6, no. 48, pp. 24885–24898, 2018.

[100] M. Salavati, "Electronic and mechanical responses of two-dimensional HfS 2, HfSe 2, ZrS 2, and ZrSe 2 from first-principles," *Front. Struct. Civ. Eng.*, vol. 13, no. 2, pp. 486–494, 2019.

[101] J. Dai, M. Li, and X. C. Zeng, "Group IVB transition metal trichalcogenides: a new class of 2D layered materials beyond graphene," *Wiley Interdiscip. Rev. Comput. Mol. Sci.*, vol. 6, no. 2, pp. 211–222, 2016.

[102] W. Zhang, Z. Huang, W. Zhang, and Y. Li, "Two-dimensional semiconductors with possible high room temperature mobility," *Nano Res.*, vol. 7, no. 12, pp. 1731–1737, 2014.

[103] M. Hamada *et al.*, "High Hall-Effect Mobility of Atomic-Layered Polycrystalline-ZrS 2 Film using Sputtering and Sulfur Annealing," in *2019 Electron Devices Technology and Manufacturing Conference (EDTM)*, 2019, pp. 194–196.

[104] M. Hamada *et al.*, "High Hall-Effect Mobility of Large-Area Atomic-Layered Polycrystalline ZrS 2 Film Using UHV RF Magnetron Sputtering and Sulfurization," *IEEE J. Electron Devices Soc.*, vol. 7, pp. 1258–1263, 2019.

[105] Y. Yoon, K. Ganapathi, and S. Salahuddin, "How good can monolayer MoS_2 transistors be?," *Nano Lett.*, vol. 11, no. 9, pp. 3768–73, 2011.

[106] G. Ding, G. Y. Gao, Z. Huang, W. Zhang, and K. Yao, "Thermoelectric properties of monolayer MSe2 (M= Zr, Hf): low lattice thermal conductivity and a promising figure of merit," *Nanotechnology*, vol. 27, no. 37, p. 375703, 2016.

[107] C. Gong, H. Zhang, W. Wang, L. Colombo, R. M. Wallace, and K. Cho, "Band alignment of two-dimensional transition metal dichalcogenides: Application in tunnel field effect transistors," *Appl. Phys. Lett.*, vol. 103, no. 5, pp. 0–4, 2013.

[108] J.-S. You, S. Fang, S.-Y. Xu, E. Kaxiras, and T. Low, "Berry curvature dipole current in the transition metal dichalcogenides family," *Phys. Rev. B*, vol. 98, no. 12, p. 121109, 2018.

[109] A. V. Kolobov, P. Fons, and J. Tominaga, "Electronic excitation-induced semiconductor-to-metal transition in monolayer MoTe2," *Phys. Rev. B - Condens. Matter Mater. Phys.*, vol. 94,

no. 9, pp. 1–6, 2016.

[110] M. Calandra, “Chemically exfoliated single-layer MoS 2: Stability, lattice dynamics, and catalytic adsorption from first principles,” *Phys. Rev. B*, vol. 88, no. 24, p. 245428, 2013.

[111] Chen, K., Deng, J., Shi, Q., Ding, X., Sun, J., Yang, S. and Liu, J.Z., 2019. Modulating Peierls distortion of 1T_prime MoS2 via charge doping: a new charge density wave phase, reversible phase transition, and excellent electromechanical properties. *arXiv preprint arXiv:1912.07717*.

[112] Choe, D.H., Sung, H.J. and Chang, K.J., 2016. Understanding topological phase transition in monolayer transition metal dichalcogenides. *Physical Review B*, *93*(12), p.125109.

[113] Manna, S., Kamlapure, A., Cornils, L., Hänke, T., Hedegaard, E.M.J., Bremholm, M., Iversen, B.B., Hofmann, P., Wiebe, J. and Wiesendanger, R., 2016. Evidence for interfacial superconductivity in a bi-collinear antiferromagnetically ordered FeTe monolayer on a topological insulator. *arXiv preprint arXiv:1606.03249*.

[114] Ashton, M., Paul, J., Sinnott, S.B. and Hennig, R.G., 2017. Topology-scaling identification of layered solids and stable exfoliated 2D materials. *Physical review letters*, *118*(10), p.106101.

[115] Li, W. and Li, J., 2016. Ferroelasticity and domain physics in two-dimensional transition metal dichalcogenide monolayers. *Nature communications*, *7*(1), pp.1-8.

[116] Ma, Y., Kou, L., Li, X., Dai, Y., Smith, S.C. and Heine, T., 2015. Quantum spin Hall effect and topological phase transition in two-dimensional square transition-metal dichalcogenides. *Physical Review B*, *92*(8), p.085427.

[117] X. Lin and J. Ni, “Insulator–metal transition in 1T′-MoS2 under uniaxial strain,” *Phys. Lett. A*, vol. 379, no. 43–44, pp. 2883–2889, 2015.

[118] Y. Qi *et al.*, “Superconductivity in Weyl semimetal candidate MoTe2,” *Nat. Commun.*, vol. 7, p. 11038, 2016.

[119] Hsu, Y.T., Vaezi, A., Fischer, M.H. and Kim, E.A., 2017. Topological superconductivity in monolayer transition metal dichalcogenides. *Nature communications*, *8*(1), pp.1-6.

[120] K. Matsuda, “Optical Properties of Atomically Thin Layered Transition Metal Dichalchogenide,” *J. Phys. Soc. Japan*, vol. 84, no. 12, p. 121009, 2015.

[121] K. F. Mak, C. Lee, J. Hone, J. Shan, and T. F. Heinz, “Atomically thin MoS 2: a new direct-gap semiconductor,” *Phys. Rev. Lett.*, vol. 105, no. 13, p. 136805, 2010.

[122] N. L. Heda *et al.*, “Journal of Physics and Chemistry of Solids Electronic properties and Compton profiles of molybdenum dichalcogenides,” *J. Phys. Chem. Solids*, vol. 71, no. 3, pp. 187–193, 2010.

[123] Z. Y. Zhu, Y. C. Cheng, and U. Schwingenschl??gl, “Giant spin-orbit-induced spin splitting in two-dimensional transition-metal dichalcogenide semiconductors,” *Phys. Rev. B - Condens. Matter Mater. Phys.*, vol. 84, no. 15, 2011.

[124] Cheiwchanchamnangij, T. and Lambrecht, W.R., 2012. Quasiparticle band structure calculation of monolayer, bilayer, and bulk MoS 2. *Physical Review B*, *85*(20), p.205302.

[125] L. Wang and M. W. Wu, “Intrinsic electron spin relaxation due to the D’yakonov–Perel’mechanism in monolayer MoS2,” *Phys. Lett. A*, vol. 378, no. 18–19, pp. 1336–1340, 2014.

[126] A. Ramasubramaniam, “Large excitonic effects in monolayers of molybdenum and tungsten dichalcogenides,” *Phys. Rev. B*, vol. 86, no. 11, p. 115409, 2012.

[127] J. S. Ross *et al.*, “Electrically tunable excitonic light-emitting diodes based on monolayer

WSe2 pn junctions," *Nat. Nanotechnol.*, vol. 9, no. 4, pp. 268–272, 2014.

[128] A. Kormányos, V. Zólyomi, V. I. Fal'ko, and G. Burkard, "Tunable Berry curvature, valley and spin Hall effect in Bilayer MoS2," in *Spintronics XII*, 2019, vol. 11090, p. 110902F.

[129] A. Rycerz, J. Tworzydło, and C. W. J. Beenakker, "Valley filter and valley valve in graphene," *Nat. Phys.*, vol. 3, no. 3, pp. 172–175, 2007.

[130] T. Yan, X. Qiao, P. Tan, and X. Zhang, "Valley depolarization in monolayer WSe2.," *Sci. Rep.*, vol. 5, p. 15625, 2015.

[131] Zhang, L. and Niu, Q., 2015. Valley contrasting chiral phonons in monolayer hexagonal systems. *APS*, *2015*, pp.L2-008.

[132] W.-Y. Tong, S.-J. Gong, X. Wan, and C.-G. Duan, "The Concept of Ferrovalley Material and Anomalous Valley Hall Effect," *Nat. Commun.*, vol. 7, no. May, pp. 1–6, 2016.

[133] Q. Zhang, S. A. Yang, W. Mi, Y. Cheng, and U. Schwingenschlögl, "Large Spin-Valley Polarization in Monolayer MoTe2 on Top of EuO(111)," *Adv. Mater.*, vol. 28, no. 5, pp. 959–966, 2016.

[134] Y. Tatsumi, K. Ghalamkari, and R. Saito, "Laser energy dependence of valley polarization in transition-metal dichalcogenides," *Phys. Rev. B*, vol. 94, no. 23, p. 235408, 2016.

[135] K. F. Mak, K. He, J. Shan, and T. F. Heinz, "Control of valley polarization in monolayer MoS2 by optical helicity," *Nat. Nanotechnol.*, vol. 7, no. 8, pp. 494–498, 2012.

[136] H. Zeng, J. Dai, W. Yao, D. Xiao, and X. Cui, "Valley polarization in MoS2 monolayers by optical pumping," *Nat. Nanotechnol.*, vol. 7, no. 8, pp. 490–493, 2012.

[137] C. R. Zhu *et al.*, "Strain tuning of optical emission energy and polarization in monolayer and bilayer MoS 2," *Phys. Rev. B*, vol. 88, no. 12, p. 121301, 2013.

[138] C. Cui, F. Xue, W.-J. Hu, and L.-J. Li, "Two-dimensional materials with piezoelectric and ferroelectric functionalities," *npj 2D Mater. Appl.*, vol. 2, no. 1, p. 18, 2018.

[139] W. Wu and Z. L. Wang, "Piezotronics and piezo-phototronics for adaptive electronics and optoelectronics," *Nat. Publ. Gr.*, no. May, pp. 1–17, 2016.

[140] Duck, F., 2009. 'The electrical expansion of quartz'by Jacques and Pierre Curie. *Ultrasound*, *17*(4), pp.197-203.

[141] S. R. Anton and H. A. Sodano, "A review of power harvesting using piezoelectric materials (2003–2006)," *Smart Mater. Struct.*, vol. 16, no. 3, p. R1, 2007.

[142] O. Elmazria, M. B. Assouar, P. Renard, and P. Alnot, "Electrical properties of piezoelectric aluminium nitride films deposited by reactive dc magnetron sputtering," *Phys. status solidi*, vol. 196, no. 2, pp. 416–421, 2003.

[143] N. Sinha *et al.*, "Piezoelectric aluminum nitride nanoelectromechanical actuators," *Appl. Phys. Lett.*, vol. 95, no. 5, p. 53106, 2009.

[144] Z. Lin and J. Song, "Piezoelectric Nanogenerators Based on Zinc Oxide Nanowire Arrays Author(s): Zhong Lin Wang and Jinhui Song Source:," *Science (80-.).*, vol. 312, no. 5771, pp. 242–246, 2006.

[145] D. A. Parks and B. R. Tittmann, "Radiation tolerance of piezoelectric bulk single-crystal aluminum nitride," *IEEE Trans. Ultrason. Ferroelectr. Freq. Control*, vol. 61, no. 7, pp. 1216–1222, 2014.

[146] Y. Luo *et al.*, "Nanoshell tubes of ferroelectric lead zirconate titanate and barium titanate," *Appl. Phys. Lett.*, vol. 83, no. 3, pp. 440–442, 2003.

[147] K. Shimamura, H. Takeda, T. Kohno, and T. Fukuda, “Growth and characterization of lanthanum gallium silicate La3Ga5SiO14 single crystals for piezoelectric applications,” *J. Cryst. Growth*, vol. 163, no. 4, pp. 388–392, 1996.

[148] M. M. Aly??r??k, Y. Aierken, D. ??aklr, F. M. Peeters, and C. Sevik, “Promising Piezoelectric Performance of Single Layer Transition-Metal Dichalcogenides and Dioxides,” *J. Phys. Chem. C*, vol. 119, no. 40, pp. 23231–23237, 2015.

[149] Sherrit, S. and Mukherjee, B.K., 2007. Characterization of piezoelectric materials for transducers. *arXiv preprint arXiv:0711.2657*.

[150] M. Akhnak, O. Martinez, L. G. Ullate, and F. Montero De Espinosa, “64 Elements two-dimensional piezoelectric array for 3D imaging,” *Ultrasonics*, vol. 40, no. 1–8, pp. 139–143, 2002.

[151] G. Piazza, P. J. Stephanou, and A. P. Pisano, “Piezoelectric aluminum nitride vibrating contour-mode MEMS resonators,” *J. Microelectromechanical Syst.*, vol. 15, no. 6, pp. 1406–1418, 2006.

[152] A. Arnau, *Piezoelectric transducers and applications*, vol. 2004. Springer, 2004.

[153] K. A. N. Duerloo and E. J. Reed, “Flexural electromechanical coupling: A nanoscale emergent property of boron nitride bilayers,” *Nano Lett.*, vol. 13, no. 4, pp. 1681–1686, 2013.

[154] M. N. Blonsky, H. L. Zhuang, A. K. Singh, and R. G. Hennig, “Ab Initio Prediction of Piezoelectricity in Two-Dimensional Materials,” *ACS Nano*, vol. 9, no. 10, pp. 9885–9891, 2015.

[155] X. Wen, W. Wu, C. Pan, Y. Hu, Q. Yang, and Z. Lin Wang, “Development and progress in piezotronics,” *Nano Energy*, vol. 14, pp. 276–295, 2014.

[156] R. Hinchet, U. Khan, C. Falconi, and S.-W. Kim, “Piezoelectric properties in two-dimensional materials: Simulations and experiments,” *Mater. Today*, vol. 21, no. 6, pp. 611–630, 2018.

[157] M. Sitti, “Micro-and nano-scale robotics,” in *Proceedings of the 2004 American Control Conference*, 2004, vol. 1, pp. 1–8.

[158] T. Wang *et al.*, “Mechano-Based Transductive Sensing for Wearable Healthcare,” *Small*, vol. 14, no. 11, p. 1702933, 2018.

[159] H. Zhu *et al.*, “Observation of piezoelectricity in free-standing monolayer MoS_2.,” *Nat. Nanotechnol.*, vol. 10, no. 2, pp. 151–5, 2015.

[160] T. D. Nguyen *et al.*, “Piezoelectric nanoribbons for monitoring cellular deformations,” *Nat Nanotechnol*, vol. 7, no. 9, pp. 587–593, 2012.

[161] R. Fei, W. Li, J. Li, and L. Yang, “Giant piezoelectricity of monolayer group IV monochalcogenides: SnSe, SnS, GeSe, and GeS,” *Appl. Phys. Lett.*, vol. 107, no. 17, pp. 1–5, 2015.

[162] Y. Chen, J. Liu, J. Yu, Y. Guo, and Q. Sun, “Symmetry-breaking induced large piezoelectricity in Janus tellurene materials,” *Phys. Chem. Chem. Phys.*, vol. 21, no. 3, pp. 1207–1216, 2019.

[163] H. Zhu *et al.*, “Observation of piezoelectricity in free-standing monolayer MoS_2.,” *Nat. Nanotechnol.*, vol. 10, no. 2, pp. 151–5, 2015.

[164] D. Ovchinnikov, A. Allain, Y.-S. Huang, and D. Dumcenco, “Electrical Transport Properties of Single-Layer WS 2,” *ACS Nano*, vol. 8, no. 8, pp. 8174–81, 2014.

[165] H. Schmidt, F. Giustiniano, and G. Eda, “Electronic transport properties of transition metal

dichalcogenide field-effect devices: surface and interface effects," *Chem. Soc. Rev.*, vol. 44, pp. 7715–7736, 2015.

[166] S. Bertolazzi, J. Brivio, and A. Kis, "Stretching and breaking of ultrathin MoS2," *ACS Nano*, vol. 5, no. 12, pp. 9703–9709, 2011.

[167] Alyörük, M.M., Aierken, Y., Çakır, D., Peeters, F.M. and Sevik, C., 2015. Promising piezoelectric performance of single layer transition-metal dichalcogenides and dioxides. *The Journal of Physical Chemistry C*, *119*(40), pp.23231-23237.

[168] S. K. Kim *et al.*, "Directional dependent piezoelectric effect in CVD grown monolayer MoS2 for flexible piezoelectric nanogenerators," *Nano Energy*, vol. 22, pp. 483–489, 2016.

[169] J. Qi *et al.*, "Piezoelectric effect in chemical vapour deposition-grown atomic-monolayer triangular molybdenum disulfide piezotronics," *Nat. Commun.*, vol. 6, p. 7430, 2015.

[170] J. Kou, Y. Liu, Y. Zhu, and J. Zhai, "Progress in piezotronics of transition-metal dichalcogenides," *J. Phys. D. Appl. Phys.*, vol. 51, no. 49, p. 493002, 2018.

[171] W. Wu *et al.*, "Piezoelectricity of single-atomic-layer MoS2 for energy conversion and piezotronics," *Nature*, vol. 514, no. 7523, pp. 470–474, 2014.

[172] Z. L. Wang, "Piezopotential gated nanowire devices : Piezotronics and piezo-phototronics," *Nano Today*, vol. 5, no. 6, pp. 540–552, 2010.

[173] Y. Kim, Y. I. Jhon, J. Park, J. H. Kim, S. Lee, and Y. M. Jhon, "Anomalous Raman scattering and lattice dynamics in mono-and few-layer WTe 2," *Nanoscale*, vol. 8, no. 4, pp. 2309–2316, 2016.

[174] S. Sugai, K. Murase, S. Uchida, and S. Tanaka, "Studies of lattice dynamics in 2H□ TaS2 by Raman scattering," *Solid State Commun.*, vol. 40, no. 4, pp. 399–401, 1981.

[175] D. Christiansen *et al.*, "Phonon sidebands in monolayer transition metal dichalcogenides," *Phys. Rev. Lett.*, vol. 119, no. 18, p. 187402, 2017.

[176] P. Dey *et al.*, "Optical coherence in atomic-monolayer transition-metal dichalcogenides limited by electron-phonon interactions," *Phys. Rev. Lett.*, vol. 116, no. 12, p. 127402, 2016.

[177] N. Wakabayashi, H. G. Smith, and R. M. Nicklow, "Lattice dynamics of hexagonal Mo S 2 studied by neutron scattering," *Phys. Rev. B*, vol. 12, no. 2, p. 659, 1975.

[178] R. Saito, Y. Tatsumi, S. Huang, X. Ling, and M. S. Dresselhaus, "Raman spectroscopy of transition metal dichalcogenides," *J. Phys. Condens. Matter*, vol. 28, no. 35, p. 353002, 2016.

[179] X. Zhang, X.-F. Qiao, W. Shi, J.-B. Wu, D.-S. Jiang, and P.-H. Tan, "Phonon and Raman scattering of two-dimensional transition metal dichalcogenides from monolayer, multilayer to bulk material," *Chem. Soc. Rev.*, vol. 44, no. 9, pp. 2757–2785, 2015.

[180] W. Zhao *et al.*, "Lattice dynamics in mono-and few-layer sheets of WS 2 and WSe 2," *Nanoscale*, vol. 5, no. 20, pp. 9677–9683, 2013.

[181] B. Chakraborty, A. Bera, D. V. S. Muthu, S. Bhowmick, U. V Waghmare, and A. K. Sood, "Symmetry-dependent phonon renormalization in monolayer MoS${}_{2}$ transistor," *Phys. Rev. B*, vol. 85, no. 16, p. 161403, Apr. 2012.

[182] A. S. Pawbake, M. S. Pawar, S. R. Jadkar, and D. J. Late, "Large area chemical vapor deposition of monolayer transition metal dichalcogenides and their temperature dependent Raman spectroscopy studies," *Nanoscale*, vol. 8, no. 5, pp. 3008–3018, 2016.

[183] S. V Bhatt, M. P. Deshpande, V. Sathe, R. Rao, and S. H. Chaki, "Raman spectroscopic investigations on transition-metal dichalcogenides MX2 (M= Mo, W; X= S, Se) at high

pressures and low temperature," *J. Raman Spectrosc.*, vol. 45, no. 10, pp. 971–979, 2014.

[184] Lu, A.Y., Zhu, H., Xiao, J., Chuu, C.P., Han, Y., Chiu, M.H., Cheng, C.C., Yang, C.W., Wei, K.H., Yang, Y. and Wang, Y., 2017. Janus monolayers of transition metal dichalcogenides. *Nature nanotechnology*, *12*(8), pp.744-749.

[185] Zhang, J., Jia, S., Kholmanov, I., Dong, L., Er, D., Chen, W., Guo, H., Jin, Z., Shenoy, V.B., Shi, L. and Lou, J., 2017. Janus monolayer transition-metal dichalcogenides. *ACS nano*, *11*(8), pp.8192-8198.

[186] Dong, L., Lou, J. and Shenoy, V.B., 2017. Large in-plane and vertical piezoelectricity in Janus transition metal dichalchogenides. *ACS nano*, *11*(8), pp.8242-8248.

[187] D. Er, H. Ye, N. C. Frey, H. Kumar, J. Lou, and V. B. Shenoy, "Prediction of enhanced catalytic activity for hydrogen evolution reaction in Janus transition metal dichalcogenides," *Nano Lett.*, vol. 18, no. 6, pp. 3943–3949, 2018.

[188] Y. Ji *et al.*, "Janus Structures of Transition Metal Dichalcogenides as the Heterojunction Photocatalysts for Water Splitting," *J. Phys. Chem. C*, vol. 122, no. 5, pp. 3123–3129, 2018.

[189] W. Kohn and L. J. Sham, "Self-Consistent Equations Including Exchange and Correlation Effects," *Physical Review*, vol. 140, no. 4A. pp. A1133–A1138, 1965.

[190] J. P. Perdew, K. Burke, and M. Ernzerhof, "Generalized Gradient Approximation Made Simple," *Phys. Rev. Lett.*, vol. 77, no. 18, pp. 3865–3868, 1996.

[191] J. W. Negele, "Structure of finite nuclei in the local-density approximation," *Phys. Rev. C*, vol. 1, no. 4, p. 1260, 1970.

[192] B. Santra, A. Michaelides, M. Fuchs, A. Tkatchenko, C. Filippi, and M. Scheffler, "On the accuracy of density-functional theory exchange-correlation functionals for H bonds in small water clusters. II. The water hexamer and van der Waals interactions," *J. Chem. Phys.*, vol. 129, no. 19, p. 194111, 2008.

[193] M. Grodzicki, J. M. Seminario, and P. Politzer, "Energy barriers of symmetry-forbidden reactions: Local density functional calculations," *J. Chem. Phys.*, vol. 94, no. 2, pp. 1668–1669, 1991.

[194] O. Gunnarsson and R. O. Jones, "Total-energy differences: Sources of error in local-density approximations," *Phys. Rev. B*, vol. 31, no. 12, p. 7588, 1985.

[195] I. N. Yakovkin and P. A. Dowben, "The problem of the band gap in LDA calculations," *Surf. Rev. Lett.*, vol. 14, no. 03, pp. 481–487, 2007.

[196] D. C. Langreth and M. J. Mehl, "Beyond the local-density approximation in calculations of ground-state electronic properties," *Phys. Rev. B*, vol. 28, no. 4, p. 1809, 1983.

[197] C. Filippi, D. J. Singh, and C. J. Umrigar, "All-electron local-density and generalized-gradient calculations of the structural properties of semiconductors," *Phys. Rev. B*, vol. 50, no. 20, p. 14947, 1994.

[198] M. Städele, M. Moukara, J. A. Majewski, P. Vogl, and A. Görling, "Exact exchange Kohn-Sham formalism applied to semiconductors," *Phys. Rev. B*, vol. 59, no. 15, p. 10031, 1999.

[199] J. P. Perdew and W. Yue, "Accurate and simple density functional for the electronic exchange energy: Generalized gradient approximation," *Phys. Rev. B*, vol. 33, no. 12, p. 8800, 1986.

[200] J. P. Perdew, K. Burke, and Y. Wang, "Generalized gradient approximation for the exchange-correlation hole of a many-electron system," *Phys. Rev. B*, vol. 54, no. 23, p. 16533, 1996.

[201] J. P. Perdew, P. Ziesche, and H. Eschrig, "Electronic structure of solids' 91." Akademie

Verlag, Berlin, 1991.

[202] H. Peng and J. P. Perdew, “Rehabilitation of the Perdew-Burke-Ernzerhof generalized gradient approximation for layered materials,” *Phys. Rev. B*, vol. 95, no. 8, p. 81105, 2017.

[203] N. Wu *et al.*, “Strain effect on the electronic properties of 1T-HfS2 monolayer,” *Phys. E Low-dimensional Syst. Nanostructures*, vol. 93, pp. 1–5, 2017.

[204] A. P. Nayak *et al.*, “Pressure-dependent optical and vibrational properties of monolayer molybdenum disulfide,” *Nano Lett.*, vol. 15, no. 1, pp. 346–353, 2015.

[205] H. J. Conley, B. Wang, J. I. Ziegler, R. F. Haglund Jr, S. T. Pantelides, and K. I. Bolotin, “Bandgap engineering of strained monolayer and bilayer MoS2,” *Nano Lett.*, vol. 13, no. 8, pp. 3626–3630, 2013.

[206] B. Ghosh, S. Nahas, S. Bhowmick, and A. Agarwal, “Electric field induced gap modification in ultrathin blue phosphorus,” *Phys. Rev. B*, vol. 91, no. 11, p. 115433, 2015.

[207] A. D. Becke, “A new mixing of Hartree–Fock and local density-functional theories,” *J. Chem. Phys.*, vol. 98, no. 2, pp. 1372–1377, 1993.

[208] A. D. Becke, “Real-space post-Hartree–Fock correlation models,” *J. Chem. Phys.*, vol. 122, no. 6, p. 64101, 2005.

[209] J. Heyd, G. E. Scuseria, and M. Ernzerhof, “Hybrid functionals based on a screened Coulomb potential,” *J. Chem. Phys.*, vol. 118, no. 18, pp. 8207–8215, 2003.

[210] A. V. Krukau, O. A. Vydrov, A. F. Izmaylov, and G. E. Scuseria, “Influence of the exchange screening parameter on the performance of screened hybrid functionals,” *J. Chem. Phys.*, vol. 125, no. 22, 2006.

[211] J. Heyd and G. E. Scuseria, “Efficient hybrid density functional calculations in solids: Assessment of the Heyd-Scuseria-Ernzerhof screened Coulomb hybrid functional,” *J. Chem. Phys.*, vol. 121, no. 3, pp. 1187–1192, 2004.

[212] A. Carvalho, S. Öberg, M. J. Rayson, and P. R. Briddon, “Electronic properties, doping, and defects in chlorinated silicon nanocrystals,” *Phys. Rev. B*, vol. 86, no. 4, p. 45308, 2012.

[213] T. M. Henderson, J. Paier, and G. E. Scuseria, “Accurate treatment of solids with the HSE screened hybrid,” *Phys. status solidi*, vol. 248, no. 4, pp. 767–774, 2011.

[214] D. S. Koda, F. Bechstedt, M. Marques, and L. K. Teles, “Trends on band alignments: Validity of Anderson’s rule in SnS 2-and SnSe 2-based van der Waals heterostructures,” *Phys. Rev. B*, vol. 97, no. 16, p. 165402, 2018.

[215] S. Bhattacharyya and A. K. Singh, “Semiconductor-metal transition in semiconducting bilayer sheets of transition-metal dichalcogenides,” *Phys. Rev. B - Condens. Matter Mater. Phys.*, vol. 86, no. 7, pp. 1–16, 2012.

[216] X. Wu, D. Vanderbilt, and D. R. Hamann, “Systematic treatment of displacements, strains, and electric fields in density-functional perturbation theory,” *Phys. Rev. B - Condens. Matter Mater. Phys.*, vol. 72, no. 3, pp. 1–13, 2005.

[217] S. Baroni *et al.*, “Phonons and related crystal properties from density-functional perturbation theory,” *Rev. Mod. Phys.*, vol. 73, no. 2, p. 515, 2001.

[218] Landolt, G., Eremeev, S.V., Koroteev, Y.M., Slomski, B., Muff, S., Neupert, T., Kobayashi, M., Strocov, V.N., Schmitt, T., Aliev, Z.S. and Babanly, M.B., 2012. Disentanglement of surface and bulk Rashba spin splittings in noncentrosymmetric BiTeI. *Physical review letters*, *109*(11), p.116403.

[219] Dil, J.H., 2009. Spin and angle resolved photoemission on non-magnetic low-dimensional systems. *Journal of Physics: Condensed Matter*, *21*(40), p.403001.

[220] Ideue, T., Hamamoto, K., Koshikawa, S., Ezawa, M., Shimizu, S., Kaneko, Y., Tokura, Y., Nagaosa, N. and Iwasa, Y., 2017. Bulk rectification effect in a polar semiconductor. *Nature Physics*, *13*(6), pp.578-583.

[221] Isasa, M., Martínez-Velarte, M.C., Villamor, E., Magén, C., Morellón, L., De Teresa, J.M., Ibarra, M.R., Vignale, G., Chulkov, E.V., Krasovskii, E.E. and Hueso, L.E., 2016. Origin of inverse Rashba-Edelstein effect detected at the Cu/Bi interface using lateral spin valves. *Physical Review B*, *93*(1), p.014420.

[222] M. Chhowalla, H. S. Shin, G. Eda, L.-J. Li, K. P. Loh, and H. Zhang, "The chemistry of two-dimensional layered transition metal dichalcogenide nanosheets," *Nat. Chem.*, vol. 5, no. 4, pp. 263–275, 2013.

[223] Schmidt, H., Giustiniano, F. and Eda, G., 2015. Electronic transport properties of transition metal dichalcogenide field-effect devices: surface and interface effects. *Chemical Society Reviews*, *44*(21), pp.7715-7736.

[224] Q. H. Wang, K. Kalantar-zadeh, A. Kis, J. N. Coleman, and M. S. Strano, "transition metal dichalcogenides," *Nat. Publ. Gr.*, vol. 7, no. 11, pp. 699–712, 2012.

[225] X. Duan, C. Wang, A. Pan, R. Yu, and X. Duan, "Chem Soc Rev Two-dimensional transition metal dichalcogenides as atomically thin semiconductors : opportunities and challenges," *Chem. Soc. Rev.*, vol. 44, pp. 8859–8876, 2015.

[226] K. F. Mak and J. Shan, "transition metal dichalcogenides," *Nat. Publ. Gr.*, vol. 10, no. 4, pp. 216–226, 2016.

[227] B. Radisavljevic, A. Radenovic, J. Brivio, V. Giacometti, and A. Kis, "Single-layer MoS2 transistors," *Nat Nano*, vol. 6, no. 3, pp. 147–150, 2011.

[228] Bercioux, D. and Lucignano, P., 2015. Quantum transport in Rashba spin–orbit materials: a review. *Reports on Progress in Physics*, *78*(10), p.106001.

[229] T. Cao *et al.*, "Valley-selective circular dichroism of monolayer molybdenum disulphide," *Nat. Commun.*, vol. 3, no. May, pp. 885–887, 2012.

[230] Z. Wu *et al.*, "Even–odd layer-dependent magnetotransport of high-mobility Q-valley electrons in transition metal disulfides," *Nat. Commun.*, vol. 7, pp. 1–8, 2016.

[231] Z. Gong *et al.*, "Magnetoelectric effects and valley-controlled spin quantum gates in transition metal dichalcogenide bilayers.," *Nat. Commun.*, vol. 4, no. May, p. 2053, 2013.

[232] M. A. Cazalilla, H. Ochoa, and F. Guinea, "Quantum spin hall effect in two-dimensional crystals of transition-metal dichalcogenides," *Phys. Rev. Lett.*, vol. 113, no. 7, pp. 1–6, 2014.

[233] Ye, Y., Xiao, J., Wang, H., Ye, Z., Zhu, H., Zhao, M., Wang, Y., Zhao, J., Yin, X. and Zhang, X., 2016. Electrical generation and control of the valley carriers in a monolayer transition metal dichalcogenide. *Nature nanotechnology*, *11*(7), pp.598-602.

[234] H. Yu, G.-B. Liu, P. Gong, X. Xu, and W. Yao, "Dirac cones and Dirac saddle points of bright excitons in monolayer transition metal dichalcogenides," *Nat. Commun.*, vol. 5, no. 1, p. 3876, 2014.

[235] S. C. Masmanidis, R. B. Karabalin, I. De Vlaminck, G. Borghs, M. R. Freeman, and M. L. Roukes, "Multifunctional nanomechanical systems via tunably coupled piezoelectric actuation," *Science (80-.).*, vol. 317, no. 5839, pp. 780–783, 2007.

[236] López-Suárez, M., Pruneda, M., Abadal, G. and Rurali, R., 2014. Piezoelectric monolayers as

nonlinear energy harvesters. *Nanotechnology*, *25*(17), p.175401.

[237] Dong, L., Lou, J. and Shenoy, V.B., 2017. Large in-plane and vertical piezoelectricity in Janus transition metal dichalchogenides. *ACS nano*, *11*(8), pp.8242-8248.

[238] E. I. Rashba, "Properties of semiconductors with an extremum loop. I. Cyclotron and combinational resonance in a magnetic field perpendicular to the plane of the loop," *Sov. Physics, Solid State*, vol. 2, pp. 1109–1122, 1960.

[239] Y. C. Cheng, Z. Y. Zhu, M. Tahir, and U. Schwingenschlögl, "Spin-orbit-induced spin splittings in polar transition metal dichalcogenide monolayers," *Epl*, vol. 102, no. 5, 2013.

[240] LaShell, S., McDougall, B. and Jensen, E., 1996. Spin splitting of an Au (111) surface state band observed with angle resolved photoelectron spectroscopy. *Physical review letters*, *77*(16), p.3419.

[241] Krupin, O., Bihlmayer, G., Starke, K., Gorovikov, S., Prieto, J.E., Döbrich, K., Blügel, S. and Kaindl, G., 2005. Rashba effect at magnetic metal surfaces. *Physical Review B*, *71*(20), p.201403.

[242] Crepaldi, A., Moreschini, L., Autes, G., Tournier-Colletta, C., Moser, S., Virk, N., Berger, H., Bugnon, P., Chang, Y.J., Kern, K. and Bostwick, A., 2012. Giant ambipolar Rashba effect in the semiconductor BiTeI. *Physical review letters*, *109*(9), p.096803.

[243] Nitta, J., Akazaki, T., Takayanagi, H. and Enoki, T., 1997. Gate Control of Spin-Orbit Interaction in an Inverted I n 0.53 G a 0.47 As/I n 0.52 A l 0.48 As Heterostructure. *Physical Review Letters*, *78*(7), p.1335.

[244] Dedkov, Y.S., Fonin, M., Rüdiger, U. and Laubschat, C., 2008. Rashba effect in the graphene/Ni (111) system. *Physical review letters*, *100*(10), p.107602.

[245] D. Zhong *et al.*, "Van der Waals engineering of ferromagnetic semiconductor heterostructures for spin and valleytronics," *Sci. Adv.*, vol. 3, no. 5, p. e1603113, 2017.

[246] A. H. . Castro Neto, N. M. R. . Peres, K. S. . Novoselov, A. K. . Geim, and F. Guinea, "The electronic properties of graphene," *Rev. Mod. Phys.*, vol. 81, no. 1, pp. 109–162, 2009.

[247] Datta, S. and Das, B., 1990. Electronic analog of the electro-optic modulator. *Applied Physics Letters*, *56*(7), pp.665-667.

[248] H. Yuan *et al.*, "Zeeman-type spin splitting controlled by an electric field," *Nat. Phys.*, vol. 9, no. 9, pp. 563–569, 2013.

[249] G. Kresse and J. Hafner, "Ab Initio Molecular-Dynamics Simulation of the Liquid-Metal-Amorphous-Semiconductor Transition in Germanium," *Physical Review B: Condensed Matter and Materials Physics*, vol. 49, no. 20. pp. 14251–14269, 1994.

[250] G. Kresse and J. Furthmüller, "Efficiency of ab-initio total energy calculations for metals and semiconductors using a plane-wave basis set," *Comput. Mater. Sci.*, vol. 6, no. 1, pp. 15–50, 1996.

[251] G. and J. F. Kresse and J. Furthmüller, "Efficient iterative schemes for ab initio total-energy calculations using a plane-wave basis set," *Phys. Rev. B*, vol. 54, no. 16, p. 11169, 1996.

[252] P. E. Blöchl, "Projector augmented-wave method," *Physical Review B*, vol. 50, no. 24. pp. 953–979, 1994.

[253] A. Togo and I. Tanaka, "First principles phonon calculations in materials science," *Scr. Mater.*, vol. 108, pp. 1–5, 2015.

[254] M. Kamaratos and C. A. Papageorgopoulos, "Adsorption studies on Ar+ -sputtered

MoS2(0001)," *Surf. Sci.*, vol. 178, no. 1–3, pp. 865–871, Dec. 1986.

[255] I. T. McGovern, R. H. Williams, and C. H. B. Mee, "Electronic properties of cleaved molybdenum disulphide surfaces," *Surf. Sci.*, vol. 46, no. 2, pp. 427–440, Dec. 1974.

[256] J. C. McMenamin and W. E. Spicer, "Photoemission studies of layered transition-metal dichalcogenides: Mo S 2," *Phys. Rev. B*, vol. 16, no. 12, pp. 5474–5487, Dec. 1977.

[257] Michaelson, H.B., 1977. The work function of the elements and its periodicity. *Journal of applied physics*, *48*(11), pp.4729-4733.

[258] L. Song *et al.*, "Large scale growth and characterization of atomic hexagonal boron nitride layers," *Nano Lett.*, vol. 10, no. 8, pp. 3209–3215, 2010.

[259] D. Xiao, G. Bin Liu, W. Feng, X. Xu, and W. Yao, "Coupled spin and valley physics in monolayers of MoS 2 and other group-VI dichalcogenides," *Phys. Rev. Lett.*, vol. 108, no. 19, pp. 1–5, 2012.

[260] M. Chhowalla, H. S. Shin, G. Eda, L.-J. Li, K. P. Loh, and H. Zhang, "The chemistry of two-dimensional layered transition metal dichalcogenide nanosheets," *Nat. Chem.*, vol. 5, no. 4, pp. 263–275, 2013.

[261] K. K. Kam and B. A. Parkinson, "Detailed photocurrent spectroscopy of the semiconducting group VIB transition metal dichalcogenides," *J. Phys. Chem.*, vol. 86, no. 4, pp. 463–467, 1982.

[262] A. Kuc, N. Zibouche, and T. Heine, "Influence of quantum confinement on the electronic structure of the transition metal sulfide T S 2," *Phys. Rev. B*, vol. 83, no. 24, p. 245213, 2011.

[263] RadisavljevicB *et al.*, "Single-layer MoS2 transistors," *Nat Nano*, vol. 6, no. 3, pp. 147–150, 2011.

[264] Mohammad Tabatabaei, S., Noei, M., Khaliji, K., Pourfath, M. and Fathipour, M., 2013. A first-principles study on the effect of biaxial strain on the ultimate performance of monolayer MoS2-based double gate field effect transistor. *Journal of Applied Physics*, *113*(16), p.163708.

[265] J. Feng, X. Qian, C.-W. Huang, and J. Li, "Strain-engineered artificial atom as a broad-spectrum solar energy funnel," *Nat. Photonics*, vol. 6, no. 12, pp. 866–872, 2012.

[266] H. Shi, H. Pan, Y. W. Zhang, and B. I. Yakobson, "Quasiparticle band structures and optical properties of strained monolayer MoS2 and WS2," *Phys. Rev. B - Condens. Matter Mater. Phys.*, vol. 87, no. 15, pp. 1–8, 2013.

[267] H. Peelaers and C. G. Van de Walle, "Effects of strain on band structure and effective masses in MoS 2," *Phys. Rev. B*, vol. 86, no. 24, p. 241401, 2012.

[268] D. Fu *et al.*, "Mechanically modulated tunneling resistance in monolayer MoS2," *Appl. Phys. Lett.*, vol. 103, no. 18, p. 183105, 2013.

[269] M. Hosseini, M. Elahi, M. Pourfath, and D. Esseni, "Strain induced mobility modulation in single-layer MoS2," *J. Phys. D-Applied Phys.*, vol. 48, no. 37, p. 11, 2015.

[270] S. Yu, H. D. Xiong, K. Eshun, H. Yuan, and Q. Li, "Phase transition, effective mass and carrier mobility of MoS2 monolayer under tensile strain," *Appl. Surf. Sci.*, vol. 325, pp. 27–32, 2015.

[271] A. Castellanos-Gomez, M. Poot, G. a. Steele, H. S. J. van der Zant, N. Agrait, and G. Rubio-Bollinger, "Mechanical properties of freely suspended semiconducting graphene-like layers based on MoS2," *Nanoscale Res. Lett.*, vol. 7, no. 1, p. 233, 2012.

[272] Gómez-Navarro, C., Burghard, M. and Kern, K., 2008. Elastic properties of chemically

derived single graphene sheets. *Nano letters*, *8*(7), pp.2045-2049.

[273] H. P. Komsa, S. Kurasch, O. Lehtinen, U. Kaiser, and A. V. Krasheninnikov, “From point to extended defects in two-dimensional MoS2: Evolution of atomic structure under electron irradiation,” *Phys. Rev. B - Condens. Matter Mater. Phys.*, vol. 88, no. 3, pp. 1–8, 2013.

[274] N. Jena, Dimple, S. D. Behere, and A. De Sarkar, “Strain-Induced Optimization of Nanoelectromechanical Energy Harvesting and Nanopiezotronic Response in a MoS<inf>2</inf>Monolayer Nanosheet,” *J. Phys. Chem. C*, vol. 121, no. 17, 2017.

[275] Cooper, R.C., Lee, C., Marianetti, C.A., Wei, X., Hone, J. and Kysar, J.W., 2013. Nonlinear elastic behavior of two-dimensional molybdenum disulfide. *Physical Review B*, *87*(3), p.035423.

[276] N. Zibouche, P. Philipsen, A. Kuc, and T. Heine, “Transition-metal dichalcogenide bilayers: Switching materials for spintronic and valleytronic applications,” *Phys. Rev. B - Condens. Matter Mater. Phys.*, vol. 90, no. 12, pp. 1–6, 2014.

[277] A. Ramasubramaniam, D. Naveh, and E. Towe, “Tunable band gaps in bilayer transition-metal dichalcogenides,” *Phys. Rev. B*, vol. 84, no. 20, p. 205325, 2011.

[278] Y. Wang, C. Cong, C. Qiu, and T. Yu, “Raman spectroscopy study of lattice vibration and crystallographic orientation of monolayer mos2 under uniaxial strain,” *Small*, vol. 9, no. 17, pp. 2857–2861, 2013.

[279] K. He, C. Poole, K. F. Mak, and J. Shan, “Experimental demonstration of continuous electronic structure tuning via strain in atomically thin MoS2,” *Nano Lett.*, vol. 13, no. 6, pp. 2931–2936, 2013.

[280] A. Castellanos-Gomez *et al.*, “Local strain engineering in atomically thin MoS2,” *Nano Lett.*, vol. 13, no. 11, pp. 5361–5366, 2013.

[281] C. Si, Z. Sun, and F. Liu, “Strain engineering of graphene: a review,” *Nanoscale*, vol. 8, no. 6, pp. 3207–3217, 2016.

[282] W. Wei, Y. Dai, and B. Huang, “Straintronics in two-dimensional in-plane heterostructures of transition-metal dichalcogenides,” *Phys. Chem. Chem. Phys.*, vol. 19, no. 1, pp. 663–672, 2017.

[283] M. Ghorbani-Asl, S. Borini, A. Kuc, and T. Heine, “Strain-dependent modulation of conductivity in single-layer transition-metal dichalcogenides,” *Phys. Rev. B*, vol. 87, no. 23, p. 235434, 2013.

[284] G. Sallen *et al.*, “Robust optical emission polarization in MoS 2 monolayers through selective valley excitation,” *Phys. Rev. B*, vol. 86, no. 8, p. 81301, 2012.

[285] D. Xiao, M.-C. Chang, and Q. Niu, “Berry phase effects on electronic properties,” *Rev. Mod. Phys.*, vol. 82, no. 3, p. 1959, 2010.

[286] K. Kośmider, J. W. González, and J. Fernández-Rossier, “Large spin splitting in the conduction band of transition metal dichalcogenide monolayers,” *Phys. Rev. B*, vol. 88, no. 24, p. 245436, 2013.

[287] O. Gunawan, Y. P. Shkolnikov, K. Vakili, T. Gokmen, E. P. De Poortere, and M. Shayegan, “Valley susceptibility of an interacting two-dimensional electron system,” *Phys. Rev. Lett.*, vol. 97, no. 18, p. 186404, 2006.

[288] G. Kresse, “From ultrasoft pseudopotentials to the projector augmented-wave method,” *Phys. Rev. B*, vol. 59, no. 3, pp. 1758–1775, 1999.

[289] P. E. Blöchl, “Projector augmented-wave method,” *Phys. Rev. B*, vol. 50, no. 24, pp. 17953–

17979, 1994.

[290] G. Kresse and J. Hafner, “Ab initio molecular dynamics for open-shell transition metals,” *Phys. Rev. B*, vol. 48, no. 17, pp. 13115–13118, 1993.

[291] G. Kresse and J. Hafner, “Ab initio molecular-dynamics simulation of the liquid-metal–amorphous-semiconductor transition in germanium,” *Phys. Rev. B*, vol. 49, no. 20, p. 14251, 1994.

[292] G. Kresse and J. Furthmüller, “Efficient iterative schemes for ab initio total-energy calculations using a plane-wave basis set,” *Phys. Rev. B*, vol. 54, no. 16, p. 11169, 1996.

[293] J. P. Perdew, K. Burke, and M. Ernzerhof, “Generalized Gradient Approximation Made Simple,” *Phys. Rev. Lett.*, vol. 77, no. 18, pp. 3865–3868, 1996.

[294] J. P. Perdew and Y. Wang, “Accurate and simple analytic representation of the electron-gas correlation energy,” *Physical Review B*, vol. 45, no. 23. pp. 13244–13249, 1992.

[295] Fukui, T., Hatsugai, Y. and Suzuki, H., 2005. Chern numbers in discretized Brillouin zone: efficient method of computing (spin) Hall conductances. *Journal of the Physical Society of Japan*, *74*(6), pp.1674-1677.

[296] Y. Cai, G. Zhang, and Y.-W. Zhang, “Polarity-reversed robust carrier mobility in monolayer MoS2 nanoribbons,” *J. Am. Chem. Soc.*, vol. 136, no. 17, pp. 6269–6275, 2014.

[297] J. Xiao, M. Q. Long, M. J. Li, X. M. Li, H. Xu, and K. S. Chan, “Carrier mobility of MoS2 nanoribbons with edge chemical modification,” *Phys. Chem. Chem. Phys.*, vol. 17, no. 10, pp. 6865–6873, 2015.

[298] T. Jia *et al.*, “Dirac cone move and bandgap on / off switching of graphene superlattice,” *Nat. Publ. Gr.*, no. June 2015, pp. 1–11, 2016.

[299] Y. Su and X. Fan, “Germanene nanomeshes: Cooperative effects of degenerate perturbation and uniaxial strain on tuning bandgap,” *Chinese Phys. B*, vol. 26, no. 10, p. 108101, 2017.

[300] W. S. Yun, S. W. Han, S. C. Hong, I. G. Kim, and J. D. Lee, “Thickness and strain effects on electronic structures of transition metal dichalcogenides: 2H-M X 2 semiconductors (M= Mo, W; X= S, Se, Te),” *Phys. Rev. B*, vol. 85, no. 3, p. 33305, 2012.

[301] Liang, Y., Huang, S., Soklaski, R. and Yang, L., 2013. Quasiparticle band-edge energy and band offsets of monolayer of molybdenum and tungsten chalcogenides. *Applied Physics Letters*, *103*(4), p.042106.

[302] Q. Yue *et al.*, “Mechanical and electronic properties of monolayer MoS 2 under elastic strain,” *Phys. Lett. A*, vol. 376, no. 12–13, pp. 1166–1170, 2012.

[303] M. Mohr, K. Papagelis, J. Maultzsch, and C. Thomsen, “Two-dimensional electronic and vibrational band structure of uniaxially strained graphene from ab initio calculations,” *Phys. Rev. B*, vol. 80, no. 20, p. 205410, 2009.

[304] D. Dimple, N. Jena, A. Rawat, and A. De Sarkar, “Strain and pH facilitated artificial photosynthesis in monolayer MoS2 nanosheet,” *J. Mater. Chem. A*, vol. 5, pp. 22265–22276, 2017.

[305] N. Jena, S. D. Behere, and A. De Sarkar, “Strain-Induced Optimization of Nanoelectromechanical Energy Harvesting and Nanopiezotronic Response in a MoS2 Monolayer Nanosheet,” *J. Phys. Chem. C*, vol. 121, no. 17, pp. 9181–9190, 2017.

[306] M. I. Katsnelson and A. K. Geim, “Energy gaps and a zero-field quantum Hall effect in graphene by strain engineering,” *Nat. Phys.*, vol. 6, no. 1, pp. 30–33, 2009.

[307] Conley, H.J., Wang, B., Ziegler, J.I., Haglund Jr, R.F., Pantelides, S.T. and Bolotin, K.I., 2013. Bandgap engineering of strained monolayer and bilayer MoS2. *Nano letters*, *13*(8), pp.3626-3630.

[308] T. Li, "Ideal strength and phonon instability in single-layer MoS 2," *Phys. Rev. B*, vol. 85, no. 23, p. 235407, 2012.

[309] Yang, L., Cui, X., Zhang, J., Wang, K., Shen, M., Zeng, S., Dayeh, S.A., Feng, L. and Xiang, B., 2014. Lattice strain effects on the optical properties of MoS 2 nanosheets. *Scientific reports*, *4*, p.5649.

[310] P. Johari and V. B. Shenoy, "Tuning the Electronic Properties of Semi- conducting Transition Metal Dichalco- genides by Applying Mechanical Strains," *ACS Nano*, vol. 6, no. 6, pp. 5449–5456, 2012.

[311] M. Mos, J. Son, K. Kim, Y. H. Ahn, H. Lee, and J. Lee, "Strain Engineering of the Berry Curvature Dipole and Valley Magnetization," *Phys. Rev. Lett.*, vol. 123, no. 3, p. 36806, 2019.

[312] Alidoust, N., Bian, G., Xu, S.Y., Sankar, R., Neupane, M., Liu, C., Belopolski, I., Qu, D.X., Denlinger, J.D., Chou, F.C. and Hasan, M.Z., 2014. Observation of monolayer valence band spin-orbit effect and induced quantum well states in MoX 2. *Nature communications*, *5*(1), pp.1-9.

[313] Z. Wang *et al.*, "Intravalley Spin-Flip Relaxation Dynamics in Single-Layer WS2," *Nano Lett.*, vol. 18, no. 11, pp. 6882–6891, 2018.

[314] Ramasubramaniam, A., 2012. Large excitonic effects in monolayers of molybdenum and tungsten dichalcogenides. *Physical Review B*, *86*(11), p.115409.

[315] D. B. Farmer, Y. M. Lin, and P. Avouris, "Graphene field-effect transistors with self-aligned gates," *Appl. Phys. Lett.*, vol. 97, no. 1, pp. 1–3, 2010.

[316] Y. Yoon and J. Guo, "Effect of edge roughness in graphene nanoribbon transistors," *Appl. Phys. Lett.*, vol. 91, no. 7, pp. 10–13, 2007.

[317] G. Pizzi, M. Gibertini, E. Dib, N. Marzari, G. Iannaccone, and G. Fiori, "Performance of arsenene and antimonene double-gate MOSFETs from first principles," *Nat. Commun.*, vol. 7, p. 12585, 2016.

[318] F. Schwierz, J. Pezoldt, and R. Granzner, "Two-dimensional materials and their prospects in transistor electronics," *Nanoscale*, vol. 7, no. 18, pp. 8261–8283, 2015.

[319] K. S. Novoselov *et al.*, "A roadmap for graphene," *Nature*, vol. 490, no. 7419, pp. 192–200, 2013.

[320] A. K. Geim and K. S. Novoselov, "The rise of graphene," *Nat. Mater.*, vol. 6, no. 3, pp. 183–191, 2007.

[321] A. H. C. Neto, F. Guinea, N. M. R. Peres, K. S. Novoselov, and A. K. Geim, "The electronic properties of graphene," *Rev. Mod. Phys.*, vol. 81, no. 1, p. 109, 2009.

[322] Y. Zhang *et al.*, "Direct observation of a widely tunable bandgap in bilayer graphene," *Nature*, vol. 459, no. 7248, pp. 820–823, 2009.

[323] F. Xia, D. B. Farmer, Y. Lin, and P. Avouris, "Graphene field-effect transistors with high on/off current ratio and large transport band gap at room temperature," *Nano Lett.*, vol. 10, no. 2, pp. 715–718, 2010.

[324] M. Ghorbani-Asl, N. Zibouche, M. Wahiduzzaman, A. F. Oliveira, A. Kuc, and T. Heine, "Electromechanics in MoS2 and WS2: nanotubes vs. monolayers," *Sci. Rep.*, vol. 3, p. 2961, 2013.

[325] A. Kuc and T. Heine, “The electronic structure calculations of two-dimensional transition-metal dichalcogenides in the presence of external electric and magnetic fields.,” *Chem. Soc. Rev.*, vol. 44, no. 9, pp. 2603–14, 2015.

[326] Y. Shi, H. Li, and L.-J. Li, “Recent advances in controlled synthesis of two-dimensional transition metal dichalcogenides via vapour deposition techniques.,” *Chem. Soc. Rev.*, vol. 44, no. 9, pp. 2744–56, 2015.

[327] B. Radisavljevic and A. Kis, “Mobility engineering and a metal-insulator transition in monolayer MoS_2.,” *Nat. Mater.*, vol. 12, no. 9, pp. 815–20, 2013.

[328] T. Wu and H. Zhang, “Piezoelectricity in Two-Dimensional Materials,” *Angew. Chemie - Int. Ed.*, vol. 54, no. 15, pp. 4432–4434, 2015.

[329] M. M. Alyörük, Y. Aierken, D. Çakır, F. M. Peeters, and C. Sevik, “Promising piezoelectric performance of single layer transition-metal dichalcogenides and dioxides,” *J. Phys. Chem. C*, vol. 119, no. 40, pp. 23231–23237, 2015.

[330] W. Wu *et al.*, “Piezoelectricity of single-atomic-layer MoS2 for energy conversion and piezotronics,” *Nature*, vol. 514, no. 7523, pp. 470–474, 2014.

[331] A. R. Rezk *et al.*, “Acoustically-Driven Trion and Exciton Modulation in Piezoelectric Two-Dimensional MoS2,” *Nano Lett.*, vol. 16, no. 2, pp. 849–855, 2016.

[332] W. Liu, A. Zhang, Y. Zhang, and Z. L. Wang, “Density functional studies on edge-contacted single-layer MoS2 piezotronic transistors,” *Appl. Phys. Lett.*, vol. 107, no. 8, p. 083105, 2015.

[333] X. Q. Yu, Z. G. Zhu, G. Su, and A. P. Jauho, “Thermally Driven Pure Spin and Valley Currents via the Anomalous Nernst Effect in Monolayer Group-VI Dichalcogenides,” *Phys. Rev. Lett.*, vol. 115, no. 24, pp. 1–5, 2015.

[334] J. Zhou, C. Huang, E. Kan, and P. Jena, “Valley contrasting in epitaxial growth of In/Tl homoatomic monolayer with anomalous Nernst conductance,” *Phys. Rev. B - Condens. Matter Mater. Phys.*, vol. 94, no. 3, pp. 1–7, 2016.

[335] D. Q. Zheng, Z. Zhao, R. Huang, J. Nie, L. Li, and Y. Zhang, “High-performance piezo-phototronic solar cell based on two-dimensional materials,” *Nano Energy*, vol. 32, no. December 2016, pp. 448–453, 2017.

[336] B. Amin, T. P. Kaloni, and U. Schwingenschlögl, “Strain engineering of WS_2, WSe_2, and WTe_2,” *RSC Adv.*, vol. 4, no. 65, p. 34561, 2014.

[337] Sa, B., Li, Y.L., Qi, J., Ahuja, R. and Sun, Z., 2014. Strain engineering for phosphorene: the potential application as a photocatalyst. *The Journal of Physical Chemistry C*, *118*(46), pp.26560-26568.

[338] W. Zhou and N. Umezawa, “Band gap engineering of bulk and nanosheet SnO : an insight into the interlayer Sn – Sn lone pair,” *Phys. Chem. Chem. Phys.*, vol. 17, pp. 17816–17820, 2015.

[339] D. M. Guzman and A. Strachan, “Role of strain on electronic and mechanical response of semiconducting transition-metal dichalcogenide monolayers: An ab-initio study,” *J. Appl. Phys.*, vol. 115, no. 24, 2014.

[340] S. Dai, M. Gharbi, P. Sharma, and H. S. Park, “Surface piezoelectricity: Size effects in nanostructures and the emergence of piezoelectricity in non-piezoelectric materials,” *J. Appl. Phys.*, vol. 110, no. 10, pp. 1–7, 2011.

[341] A. Mahmoud, A. Erba, K. E. El-Kelany, M. Rérat, and R. Orlando, “Low-temperature phase of BaTiO 3: Piezoelectric, dielectric, elastic, and photoelastic properties from ab initio simulations,” *Phys. Rev. B*, vol. 89, no. 4, p. 45103, 2014.

[342] K. E. El-Kelany, A. Erba, P. Carbonnière, and M. Rérat, “Piezoelectric, elastic, structural and dielectric properties of the Si1− xGexO2 solid solution: a theoretical study,” *J. Phys. Condens. Matter*, vol. 26, no. 20, p. 205401, 2014.

[343] P. Hohenberg and W. Kohn, “Inhomogeneous electron gas,” *Phys. Rev.*, vol. 136, no. 3B, p. B864, 1964.

[344] G. Kresse and J. Furthmüller, “Efficiency of ab-initio total energy calculations for metals and semiconductors using a plane-wave basis set,” *Comput. Mater. Sci.*, vol. 6, no. 1, pp. 15–50, 1996.

[345] J. P. Perdew, K. Burke, and M. Ernzerhof, “Generalized Gradient Approximation Made Simple- ERRATA,” *Phys. Rev. Lett.*, vol. 77, no. 18, pp. 3865–3868, 1996.

[346] L. Jiang *et al.*, “Optimizing Hybridization of 1T and 2H Phases in MoS2 Monolayers to Improve Capacitances of Supercapacitors,” *Mater. Res. Lett.*, vol. 3, no. 4, pp. 177–183, 2015.

[347] K. M. Fair and M. J. Ford, “Phase transitions and optical properties of the semiconducting and metallic phases of single-layer MoS 2,” *Nanotechnology*, vol. 26, no. 43, p. 435705, 2015.

[348] Z. Hu, S. Zhang, Y.-N. Zhang, D. Wang, H. Zeng, and L.-M. Liu, “Modulating the phase transition between metallic and semiconducting single-layer MoS2 and WS2 through size effects,” *Phys. Chem. Chem. Phys.*, vol. 17, no. 2, pp. 1099–1105, 2015.

[349] M. Kan *et al.*, “Structures and Phase Transition of a MoS 2 Monolayer,” *J. Phys. Chem. C*, vol. 118, no. 3, pp. 1515–1522, 2014.

[350] C. Ataca, M. Topsakal, E. Aktürk, and S. Ciraci, “A comparative study of lattice dynamics of three- and two-dimensional MoS2,” *J. Phys. Chem. C*, vol. 115, no. 33, pp. 16354–16361, 2011.

[351] P. Liu, A. De Sarkar, and R. Ahuja, “Shear strain induced indirect to direct transition in band gap in AlN monolayer nanosheet,” *Comput. Mater. Sci.*, vol. 86, pp. 206–210, 2014.

[352] C. Zhang, A. De Sarkar, and R. Q. Zhang, “Strain induced band dispersion engineering in Si nanosheets,” *J. Phys. Chem. C*, vol. 115, no. 48, pp. 23682–23687, 2011.

[353] R. G. A. and X. Z. and S. M. and R. P. and A. R. R. and S. P. Karna, “Strain- and electric field-induced band gap modulation in nitride nanomembranes,” *J. Phys. Condens. Matter*, vol. 25, no. 19, p. 195801, 2013.

[354] K. A. N. Duerloo, M. T. Ong, and E. J. Reed, “Intrinsic piezoelectricity in two-dimensional materials,” *J. Phys. Chem. Lett.*, vol. 3, no. 19, pp. 2871–2876, 2012.

[355] T. Kubo *et al.*, “Suppressing molecular vibrations in organic semiconductors by inducing strain,” *Nat. Commun.*, vol. 7, p. 11156, 2016.

[356] G. Tsoukleri *et al.*, “Subjecting a graphene monolayer to tension and compression,” *Small*, vol. 5, no. 21, pp. 2397–2402, 2009.

[357] P. Lu, X. Wu, W. Guo, and X. C. Zeng, “Strain-dependent electronic and magnetic properties of MoS2 monolayer, bilayer, nanoribbons and nanotubes,” *Phys. Chem. Chem. Phys.*, vol. 14, no. 37, p. 13035, 2012.

[358] L. Dong, R. R. Namburu, T. P. O’Regan, M. Dubey, and A. M. Dongare, “Theoretical study on strain-induced variations in electronic properties of monolayer MoS2,” *J. Mater. Sci.*, vol. 49, no. 19, pp. 6762–6771, 2014.

[359] J. Bardeen and W. Shockley, “Deformation potentials and mobilities in non-polar crystals,” *Phys. Rev.*, vol. 80, no. 1, pp. 72–80, 1950.

[360] G. Wang, R. Pandey, and S. P. Karna, “Carbon phosphide monolayers with superior carrier mobility,” *Nanoscale*, vol. 8, no. 16, pp. 8819–8825, 2016.

[361] J. Zhang *et al.*, “Titanium Trisulfide Monolayer as a Potential Thermoelectric Material: A First-Principles-Based Boltzmann Transport Study,” *ACS Appl. Mater. Interfaces*, vol. 9, no. 3, pp. 2509–2515, 2017.

[362] Zhou, M., Chen, X., Li, M. and Du, A., 2017. Widely tunable and anisotropic charge carrier mobility in monolayer tin (II) selenide using biaxial strain: a first-principles study. *Journal of Materials Chemistry C*, *5*(5), pp.1247-1254.

[363] K. S. Novoselov *et al.*, “Two-dimensional atomic crystals.,” *Proc. Natl. Acad. Sci. U. S. A.*, vol. 102, no. 30, pp. 10451–3, Jul. 2005.

[364] M. Chhowalla, H. S. Shin, G. Eda, L.-J. Li, K. P. Loh, and H. Zhang, “The chemistry of two-dimensional layered transition metal dichalcogenide nanosheets,” *Nat. Chem.*, vol. 5, no. 4, pp. 263–275, 2013.

[365] C. Tan and H. Zhang, “Two-dimensional transition metal dichalcogenide nanosheet-based composites.,” *Chem. Soc. Rev.*, vol. 44, no. July 2006, pp. 2713–2731, 2015.

[366] D. Lembke, S. Bertolazzi, and A. Kis, “Single-layer MoS2 electronics,” *Acc. Chem. Res.*, vol. 48, no. 1, pp. 100–110, 2015.

[367] RadisavljevicB *et al.*, “Single-layer MoS2 transistors,” *Nat Nano*, vol. 6, no. 3, pp. 147–150, 2011.

[368] K. F. Mak, K. L. McGill, J. Park, and P. L. McEuen, “The valley Hall effect in MoS2 transistors,” *Science (80-.).*, vol. 344, no. 6191, pp. 1489–1492, 2014.

[369] Zhu, C.R., Wang, G., Liu, B.L., Marie, X., Qiao, X.F., Zhang, X., Wu, X.X., Fan, H., Tan, P.H., Amand, T. and Urbaszek, B., 2013. Strain tuning of optical emission energy and polarization in monolayer and bilayer MoS 2. *Physical Review B*, *88*(12), p.121301.

[370] D. Lloyd *et al.*, “Band Gap Engineering with Ultralarge Biaxial Strains in Suspended Monolayer MoS2,” *Nano Lett.*, vol. 16, no. 9, pp. 5836–5841, 2016.

[371] Bertolazzi, S., Brivio, J. and Kis, A., 2011. Stretching and Breaking of Ultrathin MoS2. ACS Nano, 5, 9703-9709.

[372] A. Castellanos-Gomez, M. Poot, G. A. Steele, H. S. J. Van Der Zant, N. Agraït, and G. Rubio-Bollinger, “Elastic properties of freely suspended MoS 2 nanosheets,” *Adv. Mater.*, vol. 24, no. 6, pp. 772–775, 2012.

[373] Y. Cai, J. Lan, G. Zhang, and Y. W. Zhang, “Lattice vibrational modes and phonon thermal conductivity of monolayer MoS 2,” *Phys. Rev. B - Condens. Matter Mater. Phys.*, vol. 89, no. 3, pp. 1–8, 2014.

[374] S. Bertolazzi, J. Brivio, and A. Kis, “Stretching and breaking of ultrathin MoS 2,” *ACS Nano*, vol. 5, no. 12, pp. 9703–9709, 2011.

[375] H. Sahin *et al.*, “Anomalous Raman spectra and thickness-dependent electronic properties of WSe2,” *Phys. Rev. B - Condens. Matter Mater. Phys.*, vol. 87, no. 16, pp. 1–6, 2013.

[376] Y. Ge, W. Wan, W. Feng, D. Xiao, and Y. Yao, “Effect of doping and strain modulations on electron transport in monolayer MoS2,” *Phys. Rev. B - Condens. Matter Mater. Phys.*, vol. 90, no. 3, pp. 1–6, 2014.

[377] D. Joubert, “From ultrasoft pseudopotentials to the projector augmented-wave method,” *Phys. Rev. B - Condens. Matter Mater. Phys.*, vol. 59, no. 3, pp. 1758–1775, 1999.

[378] G. Kresse and J. Hafner, “Ab initio molecular dynamics for liquid metals,” *Phys. Rev. B*, vol. 47, no. 1, p. 558, 1993.

[379] G. Kresse and J. Furthmüller, “Efficient iterative schemes for ab initio total-energy calculations using a plane-wave basis set,” *Phys. Rev. B*, vol. 54, no. 16, pp. 11169–11186, 1996.

[380] S. Baroni, S. De Gironcoli, A. Dal Corso, and P. Giannozzi, “Phonons and related crystal properties from density-functional perturbation theory,” *Rev. Mod. Phys.*, vol. 73, no. 2, p. 515, 2001.

[381] A. Togo, F. Oba, and I. Tanaka, “First-principles calculations of the ferroelastic transition between rutile-type and CaCl 2-type SiO 2 at high pressures,” *Phys. Rev. B*, vol. 78, no. 13, p. 134106, 2008.

[382] Y. Cai, G. Zhang, and Y.-W. Zhang, “Polarity-Reversed Robust Carrier Mobility in Monolayer MoS2 Nanoribbons,” *J. Am. Chem. Soc.*, vol. 136, no. 17, pp. 6269–6275, Apr. 2014.

[383] A. Molina-Sánchez and L. Wirtz, “Phonons in single-layer and few-layer MoS2 and WS2,” *Phys. Rev. B - Condens. Matter Mater. Phys.*, vol. 84, no. 15, 2011.

[384] Y. Ge and A. Y. Liu, “Phonon-mediated superconductivity in electron-doped single-layer MoS 2: A first-principles prediction,” *Phys. Rev. B - Condens. Matter Mater. Phys.*, vol. 87, no. 24, pp. 1–5, 2013.

[385] H. Li *et al.*, “From bulk to monolayer MoS2: evolution of Raman scattering,” *Adv. Funct. Mater.*, vol. 22, no. 7, pp. 1385–1390, 2012.

[386] Rice, C., Young, R.J., Zan, R., Bangert, U., Wolverson, D., Georgiou, T., Jalil, R. and Novoselov, K.S., 2013. Raman-scattering measurements and first-principles calculations of strain-induced phonon shifts in monolayer MoS 2. *Physical Review B*, *87*(8), p.081307.

[387] L. Sun *et al.*, “Spin-orbit splitting in single-layer MoS2 revealed by triply resonant raman scattering,” *Phys. Rev. Lett.*, vol. 111, no. 12, pp. 1–5, 2013.

[388] Yang, L., Cui, X., Zhang, J., Wang, K., Shen, M., Zeng, S., Dayeh, S.A., Feng, L. and Xiang, B., 2014. Lattice strain effects on the optical properties of MoS 2 nanosheets. *Scientific reports*, *4*, p.5649.

[389] N. Jena, R. Ahammed, A. Rawat, M. K. Mohanta, and A. De Sarkar, “Valley drift and valley current modulation in strained monolayer Mo S 2,” *Phys. Rev. B*, vol. 100, no. 16, p. 165413, 2019.

[390] C. Rice *et al.*, “Raman-scattering measurements and first-principles calculations of strain-induced phonon shifts in monolayer MoS 2,” *Phys. Rev. B*, vol. 87, no. 8, p. 81307, 2013.

[391] Mohiuddin, T.M.G., Lombardo, A., Nair, R.R., Bonetti, A., Savini, G., Jalil, R., Bonini, N., Basko, D.M., Galiotis, C., Marzari, N. and Novoselov, K.S., 2009. Uniaxial strain in graphene by Raman spectroscopy: G peak splitting, Grüneisen parameters, and sample orientation. *Physical Review B*, *79*(20), p.205433.

[392] M. Huang, H. Yan, C. Chen, D. Song, T. F. Heinz, and J. Hone, “Phonon softening and crystallographic orientation of strained graphene studied by Raman spectroscopy.,” *Proc. Natl. Acad. Sci. U. S. A.*, vol. 106, no. 18, pp. 7304–7308, 2009.

[393] Mouhat, F. and Coudert, F.X., 2014. Necessary and sufficient elastic stability conditions in various crystal systems. *Physical review B*, *90*(22), p.224104.

[394] Le Page, Y. and Saxe, P., 2002. Symmetry-general least-squares extraction of elastic data for strained materials from ab initio calculations of stress. *Physical Review B*, *65*(10), p.104104.

[395] Çakır, D., Peeters, F.M. and Sevik, C., 2014. Mechanical and thermal properties of h-MX2 (M= Cr, Mo, W; X= O, S, Se, Te) monolayers: A comparative study. *Applied Physics Letters*, *104*(20), p.203110.

[396] J. Kang, S. Tongay, J. Zhou, J. Li, and J. Wu, "Band offsets and heterostructures of two-dimensional semiconductors," *Appl. Phys. Lett.*, vol. 102, no. 1, pp. 22–25, 2013.

[397] Q. Peng and S. De, "Outstanding mechanical properties of monolayer MoS2 and its application in elastic energy storage.," *Phys. Chem. Chem. Phys.*, vol. 15, no. 44, pp. 19427–37, 2013.

[398] J. Li, N. V. Medhekar, and V. B. Shenoy, "Bonding charge density and ultimate strength of monolayer transition metal dichalcogenides," *J. Phys. Chem. C*, vol. 117, no. 30, pp. 15842–15848, 2013.

[399] D. M. Guzman and A. Strachan, "Role of strain on electronic and mechanical response of semiconducting transition-metal dichalcogenide monolayers: An ab-initio study," *J. Appl. Phys.*, vol. 115, no. 24, 2014.

----------**********----------

[Vita]

Nityasagar Jena joined the Institute of Nano Science and Technology Mohali (INST-Mohali) in January 2015 for his doctoral dissertation by research, and registered at the Indian Institute of Science Education and Research Mohali (IISER-Mohali) for the award of the *Degree of Doctor of Philosophy*. He has earned his Bachelor of Science degree from Ravenshaw University (A deemed University), Cuttack, and Master of Science degree from Pondicherry University (A Central University), Puducherry with Physics as his major subject. He was the recipient of the Samaj Scholarship and Prof. Pranakrushna Parija memorial award for his academic excellence.

He joined INST-Mohali as the second batch of Ph.D. student and 2nd doctoral student of Prof. Abir De Sarkar. His scientific expertise and area of research includes: *ab initio* study of layered two-dimensional materials (transition-metal dichalcogenides of group VIB elements in particular) for novel electronics and energy conversion systems.

@Nitya